

DEVELOPMENT OF EMPIRICAL AND MECHANISTIC MODELS FOR PERMANENT DEFORMATION IN SUBGRADE SOILS

January 2016

Foreword

This report presents the analyses conducted for the development of empirical and mechanistic models for permanent deformation in subgrade soils using data collected as part of the Transportation Pooled Fund Study project SPR-2(208) titled “Pavement Subgrade Performance Study.” The SPR-2(208) study was conducted at the Cold Region Research Laboratory (CRREL) of the U.S. Army Corps of Engineers in Hanover, New Hampshire, between 1999 and 2007. In this study, flexible pavements with the same granular base layer and asphalt concrete surface layer were built inside the Frost Effects Research Facility and were subjected to accelerated pavement testing (APT).

The pavements were built with a combination of four soil types (Type A-2-4, A-4, A-6 and A-7-5) and three moisture levels, which resulted in a total of 12 sets of pavement sections, named cells. Each of the four soil types were placed in the pits of the facility. For each cell, between four and six pavement sections, named windows, were subjected to accelerated pavement testing. The MARK HVS IV was used as the loading device. Up to four wheel load magnitudes were used for the windows in the same cell. The test sections were instrumented with stress, strain, moisture and temperature sensors. Surface rutting was monitored with a laser profilometer. Falling Weight Deflectometer (FWD) tests were performed on each pavement section before the application of accelerated traffic.

Empirical models for predicting permanent deformation in subgrade soils using non-linear regression analysis were developed. For each soil type and moisture content, the analysis estimated constants for three models existing in the literature, including the model incorporated

in the MEPDG model. A new model for predicting permanent deformation in subgrade soils is also proposed.

In order to gain an understanding of the fundamental influence of various soil parameters on pavement performance, advanced constitutive models that can predict the behavior of sandy and silty and clayey subgrade soil deformation under repeated traffic loading were developed. They were then implemented into the finite element software Abaqus and used to predict the observed results of the CRREL databank. Parametric studies to identify the influence of the key variables on pavement performance were then conducted.

The model for sand was based on critical state and bounding surface concepts and incorporates parameters to account for sand fabric and suction. The model was implemented into Abaqus using UMAT subroutine. The model performance was verified on a wide range of triaxial test data that includes different drainage conditions, sample preparation method, density, confining stress and mode of shear. Simulation results show that saturation level significantly affects sand performance and a modified suction based state parameter was proposed to better describe unsaturated sand behavior. This parameter was found to correlate well with increase in peak stress due to decrease in saturation level.

The model for clay and silty subgrades was based on the Drucker-Prager CAP model. The procedure of determining the parameters of Drucker-Prager (D-P) Cap model was simplified. Laboratory tests on CRREL silty and clayey soil were performed under several moisture contents and the model parameters were determined. It was found that suction had a significant effect on the model parameters.

The developed 3D FE model quantified the response of pavement subgrades under differing loading magnitudes, asphalt and base properties, and saturation levels. Subgrades built with soil type A-2-4 were simulated with sand model; Subgrades built with type A-4, A-6 and A-7-5 were simulated using the D-P Cap model. Parametric studies conducted showed that the moduli of asphalt and base and the saturation level of the subgrades influenced the vertical deformation experienced near the top of subgrade, especially for high wheel loads, but their influence gradually reduced with depth.

Notice

This document is disseminated under the sponsorship of the U.S. Department of Transportation in the interest of information exchange. The United States Government assumes no liability for the use of the information contained in this document. This report does not constitute a standard, specification, or regulation.

The United States Government does not endorse products or manufacturers. Trademarks or manufacturer's names appear in this report only because they are considered essential to the objective of the document.

Form DOT F 1700.7 (8-72)

1. Report No.	2. Government Accession No.		3. Recipient's Catalog No.	
4. Title and Subtitle <i>Modeling the Deformation of Unsaturated Granular Pavement Subgrade Materials</i>		5. Report Date January 2016		
		6. Performing Organization Code:		
7. Author(s) B. Muhunthan, S. Romanoshi, Y. Liu, S. Sutharsan		8. Performing Organization Report No.		
9. Performing Organization Name and Address Engineering & Software Consultants, Inc., Chantilly, Virginia Washington State University, Pullman, Washington Pavement Consulting Services, LLC, Irving, Texas		10. Work Unit No.		
		11. Contract or Grant No. DTFH61-11-D-00009		
12. Sponsoring Agency Name and Address		13. Type of Report and Period Covered Guidelines		
		14. Sponsoring Agency Code		
15. Supplementary Notes				
<p>16. Abstract</p> <p>This report details the development of empirical and advanced constitutive models to predict the performance of pavement subgrade materials. A statistical analysis was performed on the response and performance data collected at Pavement Subgrade Performance Study (PSPS), a major research project conducted at the Cold Region Research Laboratory (CRREL) of the U.S. Army Corps of Engineers in Hanover, New Hampshire. Empirical models for predicting permanent deformation in subgrade soils using non-linear regression analysis were developed. For each soil type and moisture content, the analysis estimated constants for three models existing in the literature, including the model incorporated in the MEPDG pavement design model. A new model for predicting permanent deformation in subgrade soils is also proposed.</p> <p>The study also includes mechanistic models based on elasto-plasticity to predict the behavior of subgrades under traffic loads. The first model for sandy soils was based on critical state surface and the second for clayey and silty soils was based on the Drucker-Prager (D-P) Cap surface. Both models were implemented into the Abaqus finite element software and their performance verified on CRREL soils. The developed 3D FE model quantifies the response of pavement subgrades under differing load magnitudes, asphalt and base properties, and saturation levels.</p>				
17. Key Words Soils, empirical models, mechanistic models, statistics, MEPDG, Simulations		18. Distribution Statement No restrictions. This document is available to the public through the National Technical Information Service, Springfield, Virginia 22161; www.ntis.gov		
19. Security Classif. (of report) Unclassified		20. Security Classif. (of this page) Unclassified	21. No. of pages 214	22. Price

Form DOT F 1700.7 (8-72)

Reproduction of completed page authorized

TABLE OF CONTENTS

TABLE OF CONTENTS	vii
LIST OF TABLES	xiii
LIST OF FIGURES	xvi
CHAPTER ONE	1
INTRODUCTION	1
1.1 General	1
1.2 Objectives of Study.....	3
1.3 Organization of Report	3
CHAPTER TWO	6
BACKGROUND	6
2.1 Empirical Permanent Deformation Models	6
2.2 Numerical analysis.....	24
2.2.1 Double Hardening Model	26
2.2.2 Volumetric Hardening Model	27
2.2.3 Cyclic densification model	27
2.2.4 Critical state two surface plasticity model	28
2.2.5 Drucker-Prager Cap model	32

2.3 Comprehensive review of SPR-2(208) products	35
2.3.1 Soil type	35
2.3.2 APT test data.....	37
CHAPTER THREE	41
DEVELOPMENT OF EMPIRICAL MODELS FOR PERMANENT DEFORMATION	41
3.1 Pavement Response Datasets.....	41
3.2 Derivation of Permanent Deformation Models of Known Form.....	47
3.3 Derivation of Permanent Deformation Models of Unknown Form.....	54
CHAPTER FOUR	65
DEVELOPMENT AND IMPLEMENTATION OF A CONSTITUTIVE MODEL FOR UNSATURATED SANDS	65
4.1 Introduction.....	65
4.2 Model Development.....	67
4.2.1 General Framework	67
4.2.2 Mapping Rules	71
4.2.3 Elastic modulus.....	74
4.2.4 Fabric anisotropy	75
4.2.5 Anisotropic state variable	76
4.2.6 State parameter.....	77

4.2.7 Dilatancy	78
4.2.8 Plastic Modulus.....	79
4.2.9 Modification for unsaturated soils	81
4.3 Verification of new sand model.....	83
4.4 Unsaturated model behavior	87
4.5 Modified Suction State Parameter	92
4.6 Cyclic loading performance of sands.....	96
4.6.1 Sand performance under repeated loading.....	100
4.6.2 Sand performance under cyclic loading.....	105
4.7 Conclusion	111
CHAPTER FIVE	112
DEVELOPMENT OF DRUCKER-PRAGER CAP MODEL	112
5.1 Introduction.....	112
5.2 Model Development.....	112
5.2.1 Parameters of D-P Cap Model	112
5.2.2 Ultimate Failure Surface	114
5.2.3 Elastic and Plastic Behavior.....	115
5.2.4 Cap Surface	117
5.3 Methods for determining the parameters of D-P Cap Model	118

5.3.1 Determination of Ultimate Failure Surface.....	118
5.3.2 Determining Elastic and Plastic Behavior	121
5.3.3 Determination of the Cap Surface.....	122
5.3.4 Determination of Hardening Law	124
CHAPTER SIX	126
LABORATORY TESTS	126
6.1 Laboratory Determination of Resilient Modulus of Aggregate Base	126
6.1.1 Selection of the test conditions	127
6.1.2 Resilient Modulus Tests.....	131
6.1.3 Laboratory Resilient Modulus Test Results.....	136
6.1.4 Development of Non-Linear Stiffness Model for the Granular Base Material	141
6.2 Tests Matrix of D-P Cap Model.....	145
6.3 Tests Performed to Determine Parameters of D-P Cap model	146
6.3.1 Standard Proctor Compaction Test	146
6.3.2 Atterberg Limits (LL and PL), and Specific Gravity (Gs) Tests	148
6.3.3 Soil Water Characteristic Curve (SWCC) Test	149
6.3.4 Indirect Tensile Strength Test (IDT).....	157
6.3.5 Unconfined Compressive Strength Tests (UCS)	163
6.3.6 Triaxial Test	167

CHAPTER SEVEN	180
3D FE MODEL ANALYSES	180
7.1 Introduction.....	180
7.2 Development of 3-D Finite Element Model	180
7.3 Verification of model performance.....	188
7.4 Subgrade performance analysis	191
7.4.1 Standard Condition	191
7.4.2 Influence of Asphalt and Base properties	195
7.4.3 Influence of suction in subgrade performance.....	203
CHAPTER EIGHT	209
CONCLUSIONS	209
8.1 Conclusions.....	209
8.2 Suggestions for future research.....	212
REFERENCES	215
APPENDIX A	228
CALIBRATION PROCEDURE OF NEW SAND MODEL PARAMETERS	228
APPENDIX B	233
MATLAB PROGRAM FOR DETERMINING D-P CAP MODEL PARAMETERS	233
APPENDIX C	245

UMAT SUBROUTINE OF THE NEW SAND MODEL	245
APPENDIX D	302
MATRIC SUCTION TEST RESULTS OF CRREL SOILS	302
APPENDIX E	305
UNIAXIAL COMPRESSIVE STRENGTH TEST RESULTS OF CRREL SOILS	305
APPENDIX F	313
RESILIENT MODULUS TEST RESULTS ON BASE MATERIAL	313

LIST OF TABLES

Table 2.1: Transfer functions for subgrade rutting models.....	9
Table 2.2: Parameters for CAP model	34
Table 2.3: Subgrade soil properties (Data from Cortez ⁽¹⁷⁾).	36
Table 2.4: Experimental test cells and windows.....	37
Table 2.5: Soil types and locations of different natural soils used in project SPR-2(208) (modified from Janoo et al. ⁽⁴⁷⁾)	40
Table 3.1: Results of the Non-linear Regression Analysis for the Odermatt model.....	50
Table 3.2: Results of the Non-linear Regression Analysis for the Theyse model	51
Table 3.3: Results of the Non-linear Regression Analysis for the MEPDG model.....	54
Table 3.4: Results of the Non-linear Regression Analysis for Model 1	61
Table 3.5: Results of the Non-linear Regression Analysis for Model 3	62
Table 3.6: Permanent Deformation Models with OMC as Independent Variable.....	64
Table 4.1: New sand model Parameters for Toyoura Sand.....	84
Table 4.2: Comparison of different sand properties	97
Table 4.3 Description of four different situations	106
Table 5.1: Cap-Model Parameters in Proposed Procedure	113
Table 6.1: Results of the Modified Proctor tests (AASHTO T 180)	128
Table 6.2: Moisture-Density test results given in the PSPS Reports	130
Table 6.3: Average in-situ density and moisture content given in project reports	131
Table 6.4: Loading Sequence during the Tri-axial Resilient Modulus Test	134

Table 6.5: As-compacted Properties of the Resilient Modulus Test Samples	137
Table 6.6: Regression Parameters Models for the original resilient modulus model	143
Table 6.7: Regression Parameters Models for the modified resilient modulus model	144
Table 6.8: Test Matrix of D-P Cap model	145
Table 6.9: OMC & MDD values of CRREL soils	146
Table 6.10: Atterberg limits and specific gravity	149
Table 6.11: Obtained Parameters of SWCC	153
Table 6.12: IDT Test Results	160
Table 6.13: Internal Friction Angle (For D-P model in Abaqus).....	162
Table 6.14: UCS test results for CRREL soils.....	164
Table 6.15: Cap position of soil Type A-6.....	169
Table 6.16: Cap position of soil Type A-4.....	170
Table 6.17: Cap position of soil Type A-75.....	170
Table 7.1: Elasticity properties of pavement layers (data from Janoo et al. ⁽⁵¹⁾)	184
Table 7.2: Parameters input in FE analysis.....	189
Table 7.3: Asphalt and Base Elastic Modulus	196
Table F.1: Resilient Modulus Test Results – Sample 1	313
Table F.2:: Resilient Modulus Test Results – Sample 2.....	314
Table F.3: Resilient Modulus Test Results – Sample 3	314
Table F.4: Resilient Modulus Test Results – Sample 4	315
Table F.5: Resilient Modulus Test Results – Sample 5	315
Table F.6: Resilient Modulus Test Results – Sample 6	316

Table F.7: Resilient Modulus Test Results – Sample 7	316
Table F.8: Resilient Modulus Test Results – Sample 8	317
Table F.9: Resilient Modulus Test Results – Sample 9	317
Table F.10: Resilient Modulus Test Results – Sample 10	318
Table F.11: Resilient Modulus Test Results – Sample 11	318
Table F.12: Resilient Modulus Test Results – Sample 12	319
Table F.13: Resilient Modulus Test Results – Sample 13	319
Table F.14: Resilient Modulus Test Results – Sample 14	320
Table F.15: Resilient Modulus Test Results – Sample 15	320
Table F.16: Resilient Modulus Test Results – Sample 16	321
Table F.17: Resilient Modulus Test Results – Sample 17	321
Table F.18: Resilient Modulus Test Results – Sample 18	322
Table F.19: Resilient Modulus Test Results – Sample 19	322
Table F.20: Resilient Modulus Test Results – Sample 20	323
Table F.21: Resilient Modulus Test Results – Sample 21	323
Table F.22: Resilient Modulus Test Results – Sample 22	324
Table F.23: Resilient Modulus Test Results – Sample 23	324
Table F.24: Resilient Modulus Test Results – Sample 24	325
Table F.25: Resilient Modulus Test Results – Sample 25	325
Table F.26: Resilient Modulus Test Results – Sample 26	326

LIST OF FIGURES

Figure 2.1: Typical evolution of accumulated permanent deformation.....	16
Figure 2.2: Comparison of predicted and measured permanent strain ⁽³¹⁾	19
Figure 2.3: Effect of freeze-thaw cycles on permanent strain - Sacul soil, AASHTO A-6 ⁽³²⁾ ...	21
Figure 2.4: Permanent downward displacement of MDD modules with increasing load repetitions ⁽³³⁾	24
Figure 2.5: Schematic illustration of drained and undrained paths in e , $\ln p$ space for a state denser than critical (point <i>a</i>) and looser than critical (point <i>b</i>) ⁽²⁾	30
Figure 2.6: Schematic illustration in the η , 1 space of the bounding (peak) stress ratio (M_{cb}), critical stress ratio (M_c), and dilatancy stress ratio (M_{cd}), the back stress ratio α , the wedge type yield surface and constant- p drained paths of Figure 2.5 ⁽²⁾	30
Figure 2.7: Modified Drucker-Prager/cap model : yield surface in the p (mean effective normal stress)- t plane. ⁽⁵⁵⁾	33
Figure 2.8: Modified Drucker-Prager/cap model: yield surface in the deviatoric plane ⁽⁵⁵⁾	34
Figure 2.9: Variety of soil types in the U.S. ⁽⁵⁶⁾	35
Figure 2.10: Subgrade soil particle distribution ⁽¹⁷⁾	36
Figure 2.11: Rut development with A-2-4 subgrade at 10% moisture content ⁽¹⁷⁾	39
Figure 3.1: Typical Evolution of Permanent Strain with the Number of Applied Load Cycles.	45
Figure 3.2: Example of Observed Evolution of Permanent (Plastic) Strain	45
Figure 3.3: Example of Joined Plastic Strain Segments	47
Figure 3.4: Chart of Unacceptable Model – Example 1	57

Figure 3.5: Chart of Unacceptable Model – Example 2	57
Figure 3.6: Chart of an Acceptable Model	58
Figure 4.1: Shear bounding surface (F_1) and cap bounding surface (F_2) (modified from Li ⁽⁴⁾) .	68
Figure 4.2: Mapping rule in deviatoric stress ratio space (modified from Li ⁽⁴⁾)	72
Figure 4.3: Illustration of relocation mechanism of projection center (modified from Li ⁽⁴⁾)....	73
Figure 4.4: Mapping rule for p under constant rij (modified from Li ⁽⁴⁾).....	74
Figure 4.5: Measurement and prediction of drained test for MT specimen with	85
Figure 4.6: Measurement and prediction of drained test	85
Figure 4.7: Measurement and prediction of undrained compression test with DD specimens at (a) $Dr=30\%$ (b) $Dr=41\%$	86
Figure 4.8: Measurement and prediction of undrained extension test with MT specimens at	87
Figure 4.9: Prediction of unsaturated drained test for (a) MT and (b) DD specimens at $e_0=0.977$ and confining stress =100 kPa	89
Figure 4.10: Prediction of unsaturated drained test for (a) MT and (b) DD specimens at $e_0=0.831$ and confining stress =100 kPa	90
Figure 4.11: $q - p$ and $e - (p/p_a)^{\xi}$ plots at (a) loose state ($e_0 = 0.977$) and (b) dense state ($e_0 = 0.831$) for MT samples.....	91
Figure 4.12: Critical state line in $e - (p/p_a)^{\xi}$ plane	92
Figure 4.13: Modification to initial state parameter of unsaturated loose sand due to suction ...	93
Figure 4.14: Modification to initial state parameter of unsaturated dense sand due to suction...	94
Figure 4.15: Percentage increase in peak deviatoric stress with $\psi MIUS$	96
Figure 4.16: Grain size distribution of different sand types	97

Figure 4.17: FE model to simulate triaxial test.....	98
Figure 4.18: Variation of deviatoric stress (q) with axial strain (ε_a).....	99
Figure 4.19: Test result of undrained cyclic triaxial on Nevada sand (Data from Arulmoli et al. ⁽⁸³⁾).....	99
Figure 4.20: Simulation of undrained cyclic triaxial results on Nevada Sand	100
Figure 4.21: Applied repeated loading	101
Figure 4.22: Variation of axial strain with number of loading cycles	102
Figure 4.23: Variation of axial permanent strain with loading cycles for loose moist tamped sample	102
Figure 4.24: Variation of axial permanent strain with loading cycles for loose dry deposited sample	103
Figure 4.25: Variation of axial permanent strain with loading cycles for dense moist tamped sample	103
Figure 4.26: Variation of axial permanent strain with loading cycles for dense dry deposited sample	104
Figure 4.27: Variation of loading cycles with saturation level.....	105
Figure 4.28: $e-(p/p_a)^\zeta$ curve (modified from Yang et al. ⁽⁷⁾)	106
Figure 4.29: Applied sinusoidal loading.....	107
Figure 4.30: $q-p$ curve during undrained cyclic triaxial test.....	108
Figure 4.31: $q-\varepsilon_a$ curve during undrained cyclic triaxial test.....	108
Figure 4.32: Variation of excess PWP with number of loading cycles in undrained cyclic triaxial test.....	109

Figure 4.33: Variation of excess PWP with number of loading cycles in undrained cyclic triaxial test at different relative density.....	110
Figure 4.34: Variation of loading cycles with relative density in undrained cyclic triaxial test	110
Figure 5.1: Relationship between Poisson's ratio and plasticity index (After Wroth ⁽⁸⁹⁾).....	121
Figure 5.2: Output of trial-and-error procedure	124
Figure 5.3: Output window of hardening law.....	125
Figure 6.1: Dry Density vs. Moisture Content for the Aggregate Base.....	129
Figure 6.2: Tri-axial Cell	133
Figure 6.3: Screen Capture Showing the Resilient Modulus Test Result.....	135
Figure 6.4: Wave shape of the Loading Pulse	135
Figure 6.5: Laboratory Resilient Modulus Results at 4.0% Moisture Content.....	138
Figure 6.6: Laboratory Resilient Modulus Results at 4.5% Moisture Content.....	138
Figure 6.7: Laboratory Resilient Modulus Results at 5.0% Moisture Content.....	139
Figure 6.8: Laboratory Resilient Modulus Results at 5.5% Moisture Content.....	139
Figure 6.9: Laboratory Resilient Modulus Results at 6.0% Moisture Content.....	140
Figure 6.10: Laboratory Resilient Modulus Results at 6.5% Moisture Content.....	140
Figure 6.11: MC-DD curves of CRREL soils.....	148
Figure 6.12: WP-4 Dewpoint PotentiaMeter device and specimens tested	150
Figure 6.13: (a) Specimens for suction test; (b) Moisture control.....	151
Figure 6.14: Matric suction vs. degree of saturation	153
Figure 6.15: Soil water characteristic curves.....	155
Figure 6.16: Soil suction characteristic curves for CRREL soils	156

Figure 6.17: Samples for IDT tests	157
Figure 6.18: Indirect tensile test on GCTS	158
Figure 6.19: Relationship between effective degree of saturation and IDT	162
Figure 6.20: UCS sample and GCTS device	163
Figure 6.21: Strain-Stress response (A-4 with 10.66% moisture content)	164
Figure 6.22: Relationship between effective degree of saturation and elastic modulus.....	166
Figure 6.23: Relationship between effective degree of saturation and UCS	166
Figure 6.24: Relationship between effective saturation degree and failure strain.....	167
Figure 6.25: Test device for CU-Triaxial	168
Figure 6.26: Plot of plastic volumetric strain vs. yield stress	172
Figure 6.27: Plot of degree of saturation vs. Cap position	174
Figure 6.28: Plot of degree of saturation vs. plastic volumetric strain of Xb	176
Figure 6.29: Relationship between degree of saturation and Cap Aspect Ratio.....	178
Figure 7.1: Plan and side view of the test cell (modified from Cortez ⁽¹⁷⁾)	181
Figure 7.2: Transverse cross section of test cell (modified from Cortez ⁽¹⁷⁾)	181
Figure 7.3: Dual tire assembly dimension (modified from Cortez ⁽¹⁷⁾)	182
Figure 7.4: Plane geometry of 3D quarter symmetric model	183
Figure 7.5: Load and boundary conditions of 3D quarter symmetric model.....	184
Figure 7.6: Vertical deformation variation with number of elements.....	185
Figure 7.7: Mesh arrangement of 3D quarter symmetric model.....	186
Figure 7.8: Plane geometry of 3D symmetric model.....	187
Figure 7.9: Load and boundaries of 3D symmetric model.	187

Figure 7.10: Mesh arrangement of 3D symmetric model.....	188
Figure 7.11: Verification of sand model and D-P cap model performance with field data.....	190
Figure 7.12: Variation of vertical stress (Soil A-2-4).....	192
Figure 7.13: Variation of vertical strain (Soil A-2-4).....	193
Figure 7.14: Variation of vertical deformation (Soil A-2-4)	193
Figure 7.15: Contour map of vertical stress.....	194
Figure 7.16: Contour map of vertical strain.....	194
Figure 7.17: Contour map of vertical deformation	195
Figure 7.18: Variation of vertical stress with asphalt and base properties at different depths ..	198
Figure 7.19: Variation of vertical strain with asphalt and base properties at different depths ..	200
Figure 7.20: Variation of vertical deformation with asphalt and base properties at different depths	203
Figure 7.21: Variation of vertical strain with saturation level at different depths.....	205
Figure 7.22: Variation of vertical deformation with saturation level at different depths	208
Figure A.1: Effect of parameters n_1 , n_2 , n_3 on suction curve (modified from Heath et al., ⁽¹⁶⁾)	232

CHAPTER ONE

INTRODUCTION

1.1 General

Subgrade granular materials in pavements undergo repeated loading and their response influences the fatigue and rutting of asphalt concrete pavements. Granular materials exhibit a wide range of mechanical behavior that depends on their composition and fabric, stress history, density, and the nature of the applied force. Over the past few decades, researchers have developed a number of constitutive models based on elasto-plasticity to account for most of these factors and to predict the response of granular soils. These models include the family of two-surface plasticity models (See references 1, 2, 3, 4, 5, 6, and 7), double hardening model (See references 8, 9, 10 and 11), CAP model ⁽¹²⁾; volumetric hardening model ^(13, 14) and cyclic densification model ⁽¹⁵⁾. Some of these models have been used to predict the response of pavement and railway subgrade materials ^(12, 15).

In addition, most subgrade materials are unsaturated and their behavior is dependent on suction and water content. Subgrades with different moisture content experience different suction force which affects their performance. But this effect has traditionally been difficult to be quantified using either empirical or mechanistic methods. Heath et al. ⁽¹⁶⁾ presented a practical mechanistic framework for quantifying the behavior of unsaturated granular materials within the range of water contents, densities, and stress states likely to be encountered under pavement field conditions. The framework utilized a simple soil suction model with three density-independent parameters.

The Transportation Pooled Fund Study project SPR-2(208) titled “Pavement Subgrade Performance Study⁽¹⁷⁾” was conducted at the Cold Region Research Laboratory (CRREL) of the U.S. Army Corps of Engineers in Hanover, New Hampshire, between 1999 and 2007. The study aimed to develop prediction models for permanent deformation in the subgrade soil that incorporate the effect of soil type and moisture content. In this project, flexible pavements with the same granular base layer and asphalt concrete surface layer were built inside the Frost Effects Research Facility and were subjected to accelerated pavement testing (APT).

The pavements were built with a combination of four soil types and three moisture levels, which resulted in a total of 12 sets of pavement sections, named cells. Each of the four soil types were placed in the pits of the facility at three moisture contents. For each cell, between four and six pavement sections, named windows, were subjected to accelerated pavement testing. The MARK HVS IV was used as the loading device. Up to four wheel load magnitudes were used for the windows in the same cell.

The test sections were instrumented with stress, strain, moisture and temperature sensors. Surface rutting was monitored with a laser profilometer. Falling Weight Deflectometer (FWD) tests were performed on each pavement section before the application of accelerated traffic. The testing phase of the project was completed and the final deliverables were received in February 2007⁽¹⁷⁾.

The above study presents an excellent opportunity to examine the current subgrade models as well as propose new models to predict the performance of pavement subgrades under traffic loads. This forms the current study.

1.2 Objectives of Study

The main objectives of the study are to:

- Develop empirical models for permanent deformation in subgrade soils consistent with, and for use with the NCHRP 1-37A Mechanistic-Empirical Pavement Design Guide (MEPDG) and the associated model parameters for the subgrade soils tested in SPR-2(208) and validate them using the performance data collected, and
- Develop fundamentally based mechanistic models for the determination of permanent deformation in subgrade soils under repeated traffic loading, and validate them through finite element modeling and the performance data collected during the experimental phase of SPR-2(208) for advancing the science of pavement design.

1.3 Organization of Report

The introduction to the study, research objectives, and the methodology used form Chapter One of the report.

Chapter Two presents a review of the current empirical models for predicting deformation in pavement subgrades, the background related to finite element models of pavements, and a review of constitutive models for granular materials. The comprehensive review of SPR-2(208) products is also provided in this section.

Chapter Three describes the development of empirical models for predicting the permanent strain in subgrade soils. A statistical analysis was done on the pavement

response data collected in the Pavement Subgrade Performance Study (PSPS), conducted at the U.S. Army Corps of Engineers, Cold Region Research Laboratory (CRREL).

Chapter Four describes the development and implementation of the sand model. This model is based on critical state and bounding surface concepts and incorporates parameters to account for sand fabric and suction. Verification of the model with a wide range of test data and a detailed study of unsaturated sandy soil behavior are also presented. Verification of cyclic loading performance of the sand model using laboratory test data is also presented.

Chapter Five describes the development of Drucker-Prager Cap model, which is applied to predict the performance of clayey soils. The parameters of D-P Cap model used in the Abaqus finite element software are introduced. This chapter also presents the procedures to determining parameters for this model. The procedure is implemented in MATLAB[®] software to facilitate the determination from test data.

Chapter Six presents details of the laboratory tests conducted to determine the model parameters. These tests include Standard Proctor, Atterberg Limit, specific gravity, Soil-Water Characteristic Curve (SWCC), uniaxial compressive strength (UCS), indirect tensile strength (IDT) and triaxial . The model parameters under various moisture content levels were obtained and the influence of suction was investigated.

Chapter Seven presents details of the development of the 3D FE model in Abaqus developed to simulate the effects of loads on the pavements. Details relating to tire geometry, loading and boundary condition, material properties and mesh arrangement are provided. The FE model was used to predict some of the CRREL test data. The chapter concludes with some parametric studies conducted to evaluate the influence of different

factors on subgrade deformation, such as asphalt and base properties, and saturation level.

Finally, conclusions drawn from this research and recommendations for future study are presented in Chapter Eight.

CHAPTER TWO

BACKGROUND

2.1 Empirical Permanent Deformation Models

Rutting is the formation of longitudinal depressions in the wheel paths with small amount of upheaval on the sides of the ruts due to the load induced permanent deformation in the pavement layers. This permanent deformation can occur in the subgrade, the base or subbase layers, or in the asphalt concrete layers. The magnitude of rutting and the contribution of each layer to the total permanent deformation depend on the magnitude and the lateral position of the wheel loads, the stresses in the individual pavement layers and the relative strength of the pavement layers. This later factor may change with temperature in the asphalt concrete layers and moisture regime in the unbound granular layers. Rutting develops progressively with the number of traffic load applications and is caused by the densification and shear deformation of the materials in the pavement structure.

Although rutting can occur in any layer of the pavement structure, early rutting prediction models assumed that rutting was primarily related to the vertical compressive strain (ϵ_v) at the top of the subgrade soil layer. Historically, this correspondence was developed in the 1960s and the 1970s, as the result of field observations of the failure of flexible pavements with relatively thin asphalt concrete layers. However, experience has proved later that the permanent deformation may develop in the unbound base and subbase layers as well as in the asphalt concrete layers, especially for structures with thick asphalt concrete layers, where the subgrade is well protected by the pavement layers above. A method to estimate the contribution of each layer to rutting of hot mix asphalt

pavements based on the shape of the transverse profile at the pavement surface was developed as part of NCHRP Project 1-34A⁽¹⁸⁾.

Many field studies have indicated that rutting may occur in the asphalt concrete surface layer only. This indicates a mix design problem, rather than a structural design deficiency. Extensive work has been conducted on this topic as part of the SHRP's Superpave Program. The implementation of the Superpave mix design and binder characterization methods has significantly reduced the occurrence of rutting in asphalt concrete layers.

Rutting and/or permanent deformation is typically modeled by:

- estimating of permanent deformation with the layer materials modeled using visco-elastic, visco-elasto-plastic or plastic models. These models are derived based on fundamental principles of visco-elasticity and plasticity.
- computing the permanent deformation using empirical relations developed from distress data, collected on in-service pavements. These models are typically incorporated in a pavement management system environment and have a low degree of accuracy.
- estimating the number of load repetitions that will generate a certain permanent deformation or rut depth defined as failure criteria using transfer functions. These transfer functions typically relate the number of load repetitions to the magnitude of stresses or strains at critical locations in the layered system.

Table 2.2 lists the major transfer functions, equations that relate the vertical compressive strain (ϵ_v) at the top of the subgrade soil layer with the number of repetitions (N_r) of the load generating that strain, that induce a rut depth equal to a failure limit (e.g. 20 mm).

The models developed above were derived based on observed deformation of in-service pavement structures. However, the models are empirical and do not always reflect the contribution of the other pavement layers to rutting.

When incorporated in mechanistic-empirical design procedure for flexible pavements, the equations above were used to compute the cumulative pavement damage. The cumulative damage is computed with the aid of Miner's law ⁽¹⁹⁾. The law was developed originally to predict metal fatigue but has been applied to other materials and forms of distress. The Miner's law is expressed by the following relationship in equation (2.1):

$$D = \sum_{i=1}^k n_i / N_i \quad (2.1)$$

n_i - number of applied loads in condition i

N_i - number of allowable repetitions in condition i

Table 2.1: Transfer functions for subgrade rutting models

1. Chevron Model (20 mm rut depth)

$$N_r = 1.077 \times 10^{18} \times (\varepsilon_v)^{-4.4843}$$

2. Shell Model (terminal serviceability = 2.5)

$$N_r = 6.15 \times 10^{-7} \times (\varepsilon_v)^{-4} \text{ at 50% reliability}$$

$$N_r = 1.945 \times 10^{-7} \times (\varepsilon_v)^{-4} \text{ at 85% reliability}$$

$$N_r = 1.05 \times 10^{-7} \times (\varepsilon_v)^{-4} \text{ at 95% reliability}$$

3. South African Model (failure of the subgrade)

$$N_r = 1.077 \times 10^{18} \times (A - 10 \times \log \varepsilon_v)^{-4.4843}$$

A = 33.5 for a terminal rut depth of 10mm and 36.5 for a terminal rut depth of 20 mm

3. Asphalt Institute Model

$$N_r = 10^M \text{ where } M = 1 / [0.25 \times (-1.553 - \log \varepsilon_v)]$$

4. U.S. Army Corp of Engineers Model

$$N_r = 10,000 \times [(0.0002347 + 0.00245 \log E_s) / \varepsilon_v]^B \text{ where } B = 0.0658 \times E_s^{0.559}$$

N_r – number of loads until failure of the subgrade

ε_v - vertical strain at the top of the subgrade layer

E_s – subgrade resilient modulus

For each load conditions, the Miner's law calculated the corresponding damage fraction consumed. The life of the pavement is considered consumed when the total damage, D, equals or exceeds unity.

Major limitations of these transfer functions are:

- are empirical in nature,
- are valid only for the subgrade soils they were derived for,

- are valid only for the lateral wheel wander and the tire inflation pressure they were derived for,
- are valid only if the same definition of rut depth is used (e.g. relative to a horizontal imaginary line or a 1.2 m straight edge),
- do not include the plastic limits or gradation of the subgrade soil
- ignore the contribution of upper pavement layers to the permanent deformation at pavement surface.

The NCHRP 1-37A pavement design model⁽¹⁸⁾ contains models for predicting permanent deformation in each pavement layer. The average vertical resilient strain in each layer/sublayer is computed for each analysis period of the entire design period with a linear elastic program for each axle load configuration. Rutting distress is predicted in absolute terms and not computed based on Miner's law; the incremental distress computed for each analysis period is directly accumulated over the entire target design life of the pavement.

The model used for unbound materials has the form in Equation (2.2):

$$\delta_a(N) = \beta_1 * (\varepsilon_0 / \varepsilon_r) * \varepsilon_v * h * \text{EXP}[-(\rho/N)^\beta] \quad (2.2)$$

where:

δ_a – Permanent deformation for the layer/sublayer

β_1 - Calibration factor for the unbound granular and subgrade materials

ε_0 , β and ρ – Material properties with $\log \beta = -0.6119 - 0.017638 * w_c$

ε_r – resilient strain imposed in laboratory test to obtain the above listed material properties

ε_v – Average vertical resilient strain in the layer/sublayer

h – thickness of the layer/sublayer w_c – water content in the layer/sublayer

N – Number of traffic repetitions

All parameters, except for β_1 , were computed function of the resilient modulus of the layer/sublayer and water content, estimated based on the ground water table depth. The final calibrated model parameters, derived from the permanent deformation data collected on 88 LTPP sections in 28 states were:

$\beta_{1GB} = 1.673$ for unbound granular base and

$\beta_{1SG} = 1.35$ for unbound subgrade soil.

The NCHRP 1-37A model for rutting in unbound materials was developed by modifying the models proposed by Tseng and Lytton ⁽²⁰⁾, which were developed originally based on laboratory tests and not on field measured permanent deformation data. However, the modifications have significantly altered the original models in that:

- the same shape of the model was proposed for unbound foundation materials and for subgrade soils
- the factor of bulk and deviatoric stresses were eliminated.

- The shape of the model was changed to reduce the scatter in the prediction of the permanent deformation during calibration with LTPP data, even though the LTPP database had not had data on measured permanent deformation in individual pavement layers; the permanent deformation in individual pavement layers was estimated based on an artificially selected contribution of each layer to the total permanent deformation.

The permanent deformation model for unbound materials incorporated in the NCHRP 1-37A pavement design model is empirical. However, a desirable feature is that it includes directly the effect of moisture content in the computation of permanent deformation, and not indirectly, through its effect on the resilient modulus of the foundation layers.

The most common procedure for studying the evolution of permanent deformation under cyclic loading for granular materials is to perform triaxial laboratory tests, in which the material is subjected to a large number of cycles at one stress level. Then an empirical model is derived from the permanent deformation, (ϵ_p), vs. number of cycles (N) curve. Well known relationships have been proposed by:

Barksdale ⁽²¹⁾,

$$\epsilon_p = a + b * \log N \quad (2.3)$$

Sweere ⁽²²⁾

$$\epsilon_p = a * N^b \quad (2.4)$$

and

Hornych et al. ⁽²³⁾:

$$\varepsilon_p = a * [1 - (N/100)^{-b}] \quad (2.5)$$

Van Niekerk et al. ⁽²⁴⁾ and Van Niekerk ⁽²⁵⁾:

- for aggregates

$$\varepsilon_p = a * (N/1000)^b + c * (\text{EXP}[d*N/1000] - 1) \quad (2.6)$$

$c = 0$ if the accumulation of permanent deformation is stable

- for sand:

$$\varepsilon_p = a * (N/1000)^b \quad (2.7)$$

Theyse et al. ⁽²⁶⁾

- unstable case:

$$\varepsilon_p \text{ or } PD = a * [\text{EXP}(b*N) - 1] - c * [\text{EXP}(-d*N) - 1] \quad (2.8)$$

- stable case

$$\varepsilon_p \text{ or } PD = m*N + c*N / [1 + (c*N/a)^b]^{1/b} \quad (2.9)$$

Theyse et al. ⁽²⁷⁾

$$PD = a * N^c * [\text{EXP}(b*\sigma_v) - 1] \quad (2.10)$$

Gidel⁽²⁸⁾:

$$\varepsilon_p = a * [1 - (N/100)^{-b}] * [L_{max}/p_a]^n / [m + s / p_{max} - q_{max}/p_{max}] \quad (2.11)$$

where

$$L_{max} = [q_{max}^2 + p_{max}^2]^{0.5} \quad p_a = 100 \text{ kPa}$$

a, b, c, d, n – model parameters

m, s – parameters of the failure line of the material, of equation $q = m*p+s$

p – deviatoric stress; q – confining stress

σ_v – vertical stress at the top of the pavement foundation

N – number of load repetitions

An interesting model is proposed by Nunez et al⁽²⁹⁾. They have performed cyclic triaxial tests on three granular base material with the maximum aggregate size of 25 mm, and identified three segments on the permanent deformation versus the number of load cycles curve (Figure 2.1):

- *an initial permanent strain (ε_{pi}), accumulated in the very beginning of the test after N_i cycles, reflecting some kind of post-compaction;*
- *a second stage with permanent deformation accumulating very slowly, for which a constant strain rate (CSR) may be computed;*

- an increasing strain rate stage, observed if the deviatoric, (σ_d), exceeds a certain threshold , ($\sigma_{I,f}$), which may cause specimen's failure.

The model is simple and allows an easy calculation of the permanent strain with the formula:

$$\varepsilon_p = \varepsilon_{pi} + CSR * (N - N_i) \quad (2.12)$$

The parameters can be determined from the results of cyclic triaxial tests performed at several levels of deviatoric stress with the following formulas:

$$\varepsilon_{pi} = a * \text{EXP}[b * \sigma_d] \quad \text{or} \quad \varepsilon_{pi} = f * \text{EXP}[g * \sigma_d / \sigma_{I,f}] \quad (2.13)$$

$$CSR = c * \text{EXP}[d * \sigma_d] \quad \text{or} \quad CSR = h * \text{EXP}[i * \sigma_d / \sigma_{I,f}] \quad (2.14)$$

A separate set of material constants, a, b, c, d, e, f, g, h and i must be determined for each density level and moisture content.

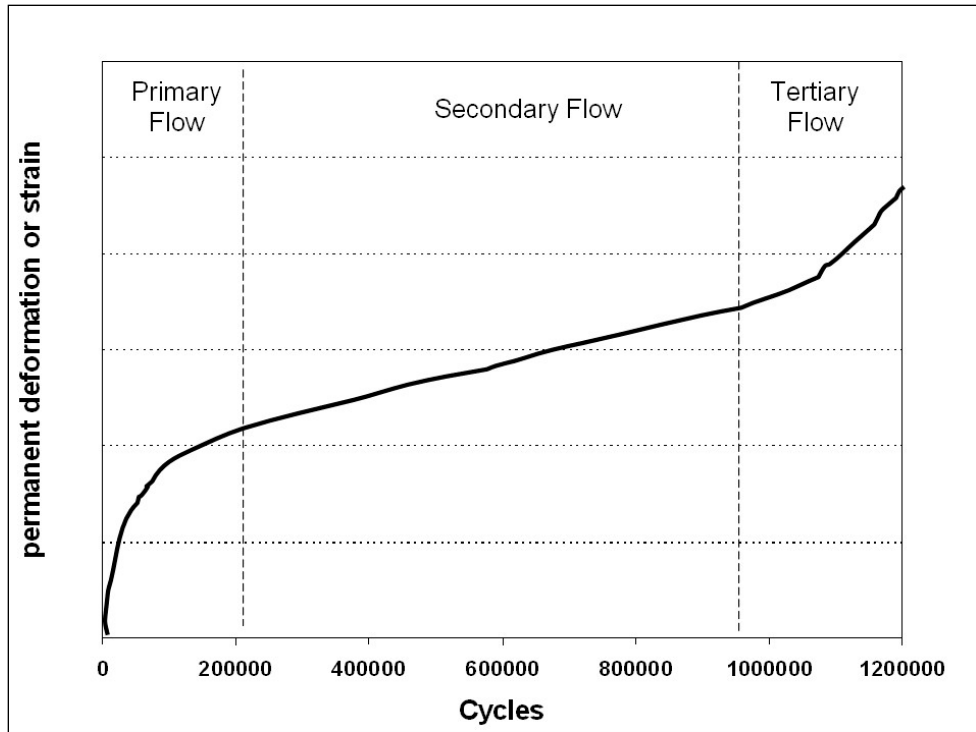


Figure 2.1: Typical evolution of accumulated permanent deformation

All the above models were derived from the results of cyclic triaxial tests on granular materials for bases and subbases. The original models proposed by Tseng and Lytton⁽²⁰⁾, which were modified and adopted in the NCHRP 1-37A model for permanent deformation in unbound materials, were also developed based on laboratory tests on granular materials. No model was found to be derived from measured permanent deformation of an unbound granular layer, from neither in-service nor APT pavement structure. For subgrade soils, such a model was developed at the Danish Road Institute⁽³⁰⁾ in the DRTM1 experiment, and was validated for DRTM2 experiment. The energy-density model has the following form:

$$\epsilon_{pz} = a * (N)^b * [0.5 * (\sigma_z / p) * \epsilon_z]^c \quad (2.15)$$

where

ε_{pz} – vertical plastic strain at a depth z (microstrain)

ε_z - vertical dynamic elastic strain at depth z, (microstrain)

N – number of load repetitions

σ_z – vertical stress at depth z (MPa)

p – reference stress (MPa) taken as atmospheric pressure (0.1 MPa)

a, b, c – constants

For the silty clayey sand, the constants were: a = 0.453, b = 0.341 and c = 0.868.

When the model was tested, it was revealed that at the same number of load repetitions, the calculated plastic strains in a pavement with a stiff subgrade were larger than for a soft subgrade, which is incorrect. The model was later improved by Odermatt ⁽³¹⁾, who analyzed the permanent deformation data from DRTM1 and CRREL's TS01 and TS02 APT sections. The improved model has the form:

$$\varepsilon_{pz} = a * (N)^b * (\sigma_z / p)^c * \varepsilon_z^d \quad (2.16)$$

Odermatt ⁽³¹⁾ estimated the four constants from permanent deformation data measured in the three APT projects. He also performed an extensive repeated triaxial testing program to compute the constant in the equation above and to study the influence of compaction, moisture content and loading frequency on the accumulation of permanent deformation.

In the triaxial tests he subjected the same subgrade soils used in the three APT tests, to over 500,000 cycles of deviatoric stress, at constant confining stress. He then found that the permanent deformations predicted with the laboratory derived constants and the field measured permanent deformations do not match. An example of the results is provided in Figure 2.2. The possible justifications for the mismatch were⁽³¹⁾:

- A reorientation of the principal stresses takes place during shear in the APT test with a rolling wheel. The principal stresses do not rotate in the triaxial test.
- Mean values of densities and moisture content from the APT tests were used in the triaxial tests.
- Some permanent strain measurements in the APT tests were unreliable.
- Horizontal stresses are difficult to measure in the APT tests
- A static confining pressure is applied in the triaxial tests, while in the APT tests, the horizontal stresses vary as the wheel passes a point in the material.

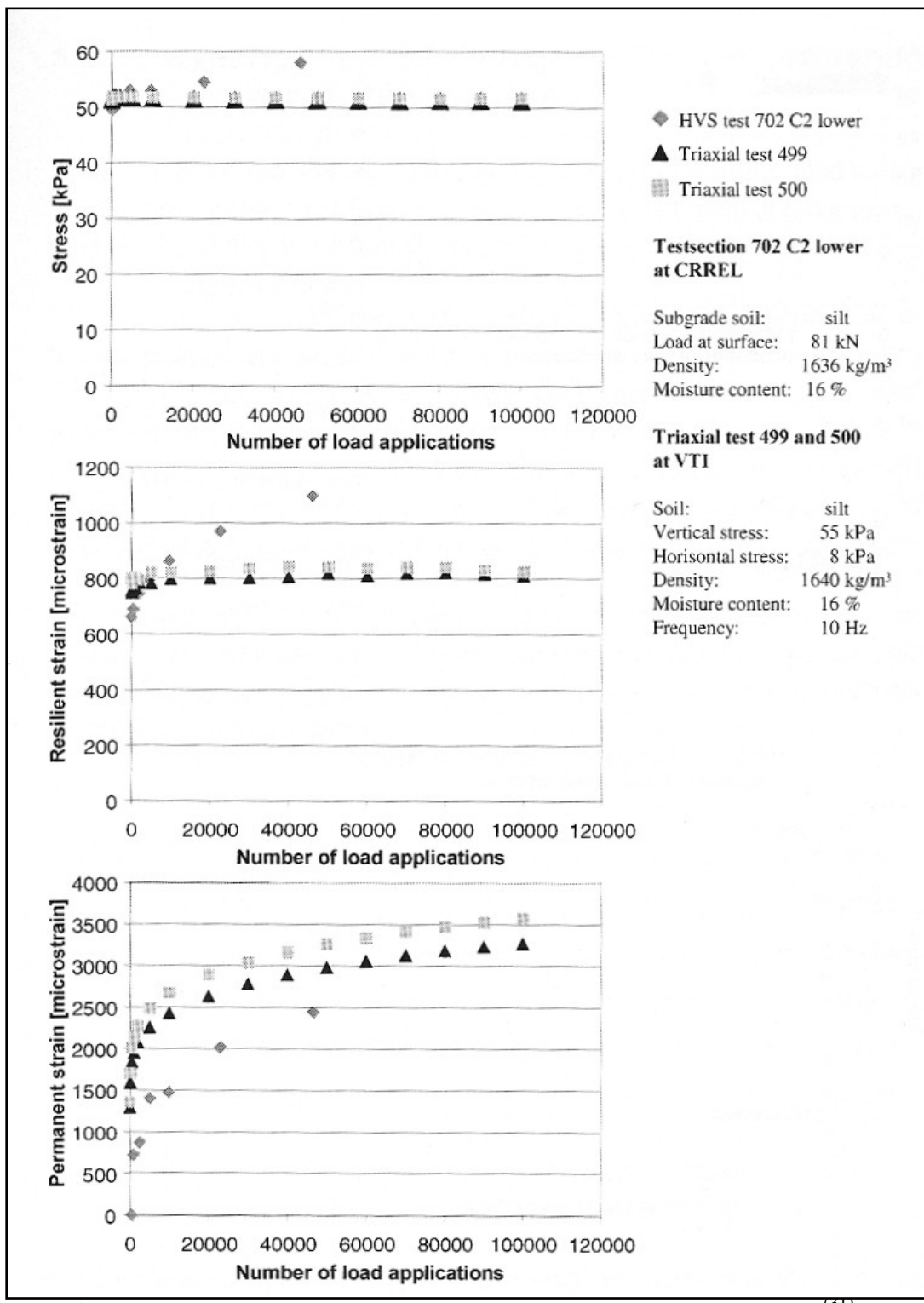


Figure 2.2: Comparison of predicted and measured permanent strain⁽³¹⁾

The trends of the accumulation of permanent strain also differed. The initial permanent strain (after the first 1,000 cycles) is higher in the cyclic triaxial test than in the APT test. This may be explained by the fact that, in the APT and in-service pavements, some permanent strain accumulated during the compaction and placement of the upper layers. This initial stage cannot be simulated in the laboratory tests. Also, the rate of increase in permanent strain after the accumulation of the initial strain is typically smaller for the cyclic triaxial test. A possible explanation is that, during the laboratory tests, the confining stress is not pulsating; it is kept constant throughout the test.

Odermatt's work suggests that no model derived solely from cyclic triaxial test data can estimate accurately the accumulation of permanent deformation in subgrade soils under a rolling wheel. Laboratory tests can be used solely to determine shift or correction factors that reflect the relative influence of moisture, compaction level and freeze-thaw cycles on the accumulation of permanent vertical strain and deformation. If the damaging effects of freeze-thaw cycles on the performance of flexible pavements are extensively described in the literature, limited information exists on the effect of freeze –thaw to the accumulation of permanent strains. Laboratory tests conducted by Elliott et al⁽³²⁾ on four representative subgrade soils in Arkansas revealed that freeze-thaw leads to higher permanent strains in subgrade soils. An example of their results for an AASHTO A-6 soil is presented in Figure 2.3; the permanent deformation is higher when the soil is subjected to increased number of freeze-thaw (FT) cycles prior to the triaxial testing.

Zhang and McDonald⁽³⁰⁾ reported on the APT work conducted at the Danish Road Institute to investigate the effect of freeze-thaw cycles on subgrade performance. They

found that even a single freeze-thaw cycle may severely impact the resistance of the subgrade soil to permanent deformation.

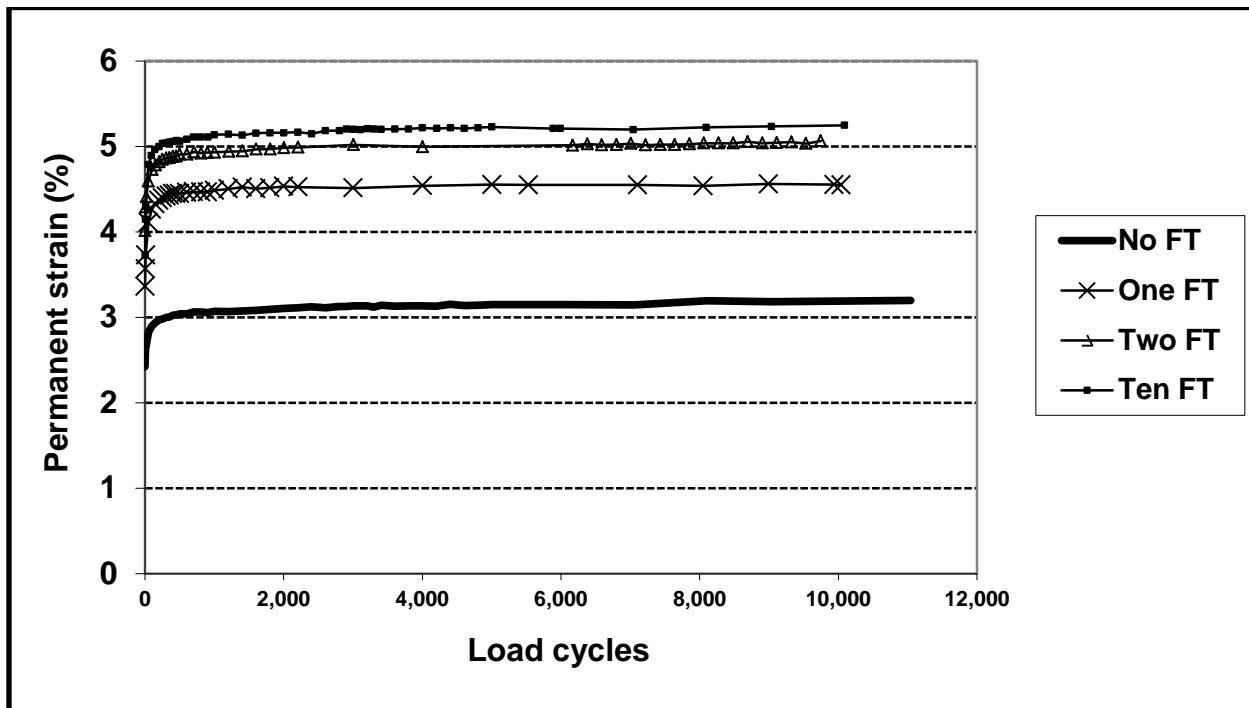


Figure 2.3: Effect of freeze-thaw cycles on permanent strain - Sacul soil, AASHTO A-6
(³²)

Theyse⁽²⁷⁾ presented a conceptual model for developing a model for the evolution of permanent deformation of unbound pavement layers. The objective of the work was to develop permanent deformation models for incorporation into the South African Pavement Mechanistic Design Method (SAMDM) based on permanent deformation data collected during HVS trials in South Africa over a long period of time. It was therefore implicitly assumed that specific loading conditions to APT experiments (reduced wheel speed, high frequency of loading, short duration of the experiments) are likely to have small effects on the development of permanent deformation in typical South African

structures, which have relatively thin hot-mix-asphalt surface layers and well-compacted unbound granular layers.

The model assumes that the permanent deformation of an unbound pavement layer, the dependent variable, depends on a number of independent variables and is fully controlled by these variables. The independent variables may be grouped as primary and secondary independent variables. The two primary independent variables are defined as the stress condition (stress or strain level) and the number of stress repetitions. Without either one of these variables, there will not be any traffic induced permanent deformation in a pavement structure. The secondary independent variables (material type or material shear strength and moisture content) will not cause any permanent deformation by themselves, but they will influence the magnitude of the permanent deformation. Their influence was not discussed in the paper by Theyse⁽²⁷⁾.

Even though the model serves a pavement design process and does not predict the performance of an in-service pavement structure when the performance of the same structure under APT condition is known, the conceptual model contains elements useful for such purpose. The same conceptual model can be used for the analysis of the permanent deformation data from the *Pavement Subgrade Performance Study*.

Permanent deformation data must be recorded for each pavement layer at regular intervals during the APT experiment. Multi-Depth Deflectometers (MDD) are used for this purpose. The MDDs consists of a stack of Linear Variable Displacement Transducers (LVDTs). The LVDTs are housed in modules that can be fixed at a predetermined depth in the pavement structure, usually at layer interfaces. A reference core runs through the

LVDT modules and is anchored at a depth of 2.5 – 3 meters⁽³³⁾. An example of the recorded evolution of permanent deformation is given in Figure 2.

Empirical equations for predicting the permanent deformation in each unbound pavement layer are developed from MDD permanent deformation data. The proposed equation for unbound foundation layers has the form:

$$PD = a * N^c * [\text{EXP}(b * \sigma_z) - 1] \quad (2.17)$$

Where:

a, b, c – model parameters, obtained by fitting the function to MDD deformation data (e.g. from Figure 2.6)

N – number of repetitions (E80 standard axles)

σ_z – vertical stress at the top of the pavement foundation computed with a linear elastic structural program, with elastic layer moduli backcalculated from deflection data measured by the MDDs.

Theyse's conceptual model is interesting and presents the advantage of utilizing an empirical equation with parameters that can be backcalculated from APT permanent deformation data. The equation does not use strain or stress data, which cannot always be measured accurately in APT experiments. However, the main limitations are:

- The conceptual model has not been validated with permanent deformation data from an in-service pavement.

- The conceptual model can be applied only to unbound granular layers.

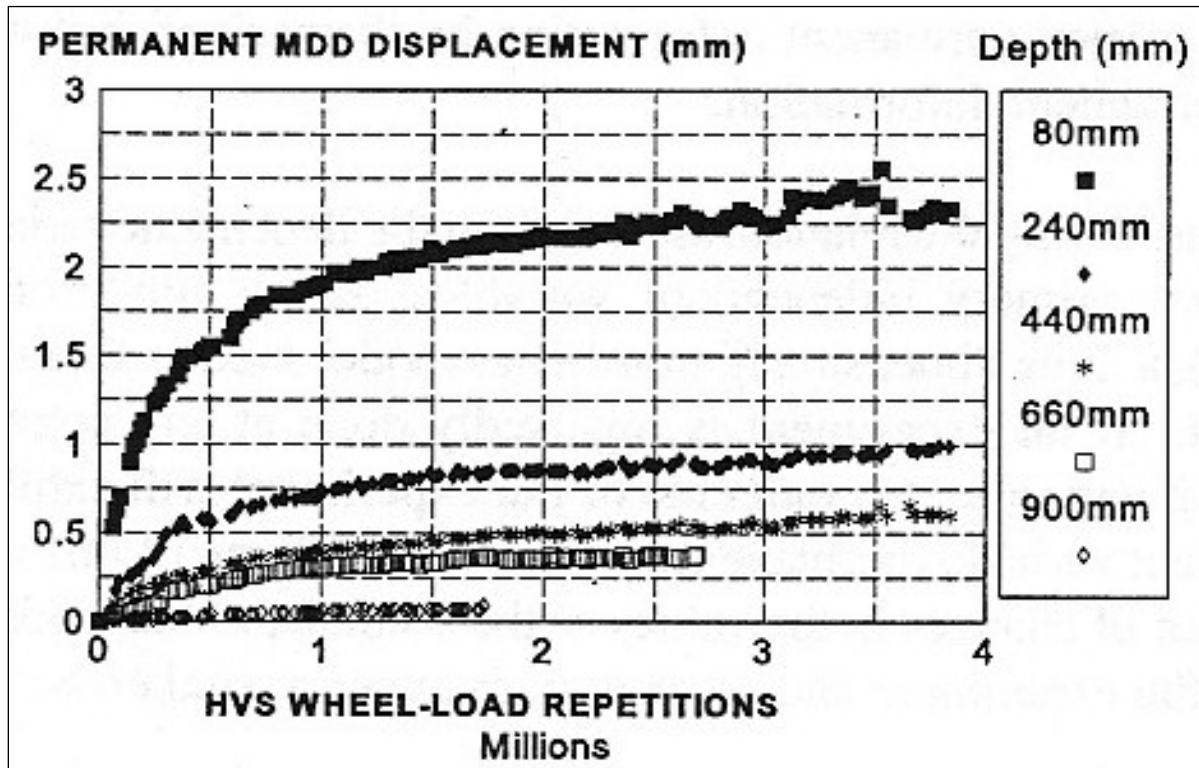


Figure 2.4: Permanent downward displacement of MDD modules with increasing load repetitions⁽³³⁾

2.2 Numerical analysis

There are three types of numerical method available: finite element method (FEM), discrete element method (DEM) and finite difference method (FDM). FEM and DEM are carried out by discretization of the analysis into several cell/grid points. FEM is much more suitable for pavement analysis than FDM, because it is easier deal with complex geometry in FEM than in FDM. DEM is also now popular, but it will not be suitable to simulate repeated loading in pavement, because it will unacceptably take too much time.

FE analysis was carried out by Duncan et al.⁽³⁴⁾ for flexible pavement in a linear elastic analysis. This FE method was programmed by Raad et al.⁽³⁵⁾ and called the ILLI PAVE computer program. Multiaxial load, fatigue cracking, etc. were included in the ILLI PAVE computer program by Lytton and Tseng⁽³⁶⁾ and called the FEXPASS. An important trade off in this program is that modification or update cannot be carried out for loading and material models.

Pavement FE analysis can be carried out with three different type of dimensions, i.e. three dimensional, two dimensional axisymmetric and two dimensional plane strain. A 3D model is important to simulate more real field loading situations because 3D has the capacity to simulate moving pressure loading and a dual tire assembly. A disadvantage is that it will take considerably more time to simulate pavement behavior than 2D models because the number of element increases significantly, resulting in a significant increment in the number of integration points. This is likely why the MEPDG design guide included 2D axisymmetric analysis. A 3D model has been used by many researchers (See references 37, 38, 39, 40 and 41) for pavement analysis. Huang et al.⁽³⁸⁾ and Wu et al.⁽⁴¹⁾ used the 3D FE model to simulate moving pressure loading in an APT section. A 2D axisymmetric model has been used by many researchers for pavement analysis^(18, 41, 42). A 2D plane strain FE analysis has also been carried out by many researchers^(43, 44, 45). Kim et al.⁽⁴⁵⁾ used a 2D plane strain model to simulate super single tire load. Cho et al.⁽⁴⁶⁾ carried out pavement analysis in 3D, 2D axisymmetric and 2D plane strain. Results showed that both 3D and 2D axisymmetric models can be used to effectively simulate loading in pavement. Furthermore, 2D plane strain can only be used to simulate line load, and therefore it cannot be used to simulate actual wheel load.

Several common purpose commercial FE software packages, such as Abaqus, ANSYS and ADINA are available. Tire geometry, boundary conditions, loading conditions, and material properties for the various layers can be very well modeled by using the Abaqus FE program, which has been used for pavement analysis by many researchers^(18, 46, 47).

Janoo et al.⁽⁴⁷⁾ carried out two dimensional static loading analyses in Abaqus. It was assumed that all of the pavement layers are isotropic elastic, and linear elastic analysis was carried out. This study revealed that loading influencing depth within subgrade is higher in elastic analysis than actual test results. Thus, this study suggested that advanced constitutive models need to be used to predict subgrade performance. In addition, it suggested the use of elasto-plastic constitutive model for subgrade to predict long term permanent deformation (rutting) because rutting is dominated by plastic phenomena rather than elastic phenomena.

Several elasto-plastic constitutive models have been used to predict sand model behavior, including the double hardening model, the volumetric hardening model, the cyclic densification model and the critical state two surface model.

2.2.1 Double Hardening Model

Koiter⁽⁴⁸⁾ developed a multiple yield mechanism from the theory of plastic potential to find plastic strain. Prevost and Hoeg⁽⁸⁾ used this concept with two separate yield mechanisms to describe the volumetric and shear behavior of soil. This is usually referred to as double hardening. This model was further modified by many researchers^(9, 10, 11).

2.2.2 Volumetric Hardening Model

Many soils and other materials exhibit volumetric hardening when subjected to both isotropic and deviatoric stress changes. Change in volumetric strain can easily be related to void ratio change or initial void ratio. It would seem obvious to use the void ratio as a measure of the hardening that occurs. Many researchers (See references 13, 49, 50 and 51) developed the stress-strain relationship by using the void ratio as a measure of hardening. Liu and Carter⁽¹⁴⁾ explained volumetric hardening as three types of postulates: elasticity and virgin loading; sub-yielding and virgin-yielding; and elasticity, sub-yielding and virgin yielding.

2.2.3 Cyclic densification model

Suiker and Borst⁽¹⁵⁾ showed that plastic deformation behavior of ballast and sub ballast material during the cyclic loading is composed of two mechanisms, namely frictional sliding and volumetric compaction. These mechanical processes can be characterized as ‘cyclic densification’ because both mechanisms densify the granular materials.

Suiker and Borst⁽¹⁵⁾ divided the stress response regions into four regions such as shakedown region, cyclic densification region, frictional failure region and tensile failure region. The cyclic response of the granular material is fully elastic in shakedown region. Cyclic loading submit the granular material to progressive plastic deformation in cyclic densification regime. Frictional collapse occurs, since the cyclic loading level exceeds the static peak strength of the granular material in the frictional failure region. Granular material instantaneously disintegrates, as it cannot sustain tensile stresses in the tensile failure region.

2.2.4 Critical state two surface plasticity model

A two-surface plasticity model was developed by Wang et al. ⁽¹⁾ based on the bounding surface plasticity theory developed by Dafalias ⁽¹⁷⁾. Manzari and Dafalias ⁽²⁾ coupled the two-surface plasticity model with the state parameter within the framework of critical state soil mechanics. Two surface models are placed in a deviatoric stress space, and state parameter ($\psi = e - e_c$) is used to define dilatancy and bounding stress ratios for sand. This model was successfully validated for cyclic and monotonic loading for sands in drained and undrained loading conditions. This model has narrow wedge shape yield surface, as shown in the Figure 2.5. Yielding surface function is given as:

$$f = \eta - \alpha \pm m = 0 \quad (2.18)$$

In this model, no plastic deformation will occur if q and p increase at constant stress ratio η because in that case the stress path will not tend to cross the oc and oe of the wedge, as shown in the Figure 2.6.

Manzari and Dafalias ⁽²⁾ explained this model (Eq. 2.18) within CSSM with a typical example, as shown in Figure 2.5 and 2.6. It describes the loading at dense and loose sand with either drained or undrained condition. Point a and b are at dense state and loose state, respectively, as shown in Figure 2.5.

According to Figure 2.5, when the constant p drained triaxial compression loading occurs at point a , initially, consolidation occurs and point a moves to point a'_d . It then starts to dilate and point a'_d passes point a and reaches critical state line at point a'_c ($e=e_c$), where it fails. Simultaneously, as shown in Figure 2.6, point a initially moves to point a'_d due to consolidation, where stress ratio is M_c^d . Then point a'_d crosses point a'_c and

reaches point a'_b , where stress ratio is M_c^b . Then, point a'_b falls back to point a'_c due to softening. When it reaches point a'_c , stress ratio is M_c (critical state) and it fails. For the undrained condition, as shown in Figure 2.5, initially, point a moves to point a''_d due to positive pore pressure development by contraction. Then, point a''_d crosses point a and reaches point a''_c due to positive pore pressure reduction by dilation. When it reaches point a''_c (critical state and $e=e_c$), it fails.

According to Figure 2.5, when the constant p drained triaxial compression loading occurs at point b , consolidation occurs and point b moves to point b'_c . When it reaches point b'_c (critical state and $e=e_c$), it fails. If the sample is not very loose, point b crosses the critical state line and reaches point b'_d . Then it comes back to the critical state line (point b'_c , $e=e_c$) due to softening, where it fails. For the undrained condition, as shown in Figure 2.5, point b moves to point b''_c due to positive pore pressure development by contraction. When it reaches b''_c (critical state and $e=e_c$), it fails. If the sample is not very loose, point b crosses the critical state line and reaches point b''_d . Then it comes back to the critical state line (point b'_c , $e=e_c$) due to softening, where it fails.

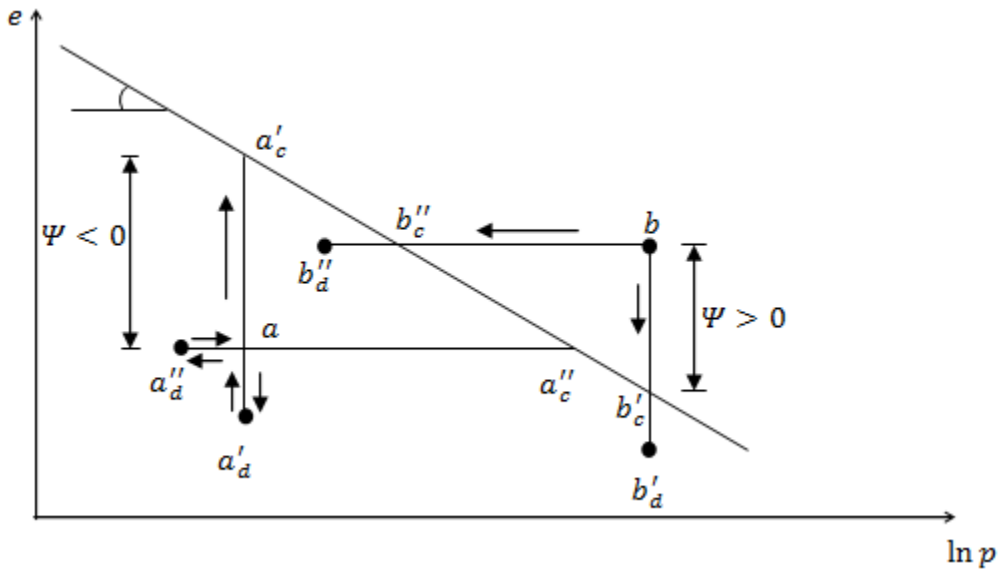


Figure 2.5: Schematic illustration of drained and undrained paths in $e, \ln p$ space for a state denser than critical (point a) and looser than critical (point b) ⁽²⁾

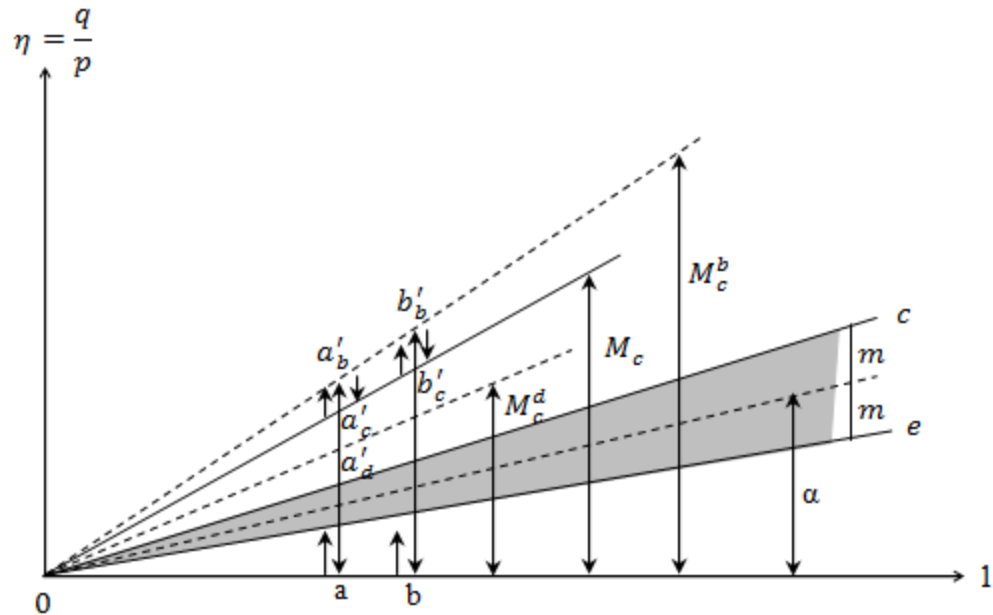


Figure 2.6: Schematic illustration in the $\eta, 1$ space of the bounding (peak) stress ratio (M_c^b), critical stress ratio (M_c), and dilatancy stress ratio (M_c^d), the back stress ratio α , the wedge type yield surface and constant- p drained paths of Figure 2.5 ⁽²⁾

Wood et al.⁽⁵²⁾ related the virtual peak or bounding stress ratio with critical stress ratio M_c by way of ψ . This relationship was further modified by Manzari and Dafalias⁽²⁾, as shown in Eq. 2.19 and 2.20.

$$M_c^b = \alpha_c^b + m = M_c + k_c^b < -\psi > \quad (2.19)$$

$$M_e^b = \alpha_e^b + m = M_e + k_e^b < -\psi > \quad (2.20)$$

where k_c^b and k_e^b are positive quantities and the Macauley brackets $< >$ define the operation $<\psi> = -\psi$ if $-\psi > 0$ and $<\psi> = 0$ if $-\psi \leq 0$. Virtual or bounding stress ratios are denoted by M_c^b for compression and M_e^b for extension. M_c^b or M_e^b is not actually the peak stress ratio which will be reached by the current stress ratio η , but it changes with ψ until it is met by η at a different value, where it becomes the peak. α_e^b or α_c^b is virtual peak or bounding back stress ratio corresponding to a given m .

Dilatancy stress ratio is used to describe the volumetric response of soils, as shown in Figure 2.16 as M_c^d . The line described by M_c^d is the phase transformation line. Soil response is contractive when $\eta < M_c^d$ and dilative when $\eta > M_c^d$. Manzari and Dafalias⁽²⁾ described dilatancy stress ratio as:

$$M_c^d = \alpha_c^d + m = M_c + k_c^d \psi \quad (2.21)$$

$$M_e^d = \alpha_e^d + m = M_e + k_e^d \psi \quad (2.22)$$

where k_c^d and k_e^d are positive quantities and α_c^d and α_e^d are back-stress dilatancy ratio. The above Eq. 2.21 and Eq. 2.22 give a dilatancy stress ratio below M_c or M_e for $\psi < 0$ (denser than critical) and above M_c or M_e for $\psi > 0$ (looser than critical), while $M_c^d =$

M_c and $M_e^d = M_e$ at $\psi=0$. In order to be consistent with CSSM, it will be required that M_c^d is variable and $M_c^d \rightarrow M_c$ as $e \rightarrow e_c$.

2.2.5 Drucker-Prager Cap model

The CAP model available in Abaqus consists of a shear yield surface based on the Drucker-Prager yield criterion initially formulated by Prager and his student Drucker⁽⁵³⁾ in 1952 as an extension to the Von Mises criterion to incorporate the influence of hydrostatic pressure on the yielding of geologic materials. The Drucker-Prager yield criterion is given by⁽⁵⁴⁾:

$$f(I_1, J_2) = \alpha_1 I_1 + \sqrt{J_2} - k = 0 \quad (2.23)$$

where α_1 and k are material constants. I_1 is the first invariant of effective stress tensor and J_2 is the second invariant of deviatoric stress tensor. f indicates that this failure criteria is a function of I_1 and J_2 . The yield surface is shown in the t-p space and the deviatoric space in Figures 2.7 and 2.8 respectively. The t parameter on the y-axis of Figure 2.7 is defined as:

$$t = \frac{1}{2} q \left\{ 1 + \frac{1}{K} - \left(1 - \frac{1}{K} \right) \left(\frac{r}{q} \right)^3 \right\} \quad (2.24)$$

$$q = \sqrt{\frac{3}{2} S_{ij} S_{ij}} \quad (2.25)$$

$$r = \left(\frac{9}{2} S_{ij} S_{jk} S_{ki} \right)^{1/3} \quad (2.26)$$

where, S_{ij} is the deviatoric stress. K is the ratio of yield stress in triaxial compression and extension. $\sqrt{\frac{3}{2}S_{ij}S_{ij}}$ and $S_{ij}S_{jk}S_{ki}$ are second and third invariant of deviatoric stress tensor.

The open nature of the Drucker-Prager shear yield surface predicts unlimited plastic volume change at higher stresses which is not the case for clays. Thus in order to constrain plastic volumetric deformation a cap is placed with a transition surface of radius α to ensure smooth transition between the shear and volumetric cap surfaces as shown in Figure 2.7.

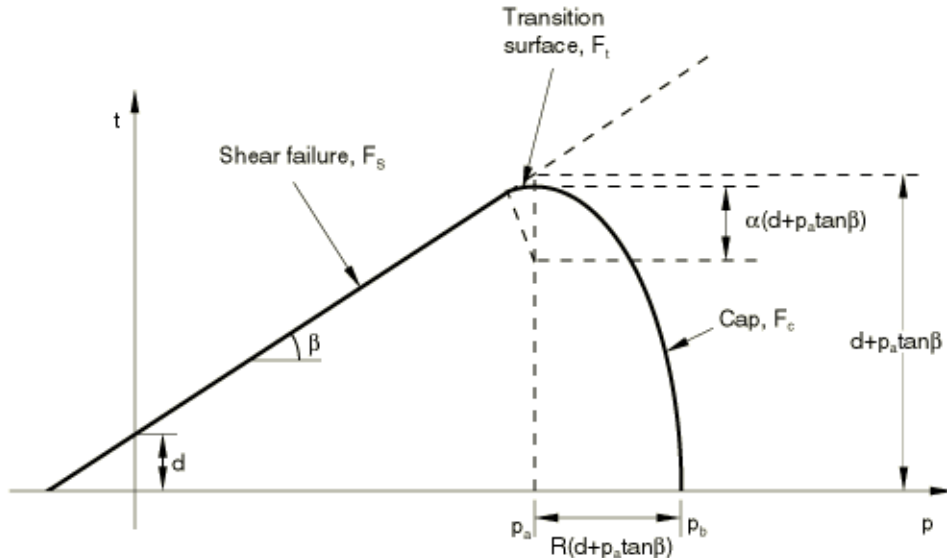


Figure 2.7: Modified Drucker-Prager/cap model : yield surface in the p (mean effective normal stress)- t plane.⁽⁵⁵⁾.

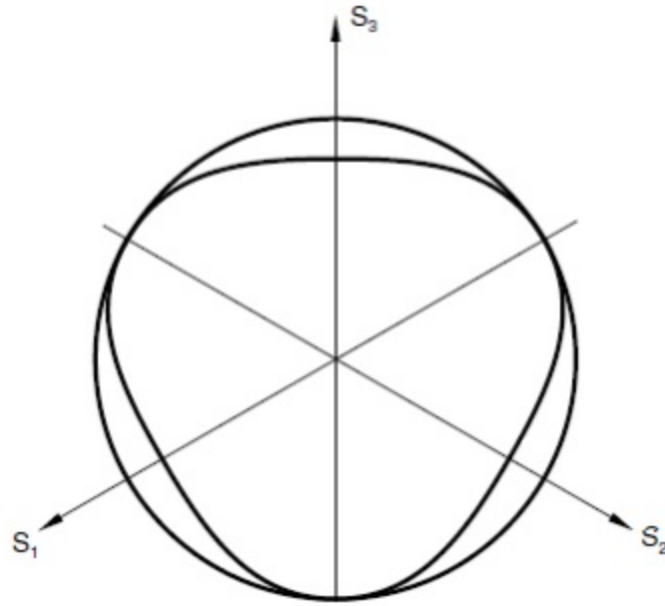


Figure 2.8: Modified Drucker-Prager/cap model: yield surface in the deviatoric plane⁽⁵⁵⁾.

The model parameters for the CAP model are summarized in Table 2.2. These parameters can be determined from experiments following the procedure by Huang and Chen⁽⁵⁴⁾ (See Chapter 6)

Table 2.2: Parameters for CAP model

Elastic parameters	Plasticity parameters
E	d
v	β
κ	R
	α
	K
	λ

2.3 Comprehensive review of SPR-2(208) products

2.3.1 Soil type

Subgrade soil types selected for this project reflect material found throughout the United States as shown in Figure 2.9. Five types of soil were used in the APT test sections. The grain size distributions of the soils are shown in Figure 2.10. Table 2.3 shows the subgrade soil properties. Note that the actual measured density in test section was found to be slightly different from these values, but these slight differences have minimal effect on the numerical analyses conducted. Thus, analyses reported here used the soil properties in Table 2.3. Only one test section was built with soil type A-6 /A-7-6 at one moisture content ⁽¹⁷⁾.

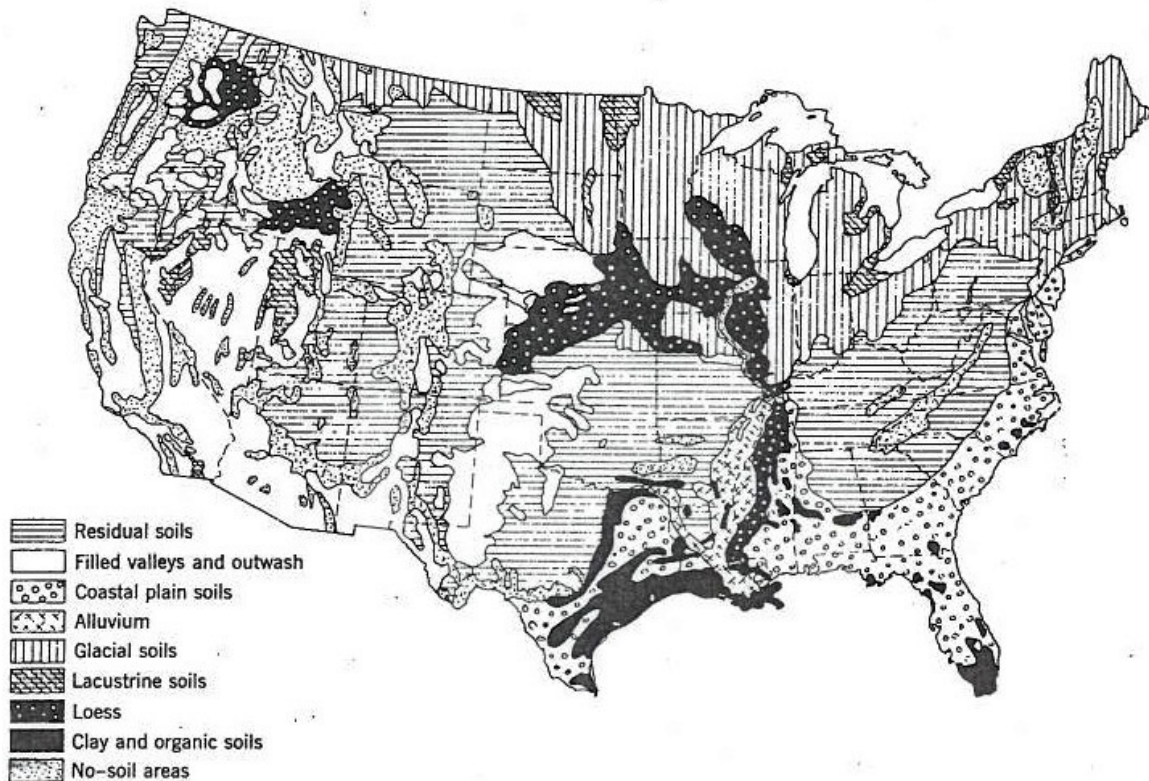


Figure 2.9: Variety of soil types in the U.S. ⁽⁵⁶⁾

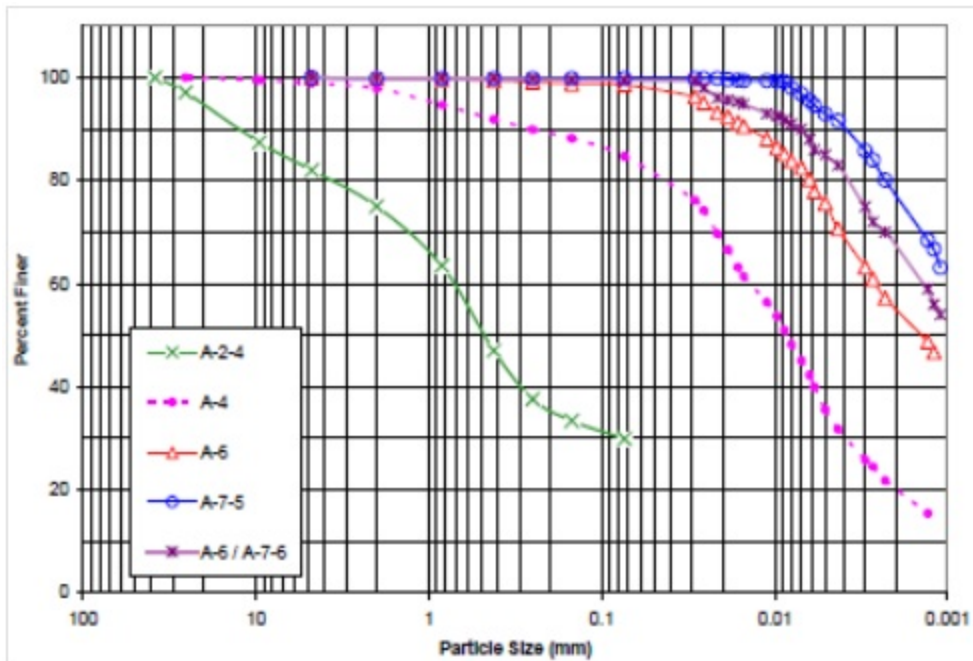


Figure 2.10: Subgrade soil particle distribution⁽¹⁷⁾.

Table 2.3: Subgrade soil properties (Data from Cortez⁽¹⁷⁾).

Soil Classification		Passing Sieve # 200 (%)	Liquid Limit	Plastic Limit	AASHTO Optimum Moisture Content (%)	AASHTO Maximum Density (kg/m ³)	Specific Gravity
AASHTO	USCS						
A-2-4	SM	29.9	30	3	10	1934	2.72
A-4	ML	84.7	28	8	16	1780	2.72
A-6	CL	98.6	33	15	16	1791	2.70

A-6/A-7-6	CL/CH	99.5	40	21	17	1800	2.72
A-7-5	MH	99.8	55	21	20	1700	2.71

2.3.2 APT test data

Comprehensive description of the data relating to the test program and measurements are available from the various products associated with SPR-2(208)⁽¹⁷⁾. A summary of the relevant data for purposes of the study are summarized herein. For example, Table 2.4 gives information on test cells, windows, the soil types, HVS loads, and moisture contents.

Table 2.4: Experimental test cells and windows.

Soil Type	Test Cell	Moisture Content (%)	Figure	Test Window	Wheel Load (kN)
A-2-4	TS701	10	F 31	1	40
				2	89
				3	103.5
	TS707	12		2	40
				4	53
				6	65
				5	80
	TS703	15		6	53.4
				3	62
				5	80
			F 32	5	53.4
A-4	TS702	17		3	62.4
				1	66.7
				2	80
				5,6	40
	TS704	19		2	44.5
				3	48.9
				1	53.4
				3	22.2
	TS705	23		1	26.7
				2	40

				5	53.4
A-6	TS709	16	F 33	6	20
				1	26.7
				4	31.1
				5	40
				3	53.4
	TS708	19		2	26.7
				5	40
				4	53.4
	TS706	22		3,4	22.2
				1	26.7
				2	40
			F 34	3,5	20
A-6/A-7-6	TS710	21		1	26.7
				6	33.4
				4	40
	TS712	20	F 35	5	40
				1	80
				2	89
				3	93.4
	TS711	25		1	26.7
					40
				3,4	80

The column titled “Figure” denotes the Figure number in the report of Cortez ⁽¹⁷⁾.

Figure 2.11 illustrates an example of the development of rutting with increase in number of cycles of loading corresponding to a cell window and load application described in Table 2.4 (soil type A-2-4; test window TS701; moisture content 10%). Note that when rut depth reached the reference depth the pavement is assumed to be in a state of failure. The reference rut depth was defined as the attainment of 12 mm permanent deformation on top of subgrade surface ⁽¹⁷⁾.

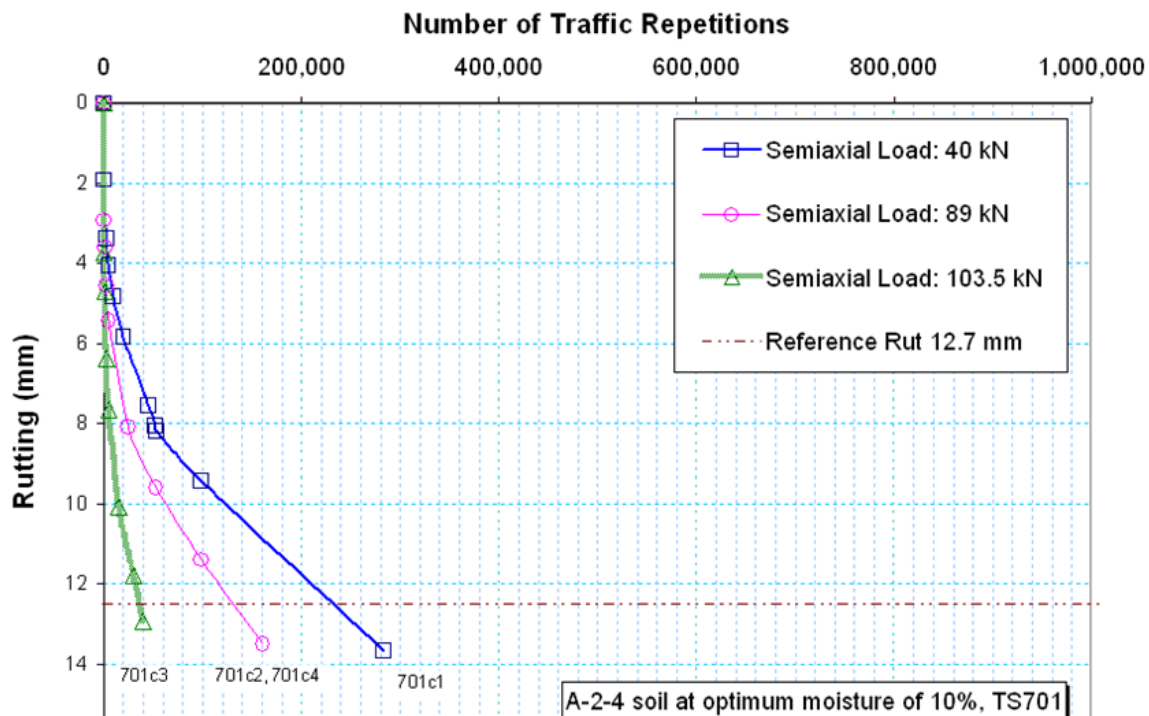


Figure 2.11: Rut development with A-2-4 subgrade at 10% moisture content⁽¹⁷⁾.

Janoo et al. ⁽⁴⁷⁾ suggested that three soil types: residual soil, glacial soil and coastal plane soil are most commonly found. Existing locations and AASHTO soil types of these three natural soils are tabulated in Table 2.5, which shows that sandy subgrade soils exist across the United States and indicating that it is important to study the sandy subgrade performance in detail. Thus, this study was restricted to the analysis of sand.

Table 2.5: Soil types and locations of different natural soils used in project SPR-2(208)
 (modified from Janoo et al.⁽⁴⁷⁾)

Natural Soil	AASHTO Soil Types	Existing Locations
Residual Soil	Sand (A2)	Existing in Interior
Glacial Soil	Gravel (A1), Sand (A2), Silt(A4), Silty clay (A6)	Northern States
Coastal Plane Soil	Sand (A2) , Gravel (A1)	Eastern sea board and gulf area

CHAPTER THREE

DEVELOPMENT OF EMPIRICAL MODELS FOR PERMANENT DEFORMATION

3.1 Pavement Response Datasets

The development of empirical models for permanent deformation from the response and performance data collected during the PSPS project required significant processing of the PSPS data in order to create a dataset to be used in the statistical analysis. This had to be done separately for each test cell, window and number of passes applied in the PSPS experiment⁽⁵⁷⁾.

After careful investigation of the available data and the variables needed to develop the empirical models, it became evident that two datasets must be created. The two separate datasets will allow the development of models having different independent variables.

The datasets were built by assembling several tables from the PSPS database and by adding new variables. The assembly of the first dataset consisted of the following steps:

1. Joining the data from the two tables containing vertical dynamic strain and vertical permanent strain. In this step, only the data marked as acceptable in the PSPS database were selected. The PSPS data that has any of the 1 to 4 removal codes was not selected.
2. Computation of vertical dynamic strain and vertical permanent strain at the depth where the vertical dynamic stress was measured in the PSPS experiment. The inconsistency of the number of stress cells used in the

PSPS project cells required that the strain estimation be done separately for each test window. This was done first by developing, for each test cell, window, and number of passes, a polynomial regression model between the vertical dynamic strain as dependent variable and the depth where the strain was measured as the independent variable. The polynomial regressions were done using the SAS software. Once the regression model was developed, the vertical dynamic strain was computed at the depth where the stress cells were installed in the PSPS experiment. The same procedure was then done for the vertical permanent strain.

3. Incremental permanent strain was then computed by subtracting the permanent strain recorded in two consecutive measurements by the same μ -coil sensor and then dividing this difference by the number of passes applied between the two measurements. As before, the incremental permanent strain was computed only for the locations where the vertical dynamic strains were measured.
4. The vertical stress, dynamic strain, permanent strain and incremental permanent strain were assembled in a single dataset. It is important to note that this dataset contains records only for which all reliable data exist for all these variables. Also, this dataset does not contain data for test cell 710 since no stress measurements were done for this cell.
5. The first dataset was needed to study models that only include strains; many such models are proposed in the literature. The inconsistency of the

number of emu gages used in the PSPS project cells requires that the strain estimation be done separately for each test window.

6. Inclusion of additional variables such as horizontal strains and stresses was not successful since most of the horizontal strain and stress data in the PSPS database is not reliable.
7. Evaluation of availability of in-situ soil dry density and moisture data led to the conclusion that this data is not sufficient enough to be included in the database.

If the first dataset included vertical compressive stresses, the second dataset includes only dynamic and permanent strains. The second dataset is not a subset of the first dataset (containing stresses). The second dataset was created separately and not from the first dataset because in this way it contains a much larger number of observations and, therefore, the regression analysis will likely lead to smaller prediction errors. The assembly of the second dataset consisted of the following steps:

1. Joining the data from the two tables containing vertical dynamic strain and vertical permanent strain. In this step, only the data marked as acceptable in the PSPS database was selected. The PSPS data that has any of the 1 to 4 removal codes was not selected.
2. Computation of incremental permanent strain was then done by subtracting the permanent strain recorded in two consecutive measurements by the same μ -coil sensor and then dividing this difference by the number of passes applied between the two measurements. As

before, the incremental permanent strain was computed only for the locations where the vertical dynamic strain were measured.

Once the two datasets were assembled, a verification of the data was conducted, to ensure that proper data has been retained. This verification first involved the plotting of the permanent strain data to check if it follows the desirable trend.

Figure 3.1 shows a typical evolution of the permanent deformation or strain in a pavement material (asphalt concrete, granular base or subgrade soil). The evolution is characterized by three regions of the curve:

- In the Primary Flow region, the permanent strain accumulates fast due to rearranging of the solid particles and the densification of the soil due to post-compaction.
- In the Secondary Flow region, the permanent strain accumulates slowly and at a constant rate.
- In the Tertiary Flow region, the permanent strain of the soil increases rapidly; the failure is imminent.

When retaining the permanent strain data from the PSPS database, it became evident that the Tertiary Flow region could not be identified since, for all experimental cells and windows, the permanent strain showed no sudden increase before the wheel loading was stopped. Therefore, it was further considered that the permanent (plastic) strain must follow the trend shown in Figure 3.2. This trend was observed for most experimental cells and test windows.

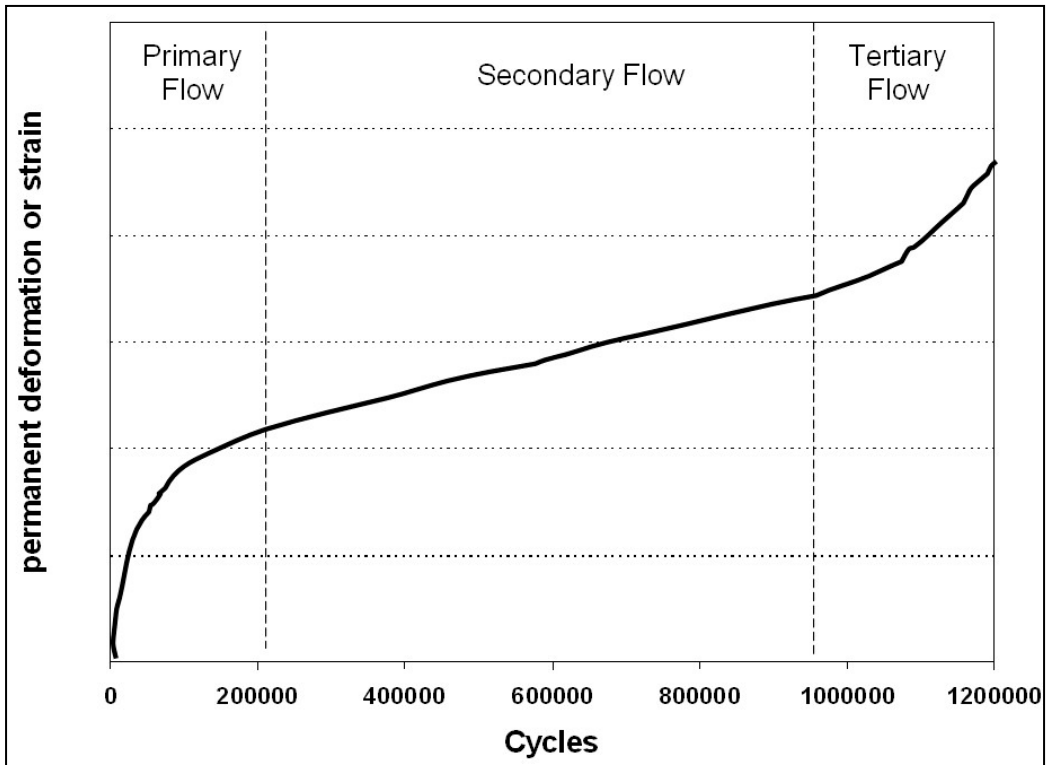


Figure 3.1: Typical Evolution of Permanent Strain with the Number of Applied Load Cycles.

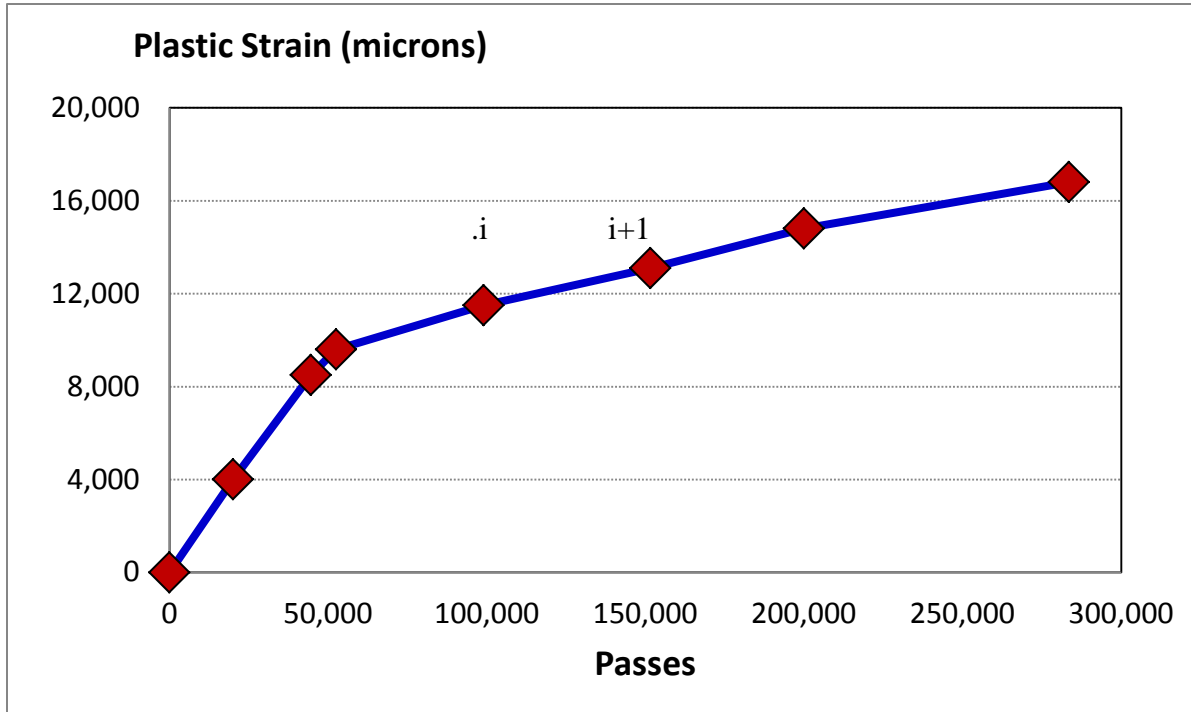


Figure 3.2: Example of Observed Evolution of Permanent (Plastic) Strain

The next step was the creation, for each segment on the permanent strain curve, of two new variables: the average plastic strain (APLS) and the incremental plastic strain (IPLS).

$$APLS_i = \frac{PLS_{i+1} - PLS_i}{2} \quad (3.1)$$

$$IPLS = 1,000 \times \frac{PLS_{i+1} - PLS_i}{Passes_{i+1} - Passes_i} \quad (3.2)$$

These two variables in Eq (3.1) and Eq (3.2) will be used in the development of permanent strain models since it is desirable to have a model for permanent strain in incremental form.

The following steps were taken in the process of data selection and retention:

- 1) Only PLS curves that have at least four segments were retained. Because of this, the strain and stress data for the following experimental cells and windows were removed: 705; 706C6; 707C4; 708C4&C4; 709C3&C5; 710C6. Also, the strain data recorded at depths higher than 550mm were also removed.
- 2) Vertical Stress for test cell 701, 702 and 703 were calculated by interpolation for the same depths where the vertical strains were measured.
- 3) Only segments for which the Incremental Plastic Strain (IPLS) is positive were retained. Figure 3.3 shows an example in which, for some segments, IPLS is negative. In such situations, several segments were joined into a single segment, which has an average IPLS.

After the data selection and retention has been conducted, two datasets resulted:

1. A dataset with 1132 observations containing plastic and elastic vertical strains.

2. A dataset with 325 observations containing plastic and elastic vertical strains and vertical stresses.

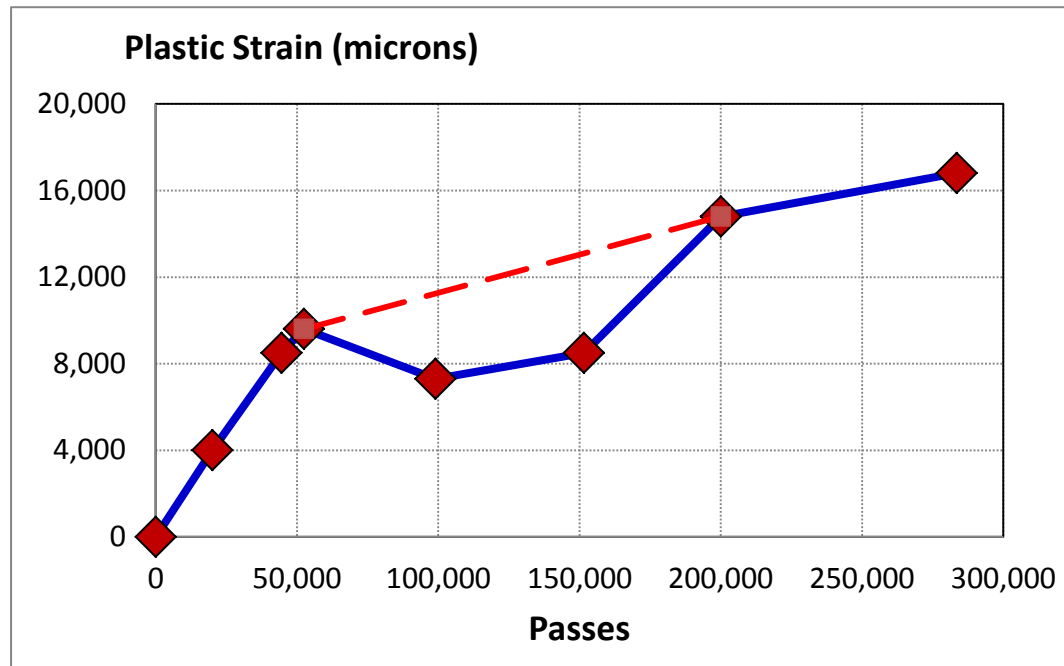


Figure 3.3: Example of Joined Plastic Strain Segments

3.2 Derivation of Permanent Deformation Models of Known Form

The next step in the development of empirical models was the derivation of models that have the form of existing models found in the literature for the permanent deformation in granular materials and asphalt mixes. The SAS statistical software is capable of performing non-linear regression analysis only when the form of the regression models is specified by the user. Therefore, the SAS software was used for this purpose.

The following models in Eq (3.3)-Eq (3.7) found in the literature review were not selected for the non-linear regression analysis since the permanent strain is expressed

only as a function of the number of passes; stresses or strains are not included as independent variables:

- Barksdale ⁽²¹⁾,

$$\varepsilon_p = a + b \times \log(N) \quad (3.3)$$

- Sweere ⁽²²⁾

$$\varepsilon_p = a \times [N^b] \quad (3.4)$$

and

- Hornyck et al. ⁽²³⁾:

$$\varepsilon_p = a \times \left[1 - \left(\frac{N}{100} \right)^{-b} \right] \quad (3.5)$$

- Van Niekerk et al. ⁽²⁴⁾ and Van Niekerk ⁽²⁵⁾:

for aggregates

$$\varepsilon_p = a \times \left[\left(\frac{N}{1000} \right)^b \right] + c \times e^{d \times \frac{N}{1000} - 1} \quad (3.6)$$

aggregates

where $c = 0$ if the accumulation of PD is stable

for sand:

$$\varepsilon_p = a \times \left[\left(\frac{N}{1000} \right)^b \right] \quad (3.7)$$

Van Niekerk model for permanent deformation for sand

Also, the model recommended by Gidel ⁽²⁸⁾ in Eq (3.8) was not selected since it requires the maximum deviatoric stress, p_{max} , and the maximum confining stresses, q_{max} . which were not obtained in the PSPS experiment.

$$\varepsilon_p = a \times \left[1 - \left(\frac{N}{100} \right)^{-b} \right] \times \left\{ \left[\frac{(q_{max}^2 + p_{max}^2)^{0.5}}{p_a} \right]^2 \right\} / [m + \frac{s}{p_{max}} - \frac{q_{max}}{p_{max}}] \quad (3.8)$$

Where $p_a = 100\text{kPa}$

a, b, c, d, n – model parameters

m, s – parameters of the failure line of the material, of equation $q = m \times p + s$

p – deviatoric stress; q – confining stress

N – number of load repetitions.

However, all variables included in the energy-density model developed at the Danish Road Institute ⁽³⁰⁾ and later modified by Odermatt ⁽³¹⁾ were obtained in the PSPS experiment. This empirical model has the form in Eq (3.9):

$$\varepsilon_{pz} = a \times [N^b] \times [0.5 \times \varepsilon_z \times \frac{\sigma_z}{p_a}]^c \quad (3.9)$$

Where: ε_{pz} – vertical plastic strain at a depth z (microstrain)

ε_z – vertical dynamic elastic strain at depth z , (microstrain)

N – number of load repetitions

σ_z – vertical stress at depth z (MPa)

p_a – reference stress = atmospheric pressure (100 kPa)

a, b, c – constants

Therefore, the a, b and c constants were obtained using non-linear statistical analysis for four soils studied in the PSPS experiment. The three constants, along with the coefficient of determination, R-square, are given in Table 3.1. The table indicates that very good fit is obtained for individual soils when the regression analysis is conducted only for the cells where the subgrade soil was constructed at the Optimum Moisture Content (OMC). However, the goodness of fit deteriorates when regression is run for all

soils at the same time. The non-linear regression could not be run for the A-7-6 soil (experimental cell 710) for which the vertical stress in the subgrade soil was not measured.

Table 3.1: Results of the Non-linear Regression Analysis for the Odermatt model

	A-2-4	A-4	A-6	A-7-5	A-7-6	All soils
Soil only at OMC						
a	87.589	0.8861	0.8871	1.5678		17.7254
b	0.545	0.4375	0.3282	0.1518		0.1937
c	-0.2977	0.6771	0.8002	0.8959		0.5656
R-square	0.9412	0.9941	0.9877	0.963		0.7787
SE _y (microstrain)	2,323	672	874	1,350		3,526
MC= OMC, OMC+2% or OMC+3%						
a	120.2	6.1934	265.4	1.5678		247.9
b	0.1464	0.2652	0.1703	0.1518		0.1667
c	0.4998	0.6188	0.2676	0.8959		0.2715
R-square	0.8086	0.8968	0.69	0.963		0.6948
SE _y (microstrain)	4,857	2,341	4,303	1,350		5,110
All Moisture Contents						
a	271.4	6.1934	960.2	11.5023		430.6
b	0.147	0.2652	0.2145	0.1262		0.1455
c	0.3672	0.6188	0.0258	0.6506		0.2216
R-square	0.8215	0.8968	0.6226	0.8956		0.6632
SE _y (microstrain)	4,675	2,341	5,266	1,788		3,526

Another simple model that uses variables measured in the PSPS experiment is the Theyse et al. ⁽²⁷⁾ empirical model in Eq (3.10):

$$\varepsilon_{pz} = a \times [N^c] \times [e^{b \times \sigma_z} - 1] \quad (3.10)$$

Where: ε_{pz} – vertical plastic strain at a depth z (microstrain)

N – number of load repetitions

σ_z – vertical stress at depth z (MPa)

a, b, c – constants

The a, b and c constants in the Theyse model were obtained using non-linear statistical analysis for four soils studied in the PSPS experiment. The three constants, along with the coefficient of determination, R-square, are given in Table 3.2. The table indicates that, when the regression analysis is conducted only for the cells where the subgrade soil was constructed at the Optimum Moisture Content (OMC), very good fit is obtained for the A-4, A-6 and A-7-5 soils. However, the goodness of fit deteriorates when regression is run for all soils at the same time.

As for the Odermatt model, the non-linear regression could not be run for the A-7-6 soil since this soil was tested only in experimental cell 710, for which the vertical stress in the subgrade soil was not measured.

Tables 3.1 and 3.2 also indicate that a better fit was obtained for the Odermatt model than the Theyse model; for the Odermatt model the coefficient of determination, R-square is higher.

The variables incorporated in the model for use in the Mechanistic Empirical Pavement Design Guide (M-E PDG) for permanent deformation in granular layers were also recorded in the PSPS experiment ⁽⁵⁷⁾.

Table 3.2: Results of the Non-linear Regression Analysis for the Theyse model

	A-2-4	A-4	A-6	A-7-5	A-7-6	All soils
Soil only at OMC						
a	4.13E-03	102.7	177,561	6E+05		2.817E+07

b	6.48E-04	4.9033	0.0529	0.1574		4.94E-04
c	2.0664	0.5148	0.2975	0.1607		0.1544
R-square	0.665	0.994	0.9403	0.8846		0.659
SE _y (microstrain)	5,632	677	1,937	2,213		4,487
MC= OMC, OMC+2% or OMC+3%						
a	9.144E+06	474.1	482.7	6.0E+05		3.5E+07
b	0.0027	9.2776	35.975	0.1574		0.00064
c	0.1372	2.513	0.1488	0.1607		0.1317
R-square	0.787	0.857	0.879	0.8846		0.704
SE _y (microstrain)	5,663	3,175	3,084	2,213		5,110
All Moisture Contents						
a	2.2E+07	474.1	472.2	1,491.4		6.925E+06
b	0.00132	9.2776	36.25	4.2938		0.00415
c	0.1225	2.513	0.159	0.1582		0.1056
R-square	0.7779	0.857	0.626	0.8516		0.6692
SE _y (microstrain)	5,235	3,175	5,407	2,323		5,288

The M-E PDG model has the form in Eq (3.11):

$$\delta_a(N) = \beta_i \times \frac{\varepsilon_0}{\varepsilon_r} \times \varepsilon_v \times h \times e^{-(\frac{\rho}{N})^\beta} \quad (3.11)$$

Where:

δ_a – Permanent deformation for the layer/sublayer

β_i – Calibration factor for the unbound granular and subgrade materials

ε_r – Resilient strain imposed in laboratory test to obtain the above listed material

properties

ε_v – Computed average vertical resilient strain in the layer/sublayer

h – Thickness of the layer/sublayer

N – Number of load repetitions

ε_0 , β and ρ – Material properties; $\log \beta = -0.6119 - 0.017638 \times w_c$.

w_c – water content in the layer/sublayer

The model can be written as: $\varepsilon_{pv}(N) = a \times \varepsilon_v \times e^{-(\frac{b}{N})^c}$

where $a = \beta_i \times \frac{\varepsilon_0}{\varepsilon_r}$; $b = \rho$ and $c = \beta$

The a , b and c constants in the M-E PDG model were obtained using non-linear statistical analysis for each of the five soils studied in the PSPS experiment. The three constants, along with the coefficient of determination, R-square, are given in Table 3.3. The table indicates that, when the regression analysis is conducted only for the cells where the subgrade soil was constructed at the Optimum Moisture Content (OMC), very good fit is obtained for the A-4, A-6 and A-7-6 soils. However, the goodness of fit deteriorates when regression is run for all soils at the same time.

Tables 3.1, 3.2 and 3.3 suggest that the best fit was obtained for the Odermatt model than the Theyse and M-E PDG models. For all soils, the coefficient of determination for the Odermatt model is the highest.

Table 3.3: Results of the Non-linear Regression Analysis for the MEPDG model

	A-2-4	A-4	A-6	A-7-5	A-7-6	All soils
Soil only at OMC						
a	10.024	5.69	1.321	1.601	1.1132	2.049
b	850	6356.8	2552	355.5	502.1	1430.7
c	1.9474	0.3363	1.6	1.842	2.4927	1.6
R-square	0.7434	0.8079	0.8639	0.7726	0.8656	0.5348
SE _y (microstrain)	4,496	3,047	2,082	1,658	2,168	4,430
MC= OMC, OMC+2% or OMC+3%						
a	11.8989	8.5044	1.6745	1.601	1.1132	2.33
b	568.8	170942	219.4	355.5	502.1	894.5
c	2.646	0.1364	1.5958	1.842	2.4927	1.0
R-square	0.773	0.7351	0.3778	0.7726	0.8956	0.4392
SE _y (microstrain)	4,817	3,255	7,197	1,658	2,168	5,735
All Moisture Contents						
a	12.7887	8.5044	1.7969	2.112	1.1132	2.4462
b	756.8	170942	247.1	874.8	502.1	852.2
c	2.8704	0.1364	1.3093	1	2.4927	1.0
R-square	0.7673	0.7351	0.3833	0.7174	0.8956	0.4249
SE _y (microstrain)	5,091	3,255	6,864	2,175	2,168	5,846

3.3 Derivation of Permanent Deformation Models of Unknown Form

The development of empirical models for the evolution of permanent deformation that do not have the form of existing models found in the literature was also conducted. The SAS statistical software, like most statistical analysis packages, is capable of performing non-linear regression analysis only when the form of the regression model is specified by the user. Therefore, the SAS software could not be used for this purpose.

The software selected for analysis was Table Curve 3D, which allows the user to find new equations to describe empirical data. The user can find models for more

complex data, including equations that might never have been considered. The built-in equation set includes a wide array of linear and nonlinear models for any application:

- Linear equations
- Polynomial and rational functions
- Logarithmic and exponential functions
- Nonlinear peak functions
- Nonlinear transition functions
- Nonlinear exponential and power equations.

In addition to standard least square minimization, the software is capable of three different robust estimations: least absolute deviation, Lorentzian minimization and Pearson VII minimization. Only the standard least square minimization was used in this research; it is the most popular.

As indicated by the name of the software package, the software is limited to developing non-linear regression analysis for maximum of two independent variables; it can provide equations that relate Z, the dependent variable, to X and Y, the independent variables. Because the number of independent variables was restricted to no more than two, the usefulness of this analysis is limited.

The analysis was conducted in the following logical steps:

1. **Data Import.** Permanent deformation data was imported from the PSPS database, the same way as it was done for the development of models with known form.
2. **Variable Selection.** The independent variable Z and the dependent variables X and Y are selected named.

3. ***Model Derivation.*** Several categories of models can be selected (e.g. linear, logarithmic, polynomial) or all categories can be selected simultaneously. The software will run thousands of built-in models and it will provide a list of models in the order of decreasing coefficient of determination (R-square) and a three-dimensional chart, in separate windows.
4. ***Model Selection.*** The user can inspect the chart and the model, and if needed, can change the chart to show the next models on the list until one is found satisfactory. This must be done to ensure that the obtained model is reasonable. For example, Figure 3.4 shows the chart for a model that cannot be accepted, because the surface representing predicted Z values must not have local extreme values (minimum or maximum). The chart given in Figure 3.5 also shows a model that cannot be accepted, because the model surface must always be above the horizontal XY plane since the incremental permanent deformation is always positive. Finally, the chart also indicates the variation of Z with Y for a given X, and the variation of Z with X for a given Y. Only models that lead to a desired variation can be selected; an example is showed in Figure 3.6.

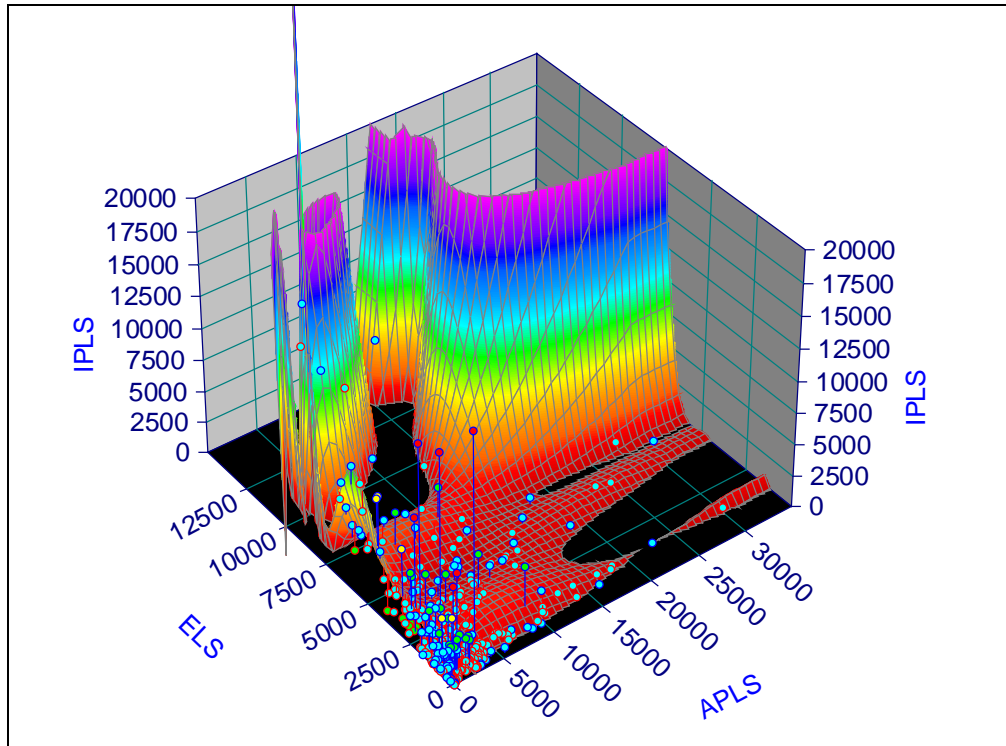


Figure 3.4: Chart of Unacceptable Model – Example 1

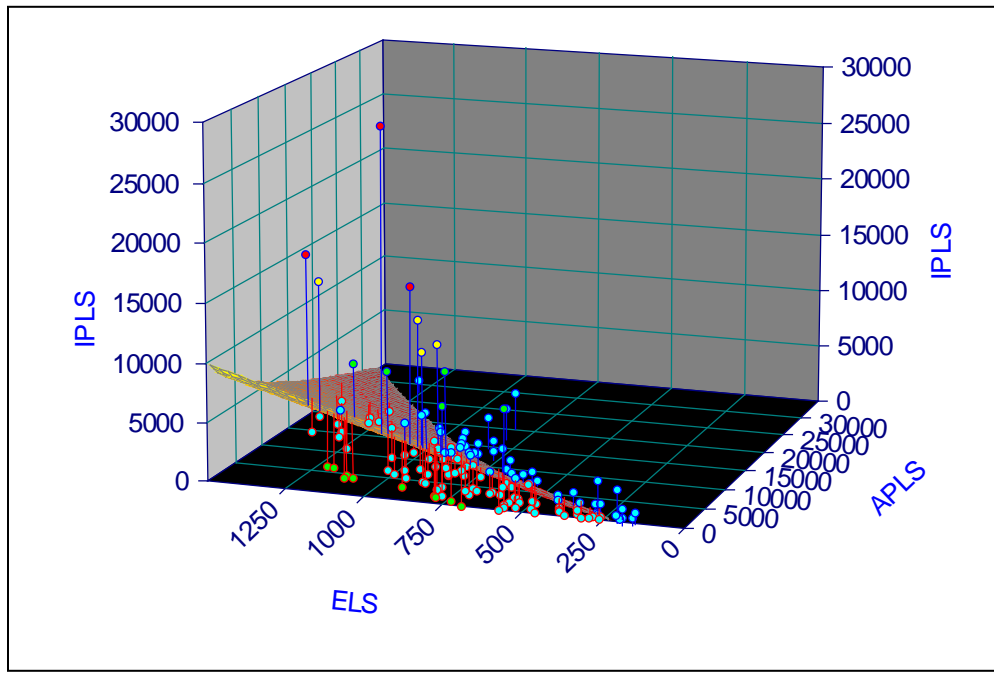


Figure 3.5: Chart of Unacceptable Model – Example 2

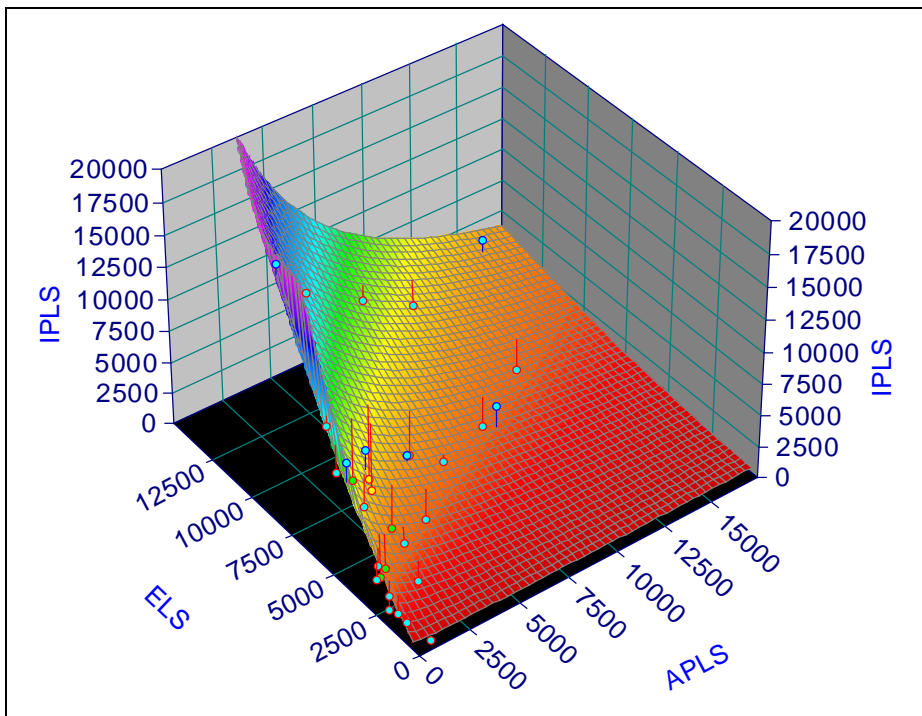


Figure 3.6: Chart of an Acceptable Model

In the chart presented in Figure 3.6 the dependent variable $Z = \text{IPLS}$ (Incremental Plastic Strain) is plotted versus the two independent variables $X = \text{APLS}$ (Accumulated Plastic Strain) and $Y = \text{ELS}$ (Elastic Strain). For a given Accumulated Plastic Strain, the Incremental Plastic Strain should increase with the increasing Elastic Strain. Also, for a given Elastic Strain, the Incremental Plastic Strain should be less for higher values of Accumulated Plastic Strain. Therefore, this is a desirable trend for any model that predicts the Incremental Plastic Strain using the values of Accumulated Plastic Strain and the Elastic Strain.

Because only models with two independent variables are accepted by the software, the moisture content of the soil, MC, could not be included as an independent variable and only four kinds of models could be analyzed:

$$\text{Model 1: } \text{IPLS} = \mathbf{F}(\text{APLS}, \text{ELS})$$

Model 2: $IPLS = F(APLS, STRESS)$

Model 3: $PLS = F(N, ELS)$

Model 4: $PLS = F(N, STRESS)$

Where:

$IPLS$ = Incremental Plastic Strain due to one additional load cycle (microstrain)

$APLS$ = Accumulated Plastic Strain prior to the load cycle (microstrain)

ELS = Elastic Strain due to the load cycle (microstrain)

$STRESS$ = Elastic Stress due to the load cycle (kPa)

PLS = Measured Plastic Strain after the load cycle (microstrain)

The trends observed on the PSPS data, as well as in the laboratory testing of soils, clearly indicated that, for a given magnitude of elastic stress or strain, $IPLS$ decreases with the number of load cycles and therefore, with the accumulated plastic strain. At the same time, when the soils has already accumulated plastic strain, $APLS$, the incremental plastic strain cause by a single load cycle, $IPLS$, is increasing with the generated elastic strain, ELS , or elastic stress stress.

The Incremental Plastic Strain, $IPLS$, was selected as the dependent variable and $APLS$ as independent variable in Models 1 and 2 because the history of loading of the subgrade soil can be represented only by $APLS$; no other information of prior loading (e.g. stress or strain) is used to compute $IPLS$. This form of the model it is the most

useful when permanent deformation or strain models are incorporated in pavement design environments. Many design software, including M-E PDG, predict permanent deformation in incremental algorithms. For example, M-E PDG divides the design life in two-week or four-week periods and calculates accumulated distresses for each period and then adds them in two-week increments.

The Odermatt and Theyse models can also be written to compute the incremental plastic strain, IPLS, as a function of accumulated plastic strain, APLS, as follows:

1. Both models can be written in Eq (3.12):

$$\varepsilon_{pz} = A \times [N^B] \quad (3.12)$$

Where: $A = a \times [0.5 \times \varepsilon_z \times \frac{\sigma_z}{p_a}]^c$ and $B=b$ for the Odermatt model;

$A = a \times [e^{b \times \sigma_z} - 1]$ and $B=c$ for the Theyse model

ε_{pz} = Accumulated plastic strain, PLS, after loading cycle N

2. The incremental plastic strain, IPLS, for loading cycle N+1 can be computed as Eq (3.13):

$$IPLS = d\varepsilon_{pz} / dN = A \times B \times [N^{B-1}] \quad (3.13)$$

3. After solving for N in equation 11, the incremental plastic strain, IPLS, can be computed as Eq (3.14):

$$IPLS = d\varepsilon_{pz} / dN = \left[A^{\frac{1}{B}} \right] \times B \times \left[\varepsilon_{pz}^{1-\frac{1}{B}} \right] = \left[A^{\frac{1}{B}} \right] \times B \times \left[PLS^{1-\frac{1}{B}} \right] \quad (3.14)$$

The non-linear regression analysis was run and the best fit equations obtained for Model 1 are given in Table 3.4. Because the moisture content of the soil, MC, could not be included as a predictor variable, the goodness of fit (expressed by the coefficient of determination, R-squared) was poor when data for multiple moisture contents was pooled together. Better goodness of fit was obtained when the data collected only for the soils tested at the optimum moisture content, OMC, the results are given in Table 3.4. The models given in Table 3.4 do not seem to be able to predict well the incremental plastic strain, IPLS, and they do not seem to be practical.

It was also attempted to run the non-linear regression analysis for Model 2. Compared to Model 1, Model 2 uses vertical stress (STRESS) as an independent variable instead of the vertical elastic strain (ELS). Unfortunately, no model was found to be reasonable in term of the desired pattern of the three-dimensional plot on the predicted surface or the goodness-of-fit.

Table 3.4: Results of the Non-linear Regression Analysis for Model 1

Model 1: z = IPLS x=APLS y=ELS	
A-2-4 Soil only at OMC	$z=a+LOGNORMX(b,c,d)+LOGNORMY(e,f,g)$ a= 485.2; b=15,486.1; c=4,104.7; d = 0.00586; e= 1,423.3; f=1,225.4; g=0.002 R-square = 0.691 Rank=34
A-4 Soil only at OMC	$z=a+by+LOGNORMX(c,d,e)$ a=475.34; b = 0.0308; c= 23,943; d= 3,350; e=-0.00263 R-square = 0.570 Rank=7
A-6 Soil only at OMC	$z=LOGNORMX(a,b,c)*GAUSSY(1,d,e)$ a=1.815E+6; b = 386.3; c= 1.0036; d= 33,500; e=8,023.5 R-square = 0.734 Rank=82
A-7-5 Soil only at OMC	$z=a+by+LOGNORMX(c,d,e)$ a=90.04; b = 0.1888; c= 294,080; d= 1,751; e=-0.0078 R-square = 0.562 Rank=60
A-7-6 Soil only at OMC	$\ln z=a+bx^{0.5}+c(\ln y)^2$ a=2.8157; b = -0.0233; c= 0.092 R-square = 0.625 Rank=6
All soils only at OMC	$z=a+LORCUMX(b,c,d)+LORCUMY(e,f,g)+LORCUMX(h,c,d)*LORCUMY(l,f,g)$

a=-5135.6; b=5611; c=1827.8; d = 446.8; e= 356,597; f=11,323; g=526.9; h=-357,485; R-square = 0.387 Rank=28
--

Rank = the rank of the equation in the decreasing order of R-square

$$GAUSSX(a,b,c) = a * EXP\{-0.5 * [(x-b)/c]^2\}$$

$$LOGNORMX(a,b,c) = a * EXP\{-0.5 * [\ln(x/b)]^2 / [c^2]\}$$

$$LORCUM \text{ is the Lorentzian cumulative function } LORCUMX(a,b,c) = (a/\pi) * \{0.5 * \pi + \arctan[(x-b)/c]\}$$

Because no model was capable to predict the incremental plastic strain well, IPLS, the non-linear regression analysis was conducted for Model 3. A power model and an exponential model seem to predict reasonably well the plastic strain, PLS, depending on the number of applied load cycles, N, and the applied elastic strain, ELS. They are given in Table 3.5.

For Model 4, that uses vertical stress (STRESS) as an independent variable instead of the vertical elastic strain (ELS), no model was found to be reasonable in terms of the desired pattern of the three-dimensional plot on the predicted surface or the goodness-of-fit.

Table 3.5: Results of the Non-linear Regression Analysis for Model 3

Power model	$PLS = a * N^b * ELS^c$	
A-2-4 Soil only at OMC a= 0.0102; b=0.2344; c=1.61785	n = 78	$R^2 = 0.7029$
A-4 Soil only at OMC a= 0.005; b=0.3888; c=1.3157	n = 183	$R^2 = 0.5749$
A-6 Soil only at OMC a= 0.001; b=0.6387; c=1.115	n = 47	$R^2 = 0.4265$
A-7-5 Soil only at OMC	n = 110	$R^2 < 0.300$
A-7-6 Soil only at OMC a= 1.37E-4; b=0.466; c=1.554	n = 32	$R^2 = 0.3125$
All soils only at OMC a= 1.9706; b=0.2733; c=0.6704	n = 450	$R^2 = 0.4209$
Exponential model	$PLS = a * \exp(N/b) * \exp(ELS/c)$	

A-2-4 Soil only at OMC		
a= 805.2; b=324,788; c=484.4	n = 78	R ² = 0.7474
A-4 Soil only at OMC		
a= 946.5; b=349,888; c=1,800.5	n = 183	R ² = 0.5749
A-6 Soil only at OMC		
a= 1,343.5; b=56,148; c=6,013	n = 47	R ² = 0.7577
A-7-5 Soil only at OMC		
a= 559.6; b=8.87E11; c=1,850	n = 110	R ² = 0.5521
A-7-6 Soil only at OMC		
a= 1,188.3; b=56,189; c=5,527	n = 32	R ² = 0.7414
All soils only at OMC	n = 450	R ² <0.300

Tables 3.1 to 3.5 give model coefficients for each of the five soil types tested in the PSPS experiment. Since it is desirable to have models that include the soil type as an independent variable, the statistical analysis was performed by adding a new independent variable, the optimum moisture content of the soil, OMC. OMC values of the soils tested are given in Table 2.3. OMC was used to represent the soil type since it is a numerical variable; the AASHTO and UCS soil types are categorical variables.

Table 3.6 gives the models obtained when OMC is included in the exponent for the elastic stress or strain terms. The models with the best fit to the experimental data are the Odermatt model and the power model. Both models seem reasonable, since the standard error of the predicted permanent deformation, SEy, is close to 3,000 microstrain.

It is important to observe that the model coefficient d, in front of the OMC term, is negative for both the Odermatt and the power models. This suggests that, for a given number of applications of the same elastic strain or stress, the permanent deformation is less for soils with higher OMC, finer soils. This confirms the observation reported by Cortez, that finer soils tested in the PSPS experiment exhibited less permanent deformation than the coarse soils ⁽¹⁷⁾.

Table 3.6: Permanent Deformation Models with OMC as Independent Variable

Odermatt model	$PLS = a * N^b * [0.5 * ELS * STRESS / p_a]^{(c+d*OMC)}$
All soils only at OMC	$a= 4.62; b=0.271; c=0.9175; d= -0.0161 \quad n = 102 \quad R^2 = 0.7204 \quad SE_y=2,747$
Theyse model	$PLS = a * N^b * \{\exp[STRESS*(c+d*OMC)] - 1\}$
All soils only at OMC	$a= 3.9*10^6; b=0.1977; c=0.0046; d= -0.00011 \quad n = 102 \quad R^2 = 0.37 \quad SE_y=4,124$
Power model	$PLS = a * N^b * ELS^{(c+d*OMC)}$
All soils only at OMC	$a= 0.1598; b=0.3017; c=1.392; d= -0.0279 \quad n = 450 \quad R^2 = 0.7677 \quad SE_y=3,125$
Exponential model	$PLS = a * \exp(N/b) * \exp[ELS/(c+d*OMC)]$
All soils only at OMC	$a= 3,068; b=455,700; c=0; d=600 \quad n = 450 \quad R^2 = 0.484 \quad SE_y=4,654$

CHAPTER FOUR

DEVELOPMENT AND IMPLEMENTATION OF A CONSTITUTIVE MODEL FOR UNSATURATED SANDS

4.1 Introduction

Granular materials exhibit a wide range of mechanical behavior that depends on their composition and fabric, stress history, density, and the nature of the applied force. Over the past few decades, researchers have developed a number of constitutive models based on elasto-plasticity to account for most of these factors and predict the response of these soils. These models include the family of two-surface plasticity models (See reference 1, 2; 3, 4, 5, 6 and 7), the double hardening model (See references 8, 9, 10 and 11), the CAP model ⁽¹²⁾; the volumetric hardening model ^(13, 14), and the cyclic densification model ⁽¹⁵⁾.

Sands with different moisture content experience difference suction, which affects their performance. But this effect has traditionally been difficult to quantify using either empirical or mechanistic methods. Heath et al. ⁽¹⁶⁾ presented a practical mechanistic framework for quantifying the behavior of unsaturated granular materials within the range of water contents, densities, and stress states. The framework utilized a simple soil suction model that has three density-independent parameters that can be determined from tests.

A two-surface plasticity model for sands was developed by Wang et al.⁽¹⁾ based on a bounding surface plasticity theory developed by Dafalias⁽⁵⁸⁾. This model was coupled with the state parameter by Manzari and Dafalias⁽²⁾ within the framework of critical state soil mechanics. This model, however, did not account the limit on plastic deformation at constant stress ratio and fabric anisotropy. Nazzal et al.⁽⁵⁹⁾ adopted Manzari and Dafalias's⁽²⁾ model and incorporated suction, following the framework proposed by Heath et al.⁽¹⁶⁾.

Li and Dafalias⁽³⁾ introduced modification to the plastic loading functions of the model by Manzari and Dafalias⁽²⁾. The model was further refined by the use of a cap to control plastic deformation at a constant stress ratio⁽⁶⁰⁾. Loading functions were also modified with stresses expressed in multiaxial. Li and Dafalias^(5, 6) introduced fabric anisotropy to Li's model with and without a cap. This model was extended in this study to account for unsaturated granular material behavior following the framework proposed by Heath et al.⁽¹⁶⁾.

The new model was implemented into the Abaqus finite element program through a user defined UMAT subroutine. FE simulation results obtained using the newly implemented sand model was verified with wide range of triaxial test data (different sample preparation methods, confining stresses, densities and drainage conditions). The model was then used to predict the behavior of unsaturated sands under shearing.

4.2 Model Development

4.2.1 General Framework

The basics of the formulation of the constitutive model are available in a number of papers (See references 3, 4, 5, 6 and 7). Thus, only the salient features of the model as needed for modification to account for fabric and unsaturated behavior are presented here.

The analytical expression of cone shaped bounding surface F_1 (Figure 4.1) is given by ⁽⁴⁾:

$$F_1 = \frac{\bar{R}}{g(\bar{\theta})} - H_1 \quad (4.1)$$

in which \bar{R} $\left(= \sqrt{\frac{3}{2}\bar{r}_{ij}\bar{r}_{ij}}\right)$ and $\bar{\theta}$ $\left(= -\frac{1}{3}\sin^{-1}\left(\frac{9\bar{r}_{ij}\bar{r}_{jk}\bar{r}_{ki}}{2\bar{R}^3}\right)\right)$ are the stress ratio and

Lode angle invariant of the image stress ratio tensor \bar{r}_{ij} . \bar{r}_{ij} is obtained by mapping the current deviatoric stress ratio r_{ij} $\left(= S_{ij}/P\right)$ to the bounding surface using mapping rules ⁽⁴⁾, details of which are provided later. S_{ij} and p are deviatoric stress and mean effective normal stress respectively. H_1 is a function of the internal state variables. F_1 is normalized in the R - θ plane with its controlled by \bar{R} , $\bar{\theta}$ and H_1 via the state variables. The function $g(\bar{\theta})$ interpolates the stress ratio invariant (\bar{R}) on the bounding surface (F_1) based on Lode angle ($\bar{\theta}$).

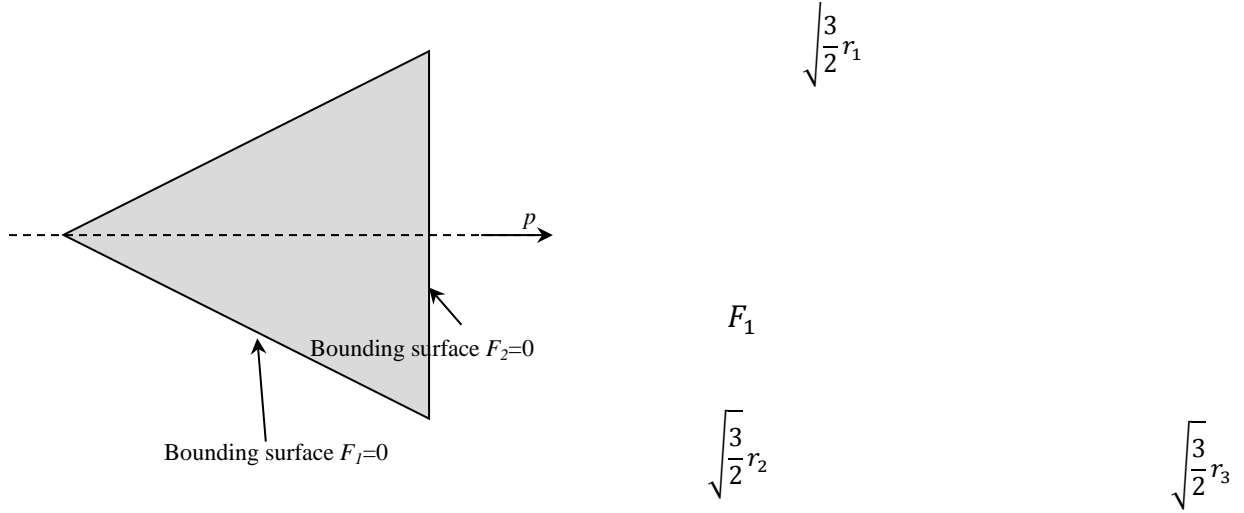


Figure 4.1: Shear bounding surface (F_1) and cap bounding surface (F_2) (modified from Li⁽⁴⁾)

Using plastic consistency condition for the cone, $dF_1 = 0$ ⁽⁴⁾:

$$p\bar{n}_{ij}d\bar{r}_{ij} - \bar{k}_{p1}dL_1 = 0 \quad (4.2)$$

The above equation is rewritten in terms of the actual stress ratio increment as:

$$p\bar{n}_{ij}dr_{ij} - k_{p1}dL_1 = 0 \quad (4.3)$$

where, \bar{n}_{ij} is the zero trace unit tensor normal to F_1 at the image stress ratio (\bar{r}_{ij}) . k_{p1} (or \bar{k}_{p1}) is the plastic modulus, and dL_1 is the scalar loading index associated with it. Evolution of F_1 is controlled by k_{p1} (or \bar{k}_{p1}) .

The flat cap segment F_2 (Figure 4.2) of the model is given by⁽⁴⁾:

$$F_2 = \bar{p} - H_2 \quad (4.4)$$

in which, \bar{p} is the image mean normal stress and H_2 is a function of the internal state variables. The position of the cap in the hydrostatic axis is defined by H_2 . \bar{p} is

obtained by mapping the current deviatoric stress ratio p to the bounding surface using mapping rules ⁽⁴⁾.

From the plastic consistency condition for the flat cap, $dF_2 = 0$,

$$d\bar{p} - \bar{k}_{p2} dL_2 = 0 \quad (4.5)$$

the above equation can be rewritten in terms of the actual stress ratio increment as:

$$dp - k_{p2} dL_2 = 0 \quad (4.6)$$

in which, \bar{k}_{p2} (or k_{p2}) is the plastic modulus controlling the evaluation of F_2 and dL_2 is the scalar loading index associated with it.

Plastic deviatoric strain (de_{ij}^p) can be calculated by assuming the associated flow rule for each yield surface and summing them up using Koiter's rule:

$$de_{ij}^p = de_{ij}^{p1} + de_{ij}^{p2} = \bar{n}_{ij} dL_1 + \bar{m}_{ij} dL_2 \quad (4.7)$$

in which, de_{ij}^{p1} and de_{ij}^{p2} are the plastic deviatoric strain increments. dL_1 and dL_2 are loading indices. \bar{n}_{ij} and \bar{m}_{ij} define the direction of the deviatoric strain increment due to change in r_{ij} and in p with constant r_{ij} , respectively. \bar{m}_{ij} takes the direction of the stress ratio (r_{ij}) ⁽¹⁾. So, \bar{m}_{ij} can be expressed as $\bar{m}_{ij} = \frac{r_{ij}}{|r_{ij}|}$.

The plastic volumetric strain increment ($d\varepsilon_v^p$) is due to $d\varepsilon_v^{p1}$ and $d\varepsilon_v^{p2}$. This can be expressed as:

$$\begin{aligned}
d\varepsilon_v^p &= d\varepsilon_v^{p1} + d\varepsilon_v^{p2} \\
&= \sqrt{\frac{2}{3}} \left(D_1 \sqrt{de_{ij}^{p1} de_{ij}^{p1}} + D_2 \sqrt{de_{ij}^{p2} de_{ij}^{p2}} \right) \\
&= \sqrt{\frac{2}{3}} (D_1 dL_1 + D_2 dL_2)
\end{aligned} \tag{4.8}$$

where D_1 and D_2 are two dilatancy functions. They are defined based on the concept of state parameter, as shown later.

Combining the above formulations following the classical elasto-plastic formalism, the incremental stress-strain relationship can be written as ⁽⁴⁾:

$$d\sigma_{ij} = \Lambda_{ijkl} d\varepsilon_{kl} \tag{4.9}$$

where

$$\Lambda_{ijkl} = E_{ijpq} \left[\delta_{pk} \delta_{ql} - \left(\bar{n}_{pq} + \sqrt{2/27} D_1 \delta_{pq} \right) \Theta_{kl} - \left(\bar{m}_{pq} + \sqrt{2/27} D_2 \delta_{pq} \right) Z_{kl} \right] \tag{4.10}$$

$$\Theta_{ij} = \frac{2G\bar{n}_{ij} - K(\bar{n}_{rs} + B)\delta_{ij}}{2G - \sqrt{2/3}KD_1(\bar{n}_{pq}r_{pq} + B) + K_{p1}} \tag{4.11}$$

$$B = \frac{2G\bar{n}_{ij}\bar{m}_{ij} - \sqrt{2/3}KD_2\bar{n}_{ij}r_{ij}}{\sqrt{2/3}KD_2 + K_{p2}} \tag{4.12}$$

$$Z_{ij} = \frac{K\delta_{ij} - \sqrt{2/3}KD_1\Theta_{ij}}{\sqrt{2/3}KD_2 + K_{p2}} \quad (\text{A.13})$$

The above relationship depends on shear modulus (G), bulk modulus (K), plastic modulus (K_{p1} and K_{p2}), and dilatancy functions (D_1 and D_2).

4.2.2 Mapping Rules

Mapping of the current stress state to bounding surface and finding the image stress state plays a central role in bounding surface plasticity theory. Two mapping rules are needed to project the current deviatoric stress ratio (r_{ij}) and mean normal effective stress (p) to their corresponding bounding surfaces.

The first mapping rule involves the projection of deviatoric stress ratio (r_{ij}) to the bounding surface (F_I) in deviatoric stress space (Figure 4.2 ⁽⁴⁾). The relocatable projection center (α_{ij}) is the point at which stress reversal occurs. When loading occurs, image deviatoric stress ratio (\bar{r}_{ij}) is obtained by projecting the current deviatoric stress ratio (r_{ij}) onto the bounding surface from projection center (α_{ij}), as shown in Figure 4.2 ⁽⁴⁾. The distance between r_{ij} and α_{ij} is ρ_1 and between \bar{r}_{ij} and α_{ij} is $\bar{\rho}_1$. The loading index dL_I is also a factor that controls the plastic deformation in the deviatoric stress space. The sign of loading index dL_I is positive or negative depending on whether the angle between \bar{n}_{ij} and dr_{ij} is acute or obtuse, respectively, as shown in Figure 4.3 ⁽⁴⁾. When loading occurs, the loading index dL_I is positive. When unloading occurs, dL_I becomes negative and results in the instantaneous relocation of the projection center (α_{ij}), as shown in Figure 4.3 to bring it back to positive. This means that dL_I is always positive or zero,

except for an instantaneous time during which the relocation of projection center due to stress reversal occurs.

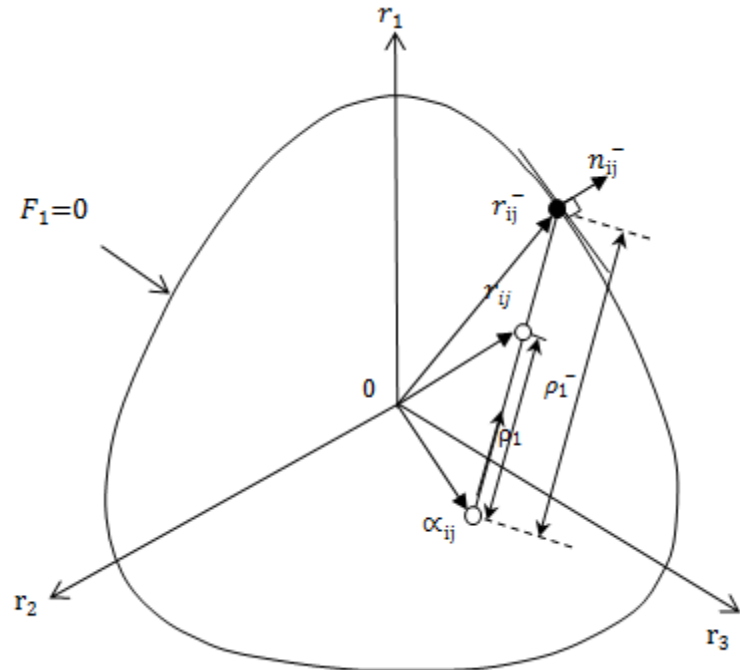


Figure 4.2: Mapping rule in deviatoric stress ratio space (modified from Li ⁽⁴⁾)

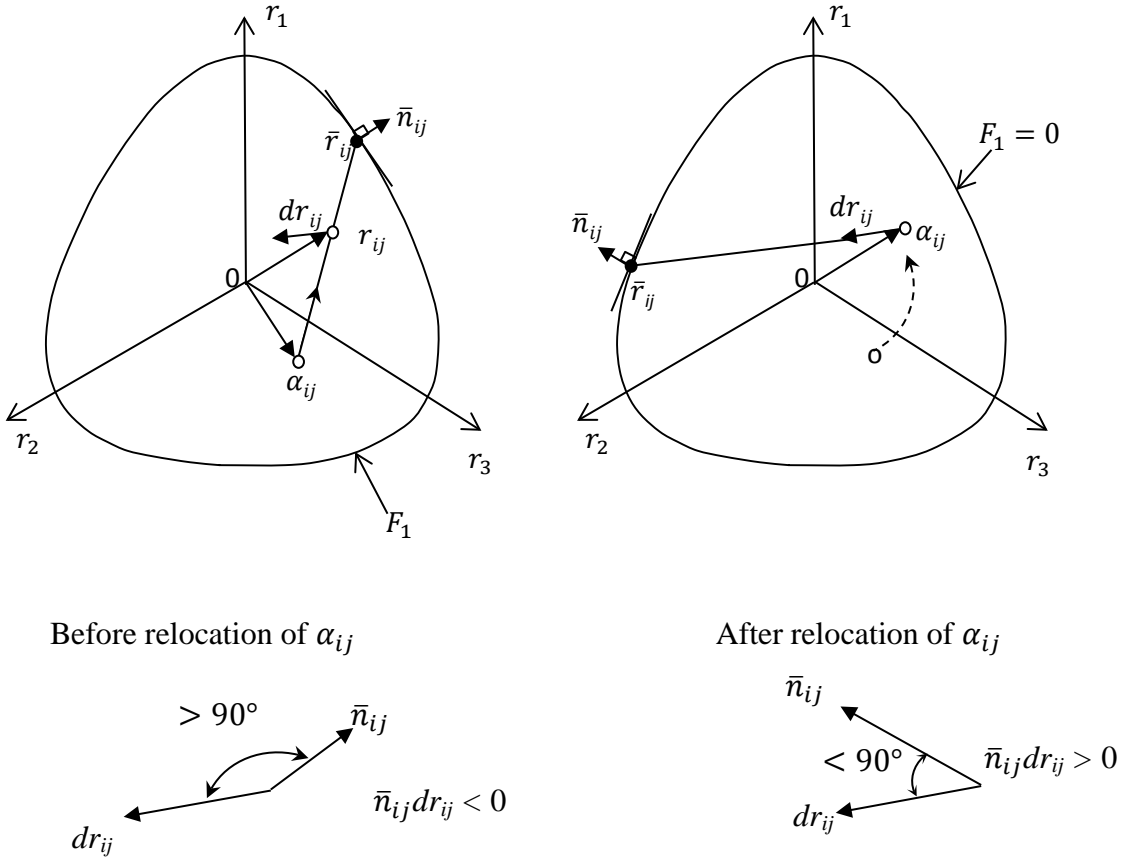


Figure 4.3: Illustration of relocation mechanism of projection center (modified from Li⁽⁴⁾)

The second mapping rule involves the projection of mean normal effective stress (p) to the bounding surface (F_2) when mean normal effective stress (p) changes at constant deviatoric stress ratio (r_{ij}). The relocatable project center (β) is the point at which the stress reversal occurs, i.e., it is the point at which the sign of dp changes. This is defined along the hydrostatic axis, as shown in Figure 4.16⁽⁴⁾. The image mean effective normal stress (\bar{p}) is obtained by projecting the mean effective normal stress (p) to bounding surface (F_2) from projection center β , as shown in Figure 4.4⁽⁴⁾. Distances between p and β ; and \bar{p} and β are ρ_2 and $\bar{\rho}_2$, respectively.

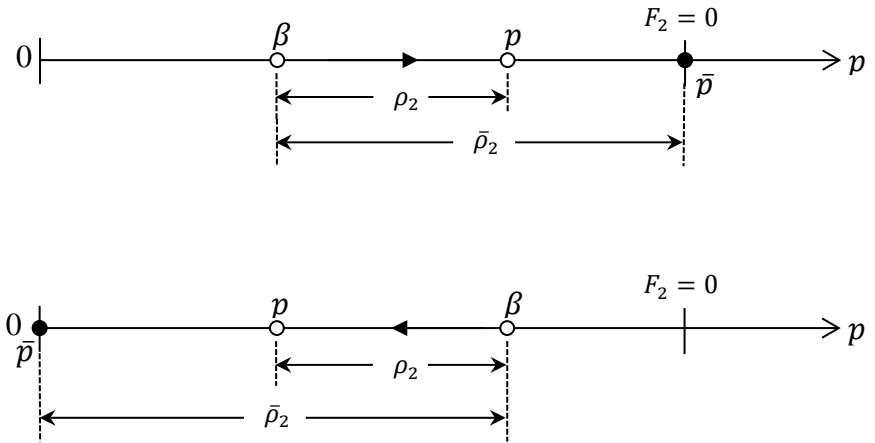


Figure 4.4: Mapping rule for p under constant r_{ij} (modified from Li⁽⁴⁾)

4.2.3 Elastic modulus

The empirical equation proposed by Richards et al.⁽⁶¹⁾ was used to find the elastic shear modulus (G). This expression has found widespread usage among many investigators (See references 1, 3, 4, 5, 62, 63, 64 and 65).

$$G = G_0 \frac{(2.97 - e)^2}{1 + e} \sqrt{pp_a} \quad (4.14)$$

where p_a is the atmospheric pressure (100 kPa). G_0 is a material constant. The bulk modulus (K) is found by:

$$K = G \frac{2(1+\nu)}{3(1-2\nu)} \quad (4.15)$$

where ν is the Poisson's ratio.

4.2.4 Fabric anisotropy

Fabric of granular media refers to the size, shape and arrangement of solid particles and associated voids. Void ratio is a common measure used to describe the state of packing of granular materials. This scalar-valued quantity, however, is not capable of characterizing the directional nature of fabric. Therefore, it is necessary to introduce tensor-valued measures that can represent the directional nature of fabric. These quantities are generally referred to as "fabric tensors" and are determined from measurements made on the solid or void phase of different microstructure-related vectors such as contact normals and particle, void or branch orientation vectors. Oda⁽⁶⁶⁾ showed that the shape of constituting particles and type of deposition process determined the characteristics of initial fabric of granular material.

The fundamental element of fabric is a unit vector n with directional cosines n_i . This unit vector can represent the orientation of any one of the different fabric parameters mentioned above, such as particles' long axes or normals to contact planes, etc. The orientation distribution function $f(n)$ of a fabric parameter of granular materials is usually described by⁽⁶⁷⁾:

$$f(n) = F_a [1 + F_{ij} n_i n_j] \quad (4.16)$$

where F_a is the average of the fabric parameter associated with n and which are randomly oriented, and the second order tensor F_{ij} is termed the fabric tensor.

Curry⁽⁶⁸⁾ introduced a parameter termed the vector magnitude, Δ , to quantify the microstructure anisotropy as follows:

$$\Delta = \frac{1}{N} \left[\sum_{k=1}^N (\cos 2\theta^k)^2 + \sum_{k=1}^N (\sin 2\theta^k)^2 \right]^{\frac{1}{2}} \quad (4.17)$$

where N is the total number of objects analyzed in an image, and θ^k is the orientation of the aforementioned unit vector n , ranging between -90° to $+90^\circ$. Theoretically, the value of Δ ranges between zero and unity. Zero indicates that objects are completely randomly distributed, which is analogous to isotropic materials. Unity indicates that objects are entirely oriented in one direction, which is analogous to perfectly transverse anisotropic materials. Oda and Nakayama⁽³³⁾ showed that for transversely isotropic elements, the fabric tensor F_{ij} can be related to Δ by the following expression of its three principal values: $F_{11} = (1 - \Delta)/(3 + \Delta)$ and $F_{22} = F_{33} = (1 + \Delta)/(3 + \Delta)$.

4.2.5 Anisotropic state variable

An anisotropic state variable was developed by the coupling loading direction and fabric. In order to couple the loading direction, the mean normalized stress $\left\{ \frac{\sigma_{ij}}{p} = \frac{s_{ij}}{p} + \delta_{ij} \right\}$ needs to be determined at critical state failure surface. The Coulomb type critical state failure surface can be expressed in multiaxial space as:

$$\bar{R} - M_c g(\bar{\theta}) = 0 \quad (4.18)$$

in which M_c is the critical stress ratio at triaxial compression. By using Eq. 4.18, the mean normalized stress at critical state failure surface ($\hat{\sigma}_{ij}$) is obtained as:

$$\hat{\sigma}_{ij} = \sqrt{\frac{3}{2}} M_c g(\bar{\theta}) l_{ij} + \delta_{ij} \quad (4.19)$$

where l_{ij} ($= \frac{\bar{r}_{ij}}{/\bar{r}_{mn}/}$) is the unit vector that shows the direction of image stress ratio \bar{r}_{ij} . Tobita ⁽⁶⁹⁾ introduced a modified stress tensor \hat{T}_{ij} to characterize anisotropic effects as:

$$\hat{T}_{ij} = \frac{1}{6} (\hat{\sigma}_{ij} F_{kj}^{-1} + F_{ik}^{-1} \hat{\sigma}_{kj}) \quad (4.20)$$

in which, F_{ij}^{-1} is the inverse of the fabric tensor F_{ij} and \hat{T}_{ij} is a symmetric second-order tensor possessing three independent isotropic invariants. Of these three, two non-trivial invariants pertinent to \hat{r}_{ij} are $\hat{R} = \sqrt{\frac{3}{2} \hat{r}_{ij} \hat{r}_{ij}}$ and $\hat{\theta} = -\frac{1}{3} \sin^{-1} \left(\frac{9 \hat{r}_{ij} \hat{r}_{jk} \hat{r}_{ki}}{2 \hat{R}^3} \right)$. A single invariant called the anisotropy state variable A can be defined by combining \hat{R} and $\hat{\theta}$ to characterize the anisotropy ⁽⁵⁾:

$$A = \frac{\hat{R}}{M_c g(\hat{\theta})} - 1 \quad (4.21)$$

4.2.6 State parameter

The state parameter was defined by Been and Jefferies ⁽⁷⁰⁾ as $\psi = e - e_c$, where, e is the current void ratio and e_c is the critical void ratio at the critical state line in the $e - \ln p$ plane corresponding to current p . Schofield and Wroth ⁽²⁷⁾ represented the critical state line by a straight line of the slope λ in $e, \ln p$ space. However, to accommodate the often observed nonlinear critical state lines for sands, Li and Wang ⁽⁷¹⁾ introduced a new relationship to predict the critical state line in void ratio, $(p/p_a)^\xi$ space as:

$$e_c = e_\tau - \lambda_c \left(\frac{p}{p_a} \right)^\xi \quad (4.22)$$

where e_τ , λ_c and ξ are the material constants.

The critical void ratio (e_τ) at intercept $p = 0$ is made as a function of the anisotropic parameter A ⁽⁵⁾. This relationship incorporates fabric anisotropic effect into the critical state void ratio. In addition, some researchers^(69, 72, 73) have shown that critical-state line in the e - p plane is dependent on the initial fabric and shear mode. In order to accommodate such dependency, following Yang et al.⁽⁷⁾, the critical-state void ratio at intercept $p = 0$ is proposed as:

$$e_\tau = e_{\tau c} - k_\tau (A_c - A)(1 - t.b) \quad (4.23)$$

where $e_{\tau c}$, k_τ and t are material constants. A_c is the anisotropy state variable during triaxial compression and b ($= \frac{\sigma_2 - \sigma_3}{\sigma_1 - \sigma_3}$) is the ratio of intermediate principal stress parameter. σ_1 , σ_2 and σ_3 are principal stresses.

4.2.7 Dilatancy

The dilatancy (d) is the ratio between plastic volumetric strain increments ($d\epsilon_v^p$) to deviatoric strain increment ($d\epsilon_q^p$). Taylor⁽⁷⁴⁾ and Rowe⁽⁷⁵⁾ suggested that dilatancy (d) is a unique function of the stress ratio (η). Roscoe and Schofield⁽⁷⁶⁾ developed a relationship for dilatancy in an original cam clay model ($d = M - \eta$) in the triaxial space, where M is the critical state stress ratio or the frictional, material constant. The dilatancy function in the original cam clay model is extended to incorporate dependency in the state parameter (ψ) in triaxial space as⁽³⁾:

$$d = d_1 \left(e^{m\psi} - \frac{\eta}{M} \right) = \frac{d_1}{M} (M e^{m\psi} - \eta) \quad (4.24)$$

where m and d_1 are material constant. The expression reduces to $d = M - \eta$, when $d_1 = M$ and $m = 0$ at the critical state as in the original cam clay. The expression for dilatancy in triaxial space can be extended to multiaxial stress-strain space as ⁽⁴⁾:

$$D_1 = \frac{d_1}{M_c g(\theta)} \left[M_c g(\theta) e^{m\psi} \sqrt{\frac{\bar{\rho}_1}{\rho_1}} - R \right] \quad (4.25)$$

where the term $\left(\frac{\bar{\rho}_1}{\rho_1} \right)$ is an internal state variable. Dilatancy is zero at critical state ($\psi=0$, $\rho_1 = \bar{\rho}_1$ and $\eta = M_c$) and phase transformation state ($\psi \neq 0$, $\rho_1 = \bar{\rho}_1$ and $\eta = M_c e^{m\psi}$), respectively.

Dilatancy due to pressure induced plastic deformation in the multiaxial space is given by ⁽⁴⁾:

$$D_2 = d_2 \left\langle \frac{M_c g(\theta)}{R} - 1 \right\rangle \frac{dp}{|dp|} \quad (4.26)$$

in which d_2 is a positive model constant. D_2 varies from zero (if $\eta = M_c = \frac{R}{g(\theta)}$) to infinity (when $R = 0$).

4.2.8 Plastic Modulus

Wood et al. ⁽⁵²⁾ developed a model where the plasticity modulus depends on state parameter (ψ). This model considered that dense sand reaches peak stress ratio followed by softening before it reaches residual stress ratio and failure occurs. Following this, Li and Dafalias ⁽³⁾ proposed a relationship to find the plastic modulus in triaxial space as:

$$k_p = hG \left(\frac{M}{\eta} - e^{n\psi} \right) = \frac{hGe^{n\psi}}{\eta} (Me^{-n\psi} - \eta) \quad (4.27)$$

where h and n are model parameters that are always positive. hG is a scaling factor for the modulus and n is a scaling factor for ψ . h value varies with soil density .

The plastic modulus function in the triaxial space can be further extended for multiaxial space as ⁽⁴⁾:

$$K_{p1} = \frac{Gh}{\bar{R}} \left[M_c g(\bar{\theta}) e^{-n\psi} \sqrt{\frac{\bar{\rho}_1}{\rho_1} - \bar{R}} \right] \quad (4.28)$$

where n is a scaling factor for ψ . K_{p1} can be positive (hardening) or negative (softening) or zero (critical state) when $M_{pk} > \bar{R}$ or $M_{pk} < \bar{R}$ or $M_{pk} = \bar{R}$, respectively. The function h is used to fit the simulation result with test data and varies with density, loading condition and fabric instead of density only in Eq. 4.27. It can be expressed as ⁽⁶⁾:

$$h = (h_1 - h_2 e)^{\left(\frac{(k_h A_c - A_e) + (1 - k_h)A}{A_c - A_e} \right)} \left\{ \left(\frac{\rho_1}{\bar{\rho}_1} \right)^k + h_3 f(L_1) \left[1 - \left(\frac{\rho_1}{\bar{\rho}_1} \right)^k \right] \right\} \quad (4.29)$$

where h_3 are material constants. A_e is anisotropic state variable A at triaxial extension. $f(L_1)$ is a function of accumulated loading index.

For virgin loading condition ($r_{ij} = \bar{r}_{ij}$ and $\rho_{ij} = \bar{\rho}_{ij}$) Eq. A.28 reduces to:

$$\bar{K}_{p1} = \frac{Gh}{\bar{R}} [M_c g(\bar{\theta}) e^{-n\psi} - \bar{R}] \quad (4.30)$$

The plastic modulus variation under constant stress ratio is given as ⁽⁴⁾:

$$K_{p2} = Gh_4 \left[\frac{M_c g(\theta)}{R} \right] \left(\frac{\bar{\rho}_2}{\rho_2} \right)^a \frac{dp}{|dp|} \quad (4.31)$$

$$K_{p2} = \begin{cases} K_{p2} & \text{if } p=\bar{p} \text{ and } dp>0 \\ 0 & \text{otherwise} \end{cases} \quad (4.32)$$

where h_4 and a are two positive model constants. Eq. 4.31 and 4.32 ensure that an isotropic compression yields no deviatoric strain. The use of term $\left(\frac{\bar{\rho}_2}{\rho_2} \right)^a$ enables the gradual change in K_{p2} , when $\frac{\bar{\rho}_2}{\rho_2}$ changes from ∞ (right after a change in the direction of dp) to 1 (when p moves onto the bounding cap F_2). Detailed description for the determination of model parameters have been provided by Li, Dafalias and their colleagues^(3, 4, 7).

4.2.9 Modification for unsaturated soils

Bishop⁽⁷⁷⁾ expressed the effective stress in unsaturated soil as:

$$\sigma'_{ij} = (\sigma_{ij} - \delta_{ij}u_a) + \delta_{ij}\chi_w(u_a - U_w) \quad (4.33)$$

σ'_{ij} = effective stress tensor component; σ_{ij} = total stress tensor component; δ_{ij} = Kronecker delta function ($\delta_{ij}=1$ if $i=j$ and $\delta_{ij}=0$ if $i\neq j$); u_a = pore air pressure; U_w = pore water pressure, χ_w = Bishop parameter (depends primarily on saturation, but also on material, compaction procedure and stress path). Denoting the effective suction confinement (p_{suc}) by:

$$p_{suc} = \chi_w(u_a - U_w) \quad (4.34)$$

Eq. 4.34 reduces to:

$$\sigma'_{ij} = \sigma_{ij} + \delta_{ij}(p_{suc} - u_a) \quad (4.35)$$

For saturation level less than 95% for granular materials, pore air pressure (u_a) is found to be much less than p_{suc} ⁽¹⁶⁾. Thus, Eq. 4.35 further reduces to:

$$\sigma'_{ij} = \sigma_{ij} + \delta_{ij}p_{suc} \quad (4.36)$$

Since suction affects the mean effective normal stress only, Eq. 4.36 can be expressed in terms of total (p_{total}) and effective (p) mean normal stress as:

$$p = p_{total} + p_{suc} \quad (4.37)$$

Heath et al.⁽¹⁶⁾ developed a relationship to find the soil suction (p_{suc}) by combining the empirical equations developed by previous researchers^(77, 78, 79) as:

$$p_{suc} \approx n_1 \left(\frac{1}{(wG_s)^{n_2}} - \frac{1}{e^{n_2}} \right)^{\frac{n_3}{n_2}} p_{at} \quad (4.38)$$

where n_1 , n_2 and n_3 are material constants. w is gravimetric water content. G_s is the specific gravity of the soil. This relationship predicts a linear relation in log-log space at intermediate and low saturation levels, and includes a smooth transition to p_{suc} at fully saturated level. Detailed description of the determination of n_1 , n_2 and n_3 have been provided by Health et al.⁽¹⁶⁾.

The proposed fabric based unsaturated sand model was implemented to Abaqus via user defined material subroutine (UMAT). FORTRAN language was used to write the UMAT coding. The complied UMAT code is attached in Appendix C.

4.3 Verification of new sand model

The implemented model was first verified by triaxial tests results conducted on Toyoura sand. Several researchers have reported test data on this sand under various conditions^(7, 80, 81). Verdugo and Ishihara⁽⁸¹⁾ reported results from drained tests on moist tamped specimens for different initial void ratios ($e_0 = 0.831$ and 0.996) with 100 kPa confining stress. Fukushima and Tatsuoka⁽⁸⁰⁾ reported tests results on air pulviated specimens for different confining stresses (100, 200, 400 kPa) and initial void ratios (0.671; 0.824; 0.816). Undrained triaxial test data have been reported by Yang et al.⁽⁷⁾ for different confining stresses (100, 200, 400 kPa), relative density ($Dr = 30\%$ and 41%), shear mode (compression and extension) and sample preparation method (moist tamped and dry deposited).

Model parameters used for Toyoura sand are shown in Table 4.1. The fabric parameters were obtained from Yang et al.⁽⁷⁾; other parameters were obtained from Li⁽⁴⁾. Most parameters can be determined from experiments; the default parameters generally remain the same for most sands. The element type used to simulate the triaxial test was an 8-node axisymmetric quadrilateral, biquadratic displacement, bilinear pore pressure, reduced integration (CAX8RP) available in Abaqus.

Table 4.1: New sand model Parameters for Toyoura Sand

(from references 4, 7 and 16)

Elastic parameters	Critical state parameters	Parameters associated with <i>dr</i> -mechanisms	Parameters associated with <i>dp</i> -mechanisms	Fabric parameters	Unsaturated parameters	Default parameters
$G_0=125$ $v=0.25$	$M_c = 1.25$ $c = 0.75$ $e_{\Gamma c} = 0.934$ $k_{\Gamma} = 0.019$ $t = 0.45$ $\lambda_c = 0.02$ $\xi = 0.7$	$d_l = 0.88$ $m = 3.5$ $h_{1DD} = 3.45$ $h_{2DD} = 3.34$ $h_{1MT} = 3.5 * h_{1DD}$ $h_{2MT} = 3.5 * h_{2DD}$ $h_3 = 2.2$ $n = 1.1$	$d_2 = 1$ $h_4 = 3.5$	$\Delta_{MT} = 0.091$ $\Delta_{DD} = 0.214$ $k_h = 0.2$	$n_l = 0.015$ $n_2 = 2$ $n_3 = 2.4$	$a=1$ $b_l=0.005$ $b_2=2$ $b_3=0.001$

Figure 4.5 shows the variation of shear stress q with axial strain ε_a and void ratio e for drained triaxial test data ⁽⁸¹⁾, along with simulation results. Figure 4.6 shows the variation of shear stress q and volumetric strain ε_{Vol} with axial strain ε_a for drained triaxial test data ⁽⁸⁰⁾ along with the simulation results. It was found that the match between test data and simulation results is very good. Figures 4.7 and 4.8 show the variation of shear stress q with mean effective normal stress p and deviatoric strain ε_q for undrained triaxial test data ⁽⁷⁾, along with the simulation results. The predictions of the effective stress paths

match well, whereas comparison between shear stress and strain needs improvement.

Similar discrepancies were observed by past researchers⁽⁷⁾.

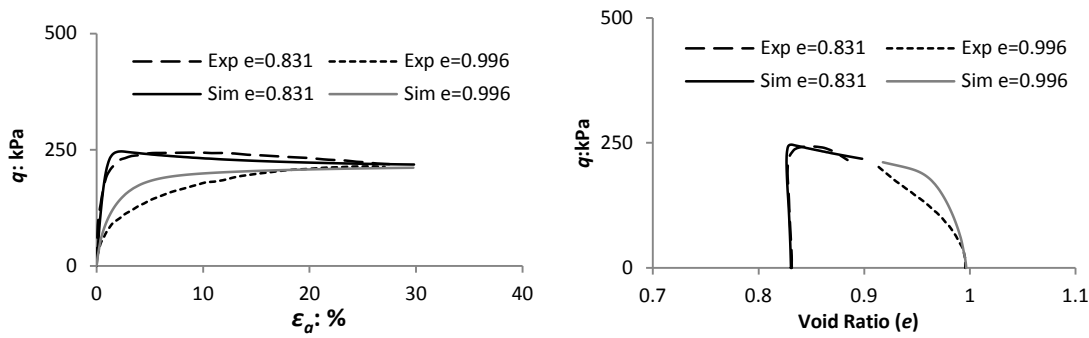


Figure 4.5: Measurement and prediction of drained test for MT specimen with confining stress =100 kPa

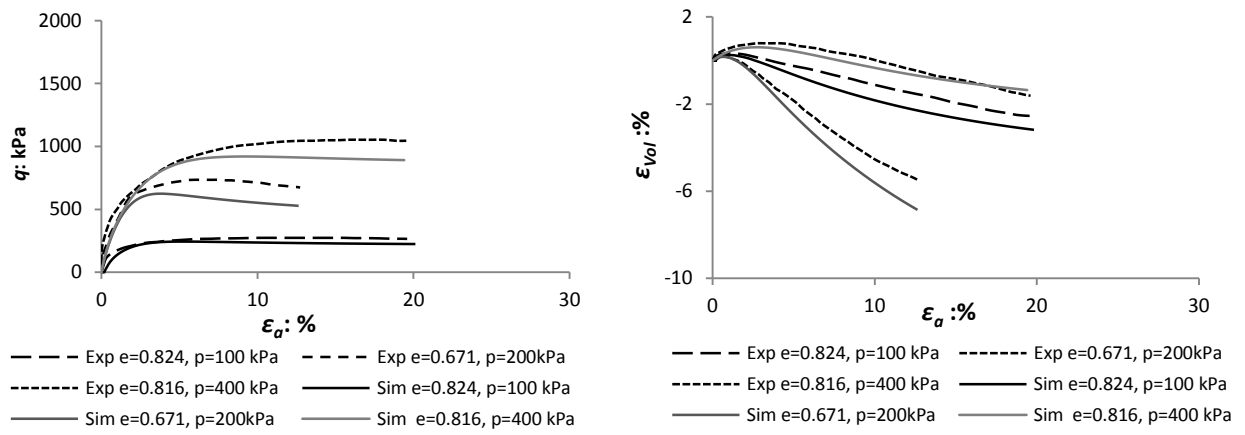


Figure 4.6: Measurement and prediction of drained test

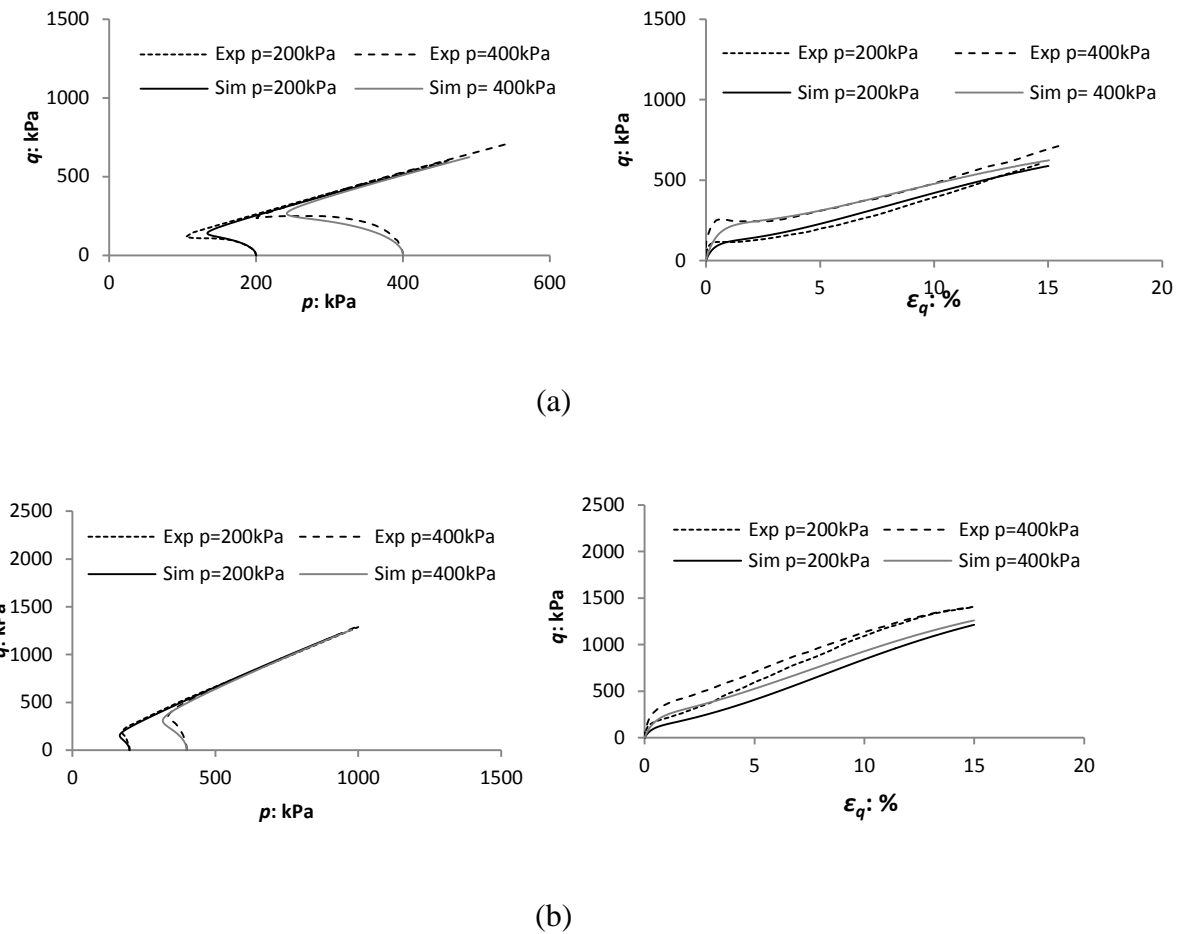


Figure 4.7: Measurement and prediction of undrained compression test with DD specimens at (a) $Dr=30\%$ (b) $Dr=41\%$

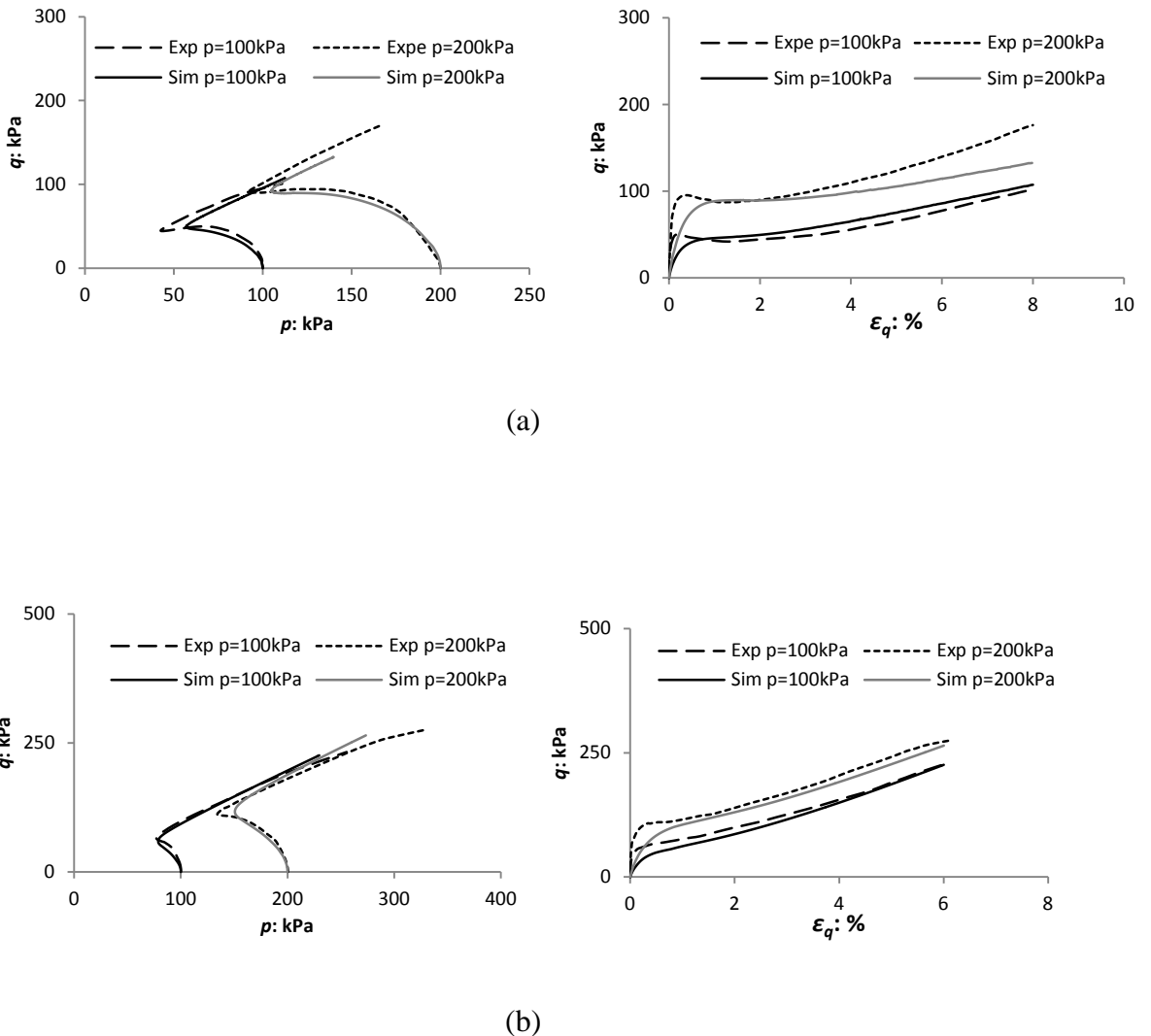


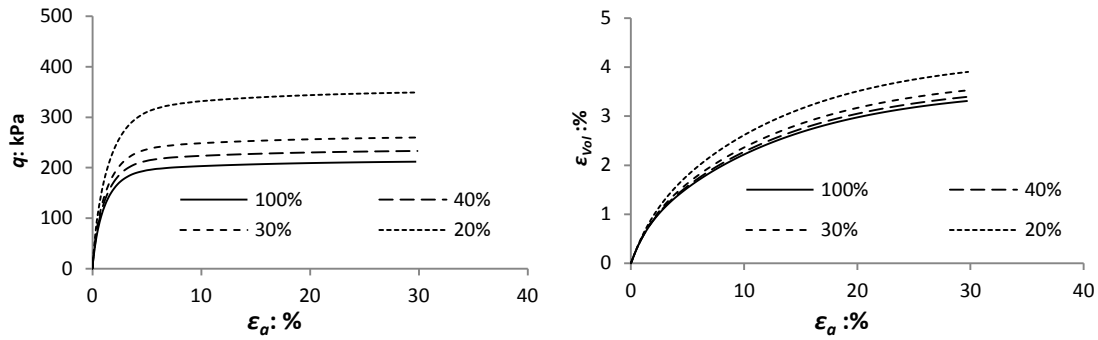
Figure 4.8: Measurement and prediction of undrained extension test with MT specimens
at
(a) $Dr=30\%$ (b) $Dr=41\%$

4.4 Unsaturated model behavior

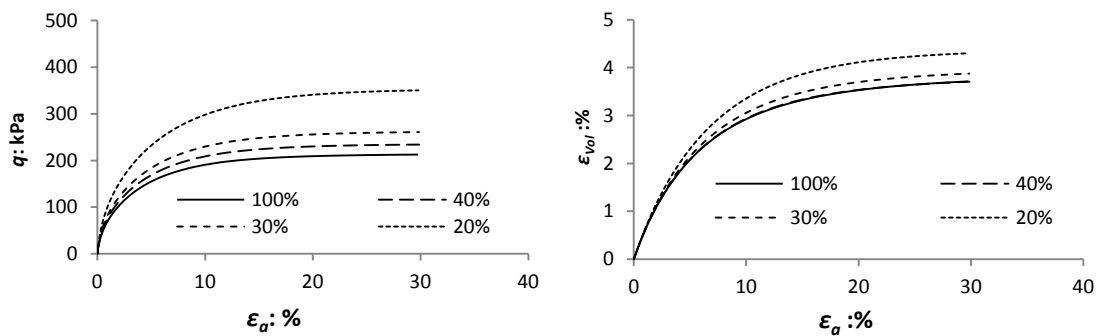
The fabric sand model was used to predict the behavior of unsaturated sand under drained conditions. Since the pore pressure element is not used for unsaturated behavior, the simple 8-node axisymmetric quadrilateral, biquadratic displacement, bilinear, reduced

integration (CAX8R) element was used. The unsaturated based model parameters listed in Table 4.1 were obtained from Heath et al.⁽¹⁶⁾.

Unsaturated drained triaxial tests were simulated for moist tamped (MT) samples at loose state ($e_0 = 0.977$) and dense state ($e_0 = 0.831$) with different initial saturation levels such as 100%, 40%, 30% and 20%. This process was repeated for dry deposited (DD) samples. All tests were carried out with 100 kPa (excluding p_{suc}) confining stress. The results of the simulations are shown in Figures 4.9 and 4.10. It can be seen that deviator stress and volumetric strain behavior changes with initial saturation level regardless of the density or sample preparation methods.

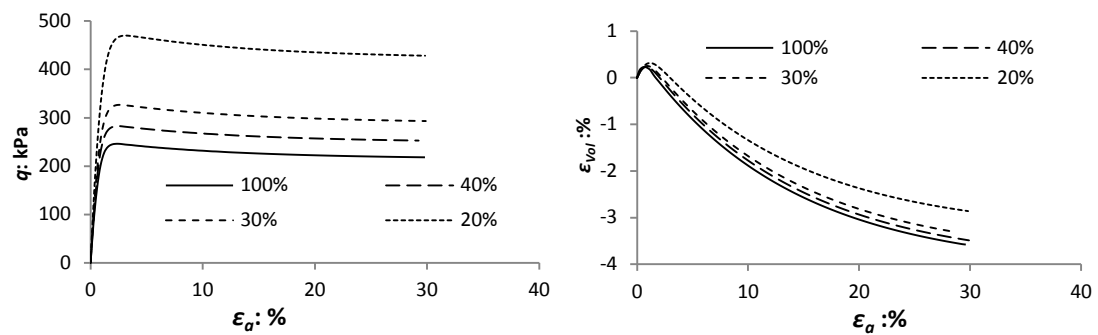


(a)

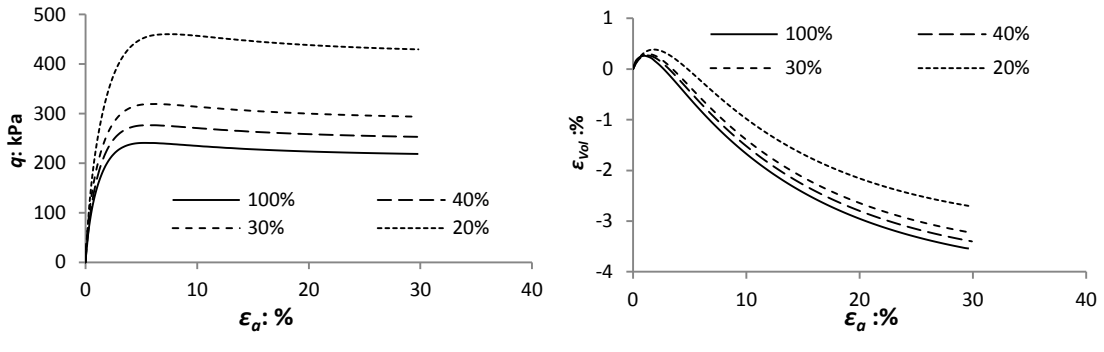


(b)

Figure 4.9: Prediction of unsaturated drained test for (a) MT and (b) DD specimens at $e_0=0.977$ and confining stress =100 kPa



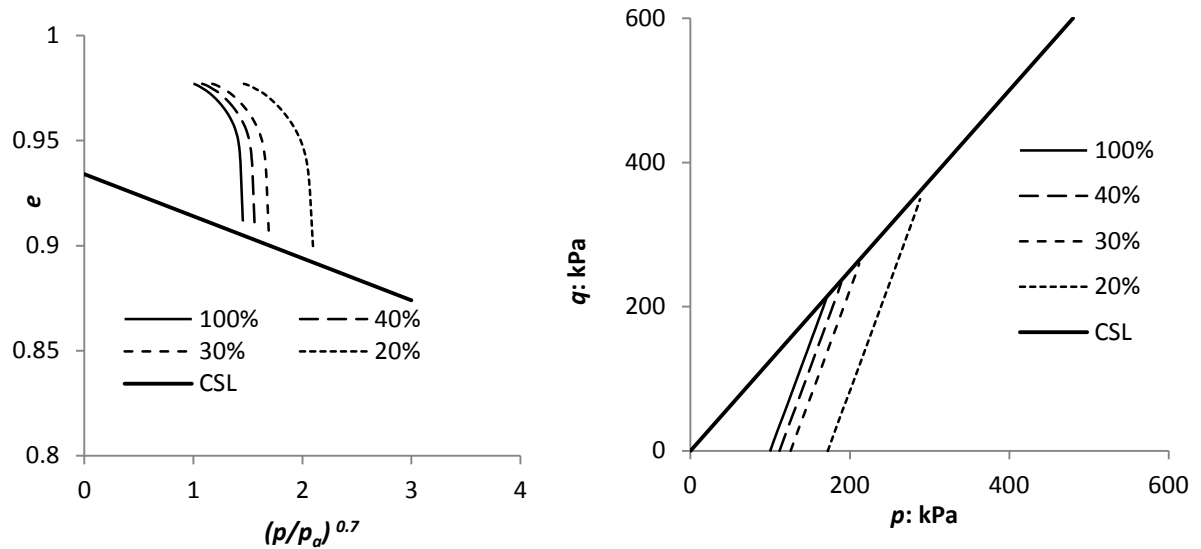
(a)



(b)

Figure 4.10: Prediction of unsaturated drained test for (a) MT and (b) DD specimens at $e_0=0.831$ and confining stress =100 kPa

It can be seen that the loose moist tamped specimens ($e_0 = 0.977$) and dense state ($e_0 = 0.831$) ultimately reach towards the CSL in $q - p$ plot and $e - (p/p_a)^{\xi}$ plot for different saturation levels at drained condition, as shown in Figure 4.11. As expected, dense specimens cross CSL, attain peak deviatoric stress, and fall back to CSL in $q-p$ plot.



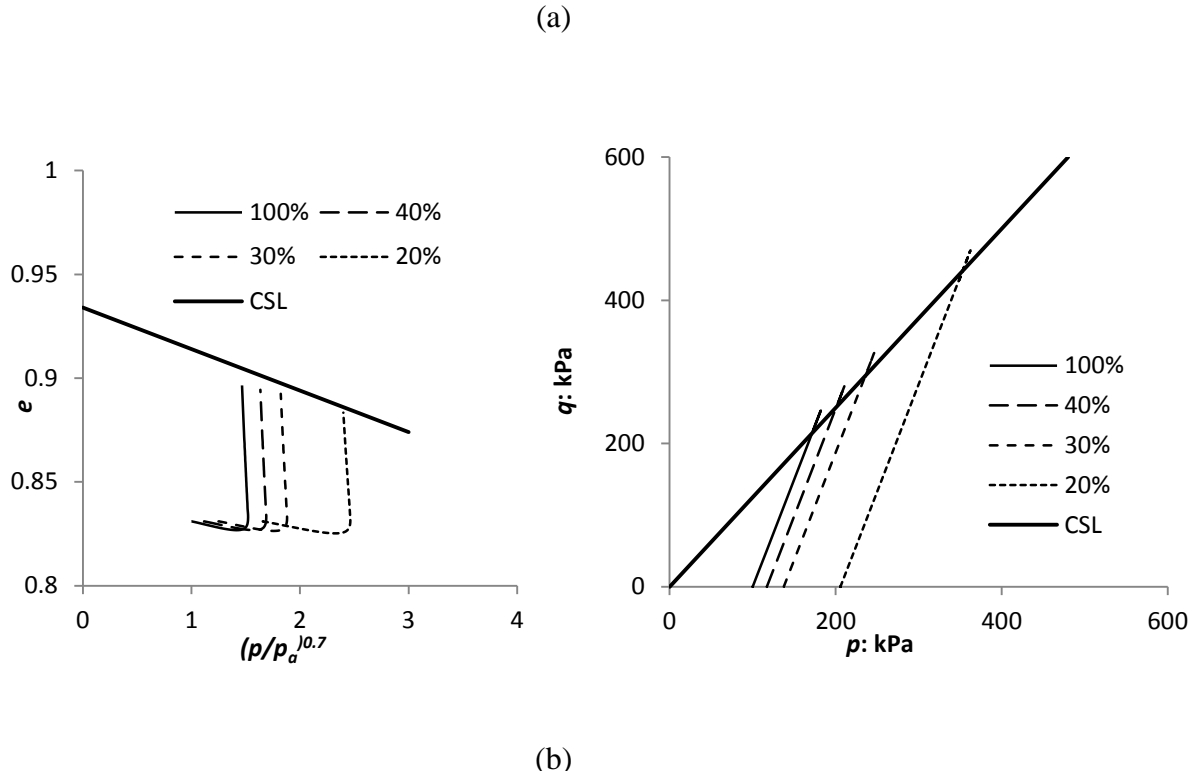


Figure 4.11: $q - p$ and $e - (p/p_a)^{\xi}$ plots at (a) loose state ($e_0 = 0.977$) and (b) dense state ($e_0 = 0.831$) for MT samples

The effect of unsaturated sand behavior can be described based on an extended critical state framework using $e - (p/p_a)^{\xi}$ plot, as shown in Figure 4.12, which shows two sets of initial locations of samples. Sets L (loose specimens with void ratio 0.977) and D (dense specimens with void ratio 0.831) have the same initial confining stress (100kPa, excluding p_{suc}), but with different initial saturation levels (20, 30, 40 and 100%). The initial state of loose sand moves away from critical state line with increase in initial p_{suc} due to a decrease in saturation level, as shown in Figure 4.12. Consequently, the initial state parameter (ψ) will increase with suction, resulting in increased contractive behavior, as observed in the ε_{Vol} - ε_a plot (Figure 4.9).

On the contrary, initial state of dense sand moves towards the critical state line with increase in initial p_{suc} , due to a decrease in initial saturation level. Consequently, initial state parameter (ψ) will increase as with suction, resulting in decreased dilative behavior, as observed in ε_{Vol} - ε_a plot (Figure 4.10).

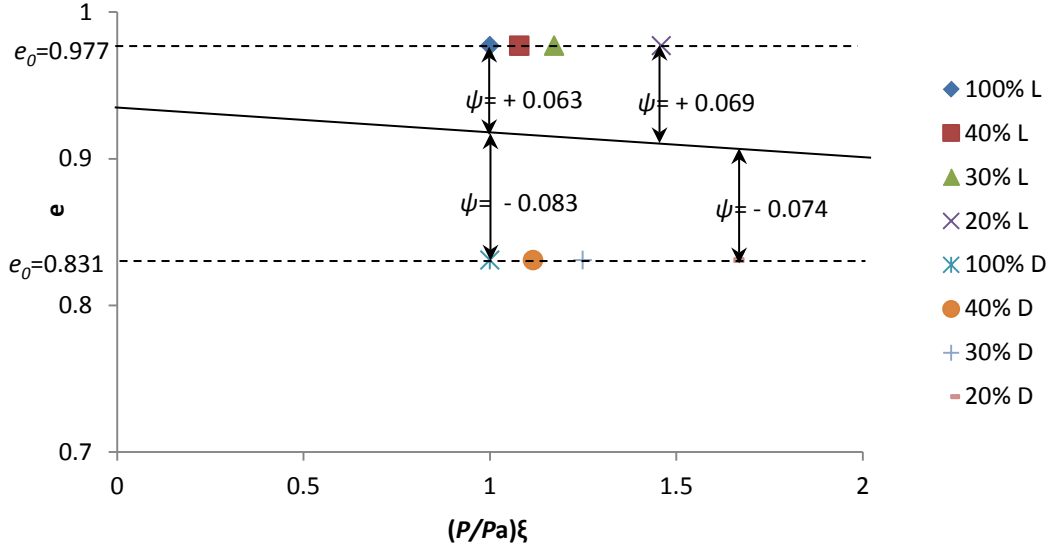


Figure 4.12: Critical state line in $e - (p/p_a)^\xi$ plane

4.5 Modified Suction State Parameter

The changes in initial state parameter due to suction and observed effects on sand behavior can be quantified in terms of a modified suction based state parameter defined as:

$$\psi_{IUS} = \psi_{IS} + \psi_{MIUS} \quad (4.39)$$

where ψ_{IUS} and ψ_{IS} are the initial values of the unsaturated state parameter and saturated state parameter, respectively. ψ_{MIUS} is the modification imposed by the level of

suction on the initial saturated state parameter. Schematic diagrams showing the different parameters are shown in Figure 4.13 (for loose sand) and Figure 4.14 (dense sand).

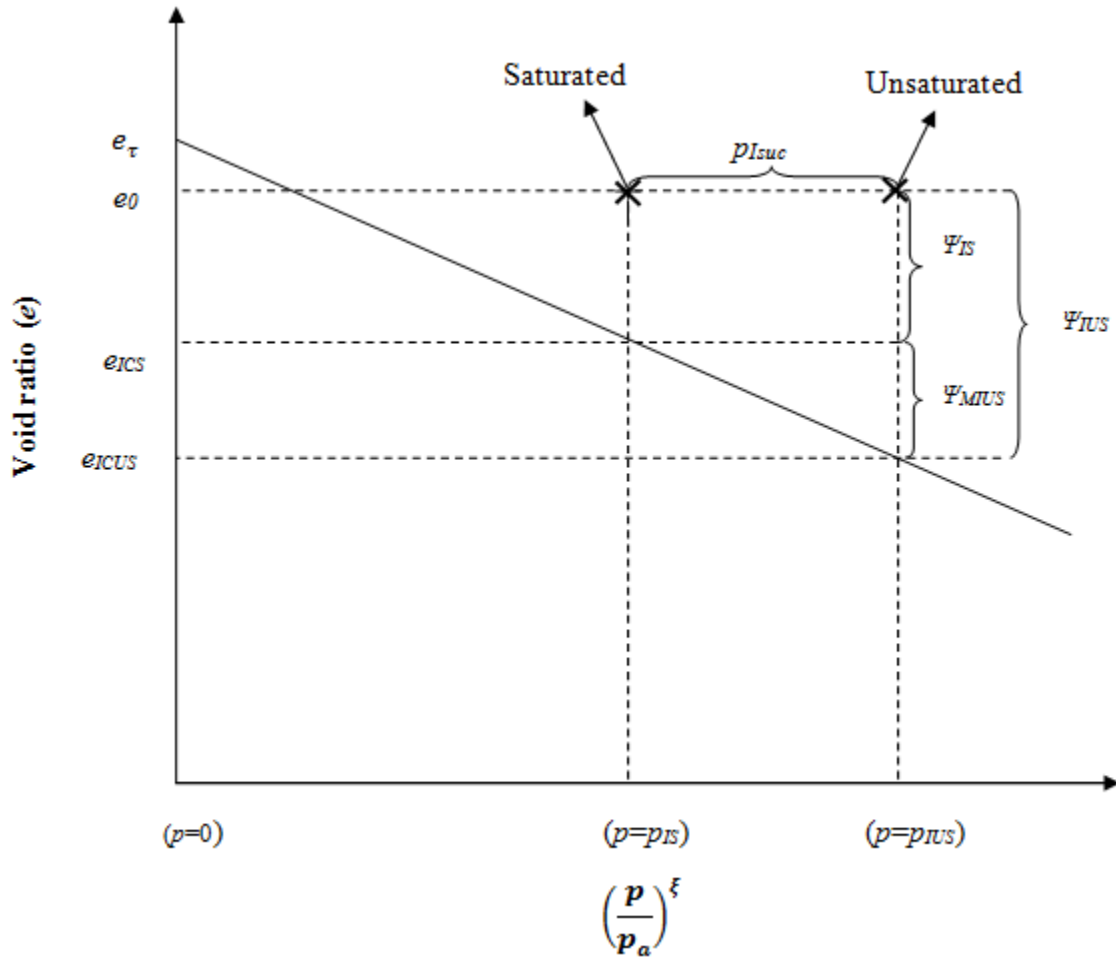


Figure 4.13: Modification to initial state parameter of unsaturated loose sand due to suction

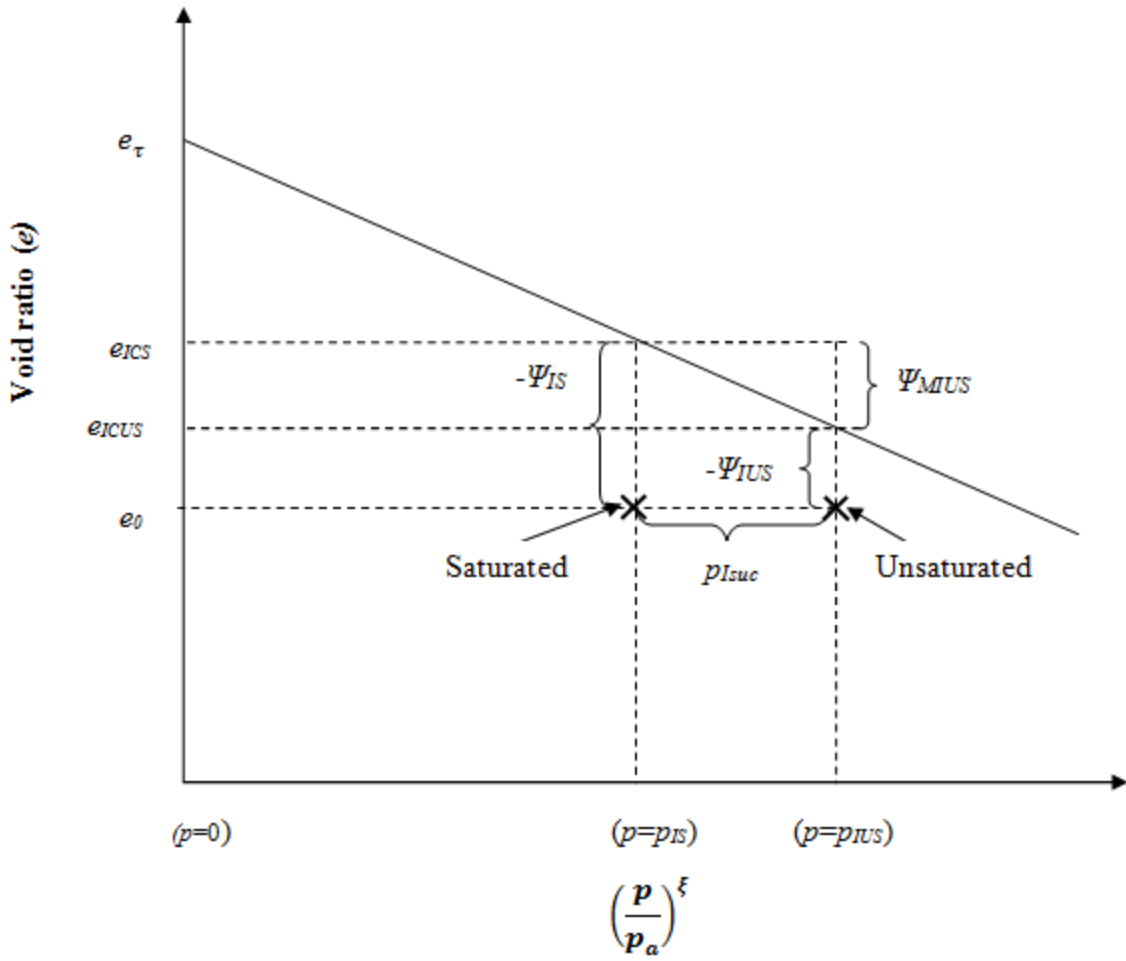


Figure 4.14: Modification to initial state parameter of unsaturated dense sand due to suction

Using the critical void ratio corresponding to mean normal effective stress (p) at initial saturated state and the unsaturated state, respectively, ψ_{MIUS} can be derived as:

$$\psi_{MIUS} = e_{ICS} - e_{ICUS} \quad (4.40)$$

where e_{ICS} and e_{ICUS} are critical void ratios corresponding to mean normal effective stress (p) at initial saturated state and unsaturated state, respectively. Using critical state equation (Eq. 4.22), e_{ICS} can be given by:

$$e_{ICS} = e_\tau - \lambda_c \left(\frac{p_{IS}}{p_a} \right)^\xi \quad (4.41)$$

Substituting the suction stress form (Eq. 37) results in e_{ICUS} as:

$$e_{ICUS} = e_\tau - \lambda_c \left(\frac{p_{IS} + p_{Isuc}}{p_a} \right)^\xi \quad (4.42)$$

where p_{IS} the mean effective normal stress at initial saturated state and p_{Isuc} is the initial suction in unsaturated soil. Substituting the above expressions leads to ψ_{MIUS} as:

$$\psi_{MIUS} = \lambda_c \left(\frac{(p_{IS} + p_{Isuc})^\xi - (p_{IS})^\xi}{p_a} \right) \quad (4.43)$$

The percentage increase in peak deviatoric stress increment due to suction (with respect to the saturated peak deviatoric stress) with ψ_{MIUS} is shown in Figure 4.15 showing a linear relationship between stress increment and ψ_{MIUS} for different densities and sample preparation methods (MT and DD). This relationship illustrates that ψ_{MIUS} is directly correlated with sand performance.

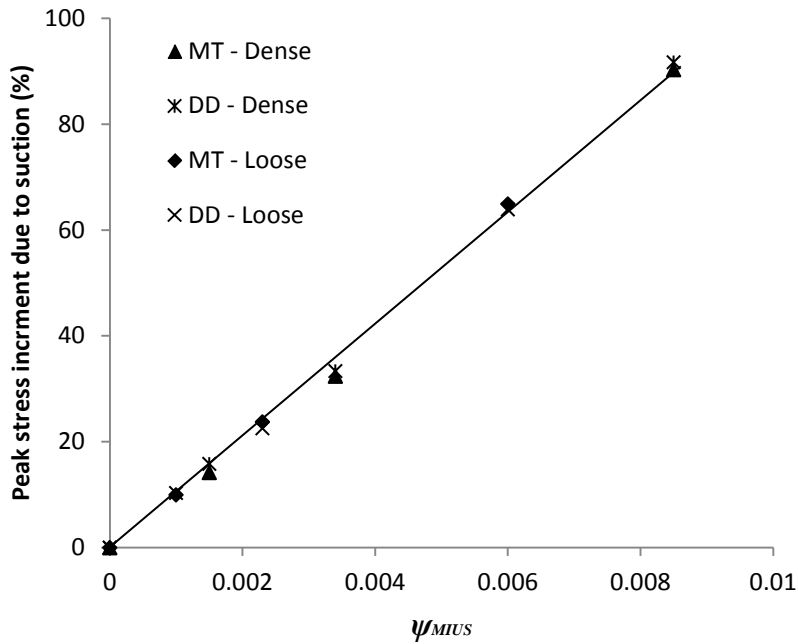


Figure 4.15: Percentage increase in peak deviatoric stress with ψ_{MIUS}

4.6 Cyclic loading performance of sands

In this section the results of the simulation of sand performance under cyclic loading using a new sand model are presented. A selected suite of experimental results from the literature for Fontainebleau sand ⁽⁸²⁾ and Nevada sand ⁽⁸³⁾ were first used for this purpose. The index properties of these sands such as grain size distribution and density values (Table 4.2 and Figure 4.16) are similar to the Toyoura sand. Therefore, in the absence of an experimental program, the model parameters of Toyoura sand were used in the simulations reported here.

The FE model used to simulate the triaxial test is shown in Figure 4.17. The element type used to simulate the fully saturated triaxial test was an 8-node axisymmetric

quadrilateral, biquadratic displacement, bilinear pore pressure, reduced integration (CAX8RP) available in Abaqus.

Table 4.2: Comparison of different sand properties

Sand type	γ_s (kN/m ³)	e_{max}	e_{min}	D_{50} (mm)	C_u	C_c
Toyoura	26	0.977	0.597	0.19	1.25	1.01
Nevada	26	0.887	0.511	0.15	1.80	0.87
Fontainebleau	26	0.844	0.527	0.17	1.57	0.64

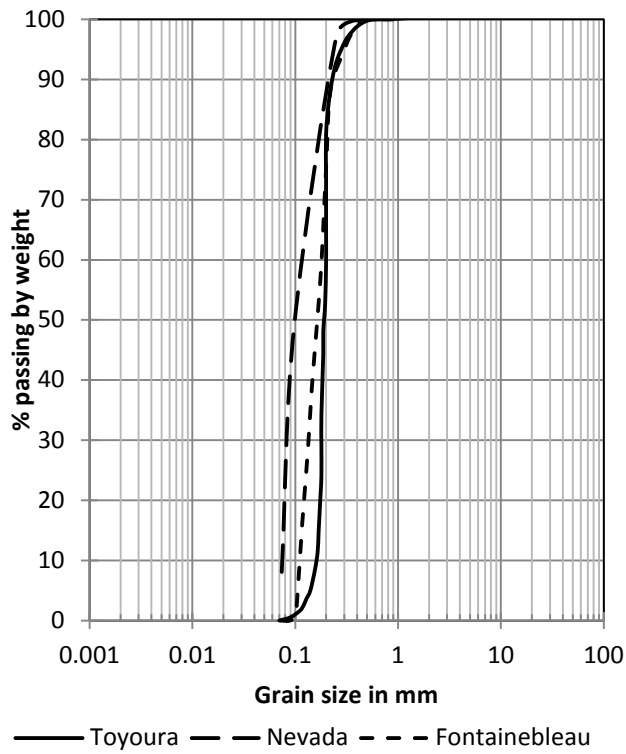


Figure 4.16: Grain size distribution of different sand types

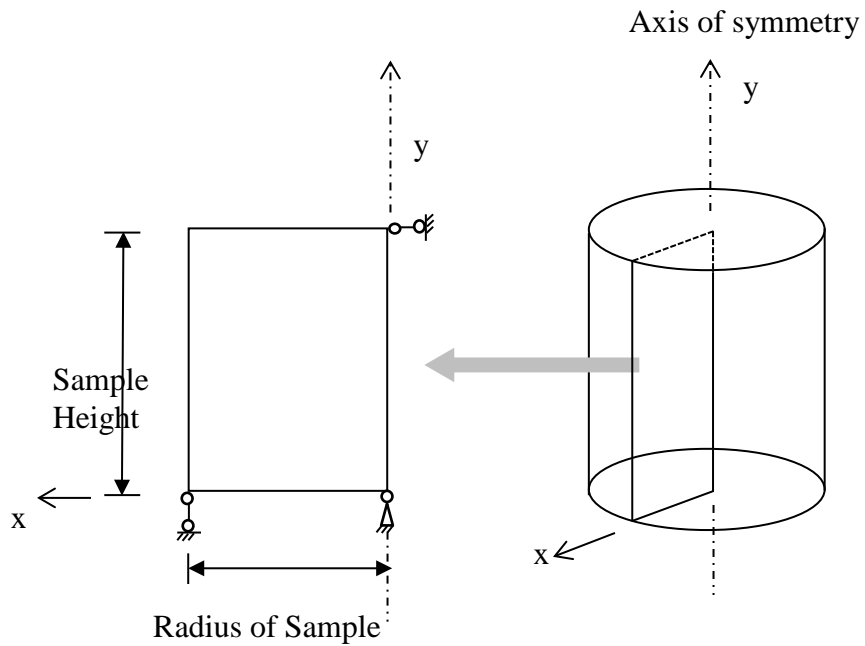


Figure 4.17: FE model to simulate triaxial test

Gaudin et al. ⁽⁸²⁾ reported results from compression tests by using conventional triaxial device in moist tamped specimen with initial relative density of 71% and confining stress of 90 kPa. Loading, unloading and reloading was carried out under drained condition. Figure 4.18 shows the variation of shear stress q with axial strain ε_a for triaxial test data ⁽⁸²⁾ along with simulation results. The model was found to capture the experimental results well.

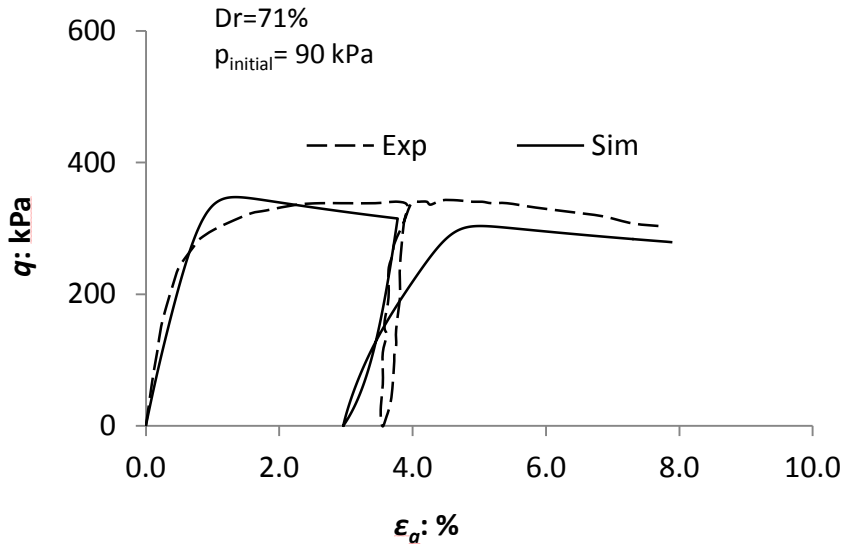


Figure 4.18: Variation of deviatoric stress (q) with axial strain (ε_a)

Arulmoli et al. ⁽⁸³⁾ reported results of consolidated undrained triaxial tests on an air-pulviated specimen with 80 kPa confining pressure and 70% relative density. Figure 4.19 shows their experimental results, and Figure 4.20 shows the corresponding simulations.

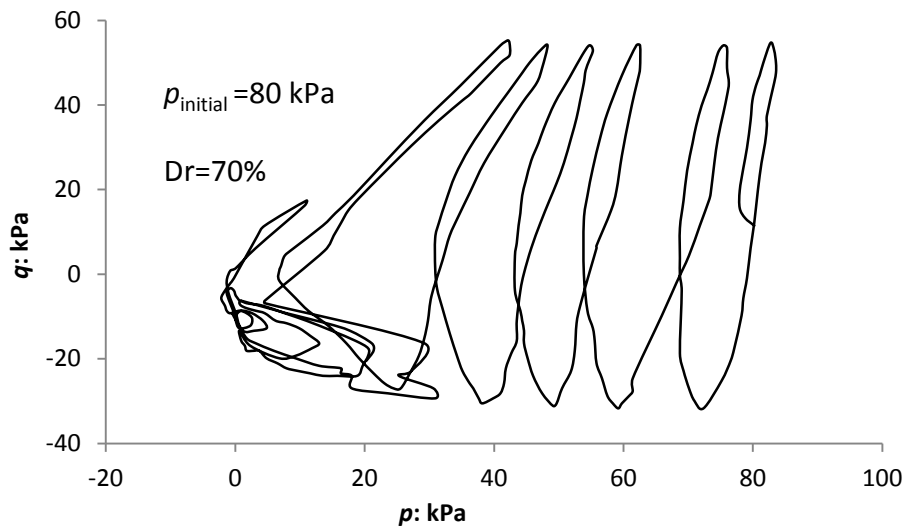


Figure 4.19: Test result of undrained cyclic triaxial on Nevada sand (Data from Arulmoli et al.⁽⁸³⁾)

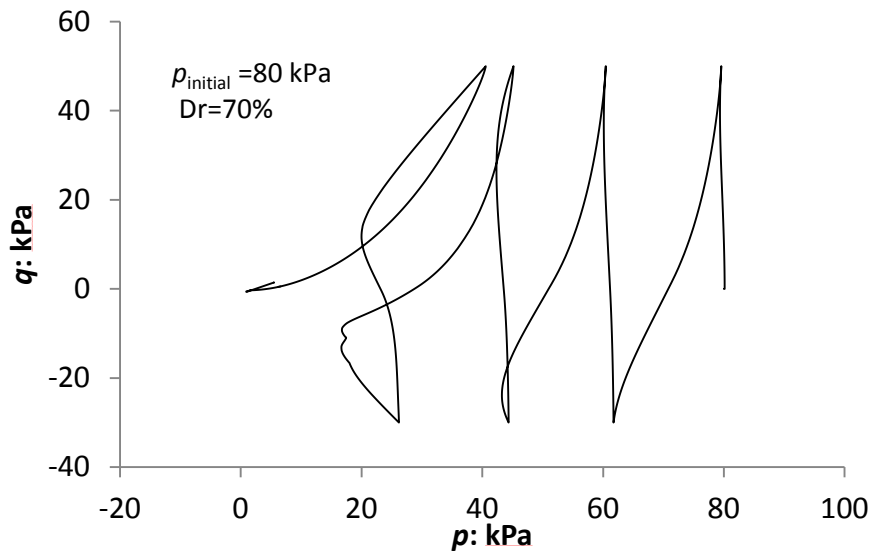


Figure 4.20: Simulation of undrained cyclic triaxial results on Nevada Sand

4.6.1 Sand performance under repeated loading

The new sand model was subsequently used to study the effects of sample preparation, saturation level, and density on stress controlled drained triaxial results under repeated loading. The loading pattern is shown in Figure 4.21.

Since the pore pressure element is not used for unsaturated behavior the simple 8-node axisymmetric quadrilateral, biquadratic displacement, bilinear, reduced integration (CAX8R) element was used.

The first series of simulations were conducted for unsaturated drained triaxial tests on moist tamped (MT) specimens at loose state ($e_0 = 0.977$) and dense state ($e_0 = 0.831$) with saturation levels of 100%, 40%, 30% and 20%. The same procedure was then

repeated for dry deposited (DD) specimens. All tests were carried out with 100 kPa initial confining stress.

The variation of axial strain with number of loading cycles for fully saturated moist tamped loose specimen is shown in Figure 4.22. The simulations were carried out until the attainment of 0.6% permanent strain. It can be seen that the specimen reached the specified permanent strain in 45 cycles. Similar simulations were performed for other cases; results are shown in number of loading cycles variation with vertical permanent strain, as shown in Figures 4.23 through 4.26.

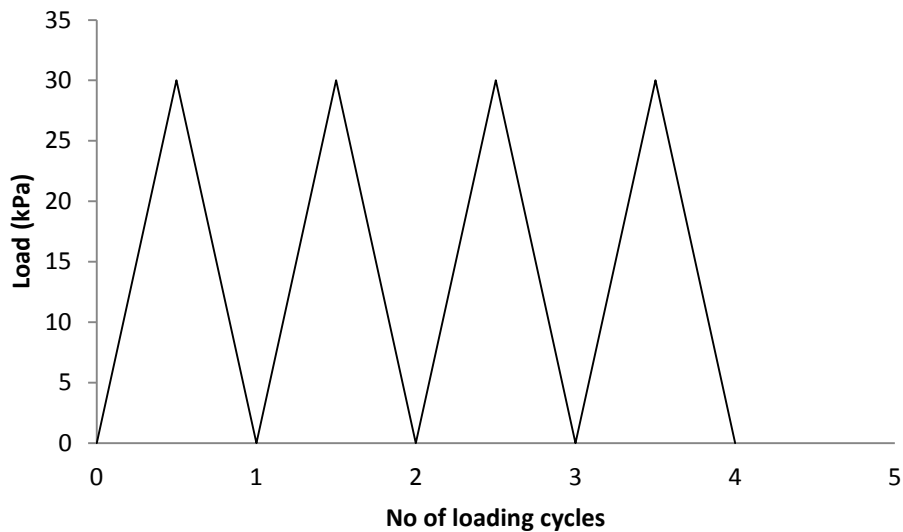


Figure 4.21: Applied repeated loading

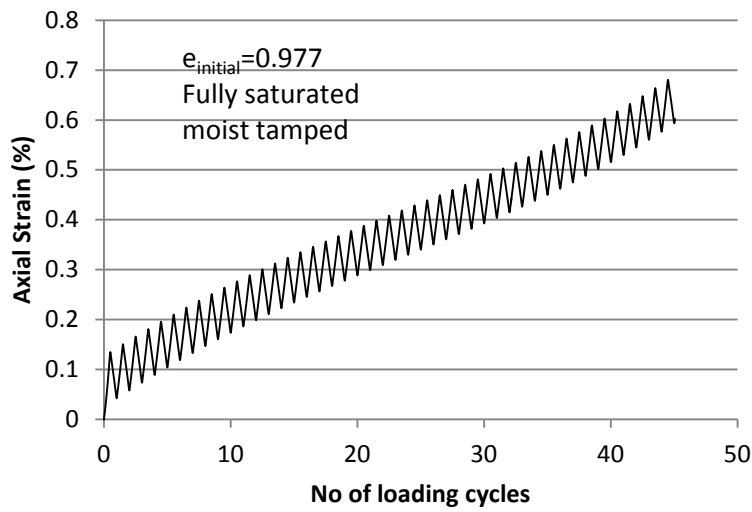


Figure 4.22: Variation of axial strain with number of loading cycles

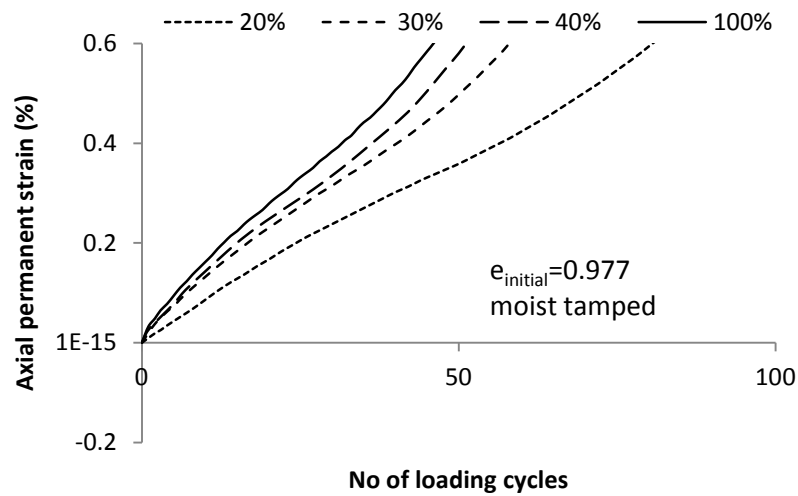


Figure 4.23: Variation of axial permanent strain with loading cycles for loose moist tamped sample

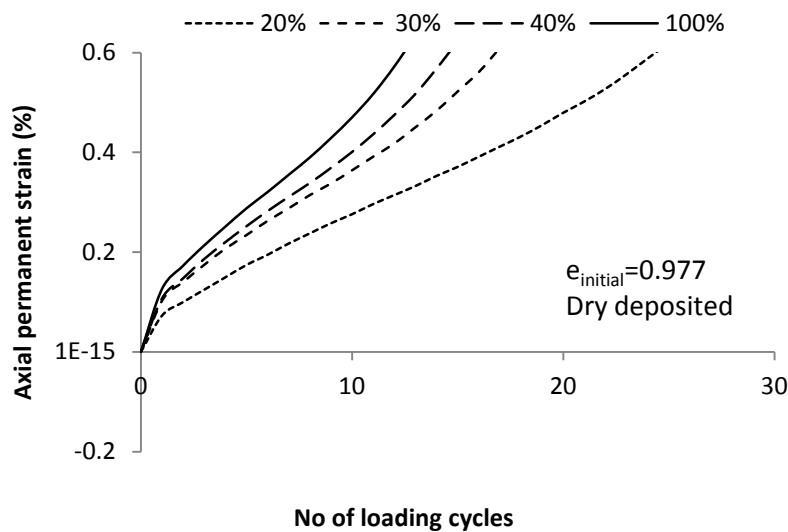


Figure 4.24: Variation of axial permanent strain with loading cycles for loose dry deposited sample

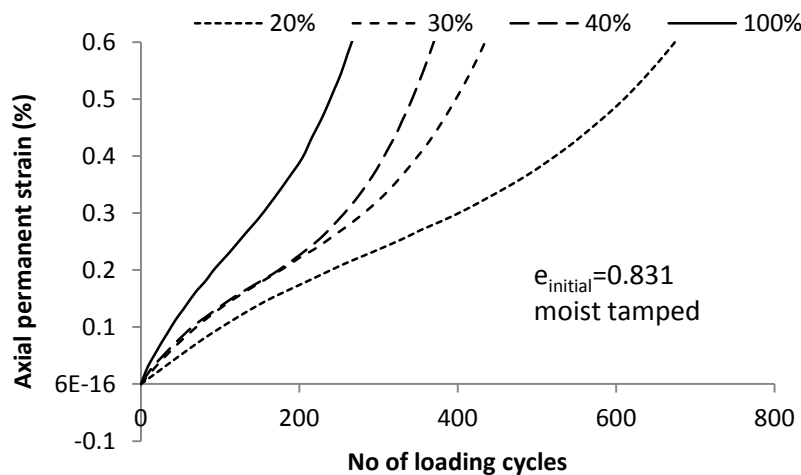


Figure 4.25: Variation of axial permanent strain with loading cycles for dense moist tamped sample

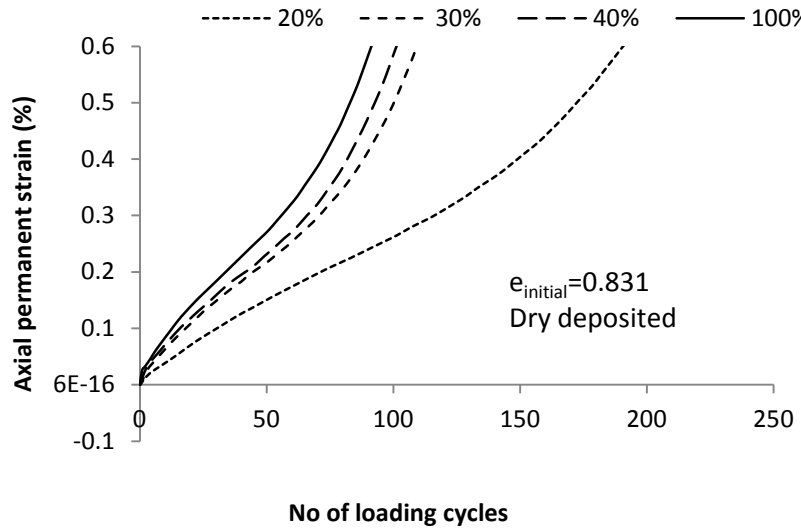


Figure 4.26: Variation of axial permanent strain with loading cycles for dense dry deposited sample

The number of cycles needed to attain 0.6% permanent strain for the various cases is summarized in Figure 4.27. It can be seen that moist tamped specimens are much more resistant to permanent deformation than dry deposited specimens. Results from past literature have also shown that moist tamped specimens may be strong due to the honey comb structure formed⁽⁸²⁾. However, at high stresses and strains, this structure collapses, resulting in a weak material. Further, dense sand shows much higher permanent deformation resistance than loose sand. Permanent deformation resistance significantly increases with saturation level reduction.

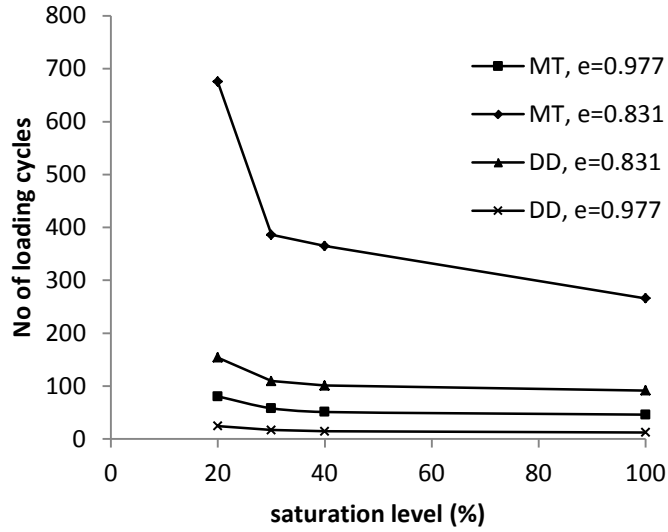


Figure 4.27: Variation of loading cycles with saturation level

4.6.2 Sand performance under cyclic loading

The critical state line of sands is dependent on the loading path and fabric, as shown in Eq. 4.23. This equation creates a sequence of straight critical-state lines running parallel to each other in the $e-p$ plane, as shown in Figure 4.28, which are altered for different loading paths and inherent fabric intensities. Sand behavior under cyclic loading is very much dependent on its initial state with respect to the relevant critical state in this diagram. In order to study these effects, Toyoura sands with four different initial states, as shown in Figure 4.28, were subjected to sinusoidal loading (Figure 4.29) under undrained condition until the sample failed. Table 4.3 gives the descriptions of the different states, and all were initially consolidated with a confining stress of 200 kPa.

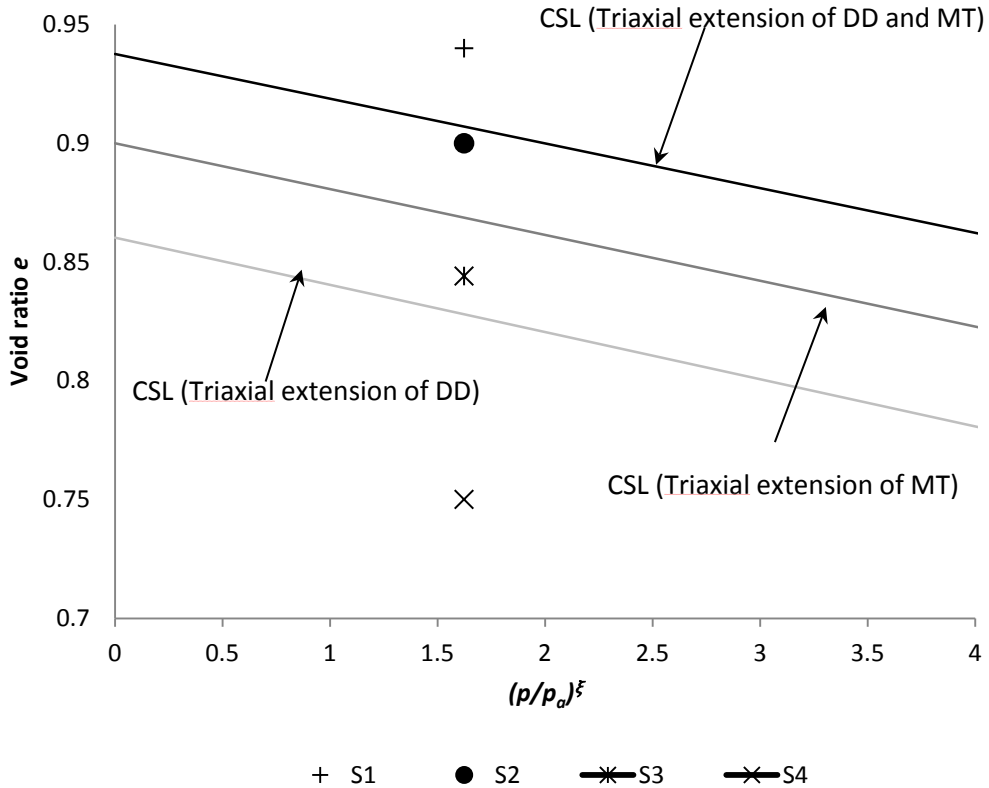


Figure 4.28: e - $(p/p_a)^\xi$ curve (modified from Yang et al. ⁽⁷⁾)

Table 4.3 Description of four different situations

Point	Void ratio (Dr %)	MT	MT	DD	DD
		Compression	Extension	Compression	Extension
S1	0.75 (60%)	Dense	Dense	Dense	Dense
S2	0.844 (35%)	Loose	Dense	Loose	Dense
S3	0.9 (20%)	Loose	Loose	Loose	Dense
S4	0.94 (10%)	Loose	Loose	Loose	Loose

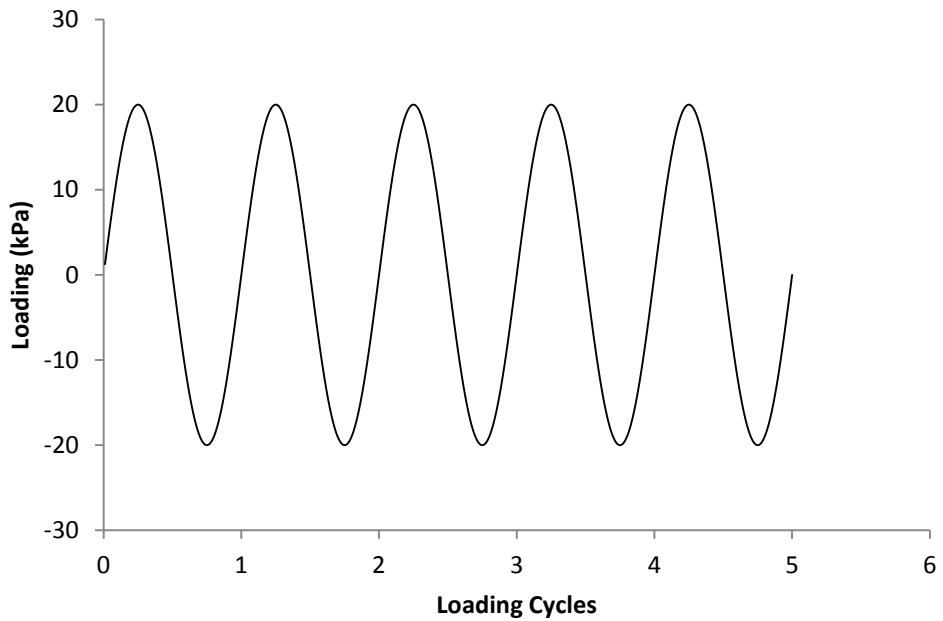


Figure 4.29: Applied sinusoidal loading

The typical variation of shear stress q with mean effective normal stress p for the moist tamped specimen is shown in Figure 4.30, along with the critical state line for the sand. It can be seen that the effective stress paths reach critical state and become zero at failure. The plot of shear stress q - axial strain ε_a for the same specimen is shown in Figure 4.31.

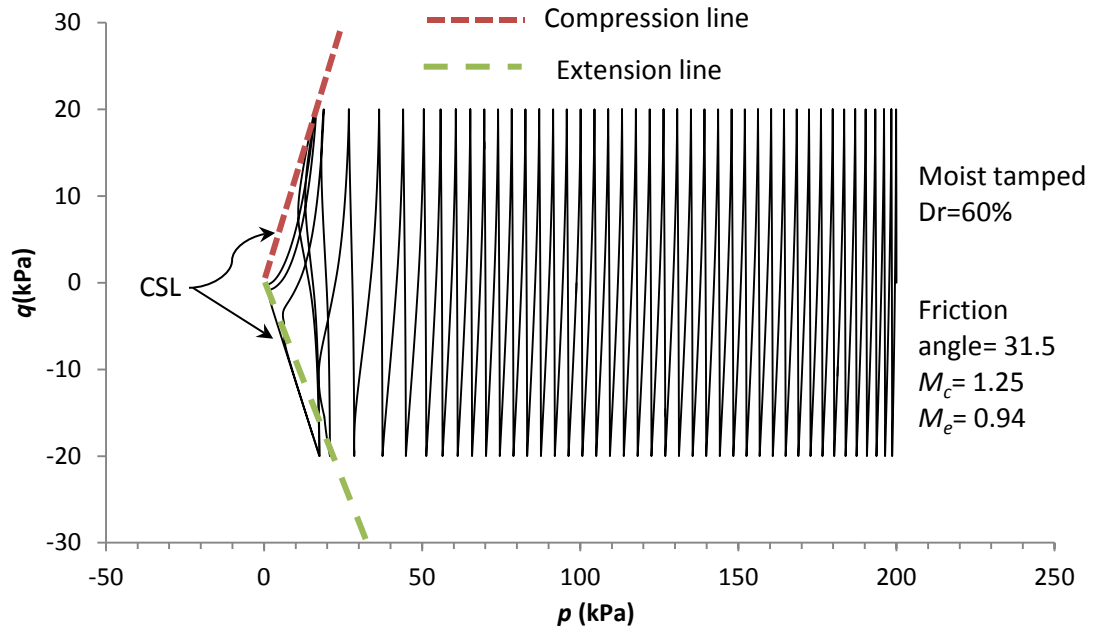


Figure 4.30: q - p curve during undrained cyclic triaxial test

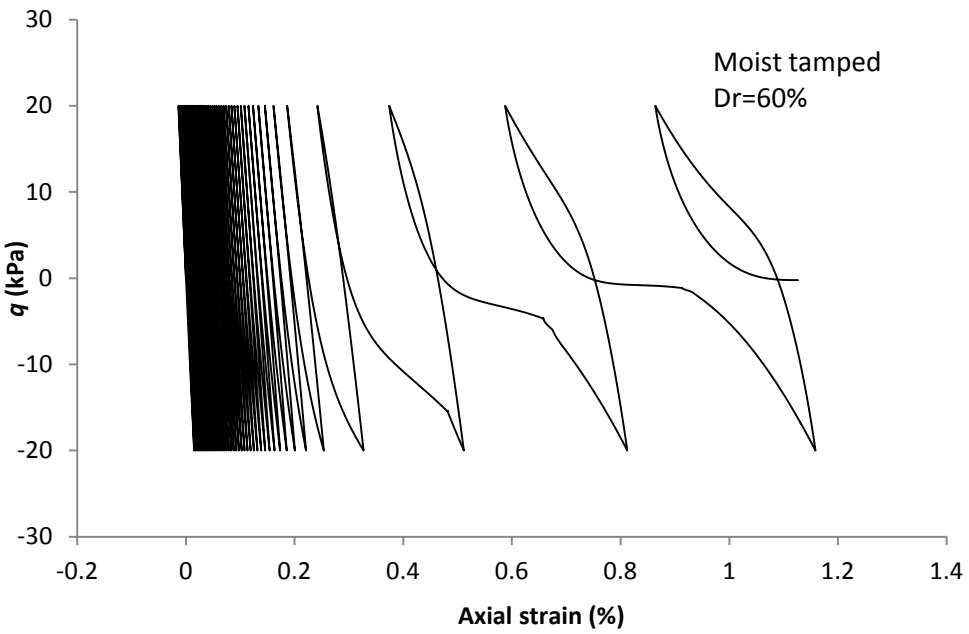


Figure 4.31: q - ϵ_a curve during undrained cyclic triaxial test

The development of excess pore pressure as a function of the number of loading cycles for the moist tamped specimens is shown in Figure 4.32, and for dry deposited

specimen in Figure 4.33. It can be seen that the pore pressure response is different for the two preparation methods. Dry deposited specimens have larger rise. In addition, for the same preparation method, pore pressure response is dependent on density.

The number of loading cycles to failure as a function of relative density is shown in Figure 4.34. It can be seen that moist tamped specimens are much more resistant to excess pore pressure development during undrained repeated cyclic triaxial loading. It is of note that Yang et al.⁽⁷⁾ previously performed monotonic undrained triaxial loading condition on the same sand and observed the same effect.

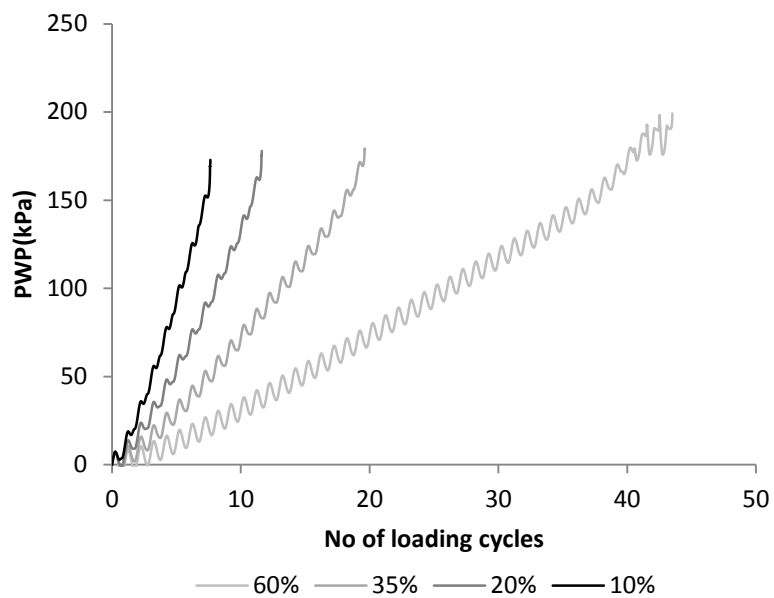


Figure 4.32: Variation of excess PWP with number of loading cycles in undrained cyclic triaxial test

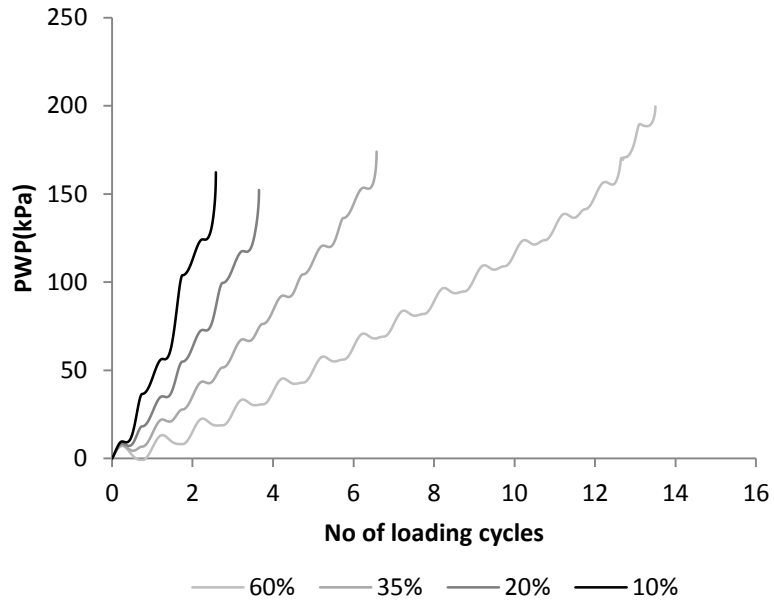


Figure 4.33: Variation of excess PWP with number of loading cycles in undrained cyclic triaxial test at different relative density

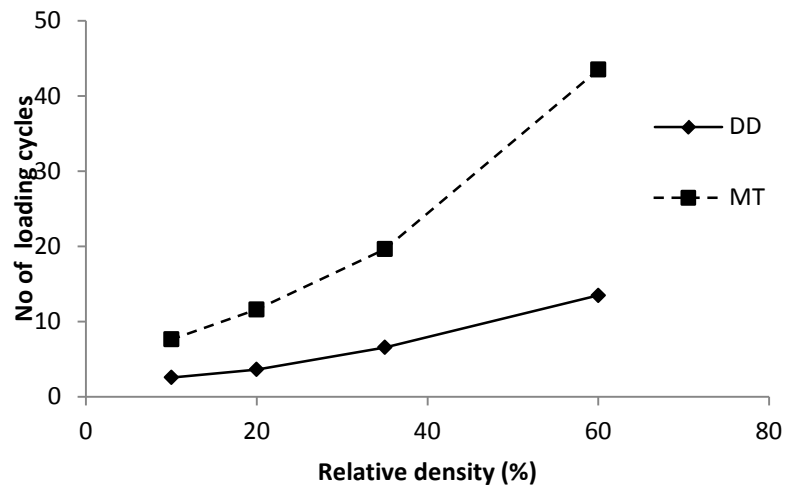


Figure 4.34: Variation of loading cycles with relative density in undrained cyclic triaxial test

4.7 Conclusion

This chapter presents a model with the capability to predict unsaturated response of sands. Inclusion of an anisotropic fabric parameter enables the model to capture the effect of sample preparation on sand response. The model is implemented into Abaqus by using a UMAT subroutine. The model was verified on a wide range of test data.

The simulation results by using the model show that saturation level significantly affects sand performance. In order to quantify the difference in observed performance of unsaturated sands for various levels of saturation, a modified initial state parameter (ψ_{MIUS}) for unsaturated sand was developed. A linear relationship between peak stress increment and ψ_{MIUS} for different densities and sample preparation methods (MT and DD) was found.

The sand model presented here is used to predict CRREL tests data using finite element as shown in Chapter 7.

CHAPTER FIVE

DEVELOPMENT OF DRUCKER-PRAGER CAP MODEL

5.1 Introduction

Drucker and Prager formulated a plasticity model for granular materials ⁽⁸⁴⁾. The modified Drucker-Prager cap model is an advancement of the original model by adding a cap shaped yield surface to the shear yield surface to present the initiation of plastic volumetric strains ⁽⁸⁵⁾. Drucker et al. introduced the cap ⁽⁸⁶⁾ in 1957 and the study by Resende and Martin ⁽⁸⁴⁾ finalized the formulation of the Drucker-Prager cap model where loadings can occur in both the shear failure surface and the cap.

There are different shapes of the Cap surface developed. Dimaggio and Sandler (See references 5, 6, 7 and 8) applied a Cap with elliptical shape, with a cap aspect ratio. This surface is widely used including the Abaqus finite element software.

5.2 Model Development

5.2.1 Parameters of D-P Cap Model

The parameters of Drucker-Prager Cap Model in numerical simulation are listed in Table 2.2. These needed to be determined by a series of laboratory tests. Huang and Chen⁽⁵⁴⁾ presented a simplified elegant procedure to determine the 12 parameters of Drucker-Prager Cap model listed in Table 5.1. They can be divided into 5 subgroups.

Table 5.1: Cap-Model Parameters in Proposed Procedure(after Huang and Chen ⁽⁵⁴⁾)

Sections	Parameters	Explanation
Ultimate Failure Surface	α	Slope in $\bar{I}_1 - J_2^{1/2}$
	k	Intercept with $J_2^{1/2}$
	T_c	Tension cutoff
Elastic and Plastic Behavior	K_{\min}	Minimum value of elastic bulk modulus
	$C_c/2.303(1 + e_0)$	Total bulk modulus parameter
	$C_r/2.303(1 + e_0)$	Elastic bulk modulus parameter
	v	Poisson's ratio
Cap	R	Cap aspect ratio
	OCR	Overconsolidated ratio
Initial stress state	γ	Unit weight of soil
	K_0	Initial coefficient of lateral earth pressure
Pore Pressure Effect	ϵ	Factor for bulk modulus of fluids

Some of the parameters required when defining material properties could be obtained directly from tests, such as Young's Modulus, cohesion, and friction angle. whereas others need to be estimated from other parameters. For example, the aspect ratio of the Cap R (Fig. 2.7) is obtained from trial-and-error method, using compression index,

swelling index, and other data gained from consolidated-drained (CU) triaxial tests. Even for the parameters that could be obtained from experiments, some of the tests are time consuming. For example, the internal friction angle requires at least two (CU) triaxial tests performed, in which the saturating period could be as long as several weeks. The relatively high number of laboratory tests limits the application of Drucker-Prager Cap Model for routine engineering applications ⁽⁸⁷⁾. Therefore, we have simplified some of the procedures of D-P Cap Model parameter determination as shown below to be useful in practice.

5.2.2 Ultimate Failure Surface

The Drucker-Prager criterion is applied here to describe the ultimate failure surface, which can be expressed as follows:

$$f(I_1, J_2) = \alpha I_1 + \sqrt{J_2} - k = 0 \quad (5.1)$$

where I_1 = the first invariant of the effective stress tensor;

J_2 = the second invariant of the deviatoric stress tensor;

α and k = material angel related to the friction angle and cohesion of the soil.

the Drucker-Prager criterion, as a smooth approximation to the Mohr-Coulomb criterion, can be made to match the latter by adjusting the size of the cone, thus the problem in numerical simulation due to the corner in the Mohr-Coulomb criterion could be solved.

For triaxial compression, the two sets of material constants are related by:

$$\alpha = \frac{2\sin\phi}{\sqrt{3}(3 - \sin\phi)} \quad (5.2)$$

$$k = \frac{6c\cos\phi}{\sqrt{3}(3 - \sin\phi)} \quad (5.3)$$

where ϕ = friction angle of the material;

c = material cohesion;

For triaxial tension, the two material constants are

$$\alpha = \frac{2\sin\phi}{\sqrt{3}(3 + \sin\phi)} \quad (5.4)$$

$$k = \frac{6c\cos\phi}{\sqrt{3}(3 + \sin\phi)} \quad (5.5)$$

In order to obtain the parameters of ultimate failure surface, a series of consolidated-undrained triaxial tests were suggested. However the triaxial tests are complicated and time-consuming, thus another method is proposed here (Section 5.4.1) to determine the internal friction angle ϕ' and to reduce the number of triaxial tests.

5.2.3 Elastic and Plastic Behavior

For virgin consolidation, the equation is

$$C_c = -\frac{de}{d(\log p)} \quad (5.6)$$

where e = the void ratio;

\bar{p} = the effective hydrostatic stress;

C_c = the compression index;

Since the total volumetric strain $d\varepsilon_p^t = -de/(1 + e_0)$, where e_0 is the initial void ratio,

Eq (5.6) becomes

$$\frac{C_c}{1 + e_0} = \frac{d\varepsilon_p^t}{d(\log\bar{p})} \quad (5.7)$$

or

$$K_t = \frac{d\bar{p}}{d\varepsilon_p^t} = \frac{\bar{p}}{A_t} \quad (5.8)$$

where K_t is the total bulk modulus, it is a function of the effective hydrostatic stress \bar{p}

and constant A_t , which can be expressed as

$$A_t = \frac{C_c}{2.303(1 + e_0)} \quad (5.9)$$

Similarly, the elastic bulk modulus K_e can be defined as

$$K_e = \frac{d\bar{p}}{d\varepsilon_v^e} = \frac{\bar{p}}{A_e} \quad (5.10)$$

with

$$A_e = \frac{C_r}{2.303(1 + e_0)} \quad (5.11)$$

where C_r is the swelling index and ε_v^e is the elastic volumetric strain.

Also, if the Poisson's ratio ν is determined, then the elastic shear modulus G can be expressed as

$$G = \frac{3K_e(1 - 2\nu)}{2(1 + \nu)} \quad (5.12)$$

5.2.4 Cap Surface

The values of \bar{I}_1 and $J_2^{1/2}$ at point A, which is on the initial Cap, are given by

$$\bar{I}_{1a} = \sigma'_{v0}(1 + 2K_0) \quad (5.13)$$

$$J_2^{1/2} = \frac{1}{\sqrt{3}}\sigma'_{v0}(1 + 2K_0) \quad (5.14)$$

The shear strength ratio s at the final Cap is given by

$$s = \frac{S_u}{\sigma'_{v0}} = \frac{(\sigma_1 - \sigma_3)_f}{2\sigma'_{v0}} \quad (5.15)$$

where $(\sigma_1 - \sigma_3)_f$ = the principal stress difference at failure in CU-Triaxial test;

σ'_{v0} = the initial vertical stress;

The second invariant of deviatoric stress tensor J_{2f} is

$$J_{2f} = \frac{1}{3}(\sigma_1 - \sigma_3)_f^2 \quad (5.16)$$

combine with the Drucker-Prager criteria we have

$$\bar{I}_{1f} = \frac{1}{\alpha} \left(-k + 2 \frac{\sigma'_{v0}}{\sqrt{3}} s \right) \quad (5.17)$$

Thus the $d\varepsilon_v^p$ can be derived as

$$d\varepsilon_v^p = -2A_e \frac{\left(-\frac{k}{\sigma'_{v0}} + \frac{2s}{\sqrt{3}}\right) - (1+2K_0)\alpha}{\left(-\frac{k}{\sigma'_{v0}} + \frac{2s}{\sqrt{3}}\right) + (1+2K_0)\alpha} \quad (5.18)$$

The evolution of Cap is

$$dX = \frac{X_a}{A_t - A_e} d\varepsilon_v^p \quad (5.19)$$

where X_a = the initial Cap position.

The aspect ratio of Cap R and initial Cap position X_a can be determined from a trial-and-error procedure by introducing the parameter L_a into Eqs.(5.20)- (5.23) below:

$$(1 - \alpha^2 R^2)L_a^2 - 2(\bar{I}_{1a} + \alpha k R^2)L_a + (\bar{I}_{1a}^2 + R^2 J_{2a} - R^2 k^2) = 0 \quad (5.20)$$

$$\left\{ \begin{array}{l} X_a = L_a + (k + \alpha L_a)R \\ X_b = X_a + dX \end{array} \right. \quad (5.21)$$

$$\left\{ \begin{array}{l} X_b = X_a + dX \\ R = \frac{X_b - \bar{I}_{1f}}{J_{2f}^{1/2}} \end{array} \right. \quad (5.22)$$

$$\left\{ \begin{array}{l} X_b = X_a + dX \\ R = \frac{X_b - \bar{I}_{1f}}{J_{2f}^{1/2}} \end{array} \right. \quad (5.23)$$

5.3 Methods for determining the parameters of D-P Cap Model

This section presents details of the procedure to determine the D-P Cap model. All the parameters discussed in section 5.2 are obtained by tests or by indirect estimation from other parameters.

5.3.1 Determination of Ultimate Failure Surface

Typically in order to obtain the parameters of ultimate failure surface, at least two CU-Triaxial tests are needed, which is very time consuming and could only obtain the

performance under saturated condition of soils. However, in most cases of subgrade layer the soils are in unsaturated conditions, thus the influence of suction stress should not be neglected.

The suction stress was express by Lu⁽⁸⁸⁾ as

$$\sigma^s = -(u_a - u_w)S_e \quad (5.24)$$

where σ^s = suction stress;

$(u_a - u_w)$ = the matric suction;

S_e = the effective degree of saturation, which is derived from

$$S_e = \frac{S - S_r}{1 - S_r} \quad (5.25)$$

where S_r = the residual degree of suction obtained from the saturation degree-suction relationship;

S = the degree of saturation given by

$$S = \frac{\omega}{1/\rho_d - 1/G_s} \times 100\% \quad (5.26)$$

where ω = the moisture content;

ρ_d = the dry density of the soil;

G_s = the specific gravity;

The Van Genuchten Soil Water Characteristic Curve (SWCC) defined the effective degree of saturation as

$$S_e = \left\{ \frac{1}{1 + [\alpha(u_a - u_w)]^n} \right\}^{1-1/n} \quad (5.27)$$

where α and n are parameters of SWCC;

By measuring the suction and moisture content of soils samples under different water content levels, the SWCC can be plotted with curve fitting method, thus the suction stress can be calculated with Eq. (5.24). Then, a procedure of calculating internal friction angle by using data obtained from indirect tensile strength (IDT) tests under different water content and SWCC can be applied following the procedure proposed by Li et al.⁽⁸⁸⁾ as follows

1. Measure dry density ρ_d and specific gravity G_s from tests.
2. Measure the suction at different moisture contents to obtain the residual degree of saturation S_r . Then SWCC can be obtained by curving fitting, and thus the SSAC could be derived.
3. Perform IDT tests at two (at least) unsaturated moisture contents
4. Calculate the effective degree of saturation S_e , the suction stress σ^s , and the effective stress σ' for the IDT test results.
5. Calculate the effective stress results in the p' - q coordinate. Slope M and the internal friction angle ϕ' can be obtained.

The details of calculation and the results of IDT tests performed on all CRREL soils are presented in Chapter 6.

The material cohesion c , can be obtained either by shear tests or CU-Triaxial tests. In this section, the cohesion c is derived by using internal friction angle ϕ' and a Mohr

circle from CU-Triaxial test result. The calculation procedure is presented in the MATLAB program (Appendix B).

5.3.2 Determining Elastic and Plastic Behavior

Young's Modulus E , can be obtained from the slope of the first 15% deformation range in strain-stress in unconfined compressive strength tests. Poisson's ratio ν can be estimated from the relationship with plasticity index shown in Figure 5.1 after Wroth⁽⁸⁹⁾, which matches data well for lightly overconsolidated soils.

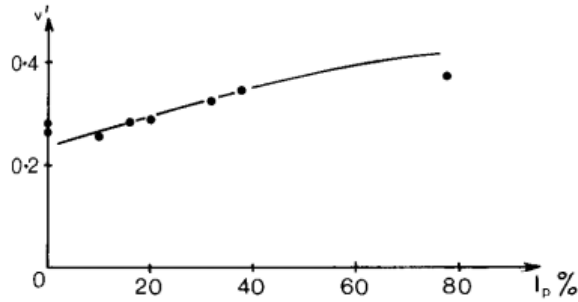


Figure 5.1: Relationship between Poisson's ratio and plasticity index (After Wroth⁽⁸⁹⁾)

In order to get total and elastic bulk modulus parameters A_t and A_e , swelling index C_r , compression index C_c and initial void ratio e_0 are needed in Eq.(5.9) and Eq. (5.11). e_0 can be calculated once the dry density of the soil ρ_d and the specific gravity G_s are obtained

$$e_0 = \frac{G_s}{\rho_d} - 1 \quad (5.28)$$

The value of C_c is usually obtained from the laboratory oedometer test, which could take several weeks. Several empirical correlations have been suggested by researchers to derive this parameter from Atterberg Limits or initial void ratio (See references 90, 91, 92 and 93). The one developed by Terzaghi and Peck⁽⁹⁴⁾ for a normally consolidated clay is used here.

$$C_c = 0.09(LL - 10) \quad (5.29)$$

in where LL is the liquid limit.

Several approaches about obtaining swelling index C_r were reviewed based on data regression⁽⁹⁵⁾, the relationship in Eq. (5.30) is adopted, which is widely used in many studies⁽⁹⁶⁾.

$$C_r = (0.1\sim0.2)C_c \quad (5.30)$$

5.3.3 Determination of the Cap Surface

The aspect ratio of cap surface R, can be evaluated when constants of Drucker-Prager criteria α and k , initial vertical effective stress σ'_{v0} , initial coefficient of lateral earth pressure K_0 , and undrained shear strength ratio S_u/σ'_{v0} , are provided.

For normally consolidated clays, the relationship between K_0 and internal friction angle is expressed as follows by Ladd et al.⁽⁹⁷⁾

$$K_0 = (1 - \sin\phi') \pm 0.05 \quad (5.31)$$

For overconsolidated soils, K_0 can be expressed using ratio OCR⁽⁹⁹⁾as:

$$K_0 = (1 - \sin\phi')OCR^{\sin\phi'} \quad (5.32)$$

The rest of the parameters needed is obtained from test result obtained from CU-Triaxial experiment.

The trial and error procedure needed to obtain the R value for the Cap surface using the set of Eqs (5.20)- (5.23) are conveniently done here using a Matlab program (Appendix B). The program also provides the other parameters of D-P Cap model. Before running the program, a range of aspect ratio for cap surface, R, are required to be input by using lower and upper limits (Rmin and Rmax), in the calculation applied for soil A-6 and A-7-5 0 and 10 were selected. Length of each trial step, the variable Accu in the program used to define the increments (0.01 was selected in the study).

The typical output window of trial-and-error procedure completed in MATLAB is shown in Figure 5.2. The range of values chosen varied from 0 to 10. The difference in assumed and calculated value is shown on the y-axis. The variation of this difference with chosen R values are shown by the blue curve. When the difference of equation is smaller than the desired error value, the final value of R is determined. The value of R, initial cap position X_a can also be output in command window.

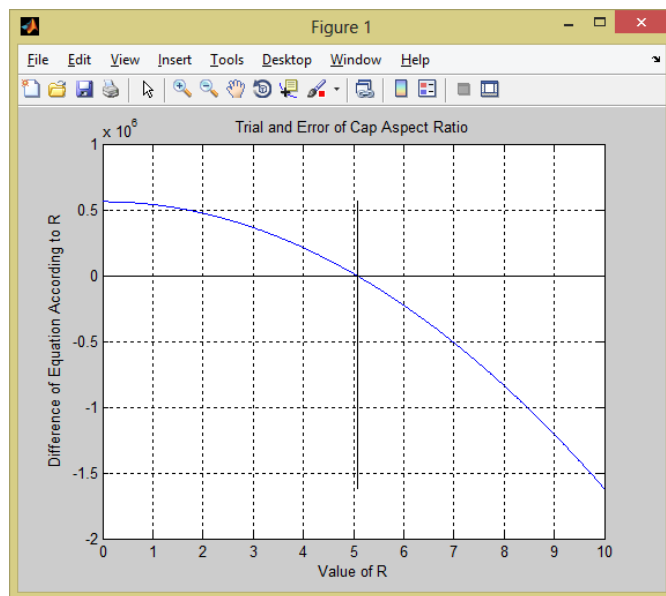


Figure 5.2: Output of trial-and-error procedure

5.3.4 Determination of Hardening Law

The associated non-linear hardening law associated with Drucker-Prager Cap model is used to describe the relationship between yield stresses and volumetric strains. Volumetric hardening is also defined as the movement of the Cap surface along the hydrostatic axis. A series of Cap surfaces will be generated in numerical simulation when yield stress state is reached, and when the Cap moves to the right an extent of elastic region will also be given.

In order to determine the parameters of the model hardening law, a series of isostatic compression tests are needed ⁽⁸⁵⁾, which makes it costly. Following the method of determining the parameters of Cap surface ⁽⁵⁴⁾ this procedure is simplified by calculation using stress state and soil properties ⁽⁹⁸⁾.

The Matlab program for determining Hardening Law was incorporated in the program for calculating D-P Cap model in Appendix B. An example of the output window of hardening law is shown in Figure 5.3. The volumetric strains corresponding to yield stresses are calculated and listed in output window, which will be applied in FE simulation.

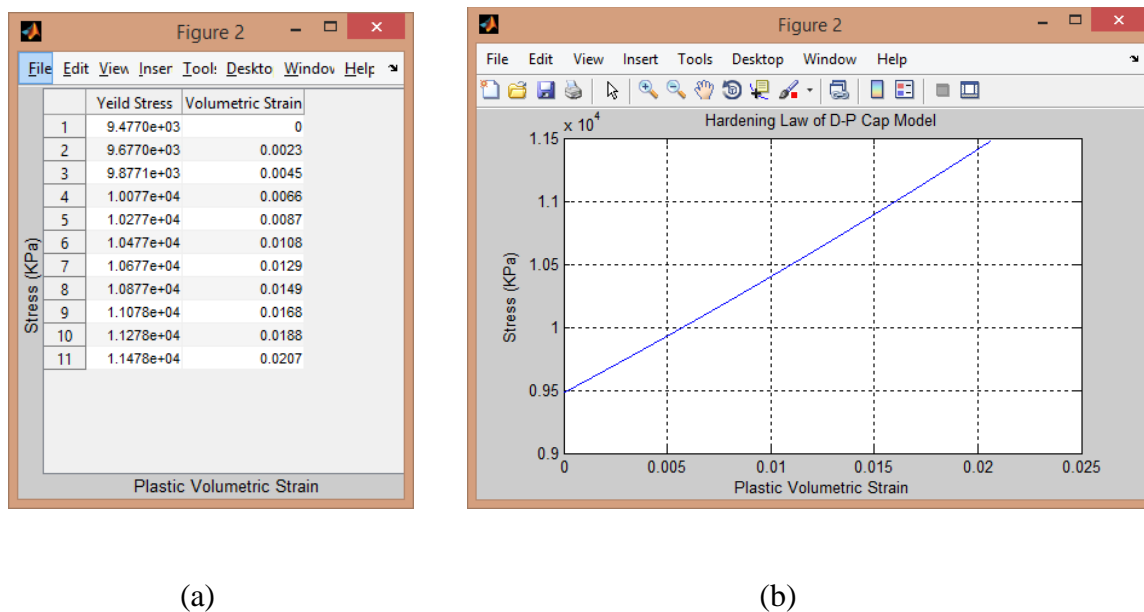


Figure 5.3: Output window of hardening law

(a) Data of hardening law (b) Plot of hardening law

CHAPTER SIX

LABORATORY TESTS

This chapter presents the details of the laboratory tests conducted on the CRREL soils.

The first series of tests consisted of the determination of the resilient modulus values that were used in the development of the empirical models presented in Chapter 3. This is followed by determination of the Drucker-Prager CAP model parameters.

6.1 Laboratory Determination of Resilient Modulus of Aggregate Base

The PSPS project aimed to develop new subgrade criteria models to be used in the design of flexible pavement structures. The laboratory testing conducted to determine the properties of aggregate base layer included:

- Gradation analysis;
- Standard Proctor Tests to determine the optimum moisture content and maximum dry density

In-situ testing of the constructed base layer included only density and moisture measurements and FWD tests on top of the constructed pavement structures.

In order to validate any current or future models for pavement response or performance, or to develop new models using the data collected in the PSPS experiment, the Resilient Modulus (M_R) of the unbound aggregate base used in the construction of the PSPS experimental pavements must be measured. Sufficient quantities of the unbound base aggregates used in the construction of the PSPS test sections were retrieved from

stockpiles at CRREL for this purpose. The material was dried and processed for the resilient modulus testing.

The Mechanistic-Empirical Design Guide (M-E PDG)⁽⁶⁰⁾ uses the Resilient Modulus determined in the triaxial test as the material property to be used for the characterization of subgrade soils and granular base and subbase materials for Level 1 design. The AASHTO T 307 "Determining the Resilient Modulus of Soils and Aggregate Materials"⁽¹⁰⁰⁾ is recommended as the test procedure to be followed for the determination of the Resilient Modulus. The most advanced design methods in Europe and Australia also use Resilient Modulus to characterize unbound foundation materials and subgrade soils. Therefore, an important task of this research project is to determine the Resilient Modulus of the aggregate base material following the AASHTO T 307 protocol.

6.1.1 Selection of the test conditions

The relative density levels and moisture content for which the coarse soil is prepared must be selected before the resilient modulus testing program is commenced. Most often, samples cannot be prepared for high moisture content since, water drains at the bottom of the samples during the compaction in the steel molds. Low values for dry density coupled with medium to high values for moisture content may lead to coarse soil samples that do not maintain their water content while being transported and installed in the triaxial cell.

The selection of the relative density levels and moisture content for which the soil samples were prepared and tested was based on:

- The optimum moisture content and the maximum dry density

- The moisture content and dry density measured in-situ during the construction of the test sections

The AASHTO T 180 (Modified Proctor)⁽¹⁰⁰⁾ test was conducted first on the aggregate base material. The results are given in Table 6.1 and displayed in Figure 6.1.

The AASHTO T 180 (Modified Proctor) test results obtained in the laboratory, are measured on the aggregate material after the aggregates have been sieved through the 19mm sieve. The proportion of oversize aggregate grains removed (larger than 19 mm) was 38% by weight for the PSPS aggregates. According to AASHTO T 224-00⁽¹⁰⁰⁾, when the percentage of oversize aggregates is between 5% and 30%, the measured Maximum Dry Density and Optimum Moisture Content must be corrected; the AASHTO T 224-00 provides the formulas for the adjustments. It is important to note that no correction method is provided for the case when the percentage of oversize particles is larger than 30%, as it is for the PSPS aggregate base material.

Even though the percentage of oversize particles was 38 percents, the correction method described in AASHTO T224-00 had been applied; the corrected values are given in Table 6.1.

Table 6.1: Results of the Modified Proctor tests (AASHTO T 180)

AASHTO T180		AASHTO T224	
MC (%)	DD (kg/m ³)	Results	Corrected Results (oversize particles = 38.6%)
3.191	2,328	OMC = 6.5% MDD = 2,355 kg/m ³	OMC = 5.4% MDD = 2,200 kg/m ³
4.729	2,341		
6.618	2,356		
8.053	2,313		
9.035	2,262		

Tables 6.1 and 6.2 show the initial (before correction) results of the AASHTO T 180 tests conducted on the aggregate samples are very close to the test results given in

project reports for the granular base for test cells 702, 704, 705, 709, 710, 711 and 712.

The maximum dry density and moisture content reported for the aggregate base used in test cell 708 are very different from the values reported for the other test cells. These reported results are erroneous; it is very likely that materials with a different gradation were tested.

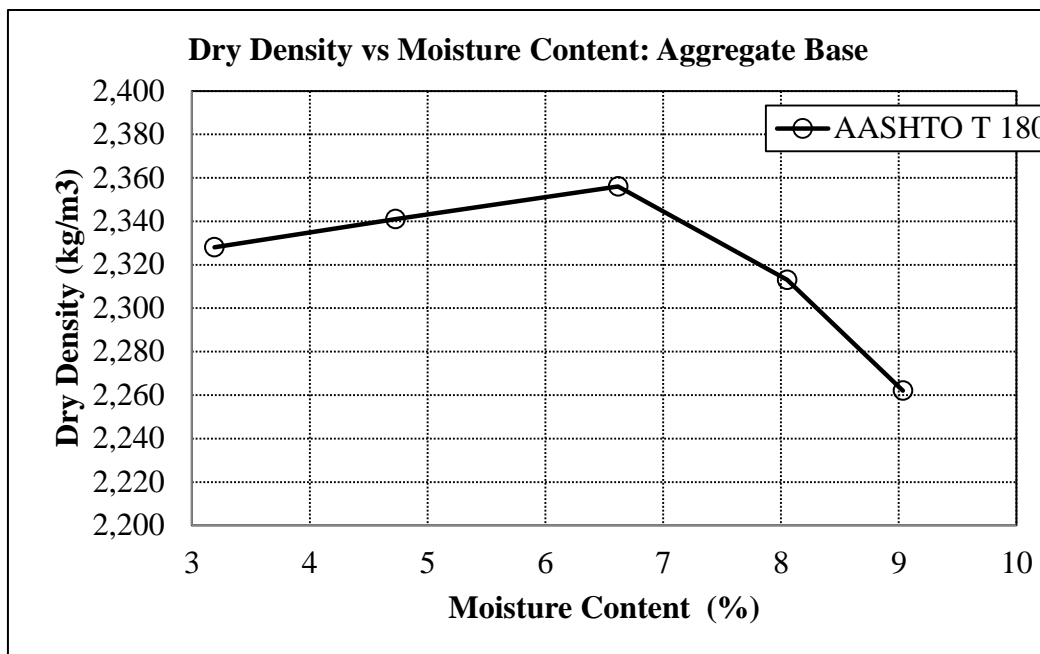


Figure 6.1: Dry Density vs. Moisture Content for the Aggregate Base

Table 6.2 also gives the reported results of the AASHTO T 99 test (Standard Proctor) conducted on the aggregate base material; normally only the AASHTO T 180 (Modified Proctor test) is conducted for coarse soils. As expected, the Maximum Dry Density values reported for the AASHTO T 99 test are lower than the values reported for the AASHTO T 180 test, while the Optimum Moisture Content in the AASHTO T 99 test is higher. Table 6.3 contains the statistics for the in-situ density and moisture content as given in project reports. In many cases, it is clear that the data were collected but the

individual values were never reported. The statistics given for the granular base layer for test cells 711 and 712 are likely wrong, since they are identical to each other. The values reported in Table 6.3 suggest that the in-situ dry density and moisture content varied significantly from one experimental test cell to another. This is reasonable since the base material cannot be effectively compacted for test cell where the moisture content of the subgrade soil was above the optimum value because the soft subgrade did not provide sufficient support to allow proper compaction of the granular base.

Because of the significant variability of the in-situ compacted material, the selection of target moisture contents and compaction levels is difficult. It was therefore decided to perform the resilient modulus tests on aggregates with a moisture content between 4.0% and 6.0%, with the maximum dry density of 2,200 kg/m³ (137.3 pcf) as the reference value.

Table 6.2: Moisture-Density test results given in the PSPS Reports

Base – AASHTO T 99 Cells: 702, 704 and 705		Base – AASHTO T 99 Cells: 706			
Report 702 – Figure 2b		Report 706 – June-02 708 - same as for 706			
Moisture Content (%)	Dry Unit Weight (kg/m ³) (pcf)	Moisture Content (%)	Dry Unit Weight (kg/m ³) (pcf)		
5.3	2,043	127.5	3.6	2,202	137.4
7.8	2,093	130.6	5.9	2,281	142.2
9.5	2,122	132.4	7.24	2,403	150
10.3	2,115	132.0	9.0	2,318	144.6
11.1	2,086	130.2			
13.0	1,996	124.6			
MDD = 2,120 kg/m ³ OMC = 9.5%		MDD = 2,403 kg/m ³ OMC = 7.5%			
Base – AASHTO T 180 Cells: 702, 704 and 705		Base – AASHTO T 180 Cells: 708		Base – AASHTO T 180 Cells: 709, 710, 711 and 712	
Report 702 – From Cortez Same as Rep 702 – Figure 2b		Report 708 – Figure 4		Report 710	
Moisture Content	Dry Unit Weight (kg/m ³) (pcf)	Moisture Content (%)	Dry Unit Weight	Moisture Content	Dry Unit Weight

(%)				(kg/m ³) (pcf)		(%)	(kg/m ³) (pcf)	
4.8	2,180	136.1	1.8	2,332	145.5	2.1	1,950	121.7
6.0	2,243	140.0	3.0	2,353	146.8	4.7	2,180	136.0
6.8	2,201	137.4	3.8	2,338	145.9	6.0	2,235	139.5
7.7	2,070	129.2	5.0	2,343	146.2	6.7	2,200	137.3
9.8	1,964	122.7	5.8	2,413	150.6	7.8	2,067	129.0
			7.25	2,423	151.2	9.8	1,955	122.0
			9.1	2,331	145.5			
MDD = 2,235 kg/m ³ OMC = 6.0%			MDD = 2,465 kg/m ³ OMC = 7.5%			MDD = 2,237 kg/m ³ OMC = 6.0%		

Table 6.3: Average in-situ density and moisture content given in project reports

	Parameter	Experimental Test Cell					
		704	708	709	710	711	712
In-situ Density (kg/m ³)	Average	2,169	2,158	2,356	2,284	2,350	2,350
	COV (%)		5.1	0.8	1.35	1.8	1.8
In-situ Moisture Content (%)	Average	2.7	4.0	4.9	4.6	5.9	5.9
	COV (%)		15	7.8	10.3	5.5	5.5

6.1.2 Resilient Modulus Tests

The resilient modulus of each soil sample was determined in the laboratory using a repeated load triaxial testing machine. The Universal Testing Machine (UTM) manufactured by Industrial Process Controls of Melbourne, Australia was used for this purpose. The test protocol for determining the Resilient Modulus followed the AASHTO T 307 test method⁽¹⁰⁰⁾.

The UTM test configuration consisted of four main components: the Computer Data Acquisition System (CDAS), the hydraulic system, a PC, and the triaxial cell. The CDAS records the signals from the transducers, digitizes the information, and then passes the information along to the PC. The CDAS also controls the testing frame and transducers, along with adjusting and applying the load through the actuator. The hydraulic system allows for strict control of the loading, and therefore, precise control of the stresses applied to the sample. The hydraulic system is connected to the actuator

through an electrically controlled hydraulic servo valve. The force applied to the sample is determined using a load cell mounted in line with the loading shaft. The triaxial cell consists of an air-tight chamber, a loading arm, and a sample platform.

The large triaxial cell used in these tests accommodated samples that were 150-mm in diameter and 300-mm tall. Confining pressure for the triaxial test is provided by means of pressurized air. A separate air tank with a pneumatic valve is connected to the triaxial cell. Using the pressure sensor, the computer system maintains a static confining pressure during the testing. Figure 6.2 shows the triaxial cell used to determine the resilient modulus of the soil samples.

After the coarse soil had been dried, the quantities of soil and water needed to obtain the desired moisture content and relative density level were determined. This was done by first testing the moisture content of the soil (although it had been dried and stored in sealed containers, some moisture might have been present). Next, the weight of water and the weight of soil required were calculated for a little more than the quantity of material needed for preparing the samples, based on the volume of the sample and molds, the desired relative density and the moisture content. The dry soil and water were mixed thoroughly and left to rest at least two hours before the samples were compacted.

After the desired quantity of wet aggregates needed for each sample was weighed, the soil samples were compacted in steel molds using a vibratory plunger in five lifts, as specified in the AASHTO T 307 protocol. After compaction, the top platen was positioned on top of the sample and the rubber membranes were extended to cover the top platens. Vacuum was then applied such that the membranes hold the aggregate particles together. After the split molds were removed, the tri-axial cell was sealed and

placed inside the testing machine. After the cell was pressurized with confining air, the actuator was lowered on the top of the top platen and was adjusted to contact the specimen. The external LVDT was placed and adjusted to ensure maximum stroke availability. Then the conditioning cycles were commenced.

The testing procedure for all samples followed the AASHTO T 307-07 (2007) protocol. Each sample was conditioned prior to the testing sequence. The sample was conditioned for 1,000 load repetitions using a deviator stress of 93.1 kPa and a confining pressure of 103.4 kPa. After the initial conditioning, all samples were tested under the 15 loading sequence given in Table 6.4.

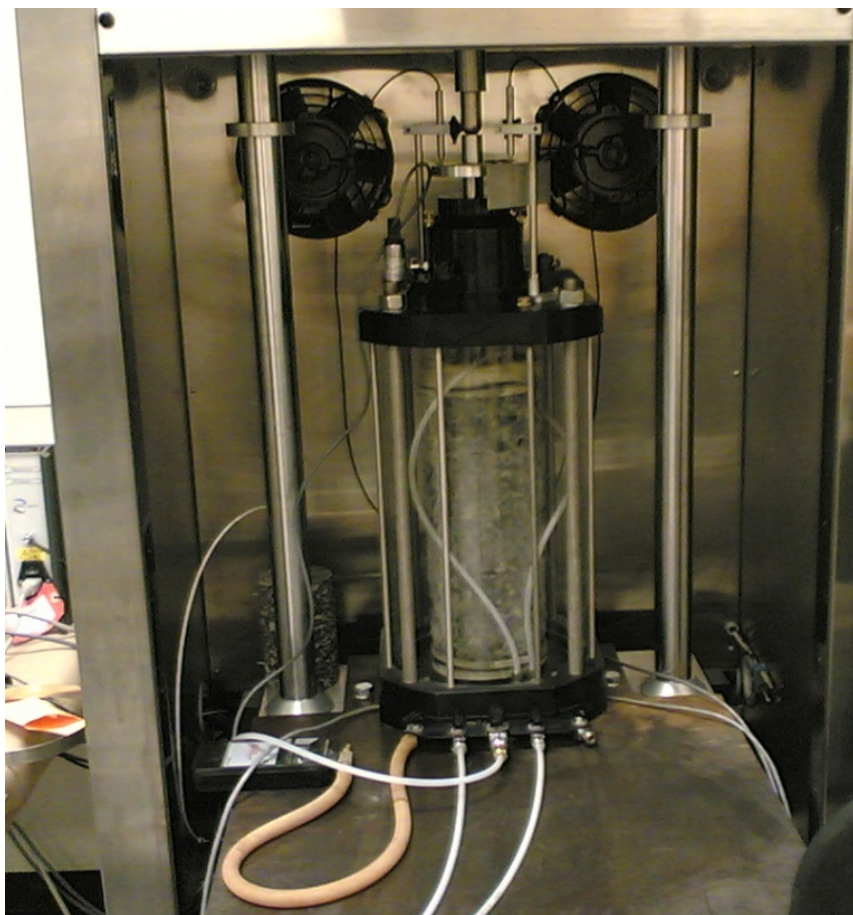


Figure 6.2: Tri-axial Cell

During each test sequences, 100 load repetitions were applied to the sample. The values recorded for the last five repetitions were averaged to calculate the resilient modulus for each loading sequence. Figure 6.3 shows an example of the typical test results for one of the loading sequence.

For each test, resilient modulus, resilient strain, permanent strain, confining pressure, cyclical stress, and contact stress were recorded for each load repetition. Only the values corresponding to the 96th to 100th loading cycles were used in calculating the final resilient modulus at each sequence. Figure 6.4 shows the haversine wave shape for one load pulse. The duration of the load pulse is 0.1 seconds followed by a rest period of 0.9 seconds.

Table 6.4: Loading Sequence during the Tri-axial Resilient Modulus Test

Sequence	Confining Pressure (kPa)	Cyclic Stress (kPa)	Seating Stress (kPa)	Number of cycles
0 - conditioning	103.4	93.1	10.3	1000
1	20.7	18.6	2.1	100
2	20.7	37.3	4.1	100
3	20.7	55.9	6.2	100
4	34.5	31.0	3.5	100
5	34.5	62.0	6.9	100
6	34.5	93.1	10.3	100
7	68.9	62.0	6.9	100
8	68.9	124.1	13.8	100
9	68.9	186.1	20.7	100
10	103.4	62.0	6.9	100
11	103.4	93.1	10.3	100
12	103.4	186.1	20.7	100
13	137.9	93.1	10.3	100
14	137.9	124.1	13.8	100
15	137.9	248.2	27.6	100

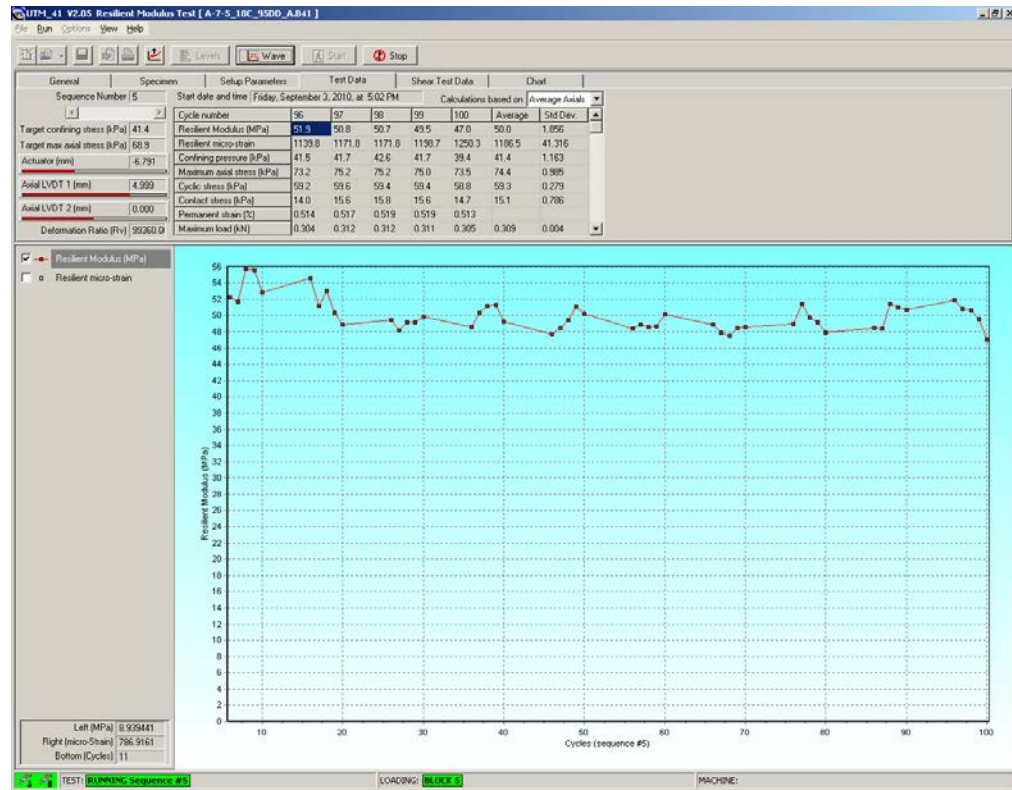


Figure 6.3: Screen Capture Showing the Resilient Modulus Test Result

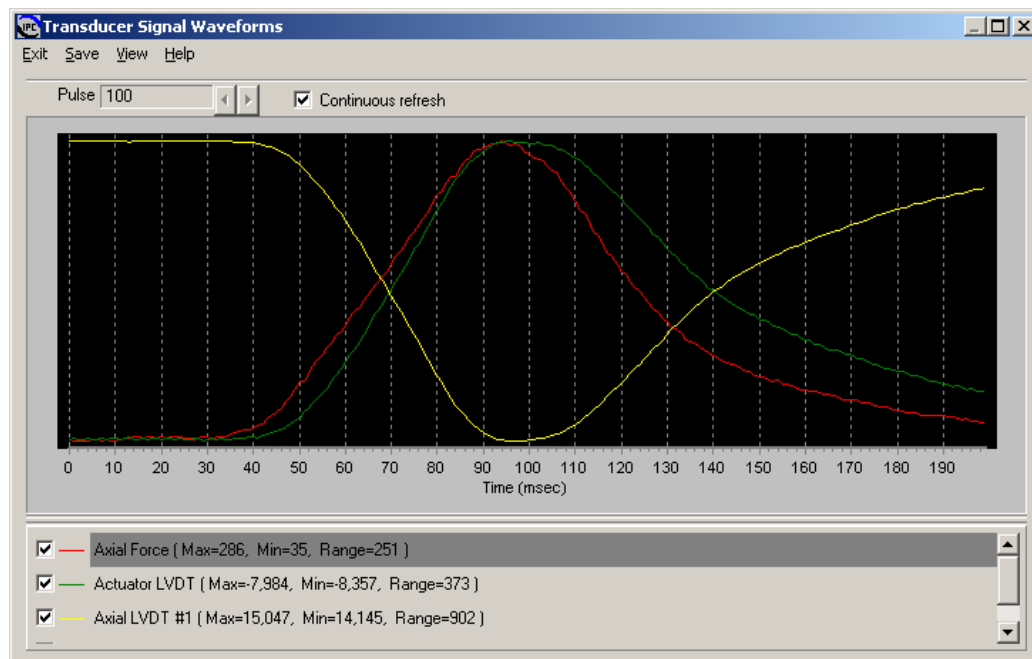


Figure 6.4: Wave shape of the Loading Pulse

6.1.3 Laboratory Resilient Modulus Test Results

Resilient modulus tests were performed in the laboratory on twenty-six samples of base aggregates. The results obtained on each sample are given in Appendix F.

It is important to note that, even though the appropriate measures were taken, it was not possible to achieve precisely any target values for relative density and moisture content. The as-compacted densities and moisture content were calculated; the values for each tested sample are given in Table 6.5.

Figures 6.5 to 6.6 show the resilient moduli values measured on the aggregate base material at each of the six moisture contents. The figures demonstrate that, for very similar density level and even when the moisture content is about the same, the resilient modulus of the aggregates varies significantly. This variability could not be reduced or eliminated even with all the measures taken to fabricate identical samples.

It is very likely that the variability is caused by the poor effectiveness of the vibratory hammer to compact such large aggregates as those used in the construction of the PSPS base layers, even though the compaction method described in the AASHTO 307-07 test protocol was strictly followed. Another factor that might have contributed to the variability of the test results is the non-uniform distribution of the moisture within the sample. For samples with moisture content above 5.5 percent, it was noticed that water tends to drain toward the bottom of the sample. At 6.5 percent moisture content, it was difficult to prevent the vacuum pump from removing the water from the samples.

Table 6.5: As-compacted Properties of the Resilient Modulus Test Samples

Sample	Moisture Content Group (%)	Moisture Content (%)	Dry Density		Relative Density (%)	Saturation Ratio (%)
			(kg/m ³)	(pcf)		
1	4.0	4.1	1,952	121.8	88.7	27.6
2		3.8	1,931	120.5	87.8	24.8
3		4.0	1,891	118.0	85.9	24.2
4		4.1	2,042	127.4	92.8	32.8
5		3.4	1,907	119.0	86.7	21.6
6	4.5	4.3	2,030	126.7	92.3	33.3
7		4.5	2,099	131.0	95.4	39.7
8		4.4	2,127	132.8	96.7	41.4
9		4.3	2,092	130.6	95.1	37.7
10		4.5	2,041	127.4	92.8	35.3
11	5.0	4.8	2,119	132.2	96.3	43.7
12		5.1	2,068	129.1	94.0	41.3
13		5.0	2,115	132.0	96.1	44.7
14		5.2	1,982	123.7	90.1	35.6
15	5.5	5.5	2,016	125.8	91.6	39.7
16		5.5	2,117	132.1	96.2	48.4
17		5.3	2,048	127.8	93.1	40.9
18		5.3	1,948	121.6	88.6	34.0
19		5.7	2,125	132.6	96.6	50.5
20	6.0	5.9	2,135	133.2	97.0	53.0
21		5.9	2,019	126.0	91.8	42.2
22		6.1	2,095	137.8	95.3	50.1
23		6.2	1,977	123.4	89.9	40.6
24	6.5	6.5	2,051	128.0	93.2	48.3
25		6.2	1,894	118.2	86.1	35.2
26		6.6	2,191	136.7	99.6	64.8

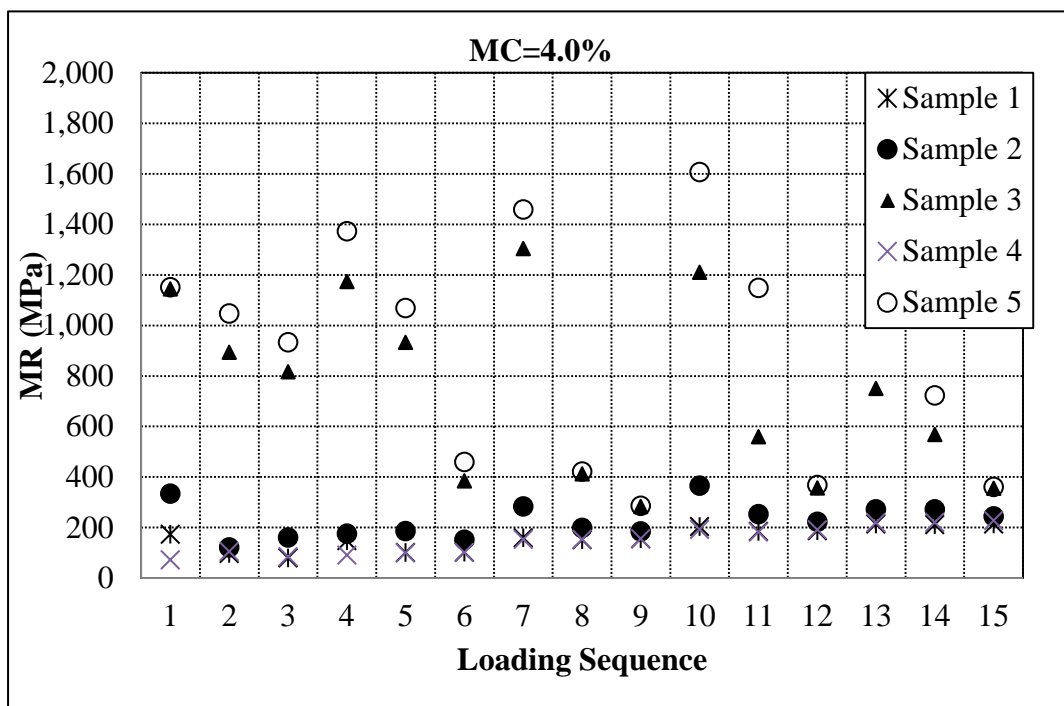


Figure 6.5: Laboratory Resilient Modulus Results at 4.0% Moisture Content

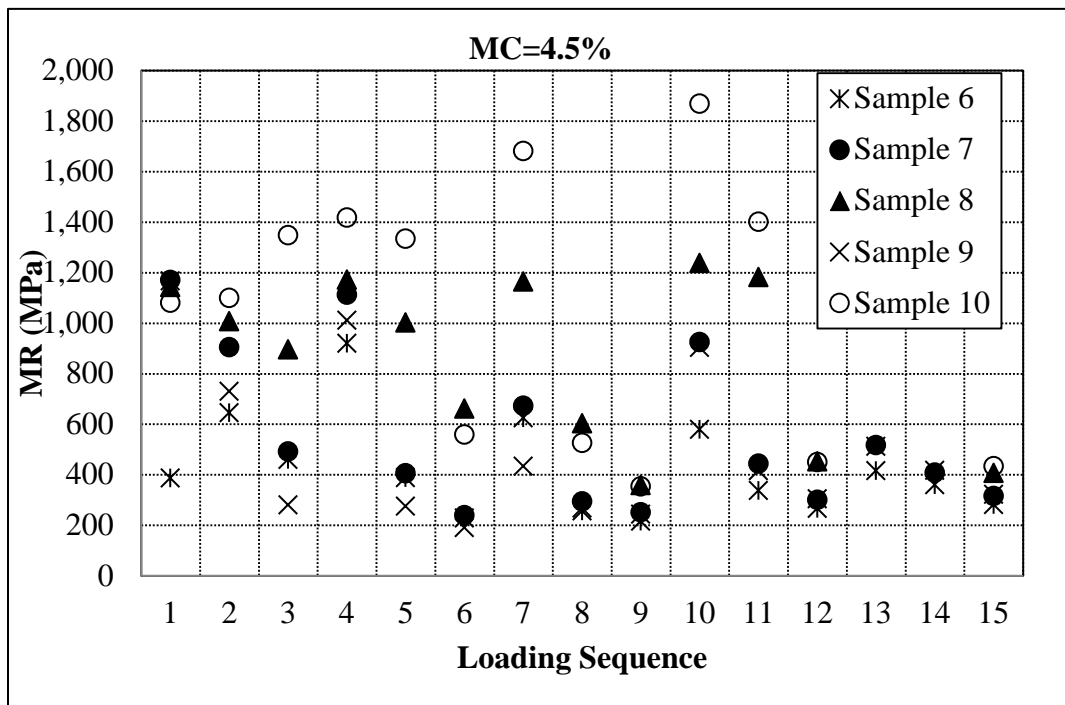


Figure 6.6: Laboratory Resilient Modulus Results at 4.5% Moisture Content

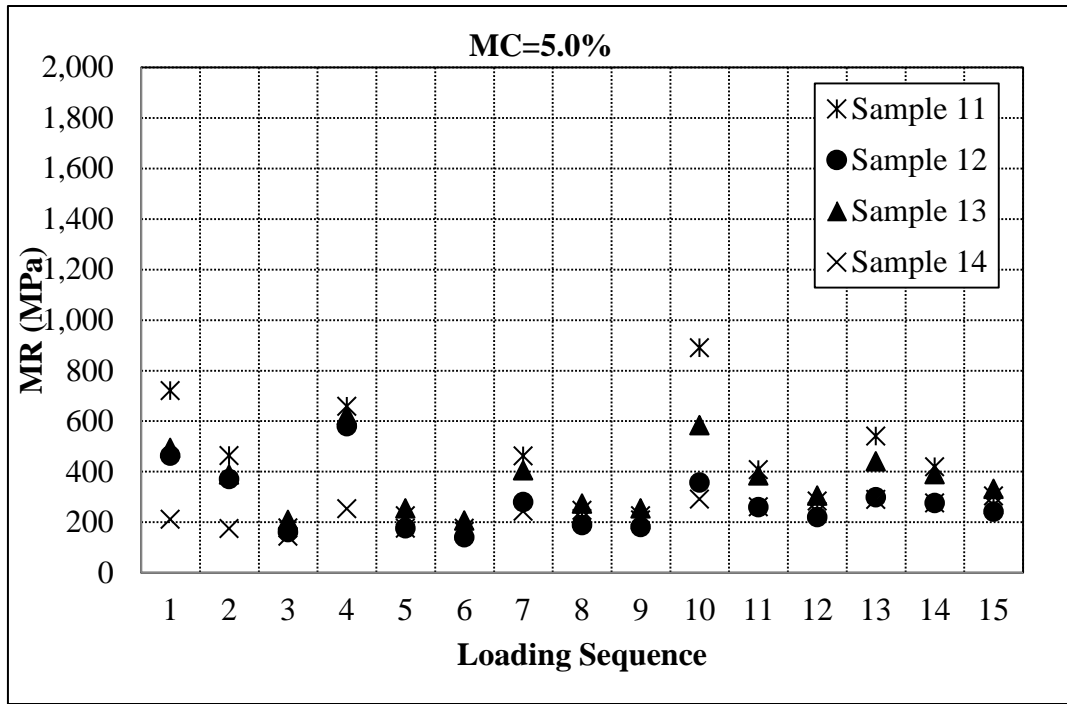


Figure 6.7: Laboratory Resilient Modulus Results at 5.0% Moisture Content

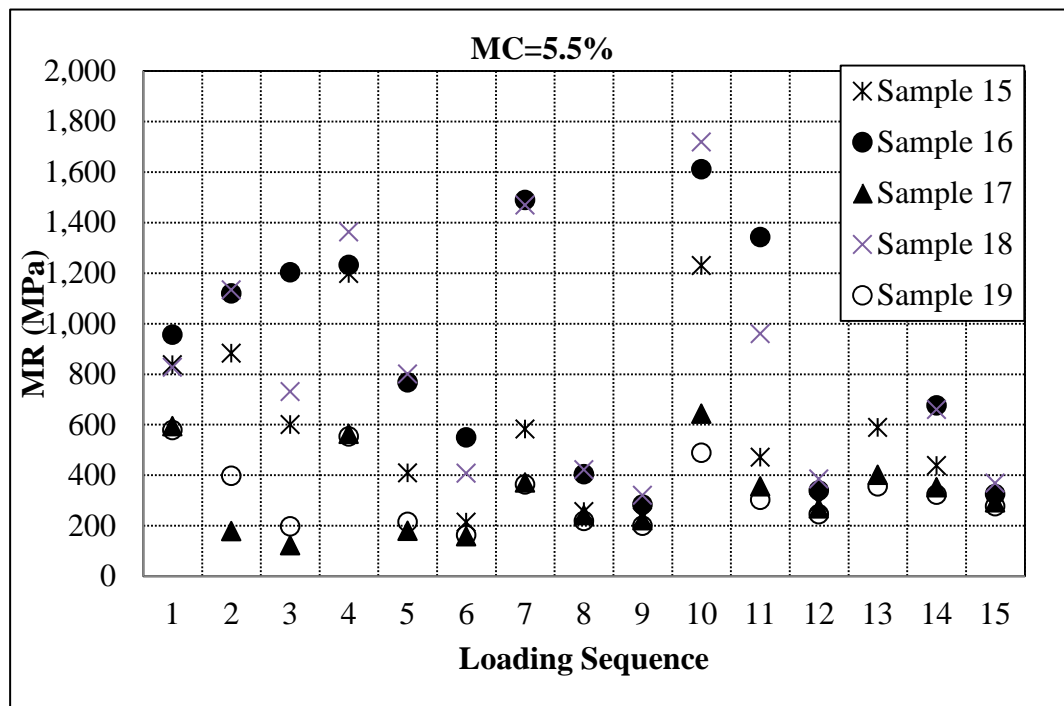


Figure 6.8: Laboratory Resilient Modulus Results at 5.5% Moisture Content

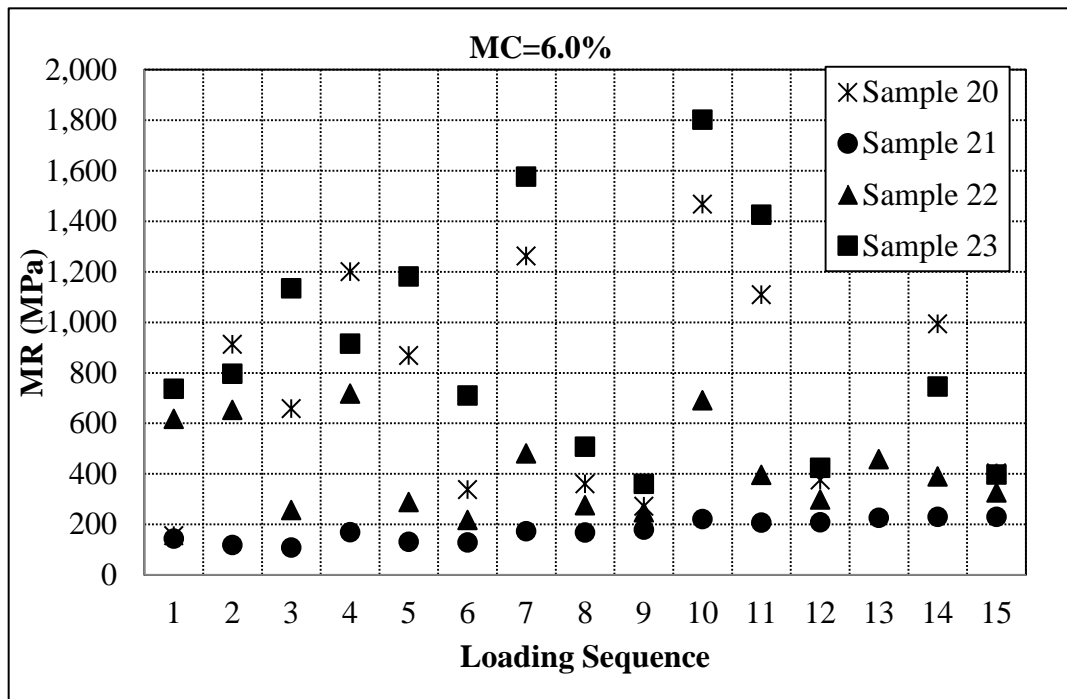


Figure 6.9: Laboratory Resilient Modulus Results at 6.0% Moisture Content

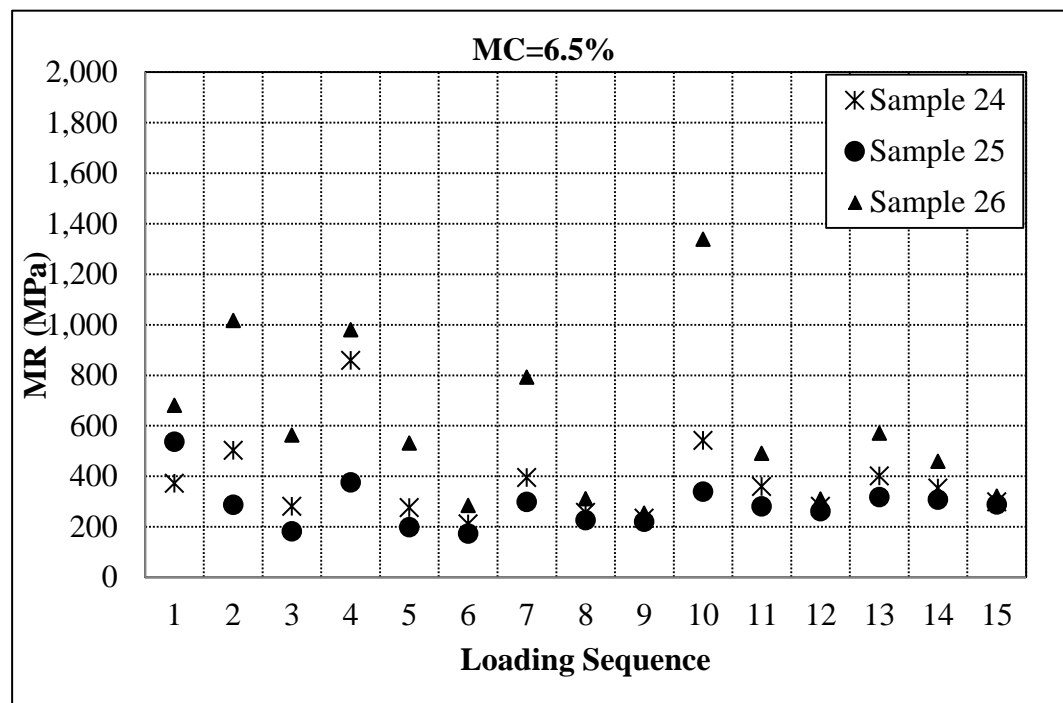


Figure 6.10: Laboratory Resilient Modulus Results at 6.5% Moisture Content

6.1.4 Development of Non-Linear Stiffness Model for the Granular Base Material

The stiffness of subgrade soils is affected by the magnitude of the stresses applied to the soil. Among the many stress dependency models available in the literature, the most commonly used model is the one incorporated in the M-E PDG ⁽⁶⁰⁾. The resilient modulus of granular materials, M_R , is dependent on the confining stress, σ_3 , and the octahedral shear stress, τ_{oct} , as given in Eq (6.1).

$$M_R = K_1 \cdot p_a \cdot (\theta / p_a)^{K_2} \cdot [(\tau_{oct} / p_a) + 1]^{K_3} \quad (6.1)$$

where,

M_R = Resilient Modulus,

K_1 , K_2 , and K_3 = Regression Constants,

Θ = bulk stress = $\sigma_v + 2 * \sigma_3$

p_a = normalizing stress (atmospheric pressure)

σ_3 = Confining Stress, and

τ_{oct} = Octahedral Shear Stress = $\{[2 * (\sigma_v - \sigma_3)^2]\}^{0.5} / 3$

σ_v = Maximum Axial Stress

The three constants, K_1 , K_2 and K_3 in the model are characteristics of each sample because they change with moisture content and dry density level. The coefficients are given in Table 6.6. They were estimated using non-linear regression analysis by fitting the model given in Eq (6.1) to the measured resilient modulus values given in Appendix E.

Table 6.7 shows that, for the majority of the samples, the resilient modulus model fits well the measured moduli values. The table also shows that the regression constants vary significantly from one sample to another.

Linear regression was attempted to derive relationships between the regression constants (K_1 , K_2 , and K_3) and the moisture content and relative density. However, no good linear fit was found; the coefficients of determination (R-square) were less than 0.15.

The non-linear regression does not indicate if the regression constants are statistically significant. However, Eq (6.2) can be converted into a linear form as:

$$\log(M_R / p_a) = \log K_1 + K_2 \cdot \log(\theta / p_a) + K_3 \cdot \log[(\tau_{oct} / p_a) + 1] \quad (6.2)$$

In this form, a new set of regression constants will be obtained because the errors are calculated for a different independent variable, $\log(M_R/p_a)$, instead of M_R . The new set of regression constants obtained for the 26 samples are given in Table 6.7. The values underlined indicate regression constants that are statistical significant at 0.05 level of significance.

It is important to observe that the new regression constants (Table 6.7) are very similar to the regression constants for the original model (Table 6.6). As for the constants of the original model, linear regression was attempted to derive relationships between the new regression constants (K_1 , K_2 , and K_3) and the moisture content and relative density. Again, no good linear fit was found; the coefficients of determination (R-square) were less than 0.15.

Table 6.6: Regression Parameters Models for the original resilient modulus model

Sample	Moisture Content (%)	Saturation Ratio (%)	MC / OMC	Relative Density (%)	K ₁	K ₂	K ₃	R ²
1	4.1	27.6	0.759	88.7	1,196.80	0.44166	-0.52056	0.727
2	3.8	24.8	0.704	87.8	2,186.19	0.41881	-1.70736	0.420
3	4.0	24.2	0.741	85.9	16,522.42	0.41827	-5.87314	0.820
4	4.1	32.8	0.759	92.8	929.68	0.60021	-0.31241	0.976
5	3.4	21.6	0.630	86.7	19,152.83	0.64242	-6.33887	0.897
6	4.3	33.3	0.796	92.3	7,338.96	0.25620	-4.27304	0.514
7	4.5	39.7	0.833	95.4	18,629.36	0.50828	-9.51173	0.815
8	4.4	41.4	0.889	96.7	14,498.27	0.45395	-3.90763	0.845
9	4.3	37.7	0.815	95.1	15,762.15	0.62783	-10.9063	0.643
10	4.5	35.3	0.833	92.8	18,731.70	0.63449	-5.29854	0.867
11	4.8	43.7	0.889	96.3	7,805.72	0.79713	-7.44727	0.623
12	5.1	41.3	0.944	94.0	4,300.24	0.20067	-3.44062	0.313
13	5.0	44.7	0.926	96.1	4,997.88	0.42103	-3.26925	0.470
14	5.2	35.6	0.963	90.1	1,988.10	0.37441	-0.94226	0.753
15	5.5	39.7	1.019	91.6	15,999.92	0.77609	-9.76933	0.780
16	5.5	48.4	1.019	96.2	17,296.85	0.58843	-5.81116	0.826
17	5.3	40.9	0.981	93.1	4,668.24	0.62333	-4.90583	0.409
18	5.3	34.0	0.981	88.6	16,629.87	0.78714	-6.79867	0.862
19	5.7	50.5	1.056	96.6	5,278.02	0.30451	-3.99771	0.413
20	5.9	53.0	1.093	97.0	10,855.47	0.98395	-5.48652	0.697
21	5.9	42.2	1.093	91.8	1,343.17	0.40436	-0.41713	0.901
22	6.1	50.1	1.130	95.3	7,513.99	0.39798	-4.90132	0.577
23	6.2	40.6	1.148	89.9	14,373.21	0.70092	-5.14507	0.831
24	6.5	48.3	1.204	93.2	5,768.51	0.32892	-3.86144	0.392
25	6.2	35.2	1.148	86.1	3,322.52	0.11045	-1.37790	0.142
26	6.6	64.8	1.222	99.6	13,799.77	0.64698	-7.49275	0.713

Table 6.7: Regression Parameters Models for the modified resilient modulus model

Sample	Moisture Content (%)	Saturation Ratio (%)	MC / OMC	Relative Density (%)	K ₁	K ₂	K ₃	R ²
1	4.1	27.6	0.759	88.7	<u>1,198.79</u>	<u>0.46083</u>	-0.6827	0.6653
2	3.8	24.8	0.704	87.8	<u>2,048.73</u>	<u>0.44591</u>	-1.5999	0.4455
3	4.0	24.2	0.741	85.9	<u>13,612.66</u>	0.32621	<u>-4.54061</u>	0.7802
4	4.1	32.8	0.759	92.8	<u>940.20</u>	<u>0.57807</u>	-0.2741	0.9516
5	3.4	21.6	0.630	86.7	<u>18,376.06</u>	<u>0.67142</u>	<u>-6.36447</u>	0.8571
6	4.3	33.3	0.796	92.3	<u>5,990.95</u>	0.20006	<u>-3.04297</u>	0.5126
7	4.5	39.7	0.833	95.4	<u>9,403.02</u>	0.209	<u>-3.9676</u>	0.5895
8	4.4	41.4	0.889	96.7	<u>15,606.65</u>	<u>0.56131</u>	<u>-4.74990</u>	0.8909
9	4.3	37.7	0.815	95.1	<u>6,708.22</u>	0.31809	<u>-3.57823</u>	0.3775
10	4.5	35.3	0.833	92.8	<u>18,850.13</u>	0.69662	<u>-5.71546</u>	0.8564
11	4.8	43.7	0.889	96.3	<u>4,863.77</u>	<u>0.6556</u>	<u>-4.07211</u>	0.4465
12	5.1	41.3	0.944	94.0	<u>3,232.05</u>	0.23178	-2.1637	0.2182
13	5.0	44.7	0.926	96.1	<u>4,202.55</u>	<u>0.43249</u>	<u>-2.54971</u>	0.3995
14	5.2	35.6	0.963	90.1	<u>1,985.42</u>	<u>0.39452</u>	<u>-1.04965</u>	0.7215
15	5.5	39.7	1.019	91.6	<u>9,356.51</u>	0.3942	<u>-4.78418</u>	0.6080
16	5.5	48.4	1.019	96.2	<u>17,611.90</u>	<u>0.61907</u>	<u>-6.23714</u>	0.8506
17	5.3	40.9	0.981	93.1	<u>3,247.46</u>	<u>0.68961</u>	<u>-3.41805</u>	0.3740
18	5.3	34.0	0.981	88.6	<u>14,383.41</u>	<u>0.69367</u>	<u>-5.69544</u>	0.8357
19	5.7	50.5	1.056	96.6	<u>3,929.25</u>	0.30786	<u>-2.55388</u>	0.3034
20	5.9	53.0	1.093	97.0	<u>9,181.00</u>	<u>1.17641</u>	<u>-5.91038</u>	0.5008
21	5.9	42.2	1.093	91.8	<u>1,356.61</u>	<u>0.40962</u>	-0.5086	0.8709
22	6.1	50.1	1.130	95.3	<u>5,489.25</u>	0.33863	<u>-3.0042</u>	0.4301
23	6.2	40.6	1.148	89.9	<u>14,258.58</u>	0.67206	<u>-5.1051</u>	0.8294
24	6.5	48.3	1.204	93.2	<u>4,564.63</u>	0.30359	<u>-2.59018</u>	0.3955
25	6.2	35.2	1.148	86.1	<u>2,967.79</u>	0.18287	-1.2424	0.1407
26	6.6	64.8	1.222	99.6	<u>9,780.55</u>	0.37837	<u>-4.46281</u>	0.6613

6.2 Tests Matrix of D-P Cap Model

From the discussion in Section 5.2.1, the laboratory tests needed to be performed to collect the parameters are summarized as Table 6.8 as follows, all the other parameters are obtained from the procedure introduced in Section 5.3. The results of tests conducted in this section are shown in Section 6.3?.

Table 6.8: Test Matrix of D-P Cap model

Sections	Parameters	Tests Performed
Ultimate Failure Surface	α	IDT, SWCC, CU-Triaxial
	k	IDT, SWCC, CU-Triaxial
Elastic and Plastic Behavior	E	UCS
	A_e	Atterberg Limit, Specific Gravity
	A_t	Atterberg Limit, Specific Gravity
	v	Atterberg Limit
Cap	R	IDT, SWCC, CU-Triaxial
	X_a	IDT, SWCC, CU-Triaxial

6.3 Tests Performed to Determine Parameters of D-P Cap model

In this section, the tests performed on CRREL soils are presented. The method applied for the testes are based on ASTM standards. All the parameters of D-P Cap model can be calculated from the tested results.

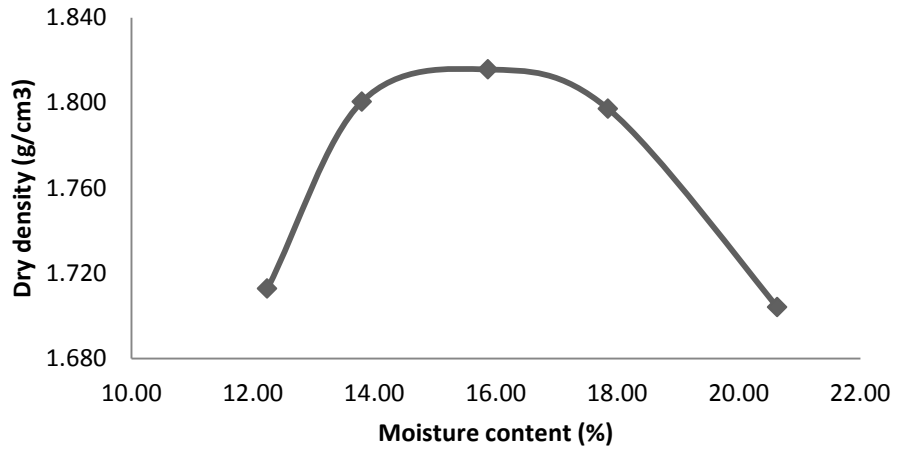
6.3.1 Standard Proctor Compaction Test

The standard proctor compaction test has been performed on all CRREL soils (Type A-6, A-4 and A-7-5). The test method is based from ASTM D698-12. “*Standard Test Methods for Laboratory Compaction Characteristics of Soil Using Standard Effort (12 400 ft-lbf/ft³ (600 kN-m/m³))*”. Optimum moisture content (OMC) and maximum dry density (MDD) of these four soils were obtained and applied to compact specimens for all tests performed.

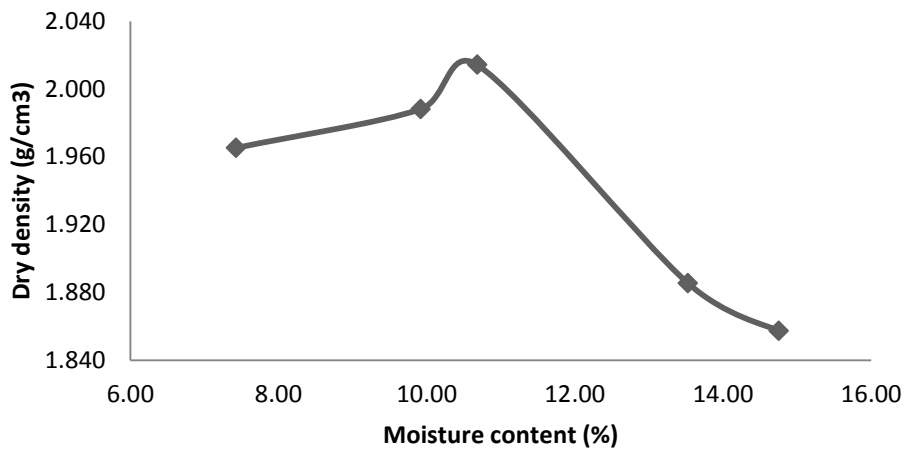
The OMC and MDD values obtained are listed in Table 6.9. The curves of water content vs. dry density are plotted in Figure 6.11.

Table 6.9: OMC & MDD values of CRREL soils

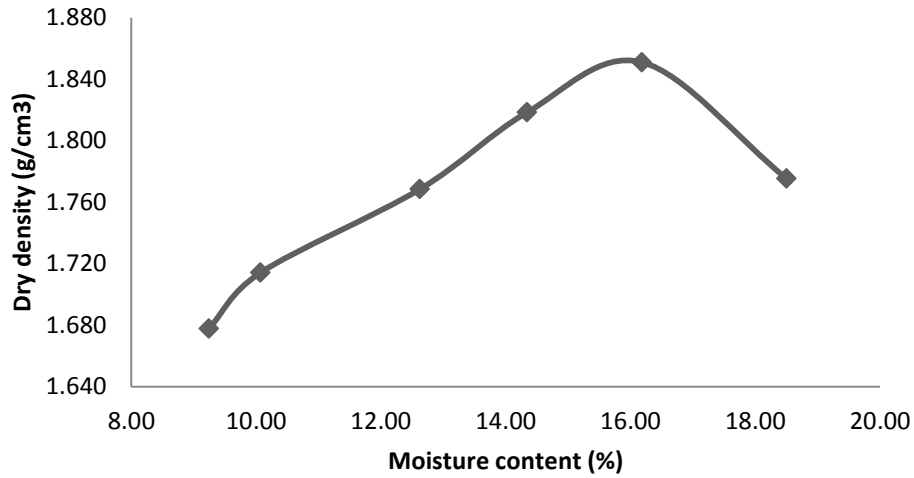
Soil Type	OMC (%)	MDD (g/cm ³)
A-6	15.87	1.816
A-4	10.68	2.014
A-7-5	16.18	1.851



(a)



(b)



(c)

Figure 6.11: MC-DD curves of CRREL soils

(a) A-4; (b) A-6; (c) A-75

6.3.2 Atterberg Limits (LL and PL), and Specific Gravity (Gs) Tests

The Atterberg limits and specific gravity are needed to plot the soil water characteristic curve (SWCC), as well as to calculate the Poisson's ratio and the parameters of D-P Cap model. In order to obtain these parameters tests were conducted according to ASTM D4318-10 “*Standard Test Methods for Liquid Limit, Plastic Limit, and Plasticity Index of Soils*” and ASTM D854-14 “*Standard Test Methods for Specific Gravity of Soil Solids by Water Pycnometer*”

The test results are listed in Table 6.10 as follows:

Table 6.10: Atterberg limits and specific gravity

Soil Type	LL	PL	Gs
A-6	33	18	2.70
A-4	28	20	2.72
A-7-5	55	34	2.72

6.3.3 Soil Water Characteristic Curve (SWCC) Test

In order to calculate the friction angle of soils using the simple procedure introduced in section 5.4, the suction stress for specimens at specific water content is needed to be obtained.

WP-4 Dewpoint PotentiaMeter device (Figure 6.12) was applied in these tests to obtain the matric suction at different moisture contents. WP-4 uses the chilled-mirror dew point technique to measure the water potential of a sample, with the range from 0-80 MPa. It only takes 5-20 minutes to measure matric suction by using WP-4, which is significantly faster than the traditional suction measure methods. The samples were oven-dried for another 12 hours to obtain the actual water content, then the plots of matric suction vs. degree of saturation could be obtained.



Figure 6.12: WP-4 Dewpoint PotentiaMeter device and specimens tested

In order to control the density of the specimens, the 4 types of soils were compacted as samples for Indirect Tensile Strength (IDT) test with their optimum moisture content and maximum dry density. Then the IDT samples were cut into small disc-like pieces with blade and shaped to fit the can for suction tests (Figure 6.13-a). The samples were shaped as big as possible for convenience to control the moisture content, the geometry of the samples should be disc-like to avoid contamination of testing device, also the disc-like shape benefits the equilibrium during moisture controlling.

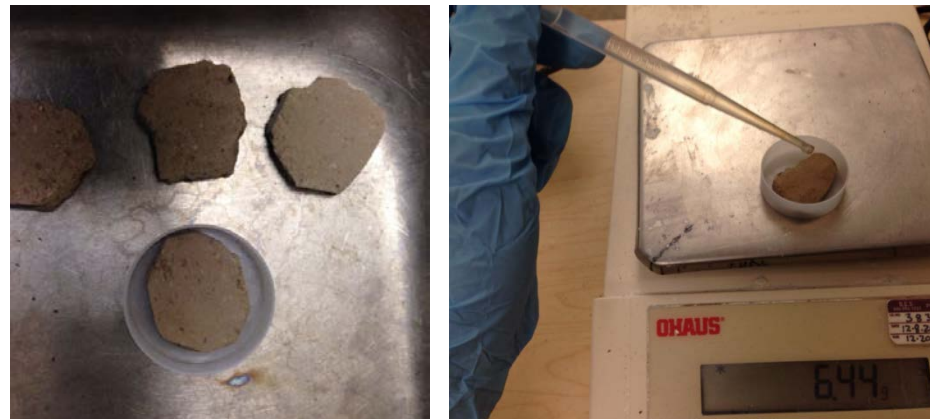


Figure 6.13: (a) Specimens for suction test; (b) Moisture control

The suction samples were dried in oven at 110°C for overnight and measured the dry weight, a dropper pipette was used to add water to reach a desired moisture content of the samples (Figure 6.13-b), which is estimated by Equation (6.3)

$$\omega' = S' \left(\frac{1}{\rho_d} - \frac{1}{G_s} \right) \quad (6.3)$$

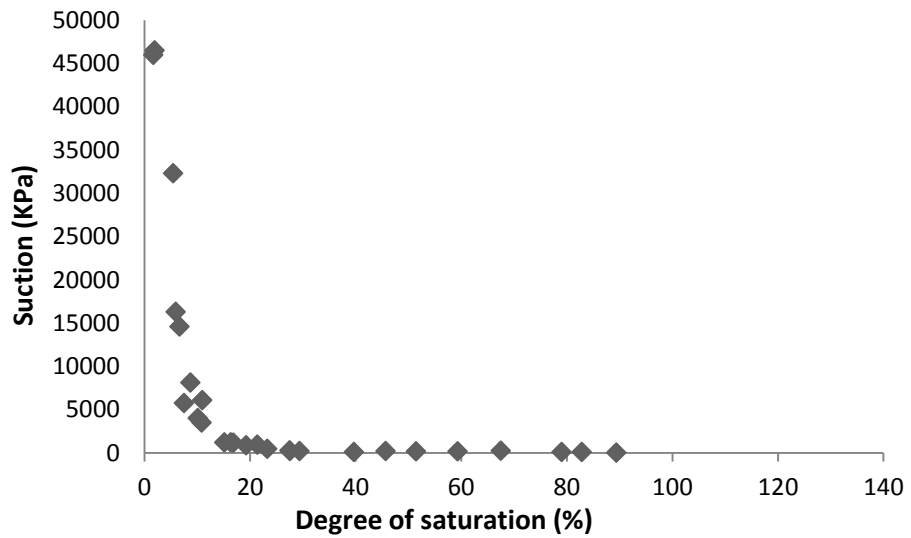
where ω' = the desired moisture content of the sample;

S' = the desired degree of saturation of the sample;

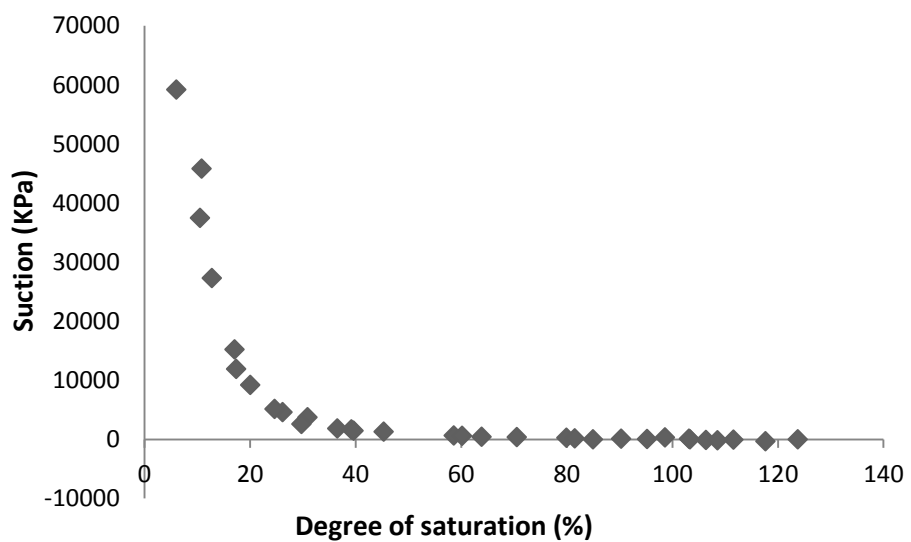
ρ_d and G_s = dry density and specific gravity of the sample;

All the samples were sealed in plastic retaining cans to reach equilibrium for more than 24 hours before tested as shown in Figure 6.13.

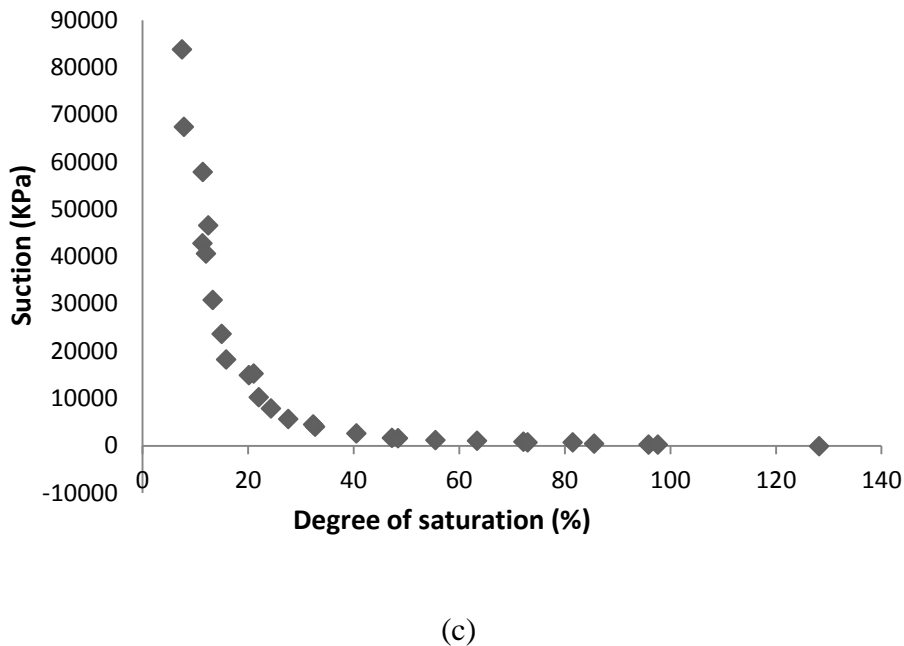
The plot of the variation of matric suction with degree of saturation for the CRREL soils are as shown in Fig. 6.14. The data used in developing these curves can be found in Appendix D.



(a)



(b)



(c)

Figure 6.14: Matric suction vs. degree of saturation

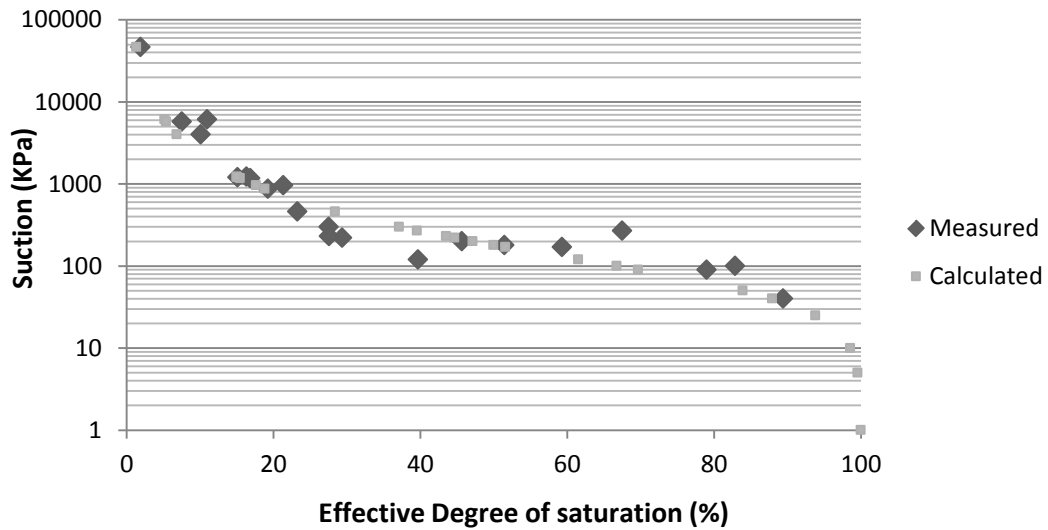
(a) A-4; (b) A-6; (c) A-7-5 soil types

From the curve of the relationship between suction and degree of saturation, the residual degree of saturation S_r can be obtained by following the procedure used by Kim and Saure⁽¹⁰¹⁾. Using S_r in Eq. (5.27) and using mathematical solver module in Excel software, the parameters α and n can be obtained by curve fitting. The results are shown in Table 6.11.

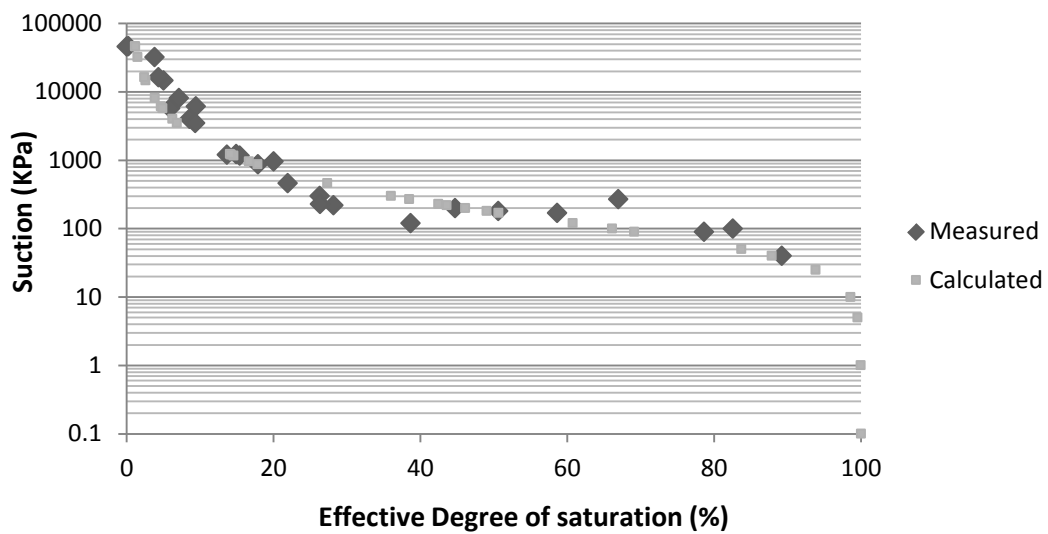
Table 6.11: Obtained Parameters of SWCC

Soil	A-4	A-6	A-7-5
ρ_d	2.014	1.816	1.851
G_s	2.72	2.70	2.72
S_r	1.87	6.00	7.46
α	0.013976	0.003475	0.001597
n	1.688322	1.571234	1.705158

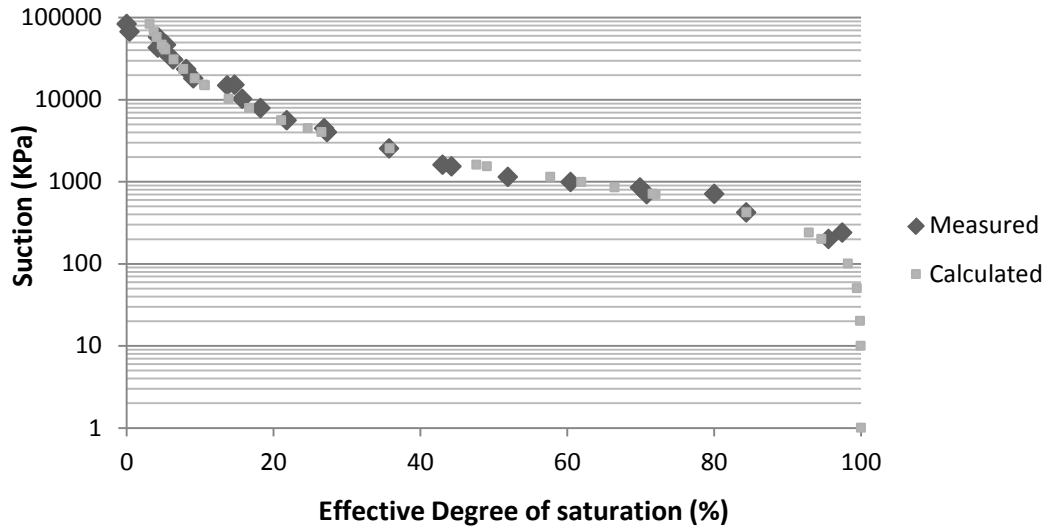
The effective degree of saturation can be calculated from Eq. (5.25). The comparison between SWCC obtained from curve fitting and tests are plotted in Figure 6.15.



(a)



(b)

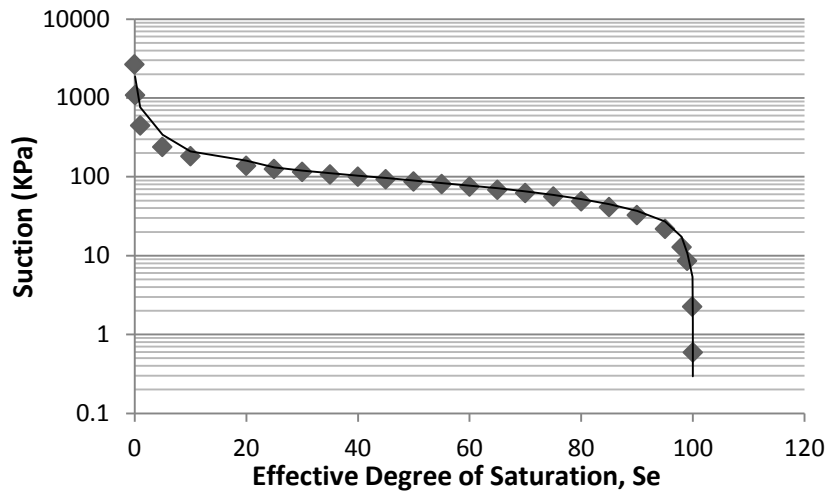


(c)

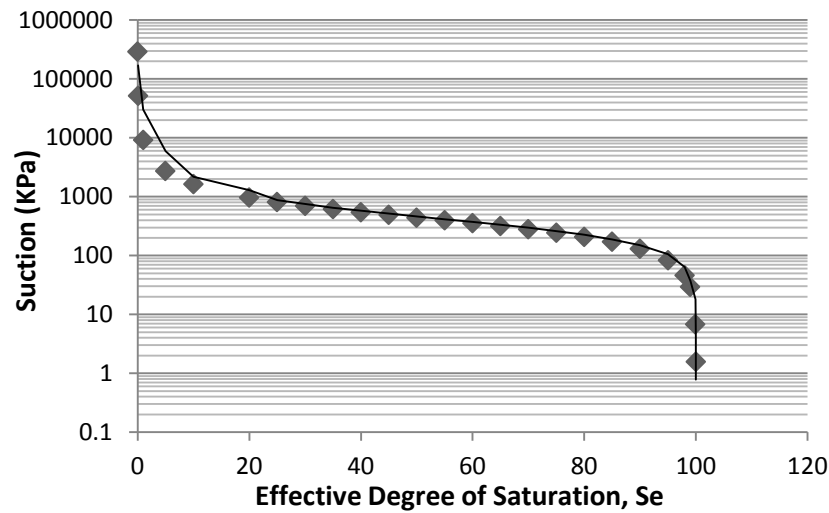
Figure 6.15: Soil water characteristic curves

(a) A-4; (b) A-6; (c) A-7-5;

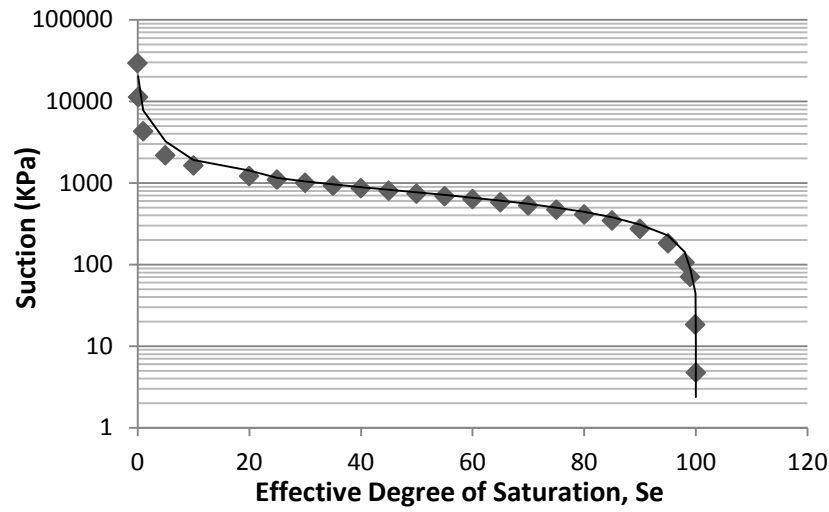
The soil suction characteristic curve (SSCC) can be obtained from SWCC and is shown in Figure 6.16.



(a)



(b)



(c)

Figure 6.16: Soil suction characteristic curves for CRREL soils

(a) A-4; (b) A-6; (c) A-7-5

6.3.4 Indirect Tensile Strength Test (IDT)

Indirect tensile strength tests were applied on all CRREL soils. In order to determine the strength variation with moisture content, samples were dried following the procedure outlined below:

1. The samples were compacted to maximum dry density (OMC) with optimum moisture content and then air-dried to specific moisture content by monitoring the sample weight.
2. A fan was used to accelerate the evaporation of the moisture. The drying process was observed by checking the weight every 30 minutes until the desired value was reached.
3. Once the target weight was reached the samples were sealed tight by using at least four layers of plastic wraps (Figure 6.17). The minimum time required for reaching moisture equilibrium is about six days.



Figure 6.17: Samples for IDT tests

The IDT tests were performed with the GCTS device available at Washington State University. The experiments were conducted as deformation controlled with speed of 1.6 mm/min (Figure 6.18). The actual moisture content of specimens was tested immediately after tests. The failed samples were used in the SWCC tests reported above.



Figure 6.18: Indirect tensile test on GCTS

The theory of effective stress for unsaturated soils considering suction^(86, 102) is

$$\sigma' = (\sigma - u_a) - \sigma^s \quad (6.4)$$

The failure stress state of IDT specimens is given by:

$$\sigma_x = \text{IDT} \quad (6.5)$$

$$\sigma_y = -3.1 \text{ IDT} \quad (6.6)$$

These stresses can be converted to the q-p' space using:

$$\begin{aligned}
q &= \frac{1}{\sqrt{2}} \sqrt{(\delta_1 - \delta_2)^2 + (\delta_1 - \delta_3)^2 + (\delta_2 - \delta_3)^2} \\
&= \frac{1}{\sqrt{2}} \sqrt{\delta_y^2 + (\delta_y - \delta_x)^2 + \delta_x^2}
\end{aligned} \tag{6.8}$$

$$p' = \frac{1}{3}(\delta_1 + \delta_2 + \delta_3) - u_a - \delta^s = \frac{1}{3}(\delta_x + \delta_y) - u_a - \delta^s \tag{6.9}$$

The failure surface in q- p' space is given by:

$$q = M p' + N \tag{6.7}$$

Using the failure surface, the internal friction angle can be derived from:

$$\phi' = \sin^{-1} \left[\frac{3M}{6 + M} \right] \tag{6.10}$$

The corresponding friction angle input in Abaqus can also be expressed as ⁽⁹⁸⁾

$$\beta = \arctan \left(\frac{6 \sin \phi}{3 - \sin \phi} \right) \tag{6.11}$$

where ϕ = friction angle in Mohr-Coulomb model;

β = friction angle input in Drucker-Prager model in Abaqus

For each type of soil, IDT tests were performed on 5 different moisture contents. The results are listed in Table 6.12

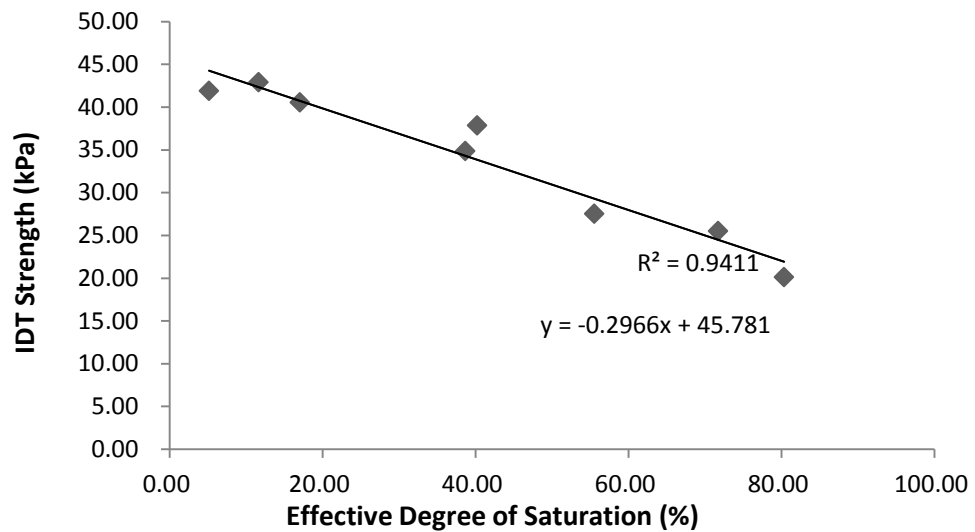
Table 6.12: IDT Test Results

Soil A-4						
w (%)	Load (N)	IDT (kPa)	S (%)	Sr (%)	Se (%)	Suction (kPa)
1.72	173.80	-42.90	13.33	1.87	11.67	1616.17
5.33	153.40	-37.86	41.35	1.87	40.23	251.15
0.89	169.70	-41.88	6.94	1.87	5.17	5290.39
5.14	141.20	-34.85	39.86	1.87	38.71	267.30
2.40	164.30	-40.55	18.62	1.87	17.07	925.98
7.27	111.50	-27.52	56.41	1.87	55.58	143.13
9.31	103.30	-25.50	72.27	1.87	71.75	81.97
10.40	81.50	-20.12	80.73	1.87	80.37	58.39

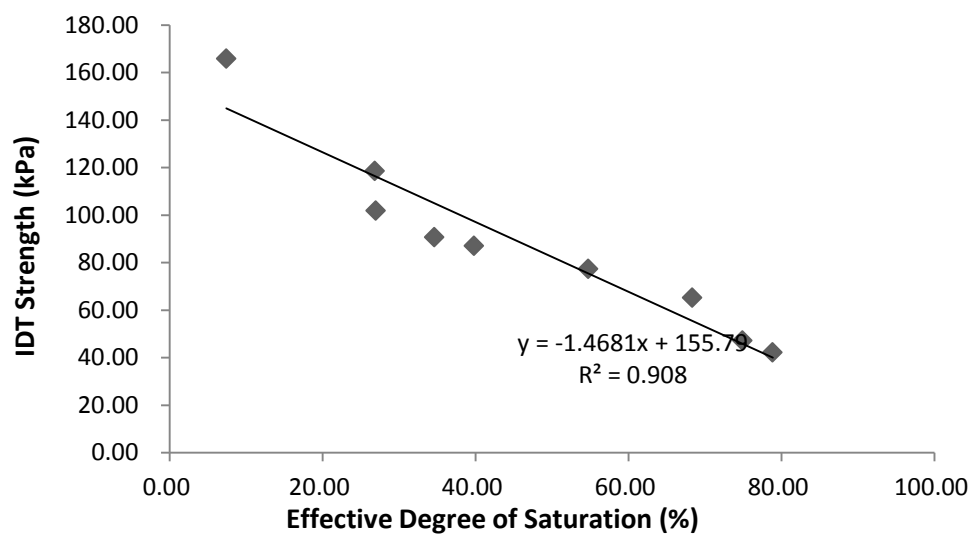
Soil A-6						
w (%)	Load (N)	IDT (kPa)	S (%)	Sr (%)	Se (%)	Suction (kPa)
5.63	480.50	-118.59	31.25	6.00	26.86	2824.06
5.65	412.60	-101.84	31.34	6.00	26.96	2804.85
6.95	367.80	-90.78	38.55	6.00	34.63	1778.18
7.83	352.90	-87.10	43.44	6.00	39.83	1367.56
2.34	671.90	-165.84	12.99	6.00	7.44	27188.13
10.36	313.60	-77.40	57.48	6.00	54.76	721.55
12.66	264.70	-65.33	70.24	6.00	68.35	425.45
13.78	191.40	-47.24	76.43	6.00	74.93	325.26
14.45	171.10	-42.23	80.14	6.00	78.87	273.12

Soil A-75						
w (%)	Load (N)	IDT (kPa)	S (%)	Sr (%)	Se (%)	Suction (kPa)
15.93	247.10	-60.99	92.27	7.46	91.65	267.65
9.76	744.00	-183.63	56.57	7.46	53.06	1333.12
13.77	543.50	-134.14	79.76	7.46	78.13	555.87
14.45	374.70	-92.48	83.74	7.46	82.43	462.05
8.33	764.30	-188.64	48.28	7.46	44.11	1831.42
13.54	422.10	-104.18	78.47	7.46	76.73	587.54
4.90	750.70	-185.28	28.41	7.46	22.64	5063.06
3.23	536.10	-132.32	18.71	7.46	12.16	12377.08
0.99	1187.50	-293.09	5.76	7.46	-1.84	-
1.30	1014.00	-250.27	7.52	7.46	0.07	18854054.91

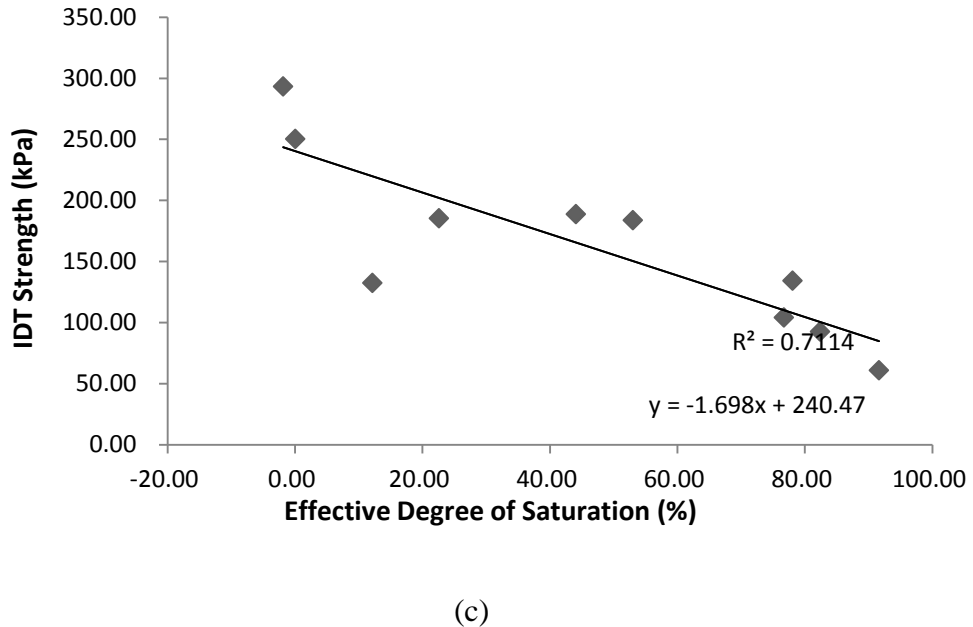
The relationship between effective degree of saturation and IDT strength for the three CRREL soils are shown in Figure 6.19.



(a)



(b)



(c)

Figure 6.19: Relationship between effective degree of saturation and IDT

(a) Soil A-4; (b) Soil A-6; (c) Soil A-75

The Matlab program (Appendix B) also incorporates the calculation procedure of obtaining the internal friction CAP parameter β value (Table 2.2) from IDT test results. The values obtained for the CRREL soils are listed in Table 6.13.

Table 6.13: Internal Friction Angle (For D-P model in Abaqus)

Groups	A-4	A-6	A-7-5
β	36.5	28.1	36.6

6.3.5 Unconfined Compressive Strength Tests (UCS)

Unconfined compressive Strength Tests of CRREL soils (A-4, A-6 and A-7-5) were performed by following ASTM D2166/D2166M-13 “*Standard Test Method for Unconfined Compressive Strength of Cohesive Soil*”.

For each type of CRREL soil, the specimens were compacted at optimum moisture content and maximum dry density. The diameter of specimen is 6.5 inch in height (165.1 mm) and 2.75 inch in diameter (69.85 mm). UCS tests were also conducted using GCTS. The experiments were deformation controlled with speed of 1.6mm/min in axial direction (Figure 6.20).



Figure 6.20: UCS sample and GCTS device

The typical stress strain response is shown in Figure 6.21. The corresponding stress-strain relationships for all soils are presented in Appendix E.

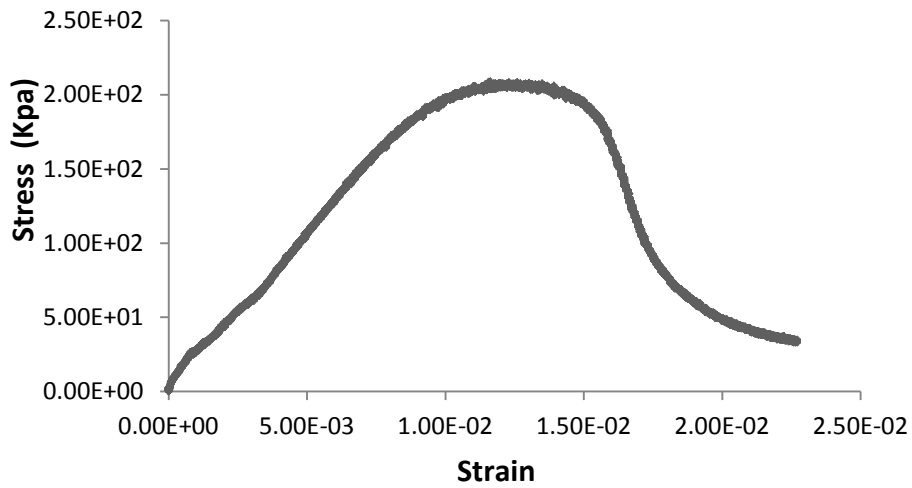


Figure 6.21: Strain-Stress response (A-4 with 10.66% moisture content)

In order to investigate the relationship between moisture content and Young's Modulus E, samples with 5 moisture contents were prepared by using the same method as in the samples for IDT tests above.

All the UCS test results of CRREL soils are shown in Table 6.14.

Table 6.14: UCS test results for CRREL soils

Soil Type	w (%)	Se (%)	Suction (kPa)	E (MPa)	UCS (kPa)	Strain at failure
A-4	10.53	80.56	57.88	20.3	1.51E+02	1.16E-02
	6.59	47.53	189.98	49.0	3.26E+02	9.93E-03
	2.96	16.39	983.42	93.5	6.38E+02	8.63E-03
	5.35	40.39	249.49	66.2	3.63E+02	7.89E-03
	8.12	62.30	113.89	45.5	2.65E+02	9.71E-03
A-6	16.80	92.67	113.84	13.6	1.54E+02	2.60E-02

	8.72	43.88	1135.13	111.0	6.50E+02	1.28E-02
	4.17	15.53	7472.19	204.1	1.04E+03	8.85E-03
	9.48	49.55	890.21	45.1	5.41E+02	1.38E-02
	5.02	23.24	3660.10	197	7.30E+02	5.32E-03
A-75	16.46	94.58	201.11	19.5	2.52E+02	3.22E-02
	9.54	47.09	1642.18	134.2	9.63E+02	1.40E-02
	4.04	8.32	21267.94	97.1	1.06E+03	1.35E-02
	9.65	52.35	1365.83	101.0	9.27E+02	1.15E-02
	5.04	23.49	4796.23	127.4	9.87E+02	7.59E-03

The relationships between effective degree of saturation and elastic modulus of the three CRREL soils were plotted in Figure 6.22; the value of elastic modulus is larger when the sample has a low moisture content. The relationship between UCS value and moisture content is shown in Figure 6.23, it can be seen that the UCS value is higher with a low moisture content. The uniaxial failure strain is higher for soils with a high moisture content (Figure 6.24).

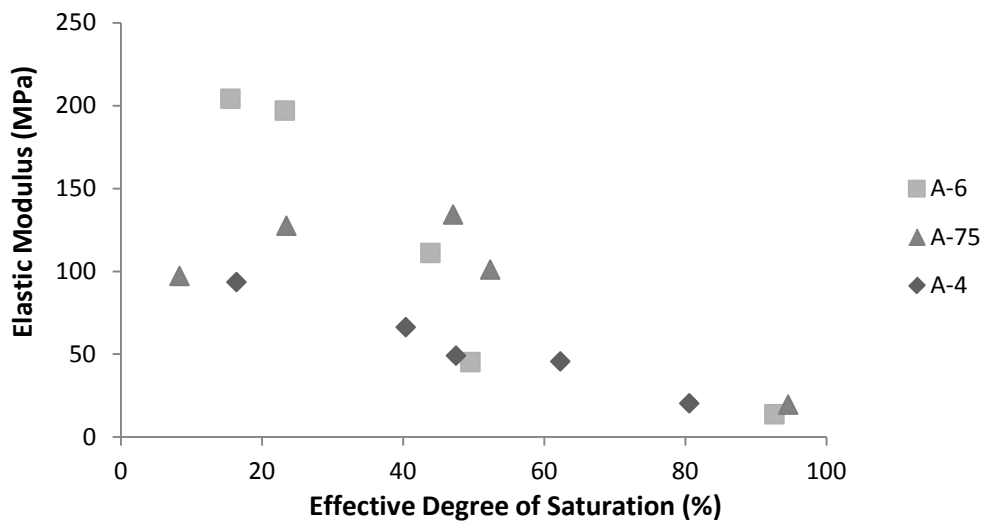


Figure 6.22: Relationship between effective degree of saturation and elastic modulus

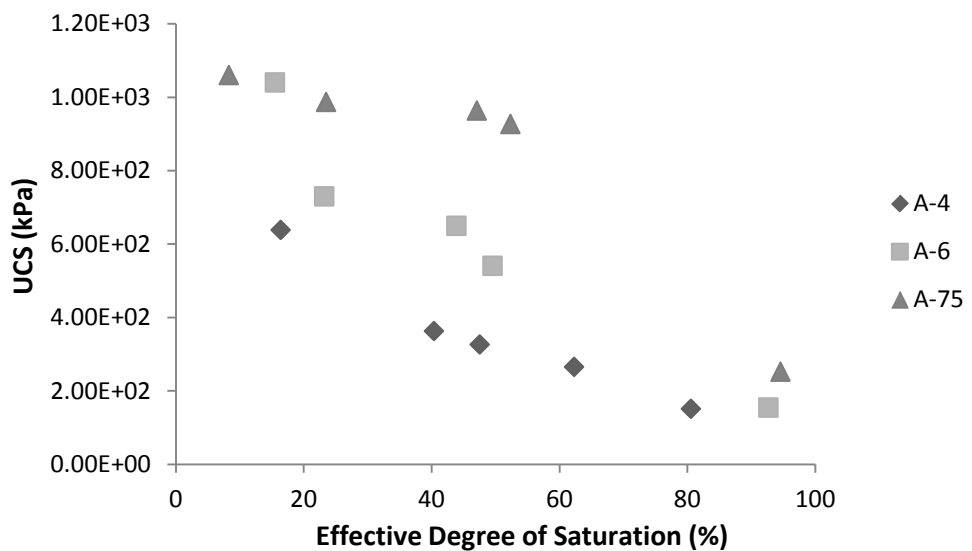


Figure 6.23: Relationship between effective degree of saturation and UCS

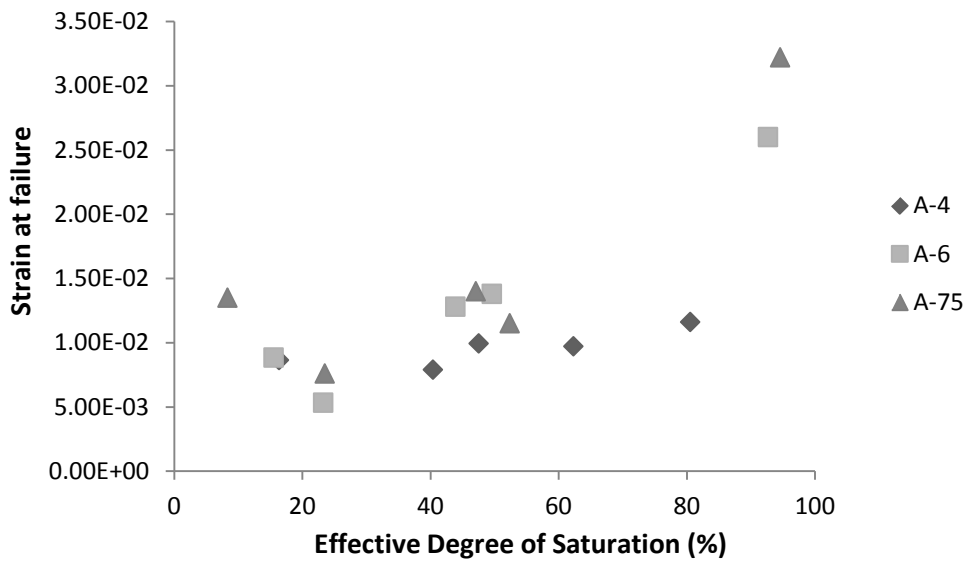


Figure 6.24: Relationship between effective saturation degree and failure strain

6.3.6 Triaxial Test

In order to obtain the parameter to calculate the aspect ratio of cap surface, Consolidated-Undrained (C-U) Triaxial Test is required for each soil. The specimens for CU-Triaxial test are in the same dimensions and properties with the ones tested in UCS. The test method followed ASTM D4767-11 “Standard Test Method for Consolidated Undrained Triaxial Compression Test for Cohesive Soils”. The device used in this test are shown in Figure 6.25.

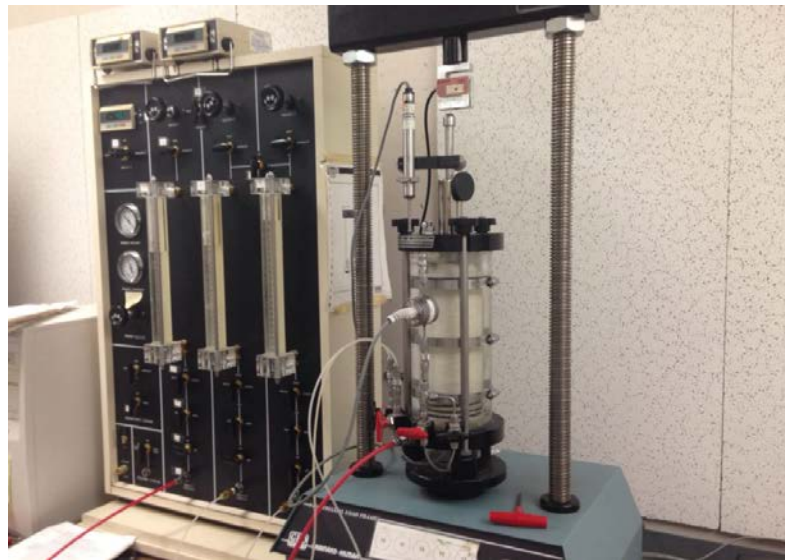


Figure 6.25: Test device for CU-Triaxial

The triaxial specimens were saturated until a B value ($\Delta\sigma_3/\Delta u$) above 0.92 was achieved. It took about 2 to 4 weeks for the saturation period of soil A-6 and A-7-5. The test was deformation controlled at 1.3mm/sec.

Since the samples are saturated and consolidated, CU Triaxial tests cannot be used to determine the Cap surface parameters for unsaturated conditions, the procedure needed to be modified.

The samples for the unsaturated Triaxial Test were prepared as same for CU Triaxial tests. After the samples were compacted (OMC and MDD), their moisture content was adjusted so as to perform tests at thus different degrees of saturation. There are two ways to control the moisture of the unsaturated triaxial samples (a) For the target moisture content lower than OMC, the samples could be air-dried under room relative humidity and temperature by using different drying time and monitoring the loss of weight; (b) For the target moisture content higher than

OMC, the samples could be placed in CU Triaxial device then the water will be added by the volumetric device, the actual moisture content will be measured from the failed sample. For this case, the mass of water needed should be determined by calculation. Regardless of the method used, sufficient time must be allowed to ensure samples achieve inner moisture equilibrium..

For the tests reported here, the moisture contents were controlled by air-drying. A fan was used to accelerate the speed of moisture evaporation. For each type of soils, 8 to 10 groups of samples were made and dried from 4 hours to 7 days. After the drying, the samples were sealed with plastic wraps for 10 days to ensure moisture equilibrium was achieved.

The test procedure followed ASTM D4767-11 “Standard Test Method for Consolidated Undrained Triaxial Compression Test for Cohesive Soils” but without the part of saturation. The initial and final position of Cap surface of three CRREL soils under different moisture contents were calculated by using the results from triaxial tests. The parameters obtained for the different soils are listed in Table 6.15-6.17.

Table 6.15: Cap position of soil Type A-6

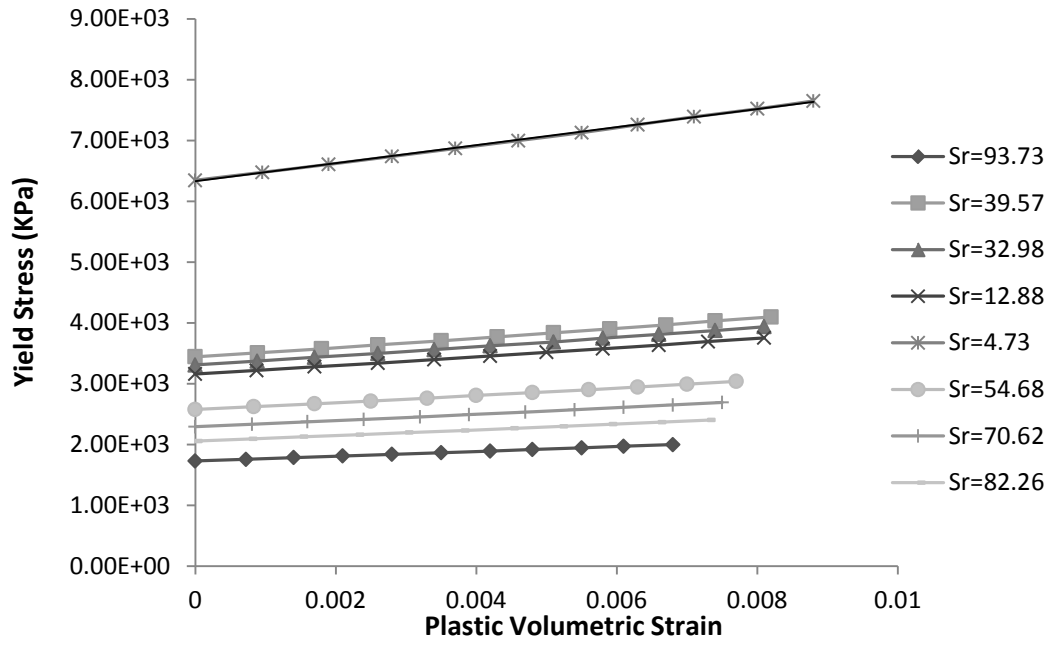
Test Case	Degree of sat.	Suction	sigma1	sigma3	sigmaV0	CapAspect	Xa	Xb
A-6-1	103.78	0.00	204.50	100	100	4.37	1067.60	1138.2
A-6-2	53.41	858.39	700.88	100	100	5.66	3306.10	3916.6
A-6-3	72.49	386.75	546.74	100	100	5.49	2597.80	3047.2
A-6-4	12.76	28865.20	1325.26	100	100	5.99	6234.50	7501.1
A-6-5	5.60	-	1252.11	100	100	5.96	5883.60	7071.9
A-6-6	22.94	5744.31	1142.39	100	100	5.93	5373.90	6448.7
A-6-7	45.89	1210.96	732.23	100	100	5.69	3452.20	4095.9
A-6-8	92.27	123.95	512.78	100	100	5.44	2444.10	2856.5

Table 6.16: Cap position of soil Type A-4

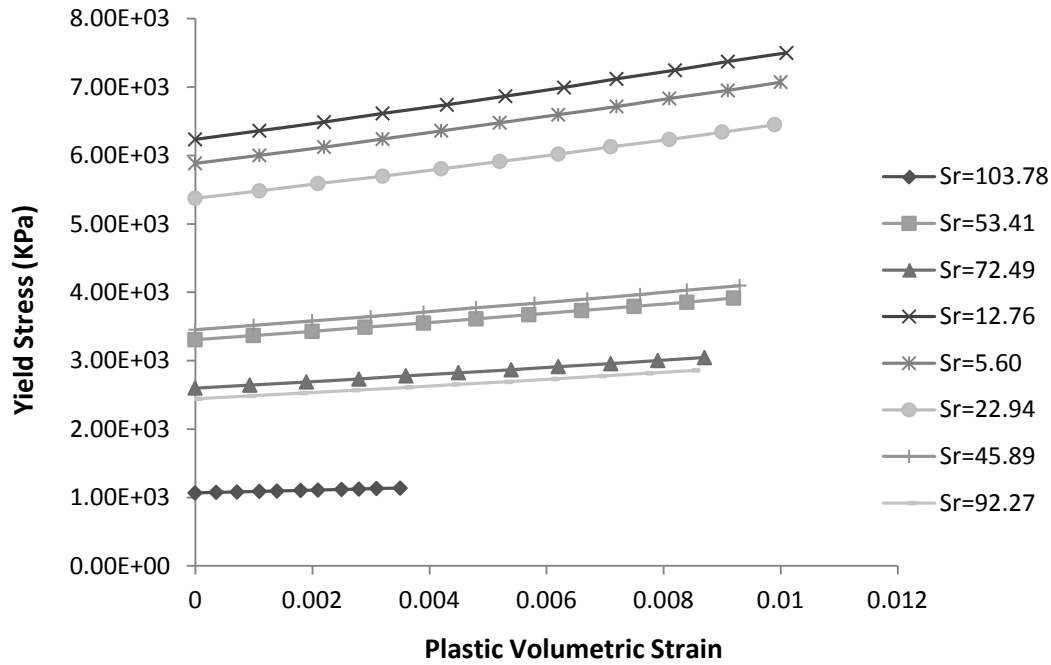
Sample	Degree of sat.	Suction	sigma1	sigma3	sigmaV0	CapAspect	Xa	Xb
A-4-1	93.73	25.55	439.63	100	100	4.36	1730.3	1999.4
A-4-2	39.57	270.58	886.36	100	100	4.80	3442.4	4099.1
A-4-3	32.98	366.15	852.40	100	100	4.78	3310.0	3937.1
A-4-4	12.88	1712.34	813.21	100	100	4.76	3159.9	3753.3
A-4-5	4.73	12150.13	1633.54	100	100	5.01	6347.0	7651.5
A-4-6	54.68	159.98	661.69	100	100	4.65	2576.6	3038.7
A-4-7	70.62	89.04	588.54	100	100	4.57	2293.7	2692.0
A-4-8	82.26	54.93	525.84	100	100	4.50	2057.0	2401.3

Table 6.17: Cap position of soil Type A-75

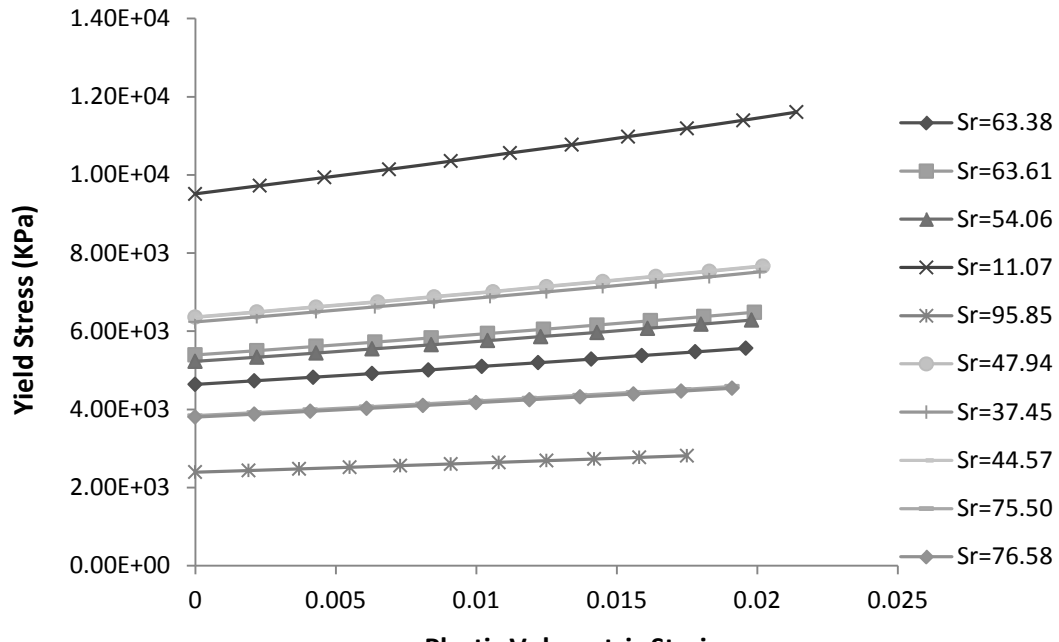
Sample	Degree of sat.	Suction	sigma1	sigma3	sigmaV0	CapAspect	Xa	Xb
A-75-1	63.38	1041.02	1194.64	100	100	4.92	4640.2	5564.4
A-75-2	63.61	1032.37	1387.96	100	100	4.97	5394.7	6487.1
A-75-3	54.06	1463.59	1346.16	100	100	4.96	5231.1	6287.1
A-75-4	11.07	62383.43	2432.96	22	22	5.24	9516.5	11608.0
A-75-5	95.85	179.29	614.66	100	100	4.60	2394.3	2815.4
A-75-6	47.94	2159.04	1636.15	100	100	5.01	6356.7	7663.4
A-75-7	37.45	3597.30	1604.80	100	100	5.01	6239.9	7520.5
A-75-8	44.57	2386.06	1638.76	100	100	5.01	6366.4	7675.3
A-75-9	75.50	685.07	990.86	100	100	4.84	3842.2	4588.5
A-75-10	76.58	648.71	980.41	100	100	4.84	3804.5	4542.3



(a)



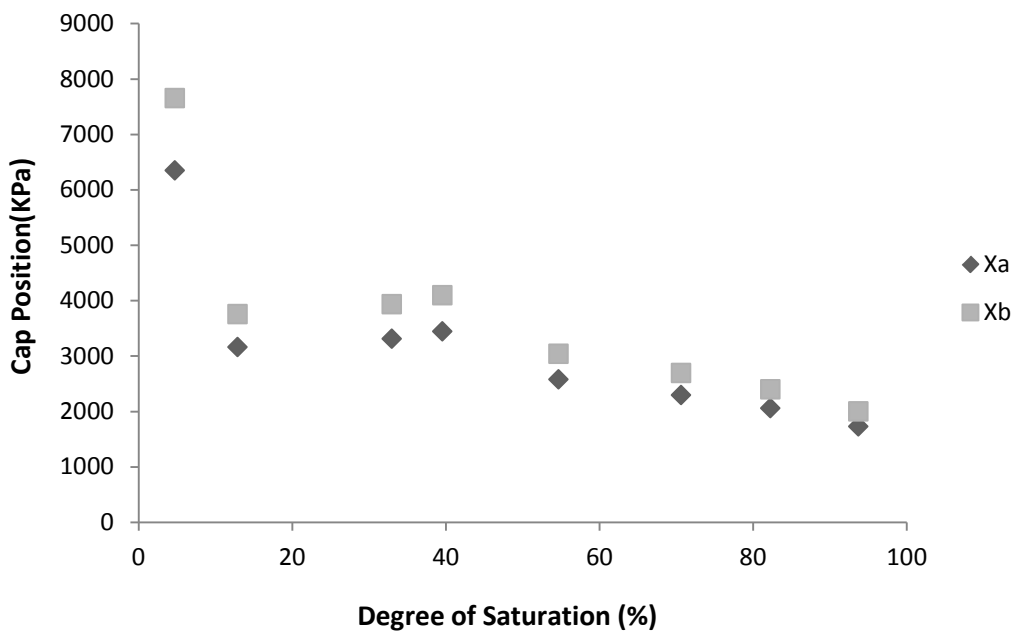
(b)



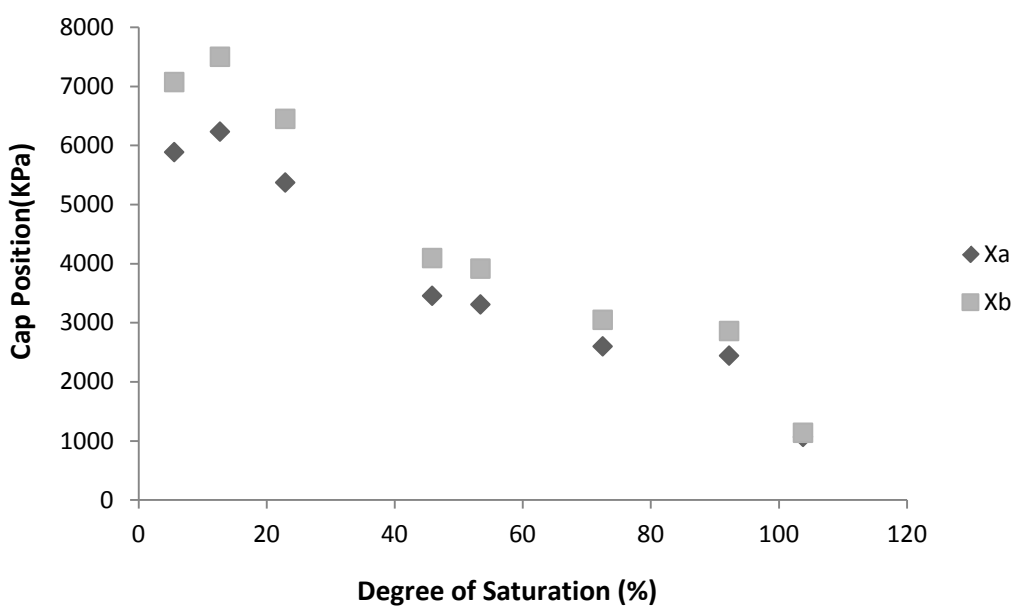
(c)

Figure 6.26: Plot of plastic volumetric strain vs. yield stress

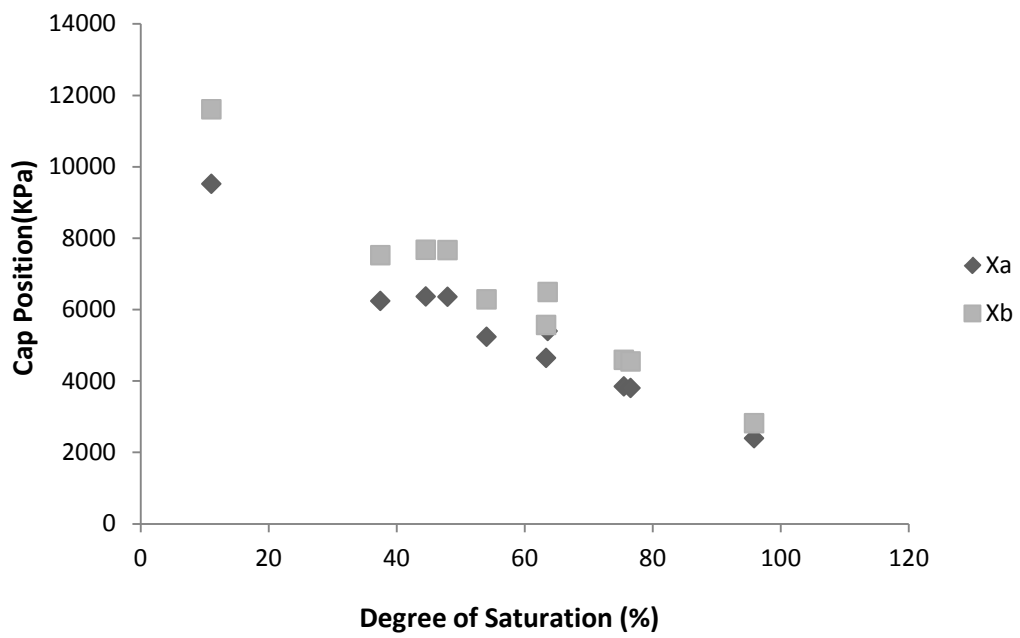
(a) Soil A-4; (b) Soil A-6; (c) Soil A-75



(a)



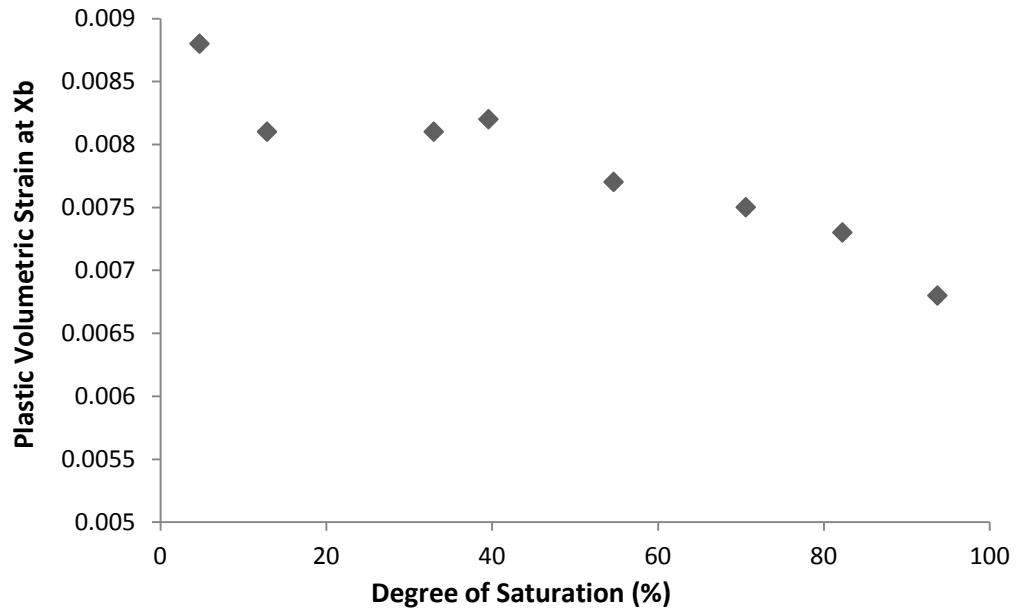
(b)



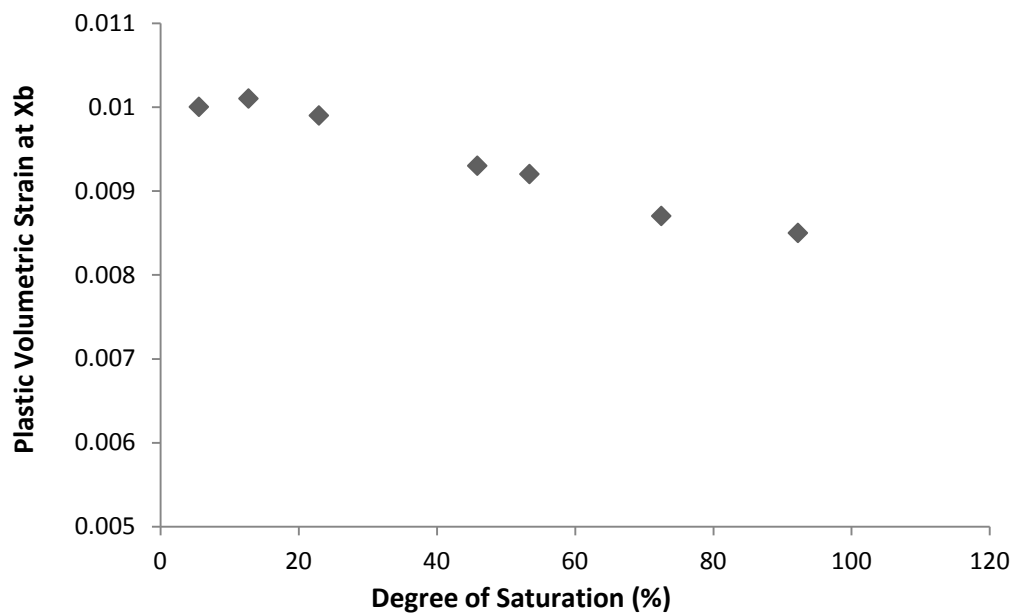
(c)

Figure 6.27: Plot of degree of saturation vs. Cap position

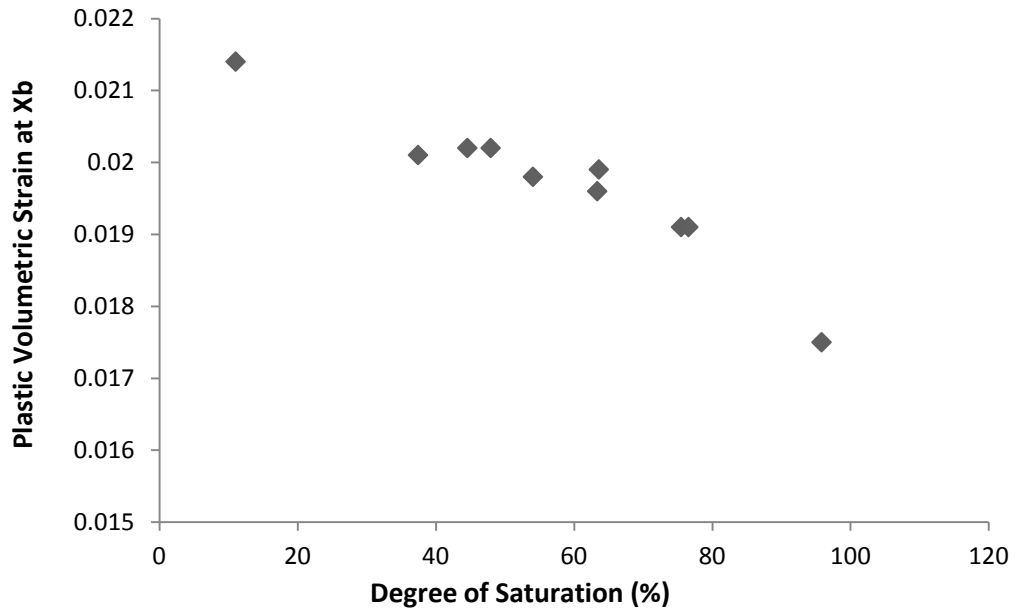
(a) Soil A-4; (b) Soil A-6; (c) Soil A-75



(a)



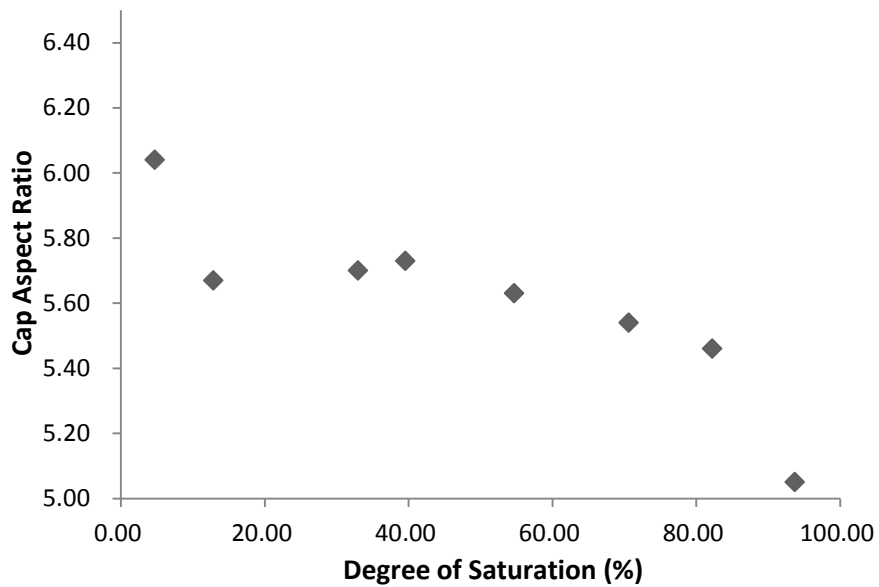
(b)



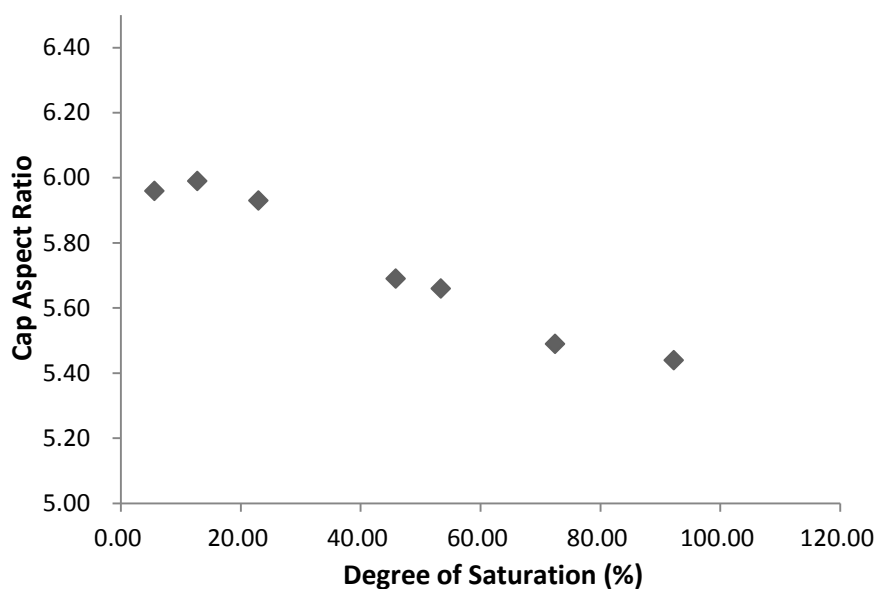
(c)

Figure 6.28: Plot of degree of saturation vs. plastic volumetric strain of Xb

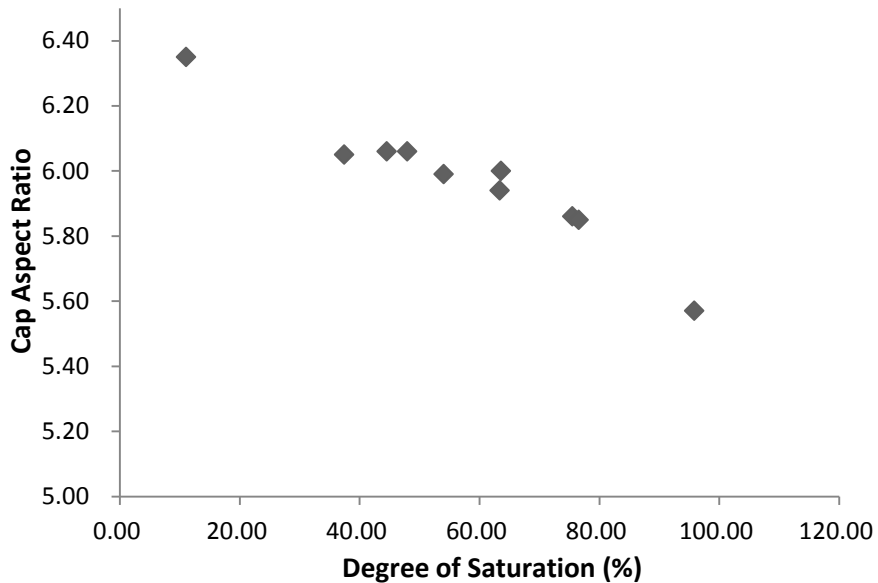
(a) Soil A-4; (b) Soil A-6; (c) Soil A-75



(a)



(b)



(c)

Figure 6.29: Relationship between degree of saturation and Cap Aspect Ratio

(a) Type A-4; (b) Type A-6; (c) Type A-75

The relationships between plastic volumetric strain and yield stress of CRREL soils at different degrees of saturation is shown in Figure 6.26, it can be seen that with a lower moisture content the yield stress is higher at the same volumetric strain. Figure 6.27 shows the relationship between degree of saturation and Cap position of CRREL soils, it is shown that the Cap position is lower when the sample has a high degree of saturation. Figure 6.28 shows the relationship between degree of saturation and Cap position at failure, similar to the relationship in Figure 6.27, the failure Cap position also is smaller when the CRREL soil has a high moisture content. Figure 6.29 shows the variation of Cap aspect ratio along the degree of saturation, the aspect ratio of the Cap surface is smaller when the CRREL soil has a high degree of saturation.

CHAPTER SEVEN

3D FE MODEL ANALYSES

7.1 Introduction

This chapter presents the details the 3D finite element model developed in Abaqus to simulate response of pavements under vehicular load on the CRREL soils. They include models relating to tire geometry, loading and boundary conditions, material properties and mesh arrangement.

The FE model was first verified on some of the observed CRREL test data. It was then used to evaluate the influence of different factors in pavement subgrade deformation, such as asphalt and base properties, and saturation level.

7.2 Development of 3-D Finite Element Model

Figures 7.1 and 7.2 show the test cell plan and side view, and transverse cross-section, respectively. There are six test windows in each cell. FE models were developed to simulate the static loading at test windows 5 and 6 that are located at the center and side of the test cell, respectively. Note that only a single dual tire acts at the center of the test window. The configuration of the dual tire is as shown in Figure 7.3. The dual tire has two 223 mm width wheels with 113 mm separation interval. The contact length of the tire along wheel path direction is assumed to be 0.305 m.

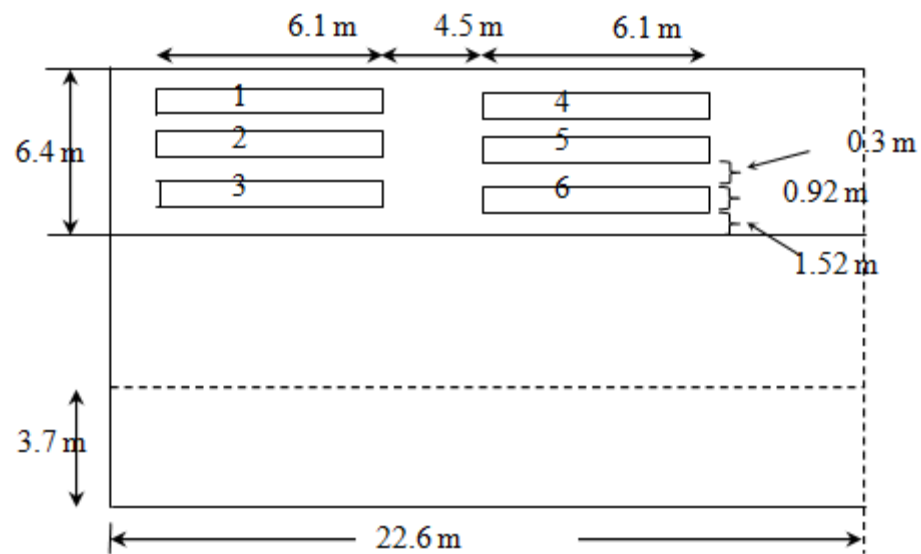


Figure 7.1: Plan and side view of the test cell (modified from Cortez ⁽¹⁷⁾).

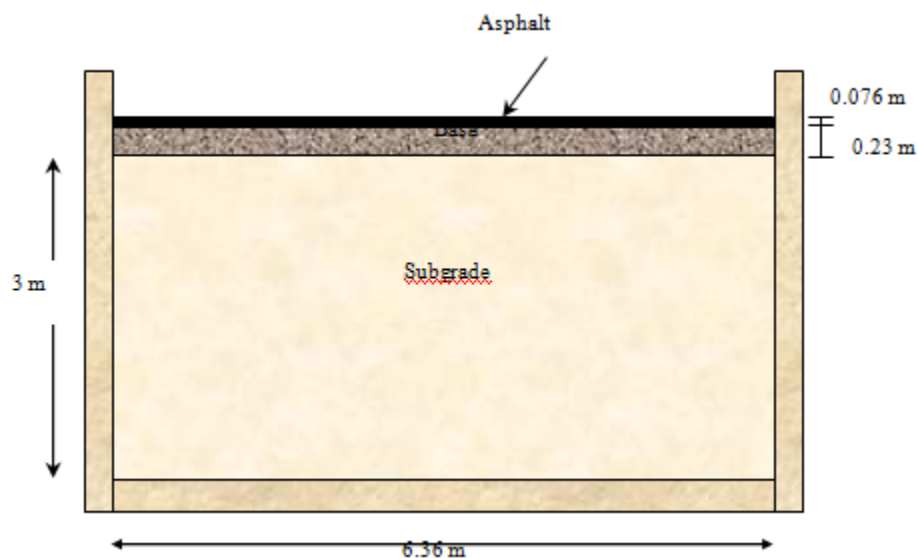


Figure 7.2: Transverse cross section of test cell (modified from Cortez ⁽¹⁷⁾)

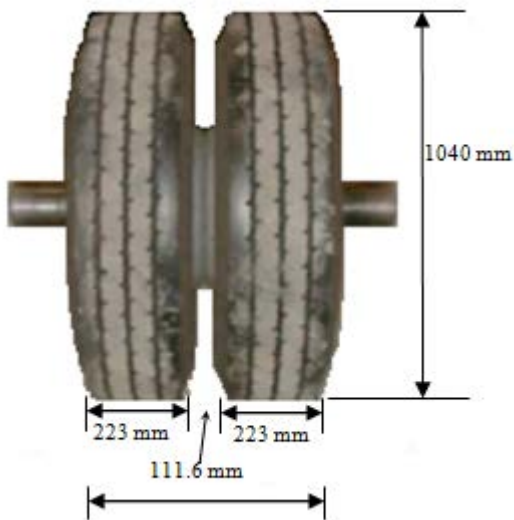


Figure 7.3: Dual tire assembly dimension (modified from Cortez ⁽¹⁷⁾)

Two sets of FE models were developed. The first set of FE models was developed to simulate the static wheel load at the center of test window 5 and window 6. It is assumed that the loading effect is negligible at 3.2 m from center of the wheel path along the longitudinal direction of the tire load. In addition, only one quarter of the loading is modeled due to the symmetric nature of the load, as shown in Figure 7.4. Point A1 is the center point of the tire, as shown in the plan view in Figure 7.1. The figure also shows the longitudinal and transverse directions of wheel load as x and y, respectively.

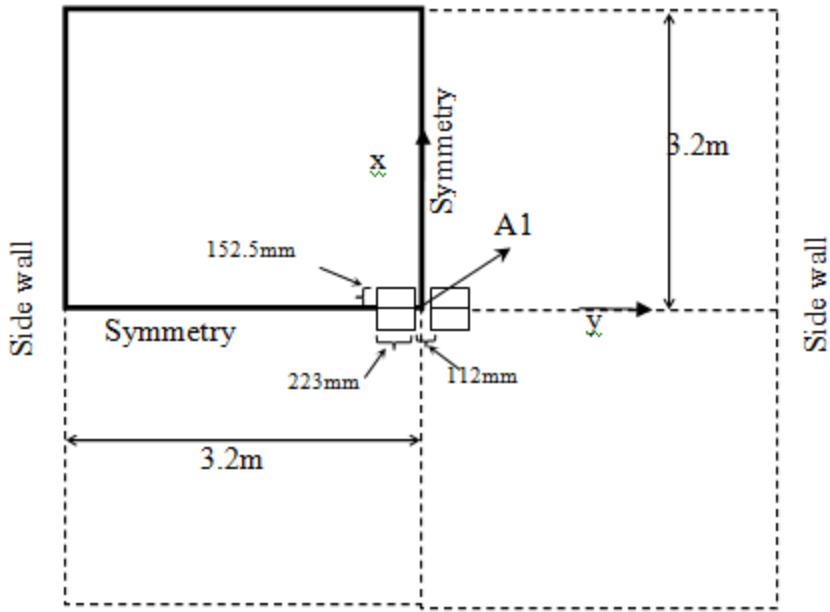


Figure 7.4: Plane geometry of 3D quarter symmetric model

Figure 7.5 shows the partitions, loading, and boundary conditions. The three segments (asphalt, base, and subgrade) of the test cell were created using the partition technique. It is assumed that there is no separation between pavement layers^(18 and 46).

Kinematic boundary conditions were used for modeling the pavement structure (See references 18, 46, 90 and 91). Horizontal movement along vertical boundaries and both the vertical and horizontal movement along the bottom boundary are restrained by the use of roller and pin supports, respectively.

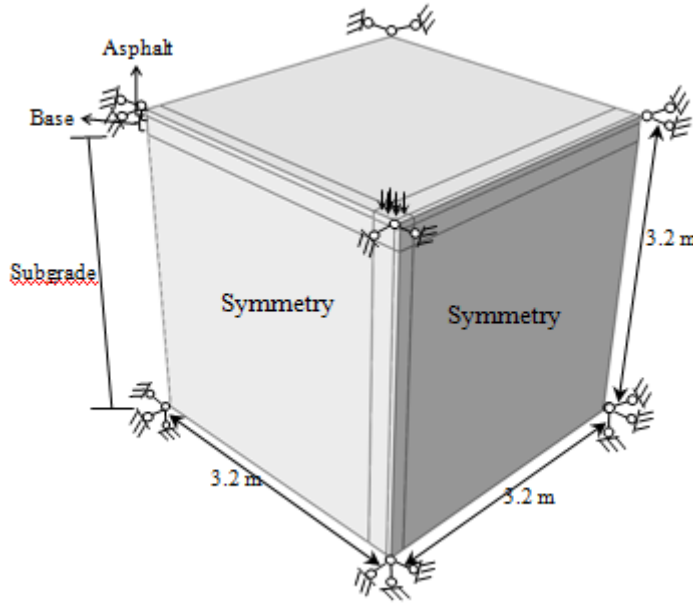


Figure 7.5: Load and boundary conditions of 3D quarter symmetric model.

A sensitivity analysis using elastic properties of the material was first carried out to choose the suitable mesh arrangement. The elastic properties used for the sensitivity analyses are tabulated in Table 7.1.

Table 7.1: Elasticity properties of pavement layers (data from Janoo et al.⁽⁵¹⁾).

Material	Elastic Modulus (MPa)	Poisson's Ratio
Asphalt	3100	0.3
Base	410	0.4
Subgrade	83	0.4

The variation of the vertical deformation at the center of the top of the HMA layer as a function of the total number of elements for 68 kN applied loading is shown in Figure 7.6.

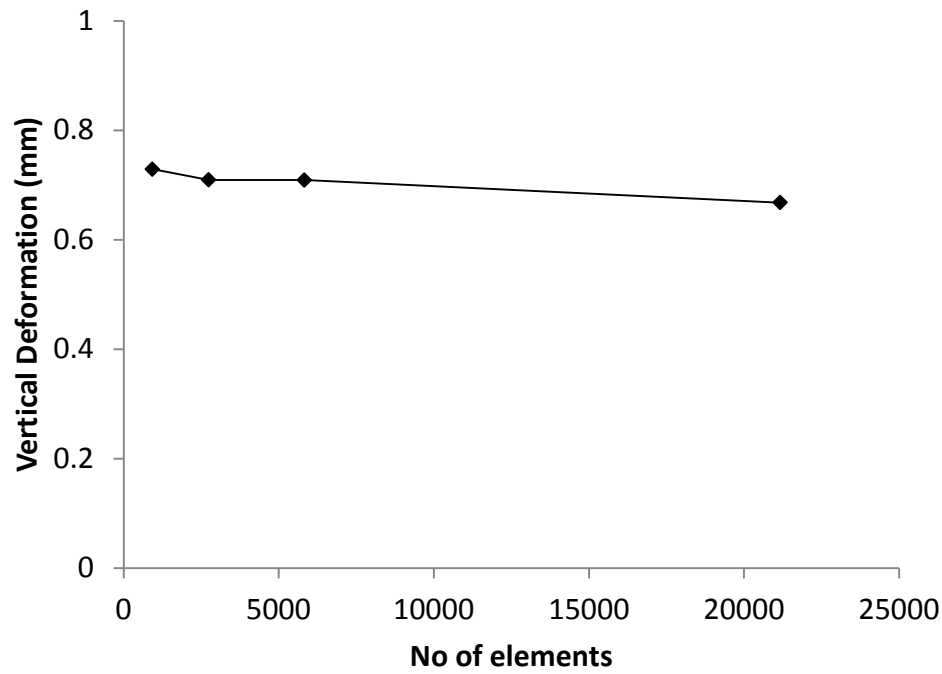


Figure 7.6: Vertical deformation variation with number of elements.

Based on the results, 5832 total elements with asphalt, base and subgrade layers consisting of 324, 972 and 4536 elements, respectively, were chosen. The FE model with the mesh arrangement is shown in Figure 7.7. The element type used is 8-node linear brick, reduced integration, hourglass control (C3D8R).

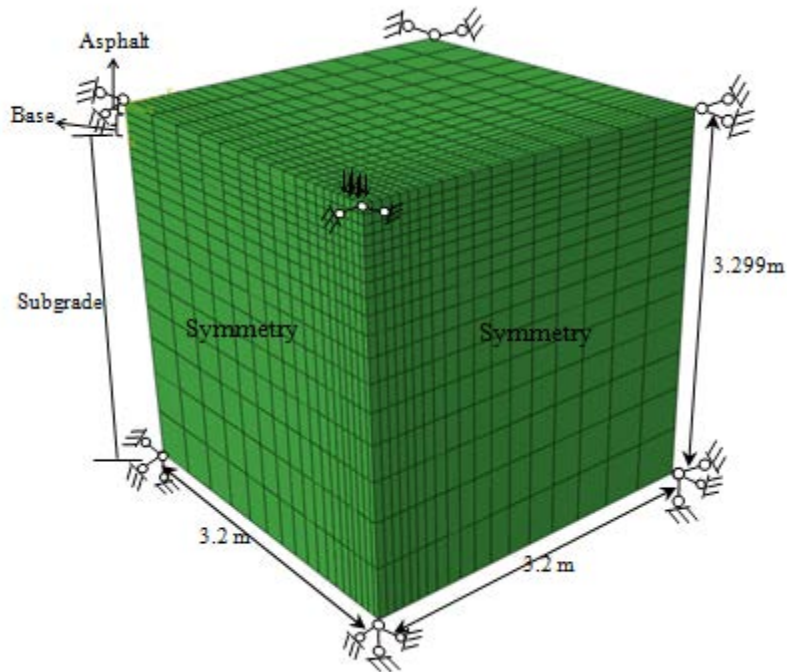


Figure 7.7: Mesh arrangement of 3D quarter symmetric model.

A similar 3D symmetric FE model was developed to simulate the loading at the center of side test window 6, but with only half of the loading due to the symmetry, as shown in Figure 7.8. Point A2 is the center point of the tire in the plan view, as shown in Figure 7.8. The figure also shows the longitudinal and transverse directions of wheel load as x and y, respectively. Figure 7.9 shows the partitions, loading and boundary conditions, respectively.

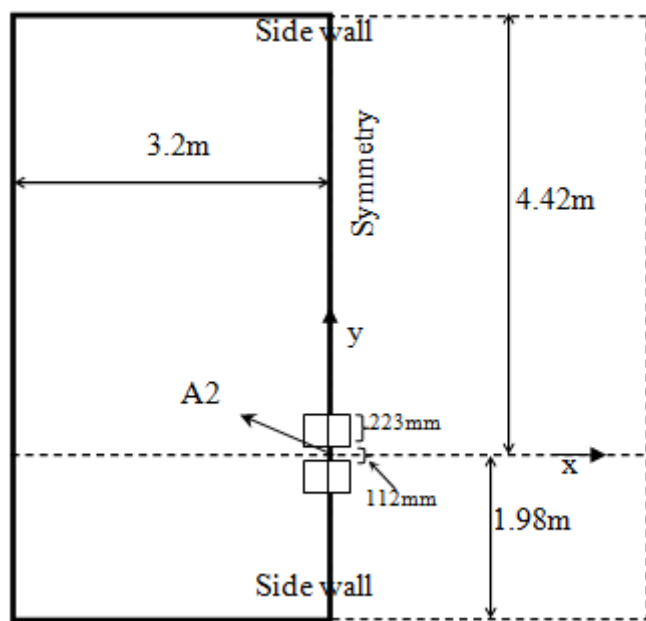


Figure 7.8: Plane geometry of 3D symmetric model.

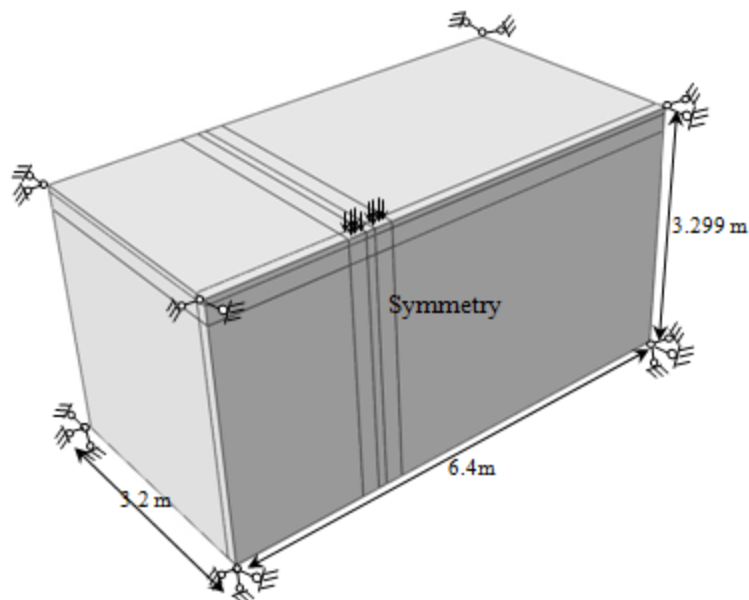


Figure 7.9: Load and boundaries of 3D symmetric model.

A total of 10,982 total elements were chosen with asphalt, base and subgrade layers consisting of 646, 1,938 and 8,398 elements, respectively. The FE model with the mesh

arrangement is shown in Figure 7.10. The element type used was 8-node linear brick, reduced integration, hourglass control (C3D8R).

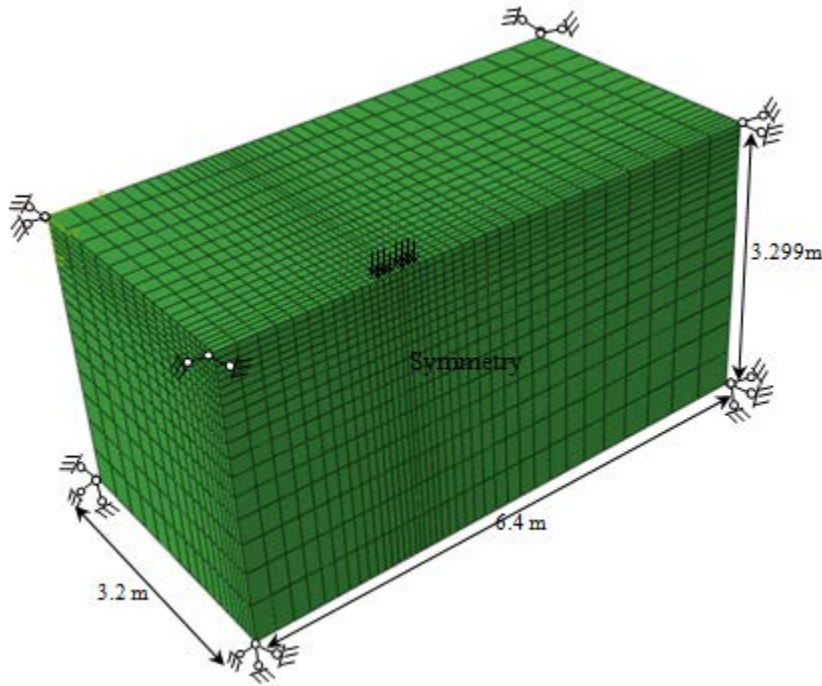


Figure 7.10: Mesh arrangement of 3D symmetric model.

7.3 Verification of model performance

Test data for the application of 27 kN wheel load on A-2-4 soil and 67 kN on soil A-7-5 were obtained from CRREL reports ⁽⁵¹⁾. Asphalt and base course layers were modeled as isotropic elastic materials; parameters used are shown in Table 7.1. The model parameters obtained from laboratory tests for the sandy subgrade and clayey subgrade (moisture content?) are tabulated in Table 7.2. The vertical strain distribution with depth beneath the center of the tire at point A2 (Figure 7.8), along with the FE predictions are shown in Figure 7.11.

Table 7.2: Parameters input in FE analysis

(a) For new sand model (A-2-4).

Elastic parameters	Critical state parameters	Parameters associated with dr -mechanisms	Parameters associated with dp -mechanisms	Unsaturated soil parameters	Default parameters
$G_0=125$ $\nu=0.25$	$M_c = 1.25$ $c = 0.75$ $e_{\Gamma c} = 0.934$ $\lambda_c = 0.02$ $\xi = 0.7$	$d_I = 0.41$ $m = 3.5$ $h_I = 3.15$ $h_2 = 3.05$ $h_3 = 2.2$ $n = 1.1$	$d_2 = 1$ $h_4 = 3.5$	$n_I = 0.015$ $n_2 = 2$ $n_3 = 2.4$	$a=1$ $b_I=0.005$ $b_2=2$ $b_3=0.001$

(b) For D-P Cap model.

Elastic Properties			Cap Plasticity		
A-7-5	A-4	A-6	A-7-5	A-4	A-6
$E= 19.5$ Mpa $\nu= 0.25$	$E= 18.0$ Mpa $\nu= 0.25$	$E= 13.6$ Mpa $\nu= 0.25$	$c = 58.4kPa$ $\beta = 36$ $R = 5.57$ $X_a = 0$ $a = 0.01$ $K = 1$	$c = 13.9kPa$ $\beta = 36$ $R = 4.36$ $X_a = 0$ $a = 0.01$ $K = 1$	$c = 70.8kPa$ $\beta = 28$ $R = 5.44$ $X_a = 0$ $a = 0.01$ $K = 1$

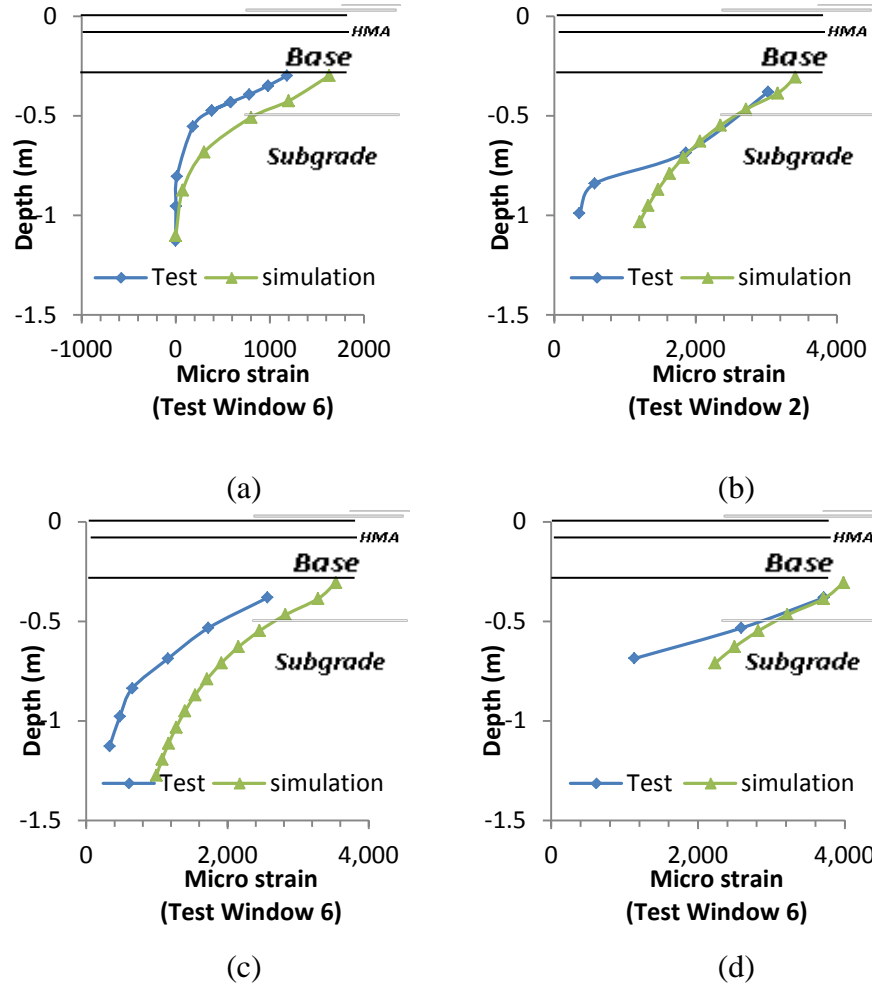


Figure 7.11: Verification of sand model and D-P cap model performance with field data.

- (a) Soil A-2-4 with sand model (b) Soil A-7-5 with D-P Cap model
- (c) Soil A-4 with D-P Cap model (d) Soil A-6 with D-P Cap model

It can be seen that the predictions match the observed results well for the most part. The strain values in FE simulation are higher than the results obtained from laboratory tests, because there is difference between the materials in project SPR-2(208) and tests conducted in this study, all the soils specimen used in this study are passing #4 sieve. There were difficulties in the simulations of repeated moving wheel loadings using finite element method, thus the wheel loading in FE models are simplified as uniform load with different numbers of cycles.

7.4 Subgrade performance analysis

The advanced features of the new sand model enabled us to study the effects of several factors such as asphalt and base properties and saturation level on pavement deformation. Their effects on vertical stress, strain and deformation at the center point of the plan view of tire geometry (point *A1* in Figure 7.8) are highlighted here, unless specified otherwise.

7.4.1 Standard Condition

The standard condition considers loading to be at the center of the test window of the APT cell (Figure 7.10), elastic asphalt properties with $E = 3100$ MPa and $\nu = 0.3$, and elastic base properties with $E = 410$ MPa, $\nu = 0.4$. The wheel load applied was 136 kN (equivalent to 1000 kPa pressure).

The variation of vertical stress, strain and deformation with depth under the application of wheel load is shown in Figures 7.12, 7.13 and 7.14, respectively. Since the interest here is in subgrade performance, variation of these parameters within the subgrade was monitored. Specifically, vertical stress, strain, and deformation were monitored at depths 0.3365, 0.4175, 0.5105 and 0.617 m, as shown in Figure 7.12. Figure 7.15, 7.16 and 7.17 shows the contour maps of vertical stress, strain, and deformation, respectively.

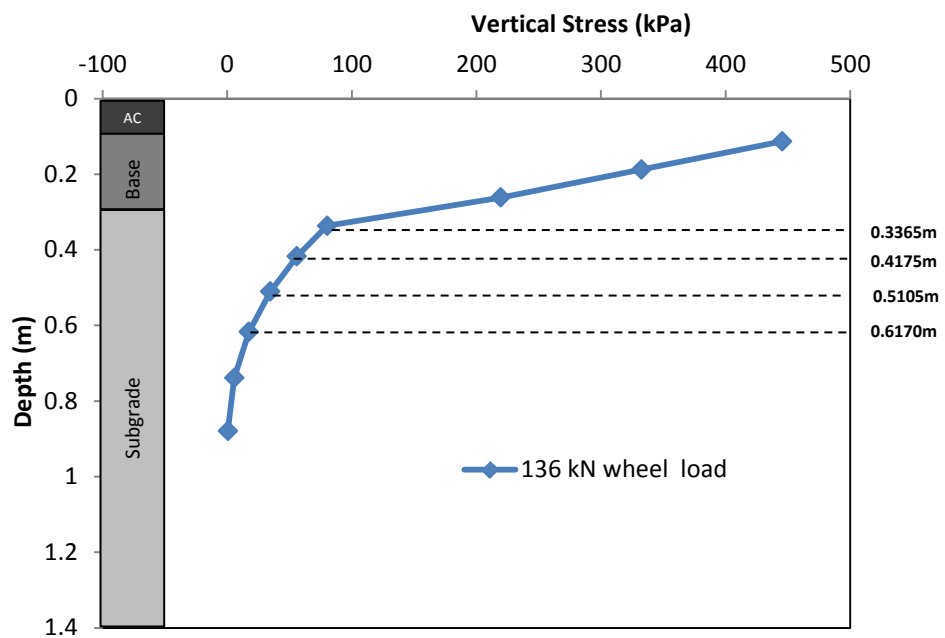


Figure 7.12: Variation of vertical stress (Soil A-2-4)

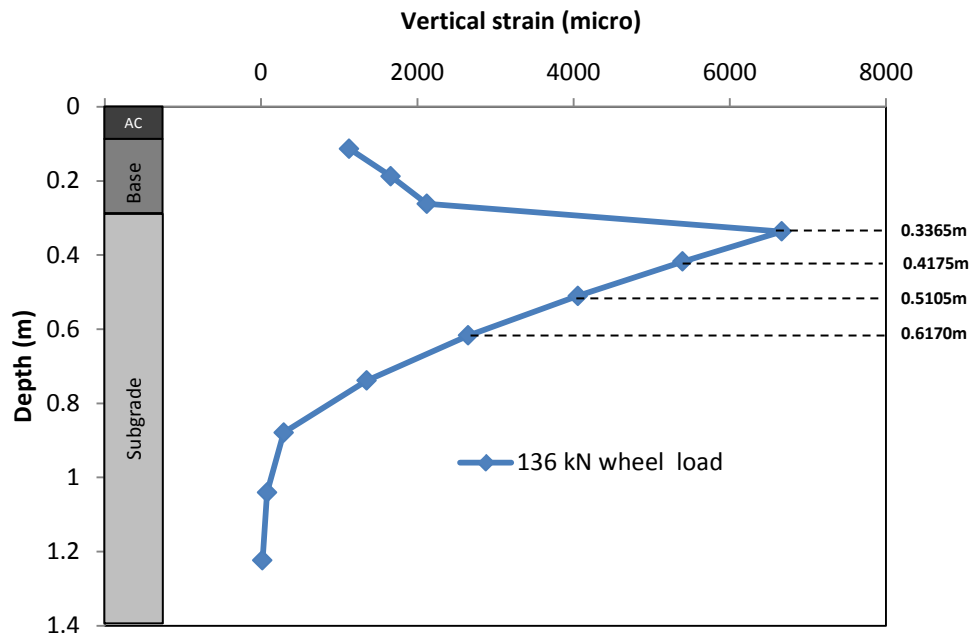


Figure 7.13: Variation of vertical strain (Soil A-2-4)

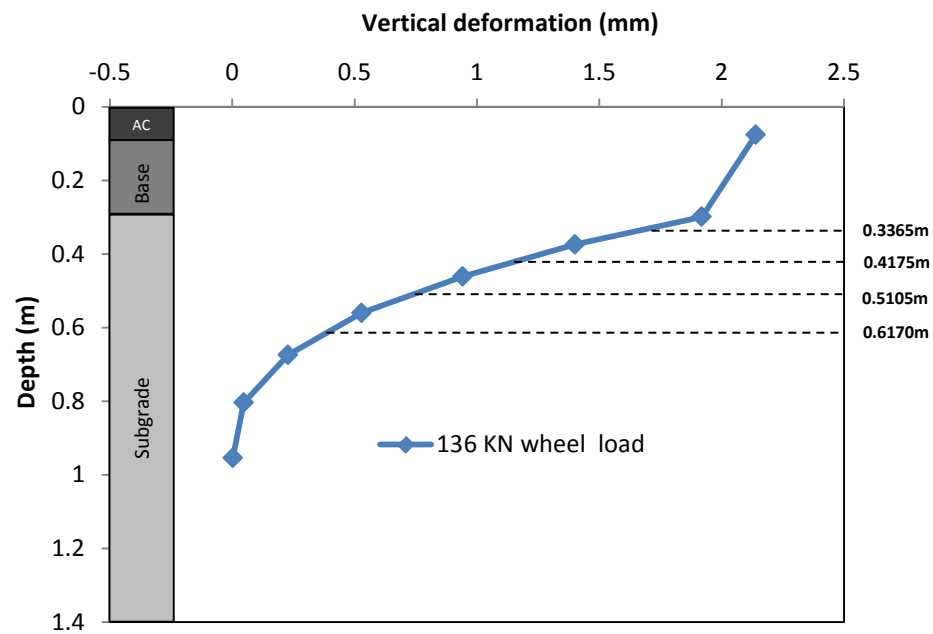


Figure 7.14: Variation of vertical deformation (Soil A-2-4)

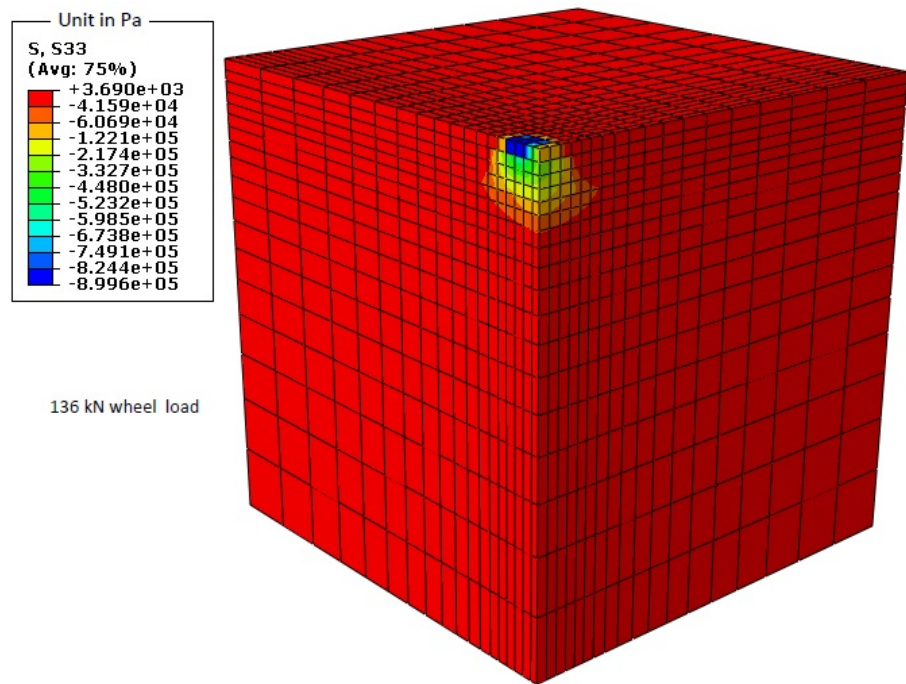


Figure 7.15: Contour map of vertical stress

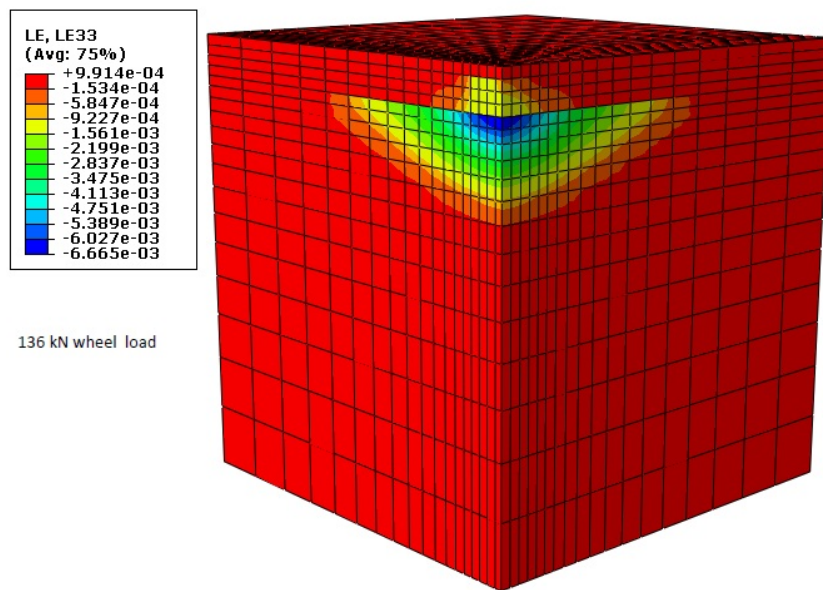


Figure 7.16: Contour map of vertical strain

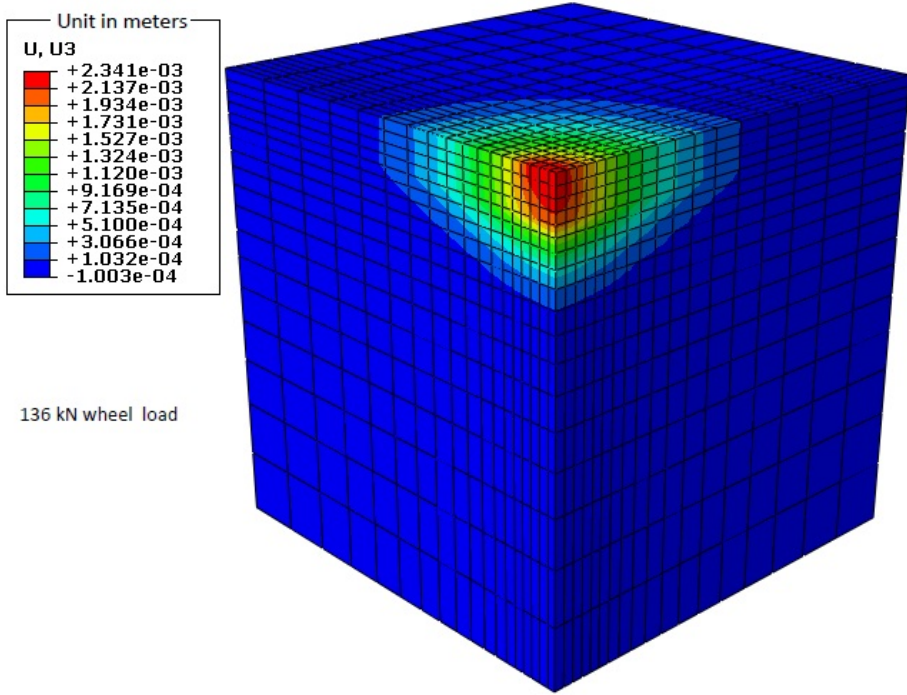


Figure 7.17: Contour map of vertical deformation

7.4.2 Influence of Asphalt and Base properties

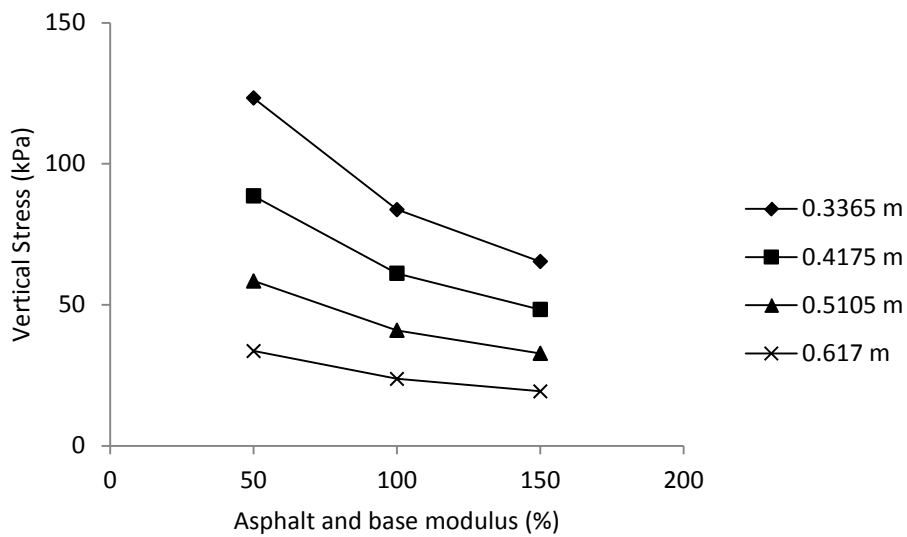
In order to examine the influence of asphalt and base properties on subgrade performance, analyses were conducted with asphalt and base elastic modulus values at 50% and 150% of the standard condition. These values are tabulated in Table 7.3. All other parameters were kept the same as in section 7.4.1.

Table 7.3: Asphalt and Base Elastic Modulus

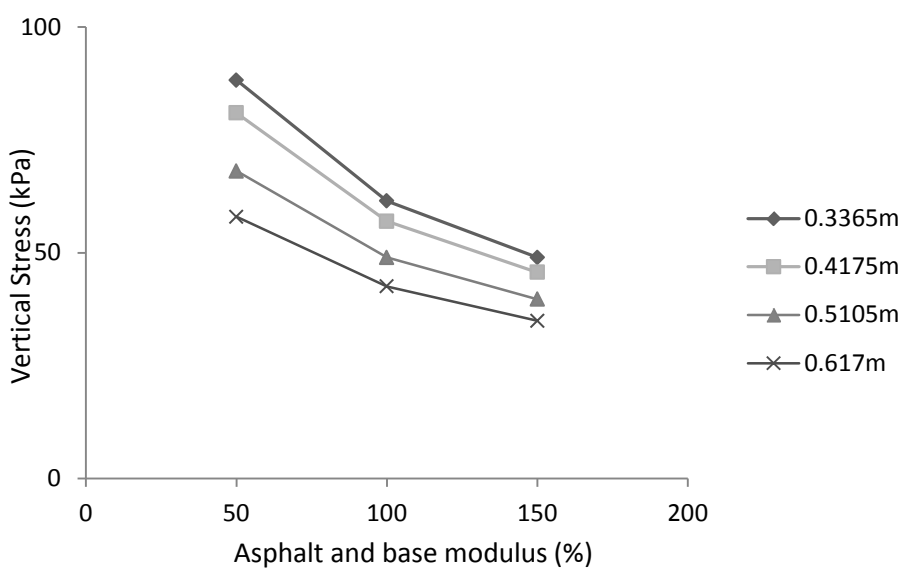
	Asphalt Modulus (MPa)	Base Modulus (MPa)
50%	1550	205
100%	3100	410
150%	4650	615

7.4.2.1 Stresses

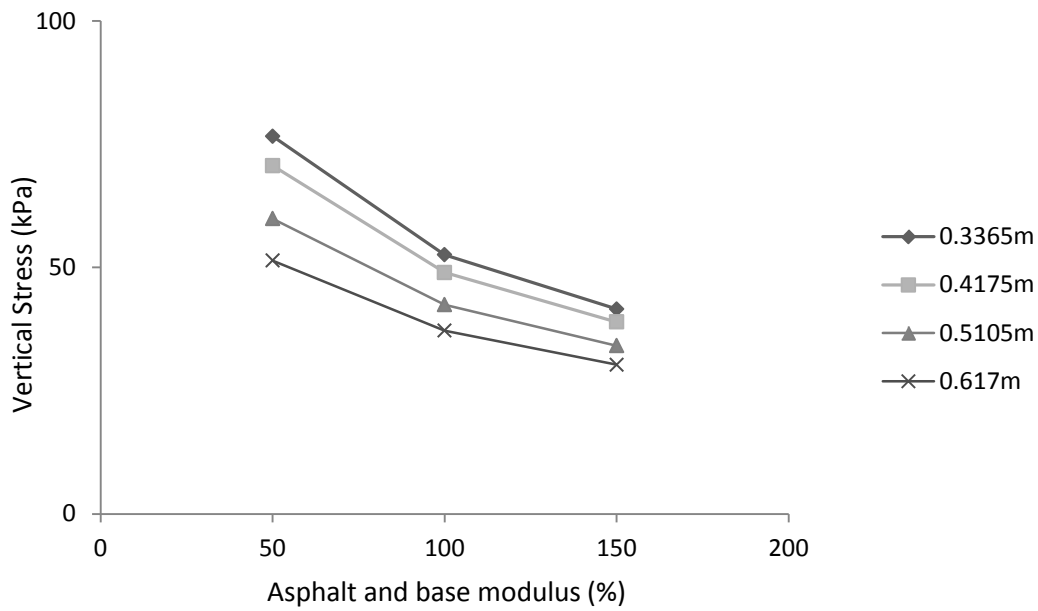
Figure 7.18 shows the influence of asphalt and base modulus on vertical stress at different depths for the case of wheel load of 136 kN. It can be seen that this influence is high near the top of subgrade surface, but gradually reduces with depth.



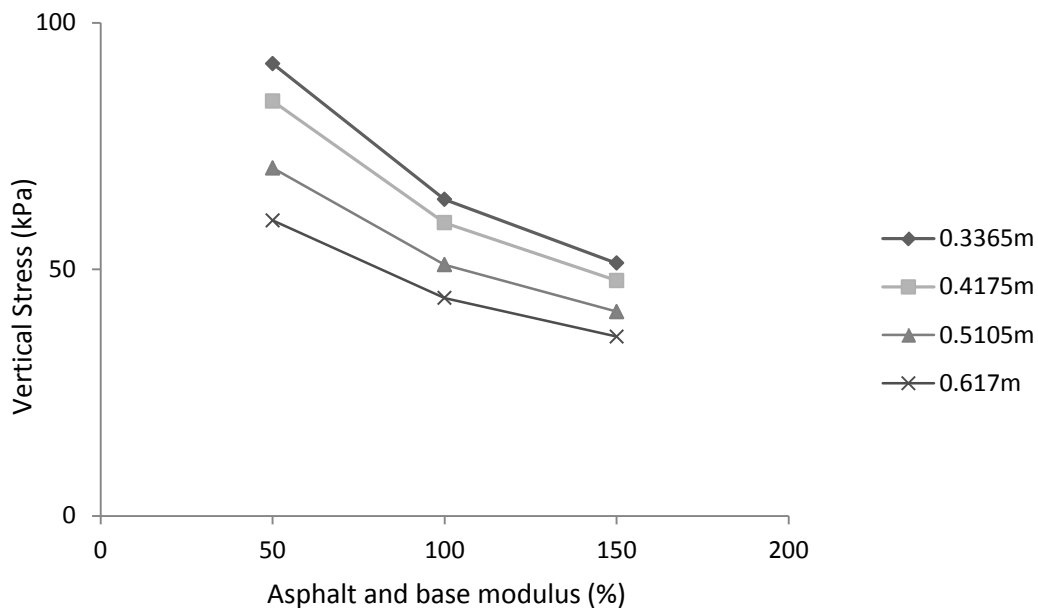
(a)



(b)



(c)



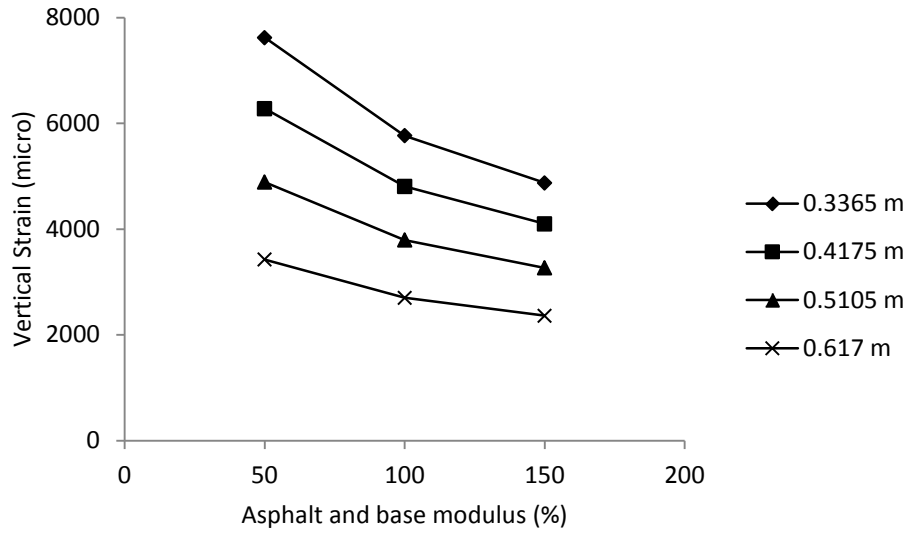
(d)

Figure 7.18: Variation of vertical stress with asphalt and base properties at different depths

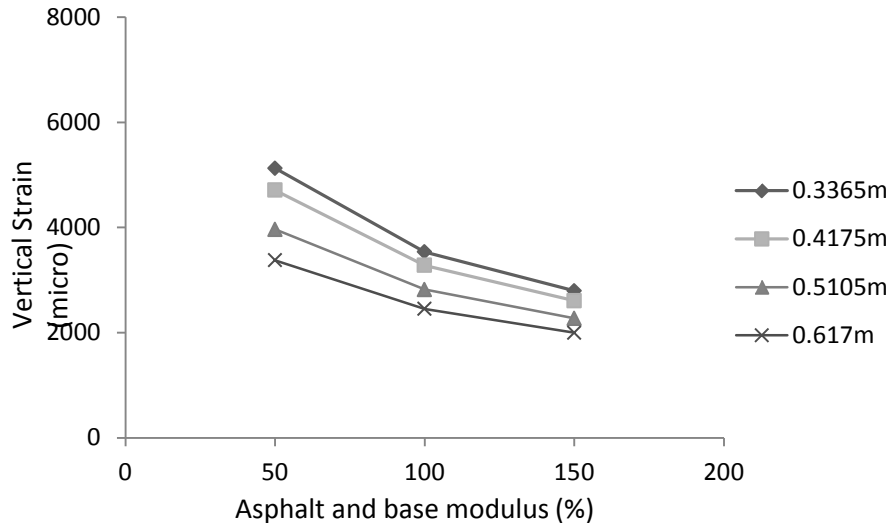
(a) Soil A-2-4; (b) Soil A-4; (c) Soil A-6; (d) Soil A-7-5

7.4.2.2 Strain

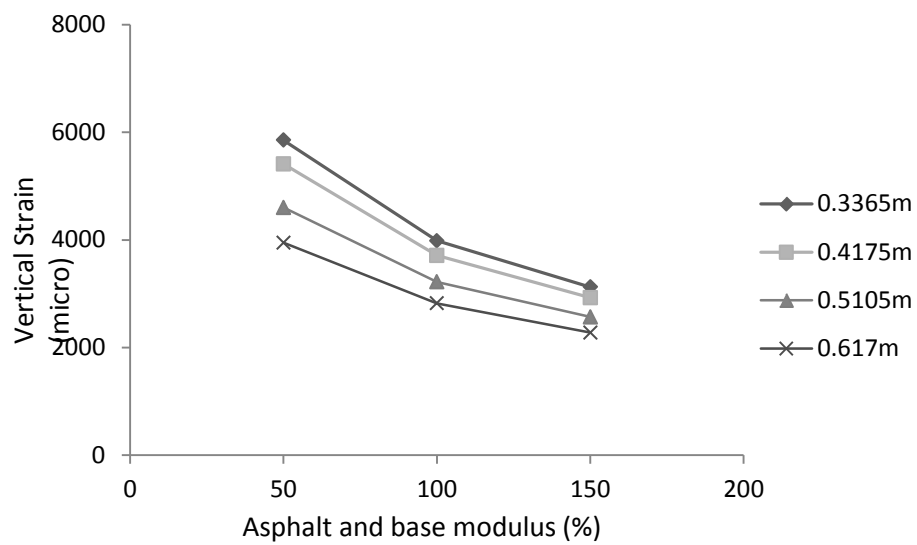
Figure 7.19 shows the influence of asphalt and base moduli on vertical strain at different depths for the case of wheel load is 136 kN. It was found that the influence is high near the top of subgrade surface, but gradually reduces with depth.



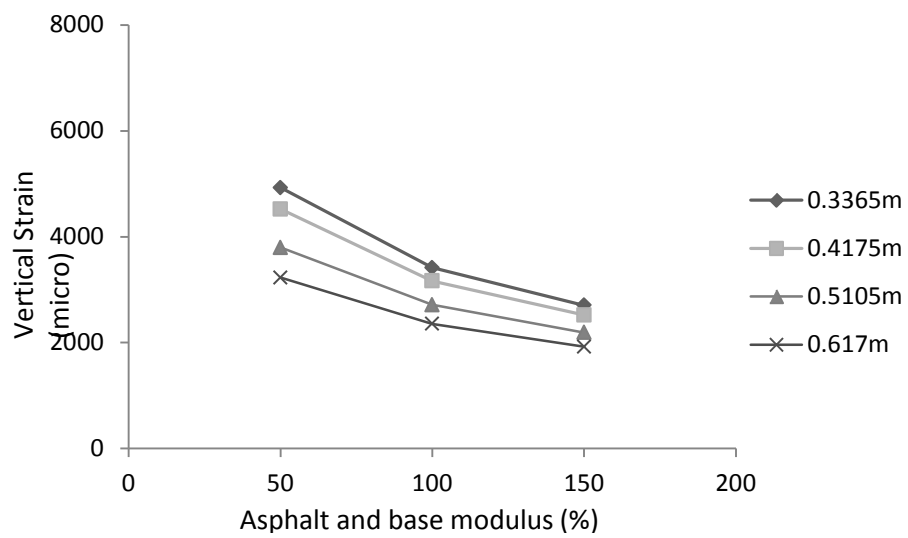
(a)



(b)



(c)



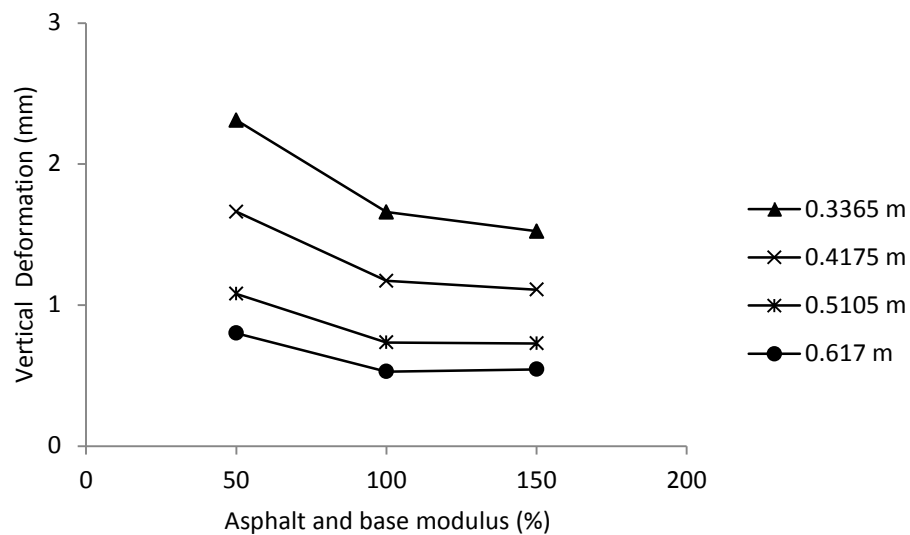
(d)

Figure 7.19: Variation of vertical strain with asphalt and base properties at different depths

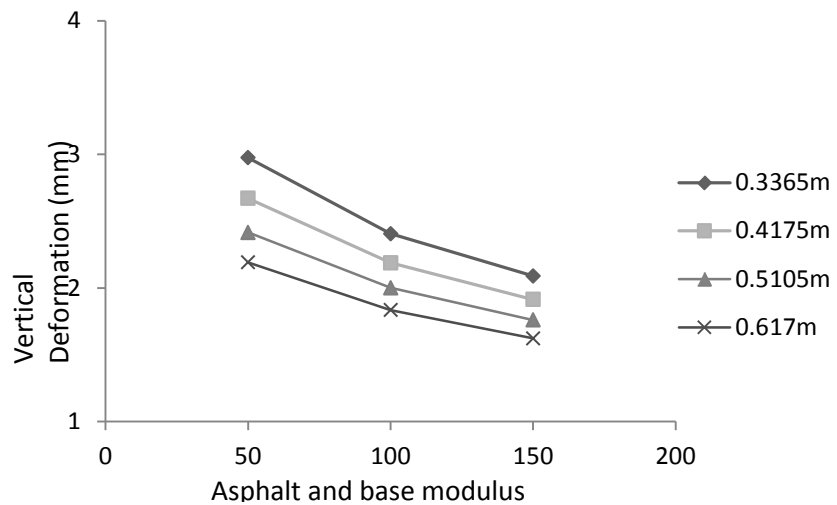
(a) Soil A-2-4; (b) Soil A-4; (c) Soil A-6; (d) Soil A-7-5

7.4.2.3 Vertical Deformation

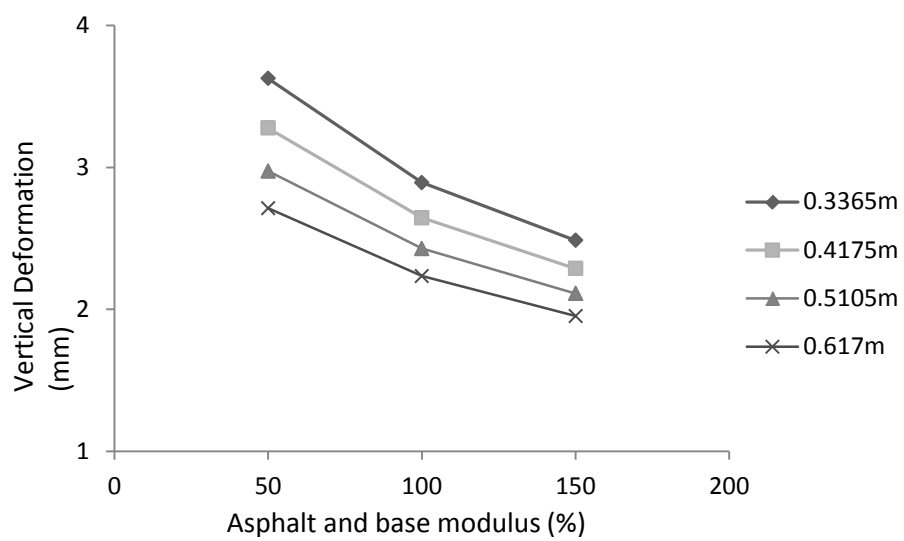
Figure 7.20 shows the influence of asphalt and base moduli on vertical deformation at different depths for the case of wheel load of 136 kN. It was found that this influence is high near the top of subgrade surface, but gradually reduces with depth.



(a)



(b)



(c)

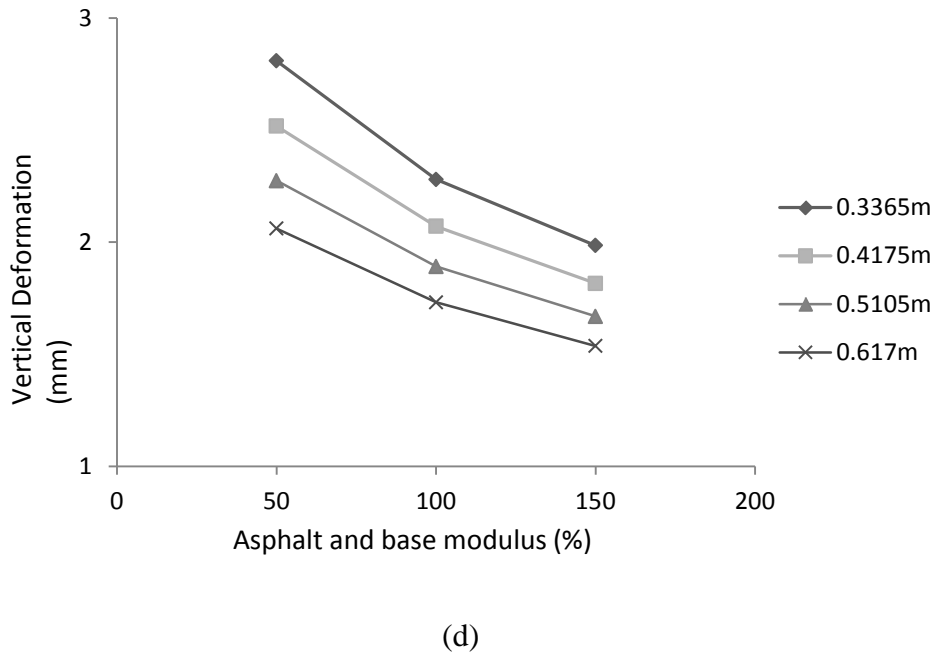


Figure 7.20: Variation of vertical deformation with asphalt and base properties at different depths

(a) Soil A-2-4; (b) Soil A-4; (c) Soil A-6; (d) Soil A-7-5

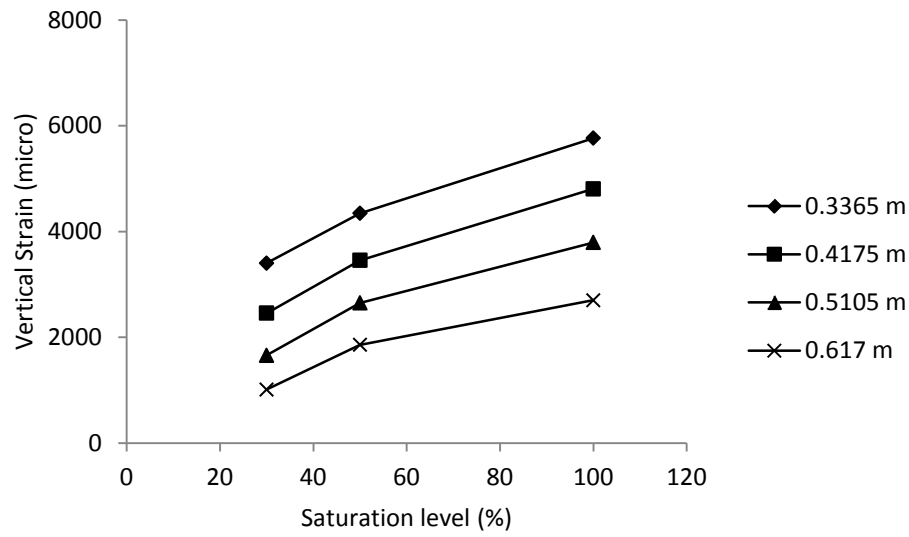
7.4.3 Influence of suction in subgrade performance

In order to examine the influence of saturation level on subgrade performance, analyses were conducted with different saturation levels (100%, 50%, and 30%). All other parameters were kept as stated in section 7.4.1.

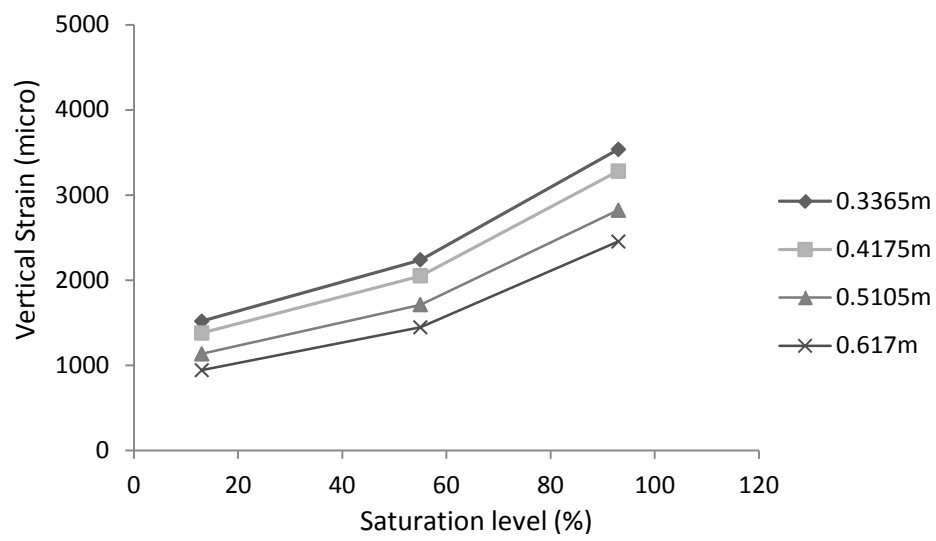
7.4.3.1 Strain

The saturation level of the subgrade was found to influence the strain experienced near the top of the subgrade, especially at high wheel loads.

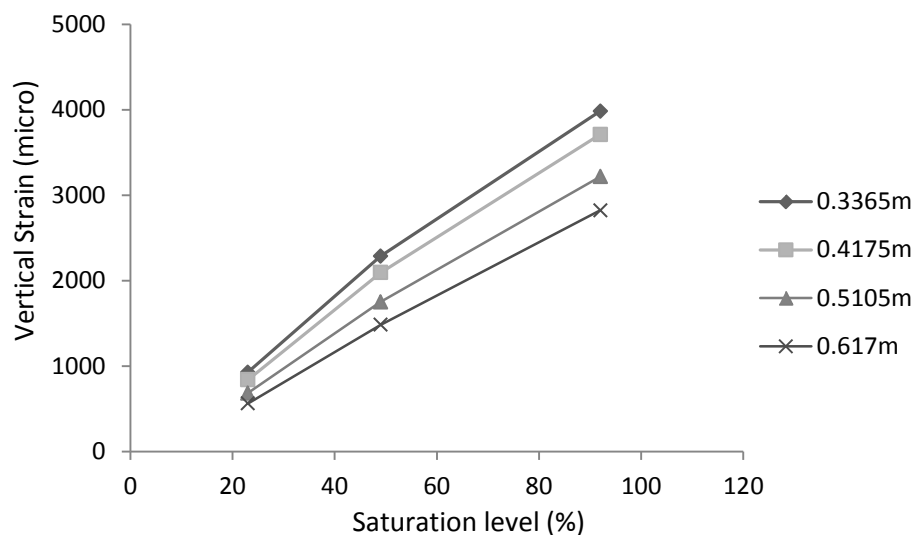
Figure 7.21 shows the influence of saturation level on vertical strain at different depths for the case of wheel load is 136 kN. It was found that this influence is high near the top of the subgrade surface, but gradually reduces with depth.



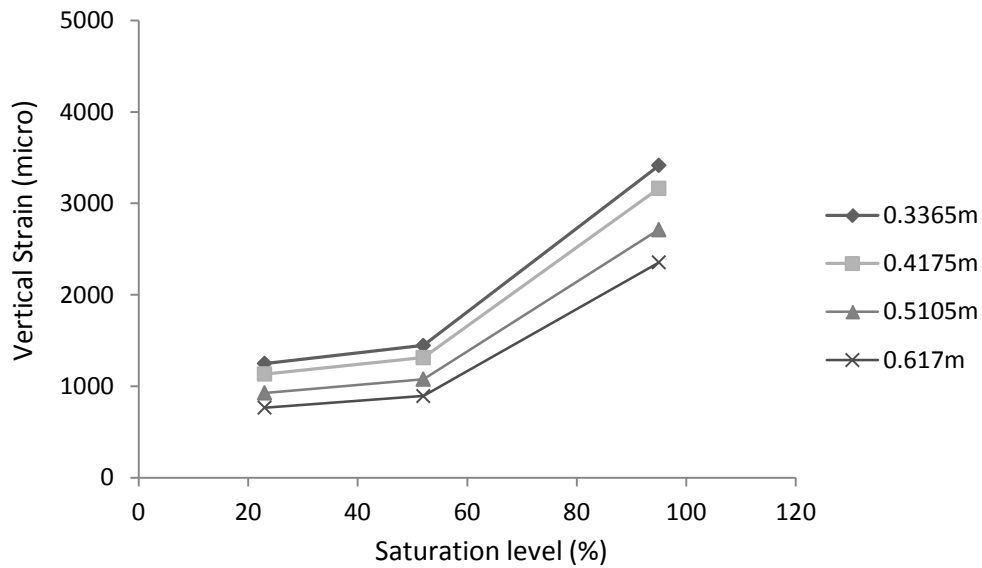
(a)



(b)



(c)



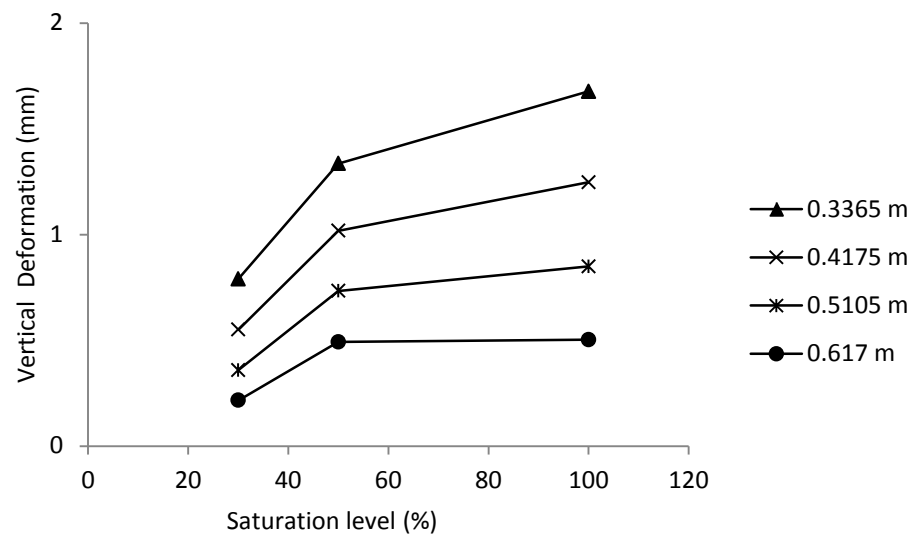
(d)

Figure 7.21: Variation of vertical strain with saturation level at different depths

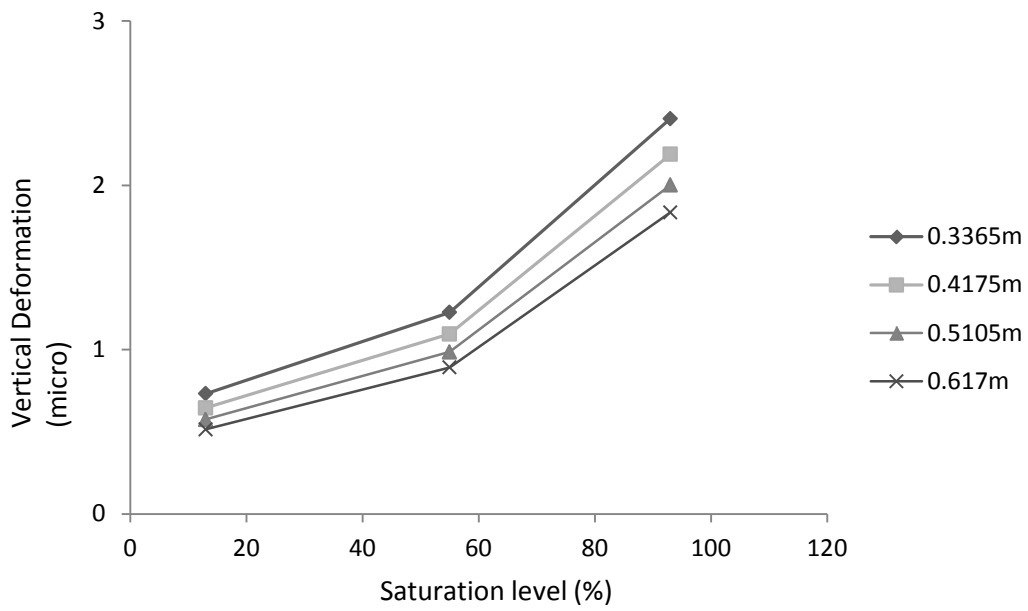
(a) Soil A-2-4; (b) Soil A-4; (c) Soil A-6; (d) Soil A-7-5

7.4.3.2 Vertical Deformation

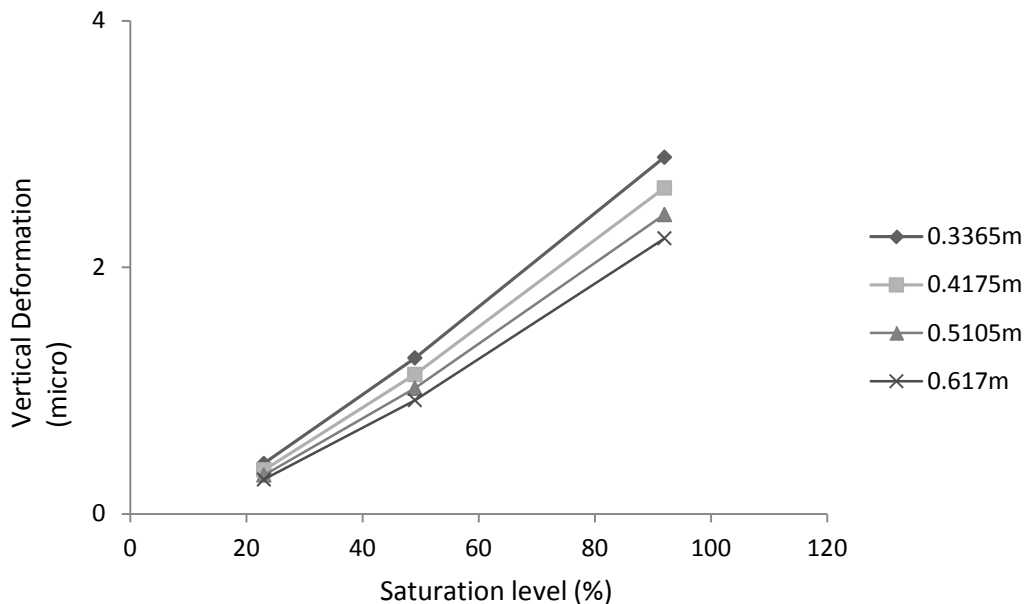
Figure 7.22 shows the influence of saturation level on vertical deformation at different depths for the case of wheel load is 136 kN. It was found that this influence is high near the top of the subgrade surface, but gradually reduces with depth.



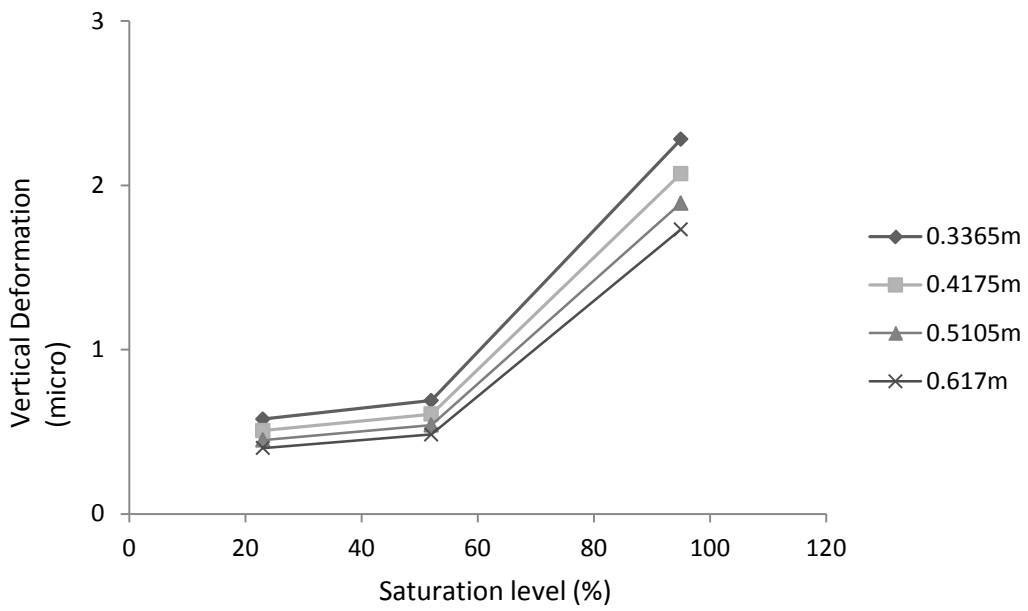
(a)



(b)



(c)



(d)

Figure 7.22: Variation of vertical deformation with saturation level at different depths

(a) Soil A-2-4; (b) Soil A-4; (c) Soil A-6; (d) Soil A-7-5

CHAPTER EIGHT

CONCLUSIONS

8.1 Conclusions

In this study, analyses were conducted using accelerated pavement testing data collected as part of the Transportation Pooled Fund Study project SPR-2(208) titled “Pavement Subgrade Performance Study” or the development of empirical and mechanistic models for permanent deformation in subgrade soils. The SPR-2(208) study was conducted at the Cold Region Research Laboratory (CRREL) of the U.S. Army Corps of Engineers in Hanover, New Hampshire, between 1999 and 2007. In the SPR-2(208) study, flexible pavements with the same granular base layer and asphalt concrete surface layer were built inside the Frost Effects Research Facility and were subjected to accelerated pavement testing (APT).

First part of the study was on developing empirical models for use in MEPDG type design framework. While empirical models are useful in practice, their applicability is often limited to the subgrade soils that were used in the data collection study. On the other hand, models based on the fundamental mechanics associated with the deformation of pavements under traffic loads are useful for scientific understanding as well as for design with confidence. The second part of the study developed advanced constitutive models that can predict the behavior of sandy and silty and clayey subgrade soil deformation under repeated traffic loading. They were then implemented into the finite element software Abaqus and used to predict the observed results of the CRREL databank. Parametric studies to identify the influence of the key variables on pavement performance were then conducted.

Empirical Models:

The pavement response data was evaluated for consistency and reasonableness and two dataset were constructed. Statistical analysis was conducted on the response datasets in order to develop new models for predicting the permanent deformation in subgrade soils and to estimate model coefficients for three models found in the literature search: Odermatt, Theyse and M-E PDG models. The major findings of the statistical analysis are:

- The vertical stress and strain data followed in general the expected patterns. The horizontal strain data was erratic and could not be included in the statistical analysis.
- A good statistical fit was obtained for all three models found in the literature. The fit was very good when each soil type is considered separately. Therefore, a pavement designer can use the model parameters specific for each soil type in order to accurately predict the permanent deformation. The statistical fit deteriorates when a model with the same coefficients are used for all soil types.
- The best statistical fit was obtained for the data collected on the experimental cells with soils placed at the optimum moisture content. The coefficient of determination decreases when data for soils placed at moisture content above OMC is incorporated.
- The best statistical fit to the recorded permanent deformation data was obtained for the Odermatt model, followed by the Theyse model and the M-E PDG model.
- A new power model for predicting the magnitude of permanent deformation is proposed. The power model proved to have a comparable goodness-of-fit to that of the Odermatt model.
- The goodness-of-fit of both the Odermatt and the power models improved when the optimum moisture content, OMC, is incorporated in the models as a predicting variable.

- The statistical analysis confirmed Cortez's (17) observation that the finer soils tested in the PSPS experiment exhibited less permanent deformation than the coarse soils.

Advanced Constitutive Models:

The study developed two models for use in modeling subgrade performance under cyclic loads. The model for sand was based on critical state and bounding surface concepts and incorporated parameters to account for sand fabric and suction. The model was implemented into Abaqus using UMAT subroutine. The model performance was verified on a wide range of triaxial test data that includes different drainage conditions, sample preparation method, density, confining stress and mode of shear. Simulation results show that saturation level significantly affects sand performance and a modified suction based state parameter was proposed to better describe unsaturated sand behavior. This parameter was found to correlate with well increase in peak stress due to decrease in saturation level.

The model for clay and silty subgrades was based on the Drucker-Prager CAP model. The procedure of determining the parameters of Drucker-Prager (D-P) Cap model was simplified. Laboratory tests on CRREL silty and clayey soil were performed under several moisture contents and the model parameters were determined. It was found that suction had a significant effect on the model parameters.

Three-dimensional FE models were developed in Abaqus to represent the layered pavement structures of the APT test configurations. Special attention was paid to tire geometry,

boundary conditions, loading conditions, and material properties for the various layers. The three segments (asphalt, base, and subgrade) of the test cell were created using the partition technique. It was assumed that there was no separation between pavement layers. Kinematic boundary conditions were used for modeling the pavement structure. Horizontal movement along vertical boundaries and both the vertical and horizontal movement along the bottom boundary were restrained by the use of roller and pin supports, respectively. Sensitivity analysis was carried out to find the suitable element size.

The first FE model was developed to simulate static wheel load at the center of test window, but only one quarter of the loading was modeled due to the symmetric nature of the load. A similar 3D symmetric FE model was developed to simulate the loading at the center of side test window 6, but with only half of the loading due to the symmetry. 3D FE model performance was verified with test data. The computing time costed for numerical simulation are varied from minutes to days for a typical 3D model, depending on the loading applied and the parameters of the model (the memory of the computer is 2GB).

The 3D FE model quantified the response of pavement subgrades under differing loading magnitudes, asphalt and base properties, and saturation level. The moduli of asphalt and base, and saturation level of subgrade were found to influence the vertical deformation experienced near the top of the subgrade, especially at high wheel loads, but their influence gradually reduced with depth.

8.2 Suggestions for future research

The following recommendations can be drawn from the statistical analysis conducted on the response data collected during the PSPS study:

- A good statistical fit was obtained for the Odermatt, Theyse, M-E PDG and the power models. Since the fit was very good when each soil type was considered separately, but became worse when a single set of model was developed for all soils, the pavement designer should use the model parameters specific for each soil type in order to predict the permanent deformation more accurately. The permanent deformation predicted this way will be more accurate than if the same set of coefficients is used for all soils.
- The pavement designer may decide to use different models (e.g. Odermatt or Theyse) and their corresponding model coefficients for different AASHTO soil types, by selecting for each soil the model which gave the best statistical fit.
- Cortez's ⁽¹⁷⁾ observation, confirmed by the statistical analysis, that the finer soils tested in the PSPS experiment exhibited less permanent deformation than the coarse soils should be further investigated.
- The PSPS study tested only one soil for four different AASHTO soil types. It is therefore necessary that similar work be conducted on additional soils for each AASHTO soil type, in order to develop a larger pavement response and performance database, which will allow the development of more precise models.

The following recommendations can be drawn from the numerical simulation conducted on the advanced model study:

- There were difficulties in the simulations of repeated moving wheel loadings using FE. This could be improved by the use of refined numerical techniques and the use of a computer with

larger RAM capacity. Such simulations are needed for predicting permanent deformation of subgrades after several hundred loading cycles in order to compare to field test data.

- The model described here used elastic parameters for the asphalt and base layers in the FE model. This can be improved by using visco-elastic properties.
- Compaction method in the field will affect subgrade sandy soil fabric orientation, and ultimately affect the subgrade deformation. Efforts must be made to correlate the fabric orientation effect due to subgrade compaction method in the field.
- More triaxial tests are needed to investigate the parameters of D-P Cap model under the moisture content between optimum moisture content and 100% degree of saturation.

REFERENCES

1. Wang, Z. L., Dafalias, Y. F. and Shen, C. K. (1990). Bounding surface hypoplasticity model for sand. *Journal of Engineering Mechanics*, Vol. 116, No. 5, pp. 983-1001.
2. Manzari, M. T. and Dafalias, Y. F. (1997). A critical state two-surface plasticity model for sands. *Géotechnique*, Vol. 47, No. 2, pp. 255–272.
3. Li, X. S. and Dafalias, Y. F. (2000). Dilatancy for cohesionless soils. *Géotechnique*, Vol. 50, No. 4, pp. 449-460.
4. Li, X. S. (2002). A sand model with state-dependent dilatancy. *Géotechnique*, Vol. 52, No. 3, pp. 173-186.
5. Li, X. S. and Dafalias, Y. F. (2002). Constitutive modeling of inherently anisotropic sand behavior. *Journal of Geotechnical and Geoenvironmental Engineering*, ASCE, Vol. 128, No. 10, pp. 868–880.
6. Li, X. S. and Dafalias, Y. F. (2004). A constitutive frame work for anisotropic sand including non-proportional loading. *Géotechnique*, Vol. 54, No. 1, pp. 41-55.
7. Yang, Z. X., Li, X. S. and Yang, J. (2008). Quantifying and modeling fabric anisotropy of granular soils. *Géotechnique*, Vol. 58, No 4, pp. 237-248.
8. Prevost, J. H. and Hoeg, K. (1975). Effective stress-strain-strength model for soils, *Journal of Geotechnical Engineering*. Vol. 101, No. 3, pp. 257-288.
9. Vermeer, P. A. (1978). A double hardening model for sand. *Géotechnique*, Vol. 29, No. 4, pp. 413-433.

10. Banerjee, S., Davis, R. O. and Sribalaskandarajah, K. (1992). Simple double-hardening model for geomaterials. *Journals of Geotechnical Engineering, ASCE*, Vol. 118, No. 6, pp. 889-901.
11. Sribalaskandarajah, K. (1996). A computational framework for dynamic soil-structure interaction analysis. PhD thesis, University of Washington, Seattle, Washington, USA.
12. Bonaquist, R. F. (1996). Development and application of a comprehensive constitutive model for granular materials in flexible pavement structures. Ph.D thesis, University of Maryland, Maryland, USA.
13. Carter, J. P., Booker, J. R., and Worth, C. P. (1982). A critical state model for cyclic loading, Ed. Pande et al., *Soil Mechanics – Transient and cyclic loading*, pp. 219-252.
14. Liu, M. D. and Carter, J. P. (2000). On the volumetric deformation of reconstituted soils. *International journal for numerical and analytical methods in geomechanics*. Vol. 24, pp. 101-133.
15. Suiker, A. S. J. and Borst, R. D. (2003). A numerical model for the cyclic deterioration of railway tracks. *International Journal for Numerical Methods in Engineering*, Vol. 57, No. 4, pp. 441-470.
16. Heath, A. C., Pestana, J. M., Harvey, J. T, and Bejerana, M. O. (2004). Normalizing behavior of unsaturated granular pavement materials. *Journal of Geotechnical and Geoenvironmental Engineering, ASCE*, Vol. 130, No. 9, pp. 896-904.

17. Cortez, E. R. (2007). Pavement Subgrade Performance Study. Final Report. ERDC - CRREL TR-13228, Cold Regions Research and Engineering Laboratory, Hanover, New Hampshire. (www.pooledfund.org/documents/SPR-2_208/SPR2-208_SubgradeProject_FinalReport.pdf)
20. Tseng, K. and Lytton, R. (1989) "Prediction of Permanent Deformation In Flexible Pavement Materials". Implication of Aggregates in the Design, Construction, and Performance of Flexible Pavements. ASTM STP 1016, ASTM, pp.154-172.
21. Barksdale, R. D. (1972). Laboratory evaluation of rutting in base course materials. *Proceedings of the Third International Conference on the Structural Design of Asphalt Pavements*, London, pp. 167-174.
22. Sweere, G. T. H. (1990). *Unbound Granular Base for Roads*. PhD Thesis, Delft University of Technology, The Netherlands.
23. Hornych P. and J.M. Piau (2002) "Towards Computation Tools for the Assessment of Rutting of Flexible Pavements". *The BCRA'02 Workshop 2 on Modeling Flexible Pavements*. The Sixth International Conference on the Bearing Capacity of Roads, Railways and Airfields, Lisbon, Portugal.
24. Van Niekerk A. A., Van Scheers J., Muraya, P. and Kisimbi, A. (2000). The effect of compaction on the mechanical behavior of mix granulate base course materials and on pavement performance. *Unbound Aggregates in Road Construction*. Proceedings of the 5th International Symposium on Pavements UNBOUND (UNBAR 5),, Nottingham, England Edited by Andrew R. Dawson, A.A. Balkema Publishers, Rotterdam. pp. 21-23.

25. Van Niekerk, A. A. (2002). Mechanical Behavior and Performance of Granular Bases and Sub-bases in Pavements, *PhD Dissertation*, Delft University of Technology, The Netherlands.
26. Theyse H. L. (2000) “The development of mechanistic-empirical permanent deformation design models for unbound pavement materials from laboratory and accelerated pavement test data”. Unbound Aggregates in Road Construction. Proceedings of the 5th International Symposium on Pavements UNBOUND (UNBAR 5). 21-23 June 2000, Nottingham, England Edited by Andrew R. Dawson, A.A. Balkema Publishers, Rotterdam.
27. Theyse, H.L.,(1998) “The Development of Multi-Dimensional Transfer Functions for the Permanent Deformation of Pavement Structures,” Proceedings of the 5th International Conference on the Bearing Capacity of Roads and Airfields, Trondheim, Norway.
28. Gidel G. (2001) Comportement et valorization des graves non traitées calcaires utilisées pour les assises de chausses souples. PhD Dissertation, University of Bordeaux, France.
29. Nunez W.P., Malysz R., Ceratti J. A. and W.Y.Y Gehling (2004). “Shear strength and permanent deformation of unbound aggregates used in Brazilian pavements” Pavements Unbound. Proceedings of the 6th International Symposium on Pavements UNBOUND (UNBAR 6). 6-8 July 2004, Nottingham, England Edited by Andrew R. Dawson, A.A. Balkema Publishers, New York.
30. Zhang, W., Ullitz, P. and McDonald, R. (1998). Pavement Subgrade Performance Study, Part II: Modelling Pavement Response and Predicting Pavement Performance. Report 87, Danish Road Institute, Roskilde, Denmark.

31. Odermatt, N. (2000). *Permanent Deformation in Fine-Grained Subgrade Materials – Triaxial and Accelerated Pavement Tests*. Licentiate Thesis. Royal Institute of Technology, Stockholm, Sweden.
32. Elliot R., Dennis N. and Y. Qiu (1999). Permanent Deformation of Subgrade Soils Phase II: Repeated Load Testing of Four Soils. Mack-Blackwell Transportation Center, University of Arkansas, Fayetteville.
33. Oda, M. and Nakayama, H. (1988). Introduction of inherent anisotropy of soils in the yield function. Micromechanics of granular materials. Ed. Satake, M. and Jenkins, J. T., pp. 81-90 Amsterdam: Elsevier Science.
34. Duncan, J. M., Monismith, C. L. and Wilson, E. L. (1968). Finite element analysis of pavements. Highway Research Record, No. 228, Highway Research Board, pp. 18-33.
35. Raad, L. and Figueroa, J. L. (1980). Load Response of Transportation Support Systems. Transportation Engineering Journal, ASCE, Vol. 106, No. 1, pp. 111-128.
36. Lytton, R. L. and Tseng, K. H. (1990). Fatigue damage properties of asphaltic concrete mpavements. In Transportation Research Record, No. 1286, Transportation Research Board, Washington, D.C., pp. 150-163.
37. White, T. D. (1998). Application of finite element analysis to pavement problems. Finite Element for Pavement Analysis and Design, Proceedings of the First National Symposium on 3D Finite Element Modeling for Pavement Analysis & Design, Charlston, W. Virginia, November 8-10.

38. Huang, B., Mohammad, L. N. and Rasoulian, M. (2001). 3-D numerical simulation of asphalt pavement at Louisiana accelerated loading facility (ALF). In Transportation Research Record 1764, Transportation Research Board, Washington, D.C., pp. 44-58.
39. Erkens, S. M. J. G., Liu, X. and Scarpas, A. (2002). 3D finite element model for asphalt concrete response simulation. The International Journal of Geomechanics. Vol. 2, No. 3, pp. 305-330.
40. Desai, C. S. (2002). Mechanistic pavement analysis and design using unified material and computer models. 3rd International Symposium on 3D Finite Elements for Pavement Analysis, Amsterdam, Netherlands, pp. 1-63.
41. Wu, Z., Chen, X. and Yang, X. (2011). Finite element simulation of structural performance on flexible pavements with stabilized base/treated subbase materials under accelerated loading. Report No. FHWA/LA.10/452, Louisiana Transportation Research Center, Baton Rouge.
42. Howard, I. L. and Warren, K. A. (2009). Finite-element modeling of instrumented flexible pavements under stationary transient loading. Journal of Transportation Engineering, ASCE, Vol. 135, No. 2, pp. 53-61.
43. Wu, Z. (2001). Finite element simulation of rutting on superpave pavements. Ph.D. Thesis, Kansas State University, Manhattan, Kansas, USA.
44. White, T. D., Haddock, J. E., Hand, A. J. T., and Fang, H. (2002). Contributions of Pavement Structural Layers to Rutting of Hot Mix Asphalt Pavements. NCHRP Report, No. 468, Transportation Research Board of the National Academics, Washington, D.C.

45. Kim, D., Salgado, R., and Altschaeffl, A. G. (2005). Effects of Supersingle Tire Loadings on Pavements. *Journal of Transportation Engineering*, ASCE, Vol. 132, No. 10, pp. 732- 743.
46. Cho, Y., McCullough, B. F., and Weissmann, J. (1996). Considerations on finite-element method application in pavement structural analysis. *Transportation Research Record*, No. 1539, Transportation Research Board, Washington, D.C., pp. 96-101.
47. Janoo, V; Irwin, L; Eaton, R. and Haehnel, R. (1999). Pavement Subgrade Performance Study. Project Overview. Cold Research and Engineering Laboratory, US Army Corps of Engineers.
48. Koiter, W. T. (1953): Stress-Strain Relations, Uniqueness and Variational Theorems for Elastic-Plastic Materials with a Singular Yield Surface. *Quarterly of Applied Mathematics*, vol. 11, pp. 350–354.
49. Schofield, A. N. and Worth, P. (1968). Critical State Soil Mechanics, McGraw-Hill.
50. Hashiguchi, K. (1985). Micrometric approaches – static – intrinsically time-independent. Proceeding of 11th International Conference on Soil Mechanics and Foundation Engineering, pp. 25-56.
51. Desai, C. S. and Toth, J. (1996). Distributed static constitutive modeling based on stress strain and non-destructive behavior. *Int. J. Solids struct*, Vol. 33, No. 1133, pp. 1619-1650.
52. Wood, M. D., Delkheir, K. and Liu, D. F. (1994). Strain softening and state parameter for sand modeling. *Géotechnique*, Vol. 44, No. 2, pp. 335-339.

53. Drucker, D. C. and Prager, W. (1952). Soil mechanics and plastic analysis for limit design. Quarterly of Applied Mathematics, vol. 10, no. 2, pp. 157–165.
54. Huang T K, Chen W F. Simple procedure for determining cap-plasticity-model parameters [J]. Journal of Geotechnical Engineering, 1990, 116(3): 492-513.
55. Abaqus 6.10 Analysis User's Manual
56. Yoder, E. J. and Witczak, M. W. (1972). Principles of pavement design. Wiley and Sons, New York.
57. Romanoschi S., (2010). Assessment of the Database from the Pavement Subgrade Performance Study.Final Report.
[\(www.pooledfund.org/documents/SPR-2_208/Data_Evaluation_Task_Final_Report.pdf\)](http://www.pooledfund.org/documents/SPR-2_208/Data_Evaluation_Task_Final_Report.pdf)
58. Dafalias, Y. F. (1986). Bounding surface plasticity I: Mathematical foundation and hypoplasticity. Journal of Engineering Mechanics, ASCE, Vol. 112, No. 9, pp. 966-987.
59. Nazzal, M. D., Abu-Farsakh, M. Y. and Mohammad, L. N. (2010). Implementation of a critical state two-surface model to evaluate the response of geosynthetic reinforced pavements. International Journal of Geomechanics, ASCE, Vol. 10, No. 5, pp. 202-212.
60. Li, X. S. and Dafalias, Y. F. (2000). Dilatancy for cohesionless soils. Géotechnique, Vol. 50, No. 4, pp. 449-460.
61. Richart, F.E. Jr., Hall, J. R. & Woods, R. D. (1970). Vibrations of soils and foundations. International Series in Theoretical and Applied Mechanics, Englewood Cliffs, NJ, Prentice-Hall.

62. Li, X. S., Dafalias, Y. F. and Wang, Z. L. (1999). State-dependent dilatancy in critical-state constitutive modeling of sand. *Canadian Geotechnical Journal*, Vol. 36, No. 4, pp. 599-611.
63. Papadimitriou A. G., Dafalias Y. F. and Yoshimine M. (2005). Plasticity modeling of the effect of sample preparation method on sand response. *Soils and Foundations*, Vol. 40, No. 2, pp. 109 – 124.
64. Shu, S. (2005). Sand state and performance analysis of micropiles. Ph.D thesis. Washington State University, Pullman, Washington, USA.
65. Sasiharan, N. (2006). Mechanics of dilatancy and its application to liquefaction problems. PhD Thesis, Washington State University, Pullman, Washington, USA.
66. Oda, M. (1972). Initial Fabrics and Their Relations to Mechanical Properties of Granular Material. *Soils and Foundations*, Vol. 12, No. 1, pp. 17 -36.
67. Kanatani, K. (1984). Stereological determination of structural anisotropy. *International Journal of Engineering Science*, Vol. 22, No. 2, pp. 531-546.
68. Curran, J. R. (1956). The analysis of two-dimensional orientation data. *Journal of Geology*, Vol. 64, No. 2, pp. 117–131.
69. Tobita, Y. (1988). Contact tensor in constitutive model for granular materials. *Proceedings of the US-Japan seminar on micromechanics of granular materials*, Sendai, pp. 263–270.
70. Been, K. and Jefferies, M. G. (1985). A state parameter for sands. *Géotechnique*, Vol. 35, No. 2, pp. 99-112.

71. Li, X. S. and Wang, Y. (1998). Linear representation of the steady-state line for sand. *Journal of Geotechnical and Geoenvironmental Engineering*, ASCE, 124, No. 12, pp. 1215-1217.
72. Riemer, M. F and Seed, R. B. (1997). Factors affecting apparent position of steady-state line. *Journal of Geotechnical and Geoenvironmental Engineering* (ASCE), Vol. 123, No. 3, pp. 281–288.
73. Chapuis, R. P. and Soulie' M. (1981) Internal structure and mechanical behavior of granular soil. *Mechanics of structured media* (ed. A. P. S. Selvadurai) Amsterdam: Elsevier. pp. 341–355.
74. Taylor, D. W. (1948). *Fundamentals of Soil Mechanics*, John Wiley, New York.
75. Rowe, P. W. (1962). The stress-dilatancy relation for static equilibrium of an assembly of particles in contact. *Proc. Roy. Soc. Lond*, A269, pp. 500-527.
76. Roscoe, K. H. and Schofield, A. N (1963). Mechanical behavior of an idealized “wet clay”. Proceeding of 2nd European Conference on Soil Mechanics and Foundation Engineering, Wiesbaden, Vol. 1, pp. 47-54.
77. Bishop. A. W. (1959). The principle of effective stress. *Tecknisk Ukeblad*, Vol. 106, No. 39, pp. 859-863.
78. Van Genuchten, M. T. (1980). A closed-form equation for predicting the hydraulic conductivity of the soils. *Soil Science Society of America Journal*, Vol. 44, No. 5, pp. 892-898.
79. Khalili, N. and Khabbaz, M. H. (1998). A unique relationship for χ for determination of the shear strength of unsaturated soils. *Géotechnique*, Vol. 48, No. 5, pp. 681-687.

80. Fukushima, S. and Tatsouka, F. (1984). Strength and deformation characteristics of saturated sand at extremely low pressures, *Soils and Foundations*, Vol. 24, No.4, pp. 30-48.
81. Verdugo, R. and Ishihara, K. (1996). The steady state of sandy soils. *Soils and Foundations*, Vol. 36, No. 2, pp. 81-91.
82. Gaudin, C., Serratrice, J. F., Thorel, L., and Garnier, J. (2002). Caractérisation du comportement d'un sol par essais triaxiaux pour la modélisation numérique d'un écran de soutènement. Symposium International Identification et détermination des paramètres des sols et des roches pour les calculs géotechniques, Paris, France, pp. 385-394.
83. Arulmoli, K, Muraleetharan, K. K, Hossain, M. M, and Fruth, L. S. (1992). VELACS: verification of liquefaction analysis by centrifuge studies – laboratory testing program, soil data report, Earth Technology Corporation.
84. Resende L, Martin J B. Formulation of Drucker-Prager Cap Model[J]. American Society of Civil Engineers, 2014, 111(7):855-881.
85. Lu, N., J. Godt, and D. T. Wu. 2010. A Closed-Form Equation for Effective Stress in Unsaturated Soil. *Water Resources Research* 46, W05515.
86. D.C. Drucker, R.E. Gibson, D.J. Henkel. Soil mechanics and work-hardening theories of plasticity. *Transactions American Society of Civil Engineers*, 122 (1957), pp. 338 – 346
87. Fossum A F, Senseny P E, Pfeifle T W, et al. Experimental determination of probability distributions for parameters of a salem limestone cap plasticity model [J]. *Mechanics of Materials*, 1995, 21(2): 119-137.

88. Lu, Ning, T. H. Kim, S. Sture, and W. J. Likos. 2009. Tensile Strength of Unsaturated Sand. Journal of Engineering Mechanics, American Society of Civil Engineers. Vol. 135, No. 12.
89. In situ measurement of initial stresses and deformation characteristics : Proc Conference on In-situ Measurements of Soil Properties, Raleigh, NC, 1 - 4 June 1975, V2, P181 - 230, disc P231 - 277
90. Nishida,Y. (1956), "A Brief Note on Compression Index of Soils", Journal of Soil Mechanics and Foundations Division, ASCE, 82, SM3, 1027-1-1027-14, 1956.
91. Azzous, A.S., Krizek, R.J., and Corotis, R.B., "Regression Analysis of Soil Compressibility", Soils and Foundations, 16(2), 19-29, 1976.
92. Hough, B.K.,(1957), "Basic Soils Engineering", The Ronald Press Company, New York, 114-115, 1957.
93. Rendon-Herrero, O. (1980), "Universal Compression Index Equation", Journal of Geotechnical Engineering Division,ASCE, GT11, pp.1179-1199
94. Terzaghi, K. and Peck, R.B. (1967), "Soil Mechanics in Engineering Practice", John Wiley & Sons Inc. New York.
95. Gunduz Z, Arman H. Possible relationships between compression and recompression indices of a low-plasticity clayey soil[J]. Arabian Journal for Science and Engineering, 2007, 32(2): 179.
96. Braja M. Das, Principles of Geotechnical Engineering. California: 5th edn., Brooks/Cole Thomson Learning, 2002.

97. Ladd, C C, Foott, R, Ishihara, K, Schlosser, F and Poulos, H G (1977). "Stress deformation and strength characteristics," International Conference on Soil Mechanics and Foundation Engineering, 9th, 1977, Tokyo, Japan. Vol.2, pp.421-494
98. Helwany, S. (2007) Consolidation, in Applied Soil Mechanics: with Abaqus Applications, John Wiley & Sons, Inc., Hoboken, NJ, USA.
99. Mayne, P.W. and Kulhawy, F.H. (1982). "Ko-OCR Relationships in Soil", Journal of the Geotechnical Engineering Division, ASCE, Vol. 108, GT6, 851-872.
100. AASHTO. *Standard Specifications for Transportation Materials and Methods of Sampling and Testing*, 34th Edition and AASHTO Provisional Standards, 2014 Edition. American State Highway and Transportation Officials, Washington, DC.
101. Kim, T. H. and S. Saure. 2008. Capillary-Induced Tensile Strength in Unsaturated Sands. Canadian Geotechnical Journal 45: 726-737.
102. Lu, N. and W. J. Likos. 2006. Suction Stress Characteristic Curve for Unsaturated Soils. Journal of Geotechnical Geoenvironmental Engineering 132 (2): 131-142.

APPENDIX A

CALIBRATION PROCEDURE OF NEW SAND MODEL PARAMETERS

G_0 and ν are elastic model parameters. G_0 can be determined by fitting independent small strain test (resonant column test or bending element test) data to Eq. 4.14. Calibration of ν is explained later in this section.

Vector magnitude (Δ) is a fabric model parameter. It can be calculated by using Eq. 4.17 for different sample preparation methods. Δ_{MT} and Δ_{DD} are vector magnitudes for moist tamped and dry deposited specimens, respectively.

Critical stress ratio at triaxial compression (M_c) and extension (M_e) in $q-p$ plane can be determined by:

$$M_c = \frac{6 \sin \phi'}{3 - \sin \phi'} \quad (A.1)$$

$$M_e = \frac{6 \sin \phi'}{3 + \sin \phi'} \quad (A.2)$$

where ϕ' is the critical state friction angle.

The critical stress ratio values for triaxial compression and extension can be directly used to find the c ($= \frac{M_c}{M_e}$). The critical state parameters λ_c , e_Γ and ξ can be determined by using Eq. 4.22. Experimental triaxial compression data can be directly fitted to critical state line at critical stress ratio in e - p plane to find these three parameters. λ_c can be calibrated independently because e_Γ and ξ are known in Eq. 4.22. Thus, parameters e_w , k_τ and t can be determined by directly fitting the different shear mode and initial fabric (sample preparation method) triaxial test data to Eq. 4.23.

Eq. 4.24 can be used to find the parameter m because $d=0$ at phase transformation state.

$$m = \frac{1}{\psi^d} \ln \frac{M^d}{M} \quad (\text{A.3})$$

where ψ^d and M^d are the values of ψ and η at the phase transformation state measured from drained or undrained test results.

Eq. 4.27 can be used to find the parameter n because $K_p=0$ at the drained peak stress.

$$n = \frac{1}{\psi^b} \ln \frac{M}{M^b} \quad (\text{A.4})$$

where ψ^b and M^b are the values of ψ and η at the phase transformation state measured from drained or undrained test results.

The parameter d_I can be calibrated by using drained test data in $\varepsilon_v - \varepsilon_q$ curves (A.5). Here elastic deformation is neglected.

$$\frac{d\varepsilon_v}{d\varepsilon_q} \approx \frac{d\varepsilon_v^p}{d\varepsilon_q^p} = d_l = d_l \left(e^{m\psi} - \frac{\eta}{M} \right) \quad (A.5)$$

$d\varepsilon_q$ can be expressed as ⁽³⁾:

$$d\varepsilon_q = d\varepsilon_p^e + d\varepsilon_q^p = \frac{dq}{3G} + \frac{pd\eta}{K_p} = \left(\frac{1}{3G} + \frac{1}{K_p} \right) dq - \frac{\eta}{K_p} dp \quad (A.6)$$

For drained tests, with either the conventional test ($dp=dq/3$) or the constant p test ($dp=0$), Eq. 4.27 and A.6 yield:

$$\frac{dq}{d\varepsilon_q} \approx \frac{dq}{d\varepsilon_q^p} = \frac{K_p}{1-a\eta} = hG_0 \left[\frac{(2.97-e)^2 \sqrt{pp_a} \left[\left(\frac{M}{\eta} \right) - e^{n\psi} \right]}{(1+e)(1-a\eta)} \right] \quad (A.7)$$

where parameter $a=1/3$ for conventional test and $a=0$ for constant p test. By using $q - \varepsilon_q$ curves, h can be calibrated independently because all of the parameters inside the bracket can be predetermined. Thus, h_1 , h_2 and k_h parameters can be calibrated by using Eq. A.8.

$$h = (h_1 - h_2 e) \left(\frac{(k_h A_c - A_e) + (1-k_h) A}{A_c - A_e} \right) \quad (A.8)$$

in which h_1 and h_2 parameters are different for different sample preparation methods.

Parameter h_3 only affects the plastic modulus (K_{p1}) during non-virgin loading, as shown in Eq. 4.29, and it can be calibrated by curve fitting the $q-p$ curve obtained from undrained cyclic triaxial test data. This calibration can be carried out after all of the parameters are determined because h_3 parameter only affects the cyclic loading.

The incremental volumetric strain $d\varepsilon_v$ can be expressed ⁽³⁾ as:

$$d\varepsilon_v = d\varepsilon_v^e + d\varepsilon_v^p = \frac{dp}{K} + d d\varepsilon_q^p = \frac{d}{K_p} dq + \left(\frac{1}{K} - \frac{d\eta}{K_p} \right) dp \quad (\text{A.9})$$

For undrained (constant volume) tests, $d\varepsilon_v = 0$, Eq. A.9 yields:

$$\frac{dq}{dp} = \eta - \frac{K_p}{Kd} = \eta - \frac{3(1-2v)}{2G_0(1+v)} \left[\frac{hG_0 \left[\left(\frac{M}{\eta} \right) - e^{n\psi} \right]}{d} \right] \quad (\text{A.10})$$

v is the only unknown parameter in the above Eq. A.10. By matching the undrained p - q responses of the model with their experimental counterparts, the value of v can be determined.

Parameter d_2 determines the quantitative relation between the dilatancy and stress path of a constant stress ratio, and can be determined by one-dimensional consolidation data. With d_2 known, parameter h_4 can be determined by the slopes of the isotropic consolidation line.

b_1 , b_2 and b_3 are used for the fine adjustment of the reverse loading responses. b_1 , b_2 and b_3 could be considered as internal constants, with default values of 0.005, 2 and 0.01, respectively.

The n_1 , n_2 and n_3 parameters for the unsaturated model (Eq. 4.38) can be determined graphically by using a soil-water characteristic curve, as shown in Figure A.11. n_1 is the intercept of the LSC at $wG_s = 1$. Parameter n_2 controls the transition to full saturation. Parameter n_3 represents the slope of the LSC in log-log space with the value of n_3 equal to the ratio of log scale changes in matrix suction to log scale changes in wG_s .

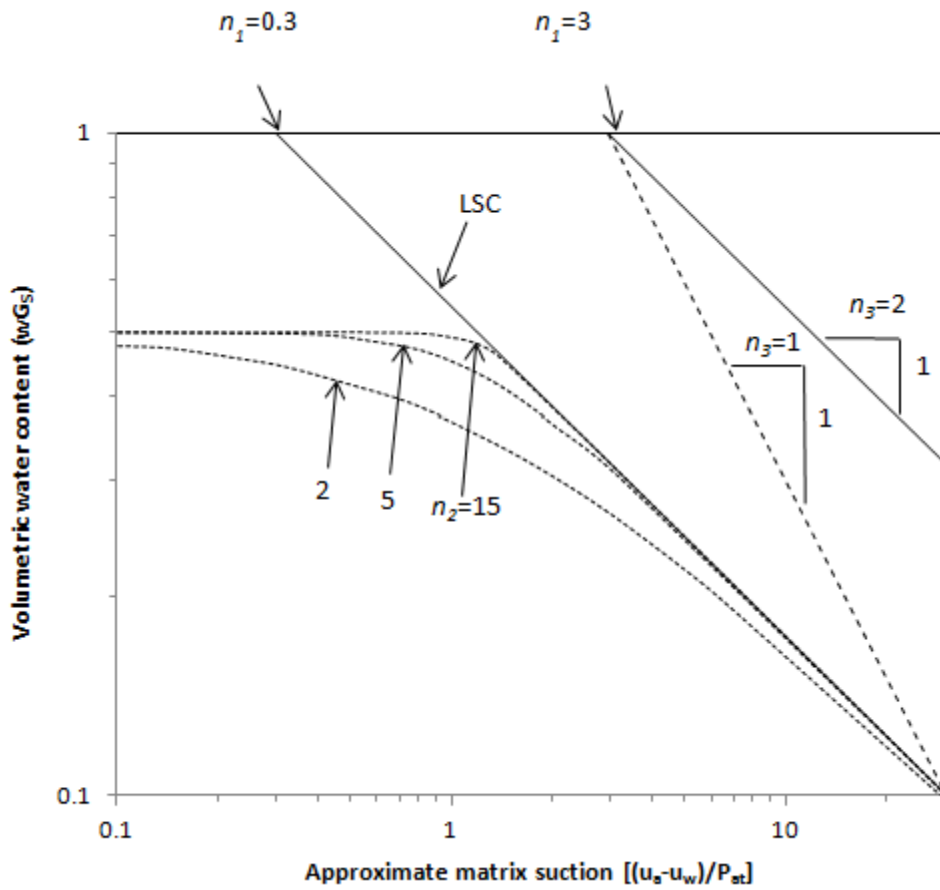


Figure A.1: Effect of parameters n_1 , n_2 , n_3 on suction curve (modified from Heath et al., ⁽¹⁶⁾)

APPENDIX B

MATLAB PROGRAM FOR DETERMINING D-P CAP MODEL PARAMETERS

```
% DP_Cap_Parameters Calculator

% =====

% [ INTRODUCTION ]

% This program is used to calculate the parameters of Drucker-Prager Cap

% Model in numerical simulation by using Abaqus FE software.

% =====

% By Dr.Muhunthan and Yilong Liu. March 2015.

% Department of Civil and Environmental Engineering.

% Washington State University.

% =====

% [ PARAMETERS INPUT ]

%

% Original parameters required (such as firction angle phi, cohesion,

% specific gravity Gs, soil wet density p, etc.) are obtained from the

% tests conducted. All the input parameters needed are listed as follows.
```

```

%
%          Parameters           Explanation
%
%-----%
%
%          phi                Friction angle in degrees
%
%          LL                 Liquid limit
%
%          E                  Young's Modulus (KPa)
%
%          v                  Poisson ratio
%
%          Gs                Specific gravity
%
%          rho               Dry density (g/cm^3)
%
%          sigmal             Mean principal stress
%
%          sigma3              Minor principal stress
%
%          sigmaV0             Initial vertical effective stress
%
%-----%
%
% [ PARAMETERS OUTPUT ]
%
%
%          Parameters           Explanation
%
%-----%
%
%          c                  Material cohesion

```

%	alpha	Material constant
%	kappa	Material constant
%	K0	Initial coefficient of lateral earth pressure
%	Cc	Compression index
%	Cr	Swelling index
%	e0	Initial void ratio
%	At	Parameter of total bulk modulus
%	Ae	Parameter of elastic bulk modulus
%	CapAspect	Cap aspect ratio
%	Xa	Initial position of Cap
%	Xb	Failure position of Cap
% =====		
clc;		
clear all;		
close all;		
global phi sigmal sigma3 sigmaV0 alpha kappa K0 Jsig c;		

```
phi=28; % Input the value of friction angle in degrees, obtained from UCS-
% IDT-Suction test;

LL=33; % Input the Liquid Limit (LL) of the soil;

E=30000; % Input the Young's Modulus in KPa;

v=0.25; % Input the poisson ratio;

Gs=2.7; rho=1.816; %Input the specific gravity (Gs) and maximum dry density
(rho);

sigmal=980; sigma3=100; % Input the failure point in triaxial tset, where
% sigmal is the mean principal stress and sigma3 is
% the minor principal stress (confining pressure)
% in KPa;
```

```

sigmaV0=100; % Input the initial vertical effective stress;

r=0.5*(sigmal-sigma3);

x=0.5*(sigmal+sigma3)-sind(phi)*r;

y=cosd(phi)*r;

c=y-tand(phi)*x % Calculate the cohesion according to the

% Mohr-Coulomb plot;

alpha=2*sind(phi)/(1.732*(3+sind(phi)));

kappa=6*cosd(phi)/(1.732*(3+sind(phi))) % Calculate alpha and kappa;

Su=0.5*(sigmal-sigma3);

Jsig=-2/1.732*(Su/sigmaV0); % Calculate the value of the ratio of (J2)^0.5

% at failure to the initial vertical effective

% stress;

K0=1-sind(phi)

Cc=0.009*(LL-10)

```

```

Cr=0.1*Cc

e0=Gs/rho-1          % Calculate & output the initial coefficient of

                      % lateral earth pressure, swelling indices,

                      % compression indices and initial void ratio

At=Cc/(2.303*(1+e0))    % Calculate parameter of total bulk modulus;

Ae=Cr/(2.303*(1+e0))    % Calculate parameter of elastic bulk modulus;

K=E/(3*(1-2*v))

I1a=sigmaV0*(1+2*K0)

J2art=0.5774*sigmaV0*(1-K0);

s=Su/sigmaV0;

J2f=1/3*(sigmal-sigma3)^2;

J2frt=0.5774*2*s*sigmaV0;

```

```

I1f=1/alpha*(-kappa+0.5774*2*sigmaV0)

deve=Ae*2*(I1f-I1a)/(I1f+I1a);

devp=-2*Ae*(-kappa/sigmaV0+2*s/1.732-(1+2*K0)*alpha)/(-
kappa/sigmaV0+2*s/1.732+(1+2*K0)*alpha);

% ===== TRIAL & ERROR PROCEDURE OF R =====

Rmin=0;           % Input the lower limit of R in Trial & Error;

Rmax=10;          % Input the upper limit of R in Trial & Error;

Accu=0.01;         % Length of step in Trial & Error;

Rc=Rmin:Accu:Rmax;

Xb=J2frt.*Rc+I1f;

Xa=Xb/(1+devp/(At-Ae));

```

```

La=(Xa-kappa.*Rc)/(1+alpha*Rc);

H=(1-alpha^2.*Rc.^2)*La.^2-
2*(I1a+alpha.*kappa.*Rc.^2)*La+(I1a.^2+Rc.^2*J2art.^2-Rc.^2.*kappa.^2);

F0=0;

plot(Rc,H,'b-');

hold on;

plot(Rc,F0,'k--');

hold off;

R=Rmin;

F=100; % Input value of F, which is the initial value of function H

% F should be positive.

while R<Rmax

F=(1-alpha^2*R^2)*La^2-2*(I1a+alpha*kappa*R^2)*La+(I1a^2+R^2*J2art^2-

```

```

R^2*kappa^2);

if F>0

    R=R+Accu;

end

if F<=0

    CapAspect=R;

    break

end

end

CapAspect      % Output the aspect ratio of cap, R;

Xa=(J2frt*CapAspect+Ilf)/(1+devp/(At-Ae)) % Output the initial position of
Cap

La=(Xa-kappa*CapAspect)/(1+alpha*CapAspect);

dX=Xa*abs(devp)/(At-Ae);

Xb=Xa+dX

% ===== Plot TRIAL & ERROR PROCEDURE OF R =====

figure(1);

```

```

plot(Rc,H,'b-');

title ('Trial and Error of Cap Aspect Ratio');

xlabel('Value of R');

ylabel('Difference of Equation According to R');

hold on;

plot(CapAspect,H,'k--');

hold on;

plot(Rc,F0,'k--');

grid on;

hold off;

% ===== Calculate the Hardening Law =====

p0=Xa;

pf=Xb;

range=pf-p0;           %Define the range of Hardening Law

delta=0.1*range;

```

```

p1=p0;ecp1=(Cc-Cr)/(2.3*(1+e0))*log(p1/p0);

p2=p0+delta;ecp2=(Cc-Cr)/(2.3*(1+e0))*log(p2/p0);

p3=p0+delta*2;ecp3=(Cc-Cr)/(2.3*(1+e0))*log(p3/p0);

p4=p0+delta*3;ecp4=(Cc-Cr)/(2.3*(1+e0))*log(p4/p0);

p5=p0+delta*4;ecp5=(Cc-Cr)/(2.3*(1+e0))*log(p5/p0);

p6=p0+delta*5;ecp6=(Cc-Cr)/(2.3*(1+e0))*log(p6/p0);

p7=p0+delta*6;ecp7=(Cc-Cr)/(2.3*(1+e0))*log(p7/p0);

p8=p0+delta*7;ecp8=(Cc-Cr)/(2.3*(1+e0))*log(p8/p0);

p9=p0+delta*8;ecp9=(Cc-Cr)/(2.3*(1+e0))*log(p9/p0);

p10=p0+delta*9;ecp10=(Cc-Cr)/(2.3*(1+e0))*log(p10/p0);

pfailure=pf;ecpf=(Cc-Cr)/(2.3*(1+e0))*log(pf/p0);

% ===== Plot the table of Hardening Law =====

f = figure('Position',[100 100 300 150]);

d=[p1,ecp1;p2,ecp2;p3,ecp3;p4,ecp4;p5,ecp5;p6,ecp6;

p7,ecp7;p8,ecp8;p9,ecp9;p10,ecp10;pfailure,ecpf];

```

```

cnames={'Yeild Stress','Volumetric Strain'};

t=uitable(f,'Data',d,'ColumnName',cnames)

Accu2=0.01;           % Define the accuarcy in plot

p=p0:Accu2:pf;

ecp=(Cc-Cr)/(2.3*(1+e0))*log(p'/p0);

plot(ecp,p,'b-');

title('Hardening Law of D-P Cap Model');

xlabel('Volumetric Strain');

ylabel('Stress (KPa)');

grid on;

```

APPENDIX C

UMAT SUBROUTINE OF THE NEW SAND MODEL

```
C+++++  
  
SUBROUTINE UMAT(STRESS,STATEV,DDSDDE,SSE,SPD,SCD,  
  
1 RPL,DDSDDT,DRPLDE,DRPLDT,STRAN,DSTRAN,  
  
2 TIME,DTIME,TEMP,DTEMP,PREDEF,DPRED,MATERL,NDI,NSHR,NTENS,  
  
3 NSTATV,PROPS,NPROPS,COORDS,DROT,PNEWDT,CELENT,  
  
4 DFGRD0,DFGRD1,NOEL,NPT,KSLAY,KSPT,KSTEP,KINC)  
  
INCLUDE 'ABA_PARAM.INC'  
  
CHARACTER*80 MATERL  
  
DIMENSION STRESS(NTENS),STATEV(NSTATV),  
  
1 DDSDDE(NTENS,NTENS),DDSDDT(NTENS),DRPLDE(NTENS),  
  
2 STRAN(NTENS),DSTRAN(NTENS),TIME(2),PREDEF(1),DPRED(1),  
  
3 PROPS(NPROPS),COORDS(3),DROT(3,3),  
  
4 DFGRD0(3,3),DFGRD1(3,3)  
  
DIMENSION STRANI(6),DSTRESS(6)  
  
COMMON /OUT/ IDBG,IDEF
```

```

CALL CSSAND(DDSDDE,STRAN,DSTRAN,STRESS,DSTRESS,PROPS,NPROPS,
+ STATEV,
2 TIME,DTIME,TEMP,DTEMP,PREDEF,DPRED,MATERL,NDI,NSHR,NTENS,
3 NSTATV,PROPS,NPROPS,COORDS,DROT,PNEWDT,CELENT,
4 DFGRD0,DFGRD1,NOEL,NPT,KSLAY,KSPT,KSTEP,KINC)

RETURN

END

C+++++++++++++++++++++++++++++++
SUBROUTINE SDVINI(STATEV,COORDS,NSTATV,NCRDS,NOEL,NPT,
1 LAYER,KSPT)

INCLUDE 'ABA_PARAM.INC'

DIMENSION STATEV(NSTATV),COORDS(NCRDS),STRESS(6),
+ STRAN(6),TSR(3,3)

NDIM=NCRDS

NTENS=4

if(NDIM.EQ.3)NTENS=6

C=0.75

```

VRI=0.75

PSUCI=21884

WRITE(6,980)NDIM,NTENS

980 FORMAT(1X,'NDIM =',I5,3X,'NTENS =',I5)

DO 10 I=1,3

STRESS(I)=-PSUCI

STRESS(I+3)=0.

STRAN(I)=0.

STRAN(I+3)=0.

10 CONTINUE

DO 40 I=1,NTENS

STATEV(I)=-STRESS(I)

STRESS(I)=-STRESS(I)

STATEV(I+6)=-STRAN(I)

40 CONTINUE

P=(STRESS(1)+STRESS(2)+STRESS(3))/3.D0

TSR(1,1)=(STRESS(1)-P)/P

```

TSR(2,2)=(STRESS(2)-P)/P

TSR(3,3)=(STRESS(3)-P)/P

TSR(1,2)=STRESS(4)/P

IF(NDIM.EQ.3) THEN

  TSR(1,3)=STRESS(5)/P

  TSR(2,3)=STRESS(6)/P

  TSR(2,1)=TSR(1,2)

  TSR(3,1)=TSR(1,3)

  TSR(3,2)=TSR(2,3)

ENDIF

DO 50 I=1,3

  DO 50 J=1,3

    STATEV(I*3-3+J+2*NTENS)=TSR(I,J)

50  CONTINUE

STATEV(22)=VRI

STATEV(23)=0.D0

STATEV(24)=0.D0

```

```

STATEV(25)=0.D0

STATEV(26)=0.D0

STATEV(27)=PSUCI

STATEV(40)=1.

WRITE(6,900)(STATEV(JJ),JJ=1,40)

900 FORMAT(1x,'STATEV'/(8E15.5))

RETURN

END

C+++++++++++++++++++++++++++++++
CSUC SIGMAT instead of SIGMA

SUBROUTINE CSSAND(CLAMDA,EPSLON,DEPSLN,SIGMAT,DSIGMA,PROP,
+ NPROP,
+ STVR,
2 TIME,DTIME,TEMP,DTEMP,PREDEF,DPRED,MATERL,NDI,NSHR,NTENS,
3 NSTVR,PROPS,NPROPS,COORDS,DROT,PNEWDT,CELENT,
4 DFGRD0,DFGRD1,NOEL,NPT,KSLAY,KSPT,KSTEP,KINC)

INCLUDE 'ABA_PARAM.INC'

```

CHARACTER*80 MATERL

PARAMETER (ERALOW=1.D-5,MAXITE=10,AMXDEP=1.D-3)

DOUBLE PRECISION CLAMDA(6,6),DEPSLN(6),DSIGMA(6),PROP(NPROP),

+ STVR(NSTVR)

DOUBLE PRECISION A,BULK,D,E(6,6),EPPSUM,EPSLON(6),G

DOUBLE PRECISION GTHETB,KP,KPBAR,LINDEX,P,QBAR,RBAR,RHO

DOUBLE PRECISION RHOBAR,RL,RM,SIGMA(6),SWINIT,TSALF(3,3)

DOUBLE PRECISION TSNBAR(3,3),TSR(3,3),TSRBAR(3,3),VR

DOUBLE PRECISION DSIGMO(6),EPSUM0,RM0,SIGMA0(6),TSALFO(3,3),VR0

DOUBLE PRECISION BESTA,BESTER,BSTTAF(3,3),BSTCLM(6,6)

DOUBLE PRECISION BSTDSG(6),BSTKPB,BSTLIX,ERALOW,EROR

DOUBLE PRECISION CLAVRG(6,6),DEPGVN(6),MAXDEP

DOUBLE PRECISION PM,PM0,PALFA,PALFA0,BSTPAF,PRHORA,DELTAP

DOUBLE PRECISION DPP,KPPP,NBPP(3,3), TIME(2)

DOUBLE PRECISION TMPA,TH(3,3),TMPC(6),AE,PME,PALFAE,SWINITE

DOUBLE PRECISION SIGMAE(6),EPSLONE(6),DEPSLNE(6),TSALFE(3,3)

DOUBLE PRECISION VRE,RME,EPPSUME,PNEWDT,PSUCE,PSUCT

```
DOUBLE PRECISION SIGMAT(6),PSUC,DPSUC,PSUC0
```

```
INTEGER I,J,MAXITE,N,NITER,NSEG
```

```
DOUBLE PRECISION C,MC,EGMA,LAMDAC,XI,G0,NU,D0,EM,
```

```
$ H1,H2,EN,H3,VRI,PATM,P1,P2,P3,HP,DP,
```

```
$ N1,N2,N3,WG,GS
```

```
COMMON /PRAMTR/C,MC,EGMA,LAMDAC,XI,G0,NU,D0,EM,
```

```
$ H1,H2,EN,H3,VRI,PATM,P1,P2,P3,HP,DP,
```

```
$ N1,N2,N3,WG,GS
```

```
C
```

```
EXTERNAL DECOMP,PROJET,UNORML,ELAS,PLAS,PROJP,PLASP
```

```
EXTERNAL LDINDX,UPDA,INVARN,DOTT,EPSTIFNB,PSUCTION
```

```
DATA E/36*0.D0/,TMPC/6*0.D0/
```

```
C*****
```

```
c Assiging model constants
```

```
C*****
```

```
C=PROP(1)
```

```
MC=PROP(2)
```

EGMA=PROP(3)

LAMDAC=PROP(4)

XI=PROP(5)

G0=PROP(6)

NU=PROP(7)

D0=PROP(8)

EM=PROP(9)

H1=PROP(10)

H2=PROP(11)

EN=PROP(12)

H3=PROP(13)

VRI=PROP(14)

PATM=PROP(15)

P1=PROP(16)

P2=PROP(17)

P3=PROP(18)

asmvl=1.E-17

```
IF (abs(P1).lt.asmvl) P1=5.D-3
```

```
IF (abs(P2).lt.asmvl) P2=2.D0
```

```
IF (abs(P3).lt.asmvl) P3=1.D-2
```

```
HP=PROP(19)
```

```
DP=PROP(20)
```

```
N1=PROP(21)
```

```
N2=PROP(22)
```

```
N3=PROP(23)
```

```
WG=PROP(24)
```

```
GS=PROP(25)
```

```
c*****
```

```
c Sub-incrementing
```

```
c*****
```

```
KCOUNT=0
```

```
DO 25 I=1,NTENS
```

```
SIGMAT(I)=-SIGMAT(I)
```

```
EPSLON(I)=-EPSLON(I)
```

```
DEPSLN(I)=-DEPSLN(I)

25  CONTINUE

DO 40 I=1,6

SIGMAE(I)=STVR(I)

EPSLONE(I)=STVR(I+6)

DEPSLNE(I)=DEPSLN(I)

40  CONTINUE

WRITE(6,975)(SIGMA(JJ),JJ=1,NTENS)

975  FORMAT(1X,'SIGMA-1'/4E15.5)

DO 50 I=1,3

DO 50 J=1,3

TSALFE(I,J)=STVR(I*3-3+J+2*NTENS)

50  CONTINUE

VRE=STVR(22)

RME=STVR(23)

EPPSUME=STVR(24)

PME=STVR(25)
```

```

PALFAE=STVR(26)

PSUCE=STVR(27)

SWINITE=STVR(40)

WRITE(6,1060)NOEL,NPT,KSPT

1060 FORMAT(1x,60(1H=)/'NOEL,NPT,KSPT = ',3I5)

WRITE(6,920)(SIGMA(ij),ij=1,6)

920 FORMAT(/1x,'stress-3d :',6e15.5)

WRITE(6,930)(DEPSLN(ij),IJ=1,6)

930 format(/1x,'DSTRAN-3d :',6e15.5)

WRITE(6,1310)D

1310 FORMAT(1X,'D =',E15.5)

TMPA=0.D0

DO 10 I=1,6

    TMPA=TMPA+DEPSLN(I)*DEPSLN(I)

10    CONTINUE

TMPA=DSQRT(TMPA)

NSEG=INT(TMPA/AMXDEP)+1

```

```

IF (NSEG.GT.1) THEN

DO 20 I=1,6

DEPGVN(I)=DEPSLN(I)

DEPSLN(I)=DEPSLN(I)/REAL(NSEG)

DO 20 J=1,6

CLAVRG(I,J)=0.D0

20      CONTINUE

PSUCT=0.D0

ENDIF

N=0

c*****
c Assigning state variables

c*****

30  CONTINUE

WRITE(6,1450)(SIGMA(IJ),IJ=1,6)

1450  FORMAT(/1X,50(1H=)/1X,'SIGMA'/(6E15.5))

WRITE(6,1455)(STVR(IJ),IJ=1,6)

```

1455 FORMAT(1X,'STVR'/6E15.5)

DO 4021 I=1,6

SIGMA(I)=STVR(I)

EPSLON(I)=STVR(I+6)

DEPSLN(I)=DEPSLN(I)

4021 CONTINUE

DO 5021 I=1,3

DO 5021 J=1,3

TSALF(I,J)=STVR(I*3-3+J+2*NTENS)

5021 CONTINUE

VR=STVR(22)

RM=STVR(23)

EPPSUM=STVR(24)

PM=STVR(25)

PALFA=STVR(26)

PSUC=STVR(27)

SWINIT=STVR(40)

```

CALL UPDA(0.D0,TMPC,TMPC,EPPSUM,EPSON,0.D0,
          $           0.D0,P,RL,RM,SIGMA,TSALF,TSR,VR,PM)

      WRITE(6,976)(SIGMA(JJ),JJ=1,NTENS)

976   FORMAT(1X,'SIGMA-2'/6E15.5)

C*****
C Keeping a copy of state variables

C*****
DO 70 I=1,6

      SIGMA0(I)=SIGMA(I)

      DSIGMA(I)=0.D0

      DSIGMO(I)=DSIGMA(I)

70   CONTINUE

DO 80 I=1,3

      DO 80 J=1,3

      TSALFO(I,J)=TSALF(I,J)

80   CONTINUE

      PSUC0=PSUC

```

```

RM0=RM

VR0=VR

PM0=PM

PALFA0=PALFA

VR=VR-(1.D0+VRI)*(DEPSLN(1)+DEPSLN(2)+DEPSLN(3))/2.D0

EPSUM0=EPPSUM

c*****
c Initializing iteration parameters

c*****
NITER=0

BESTER=1.D10

c*****
c Iteration loop starts here

c*****
CALL PSUCTION(PSUC,VR)

DPSUC=PSUC-PSUC0

SIGMA(1)=SIGMA(1)+DPSUC

```

```

SIGMA(2)=SIGMA(2)+DPSUC

SIGMA(3)=SIGMA(3)+DPSUC

CALL DECOMP(P,SIGMA,TSR)

WRITE(6,977)(SIGMA(JJ),JJ=1,NTENS)

977 FORMAT(1X,'SIGMA-3'/6E15.5)

90 CALL PROJET(GTHETB,QBAR,RBAR,RHO,RHOBAR,RM,TSALF,TSR,TSRBAR)

1025 FORMAT(1X,'NPT,RBAR =',2I7,E15.5)

CALL UNORML(A,GTHETB,QBAR,RBAR,TSNBAR,TSRBAR)

CALL ELAS (BULK,E,G,P,VR)

WRITE(6,1205)BULK,KPPP,DPP,D

1205 FORMAT(1X,'BULK-4 =',E15.5,' KPPP =',E15.5,' DPP =',E15.5,
+ ' D=',E15.5)

CALL PLAS(D,EPPSUM,G,KP,KPBAR,P,RHO,RHOBAR,RL,RM,VR,DSIGMA,GTHETB,
$ RBAR)

WRITE(6,1205)BULK,KPPP,DPP,D

CALL PROJP(DSIGMA,SIGMA0,PM,PALFA,PRHORA,DELTAP)

WRITE(6,978)(SIGMA0(JJ),JJ=1,NTENS)

```

```

978 FORMAT(1X,'SIGMA0-4'/6E15.5)

      WRITE(6,979)(DSIGMA(JJ),JJ=1,NTENS)

979 FORMAT(1X,'DSIGMA-4'/6E15.5)

      CALL PLASP(DELTAP,P,PRHORA,TSR,DPP,KPPP,NBPP,G)

      CALL LDINDX(BULK,D,DEPSLN,G,KP,LINDEX,TSNBAR,TSR,TH,
$          DPP,KPPP,NBPP)

      WRITE(6,1200)BULK,KPPP,DPP,D

1200 FORMAT(1X,'BULK-5 =',E15.5,' KPPP =',E15.5,' DPP =',E15.5,
+ ' D =',E15.5)

      IF (LINDEX.LT.0.D0) THEN

          LINDEX=0.D0

          DO 100 I=1,3

              DO 100 J=1,3

                  TSALF(I,J)=TSR(I,J)

100      CONTINUE

      ENDIF

      CALL EPSTIFNB(BULK,CLAMDA,D,E,G,LINDEX,TSNBAR,TH,DPP,KPPP,NBPP)

```

```

DO 110 I=1,6

DSIGMA(I)=0.D0

DO 110 J=1,6

DSIGMA(I)=DSIGMA(I)+CLAMDA(I,J)*DEPSLN(J)

110    CONTINUE

IF(KDBG.EQ.2)WRITE(6,1985)((CLAMDA(I,J),JJ=1,NTENS),II=1,NTENS)

1985   FORMAT(1X,'CLAMDA-5'/(6E15.5))

WRITE(6,2985)(DEPSLN(JJ),JJ=1,NTENS)

2985   FORMAT(1X,'DEPSLN-5'/6E15.5)

WRITE(6,985)(DSIGMA(JJ),JJ=1,NTENS)

985   FORMAT(1X,'DSIGMA-5'/6E15.5)

C*****
c Calculating iteration error

C*****

EROR=0.D0

TMPA=0.D0

DO 120 I=1,6

```

```

EROR=EROR+DABS(DSIGMA(I)-DSIGMO(I))/2

TMPA=TMPA+DABS(DSIGMA(I)/2)+DABS(DSIGMO(I)/2)+DABS(SIGMA(I))

120    CONTINUE

ERORT=EROR

EROR=DMAX1(EROR/TMPA,1.D-10)

WRITE(6,1100)NPT,NITER,N,NSEG,EROR

1100 FORMAT(1X,'NPT =',I5,2X,'NITER=',I8,2X,'N=',I7,' NSEG=',I7,2X,
+ 'EROR =',E15.5)

C*****
c Keeping a copy of best results

C*****

IF (EROR.LT.BESTER) THEN

  BESTA=A

  BSTKPB=KPBAR

  BSTLIX=LINDEX

  DO 130 I=1,6

    BSTDSG(I)=DSIGMA(I)

```

```
DO 130 J=1,6
```

```
BSTCLM(I,J)=CLAMDA(I,J)
```

```
130      CONTINUE
```

```
DO 140 I=1,3
```

```
DO 140 J=1,3
```

```
BSTTAF(I,J)=TSALF(I,J)
```

```
140      CONTINUE
```

```
BSTPAF=PALFA
```

```
BESTER=EROR
```

```
ENDIF
```

```
C*****
```

```
c Checking convergency & time out
```

```
C*****
```

```
IF ((EROR.GT.ERALOW).AND.(NITER.LT.MAXITE)) THEN
```

```
DO 150 I=1,6
```

```
DSIGMO(I)=DSIGMA(I)
```

```
DSIGMA(I)=DSIGMA(I)/2.D0
```

```
SIGMA(I)=SIGMA0(I)

150      CONTINUE

      WRITE(6,945)P

945  FORMAT(1X,'P =',E15.5)

      WRITE(6,995)(DSIGMO(JJ),JJ=1,NTENS)

995  FORMAT(1X,'DSIGMO-6'/6E15.5)

      WRITE(6,996)(DSIGMA(JJ),JJ=1,NTENS)

996  FORMAT(1X,'DSIGMA-6'/6E15.5)

      WRITE(6,997)(SIGMA(JJ),JJ=1,NTENS)

997  FORMAT(1X,'SIGMA-6'/6E15.5)

      DO 160 I=1,3

      DO 160 J=1,3

      TSALF(I,J)=TSALFO(I,J)

160      CONTINUE

      RM=RM0

      EPPSUM=EPSUM0

      LINDEX=LINDEX/2.D0
```

```

CALL UPDA(0.D0,DEPSLN,DSIGMA,EPPSUM,EPSON,KPBAR,
         $      LINEX,P,RL,RM,SIGMA,TSALF,TSR,VR,PM)

PALFA=PALFA0

NITER=NITER+1

KCOUNT=KCOUNT+1

GOTO 90

ENDIF

IF ((EROR.GT.0.00001D0).AND.(TIME(2).GT.0.00000000011D0)) THEN

AE=DMIN1(0.8D0*(0.00001D0/EROR)**(0.5D0),1.D0)

PNEWDT=AE

WRITE(6,1003)PNEWDT,AE,EROR

1003 FORMAT(1X,'PNEWDT,AE,EROR =',6E15.5)

DO 4011 I=1,6

STVR(I)=SIGMAE(I)

SIGMA(I)=SIGMAE(I)

STVR(I+6)=EPSLONE(I)

EPSLON(I)=EPSLONE(I)

```

4011 CONTINUE

WRITE(6,9751)(SIGMA(JJ),JJ=1,NTENS)

9751 FORMAT(1X,'SIGMA-1'/4E15.5)

DO 5011 I=1,3

DO 5011 J=1,3

STVR(I*3-3+J+2*NTENS)=TSALFE(I,J)

5011 CONTINUE

STVR(22)=VRE

STVR(23)=RME

STVR(24)=EPPSUME

STVR(25)=PME

STVR(26)=PALFAE

STVR(27)=PSUCE

STVR(40)=SWINITE

WRITE(6,9761)(SIGMA(JJ),JJ=1,NTENS)

9761 FORMAT(1X,'SIGMA-1'/4E15.5)

GOTO 201

```

ENDIF

c*****
c Updating state variables

c*****


CALL UPDA(BESTA,DEPSLN,BSTDG,EPSUM0,EPSLON,BSTKPB,
$      BSTLIX,P,RL,RM0,SIGMA0,BSTTAF,TSR,VRO,PM0)

DO 170 I=1,6

      STVR(I)=SIGMA(I)

      STVR(I+6)=EPSLON(I)

      DO 170 J=1,6

            CLAMDA(I,J)=BSTCLM(I,J)

170    CONTINUE

      DO 180 I=1,3

            DO 180 J=1,3

                  STVR(I*3-3+J+2*NTENS)=BSTTAF(I,J)

180    CONTINUE

      IF(KDBG.EQ.1)WRITE(6,1090)KCOUNT

```

```
1090 FORMAT(1x,'KCOUNT =',2I10)
```

```
C
```

```
STVR(22)=VR0
```

```
STVR(23)=RM0
```

```
STVR(24)=EPSUM0
```

```
STVR(25)=PM0
```

```
STVR(26)=BSTOPAF
```

```
STVR(27)=PSUC
```

```
STVR(40)=SWINIT
```

```
C*****
```

```
c Preparing for next sub-increment if any
```

```
C*****
```

```
IF (NSEG.GT.1) THEN
```

```
DO 190 I=1,6
```

```
DO 190 J=1,6
```

```
CLAVRG(I,J)=CLAVRG(I,J)+CLAMDA(I,J)
```

```
190      CONTINUE
```

```
PSUCT=PSUCT+PSUC

N=N+1

IF (N.LT.NSEG) THEN

GOTO 30

ELSE

DO 200 I=1,6

DEPSLN(I)=DEPGVN(I)

DO 200 J=1,6

CLAMDA(I,J)=CLAVRG(I,J)/REAL(NSEG)

200      CONTINUE

PSUC=PSUCT/REAL(NSEG)

ENDIF

ENDIF

201  DO 4014 IJ=1,NTENS

DEPSLN(IJ)=-DEPSLN(IJ)

EPSLON(IJ)=-EPSLON(IJ)

4014 CONTINUE
```

```

DO 401 IJ=1,3

SIGMAT(IJ)=-(SIGMA(IJ)-PSUC)

401 CONTINUE

SIGMAT(4)=-SIGMA(4)

SIGMAT(5)=-SIGMA(5)

SIGMAT(6)=-SIGMA(6)

WRITE(6,1085)KCOUNT,NSEG,NPT

1085 FORMAT(1x,' KCOUNT, NSEG,NPT =',3I10)

RETURN

END

C+++++SUBROUTINE PROJET(GTHETB,QBAR,RBAR,RHO,RHOBAR,
+ RM,TSALF,TSR,TSRBAR)

INCLUDE 'ABA_PARAM.INC'

DOUBLE PRECISION GTHETB,QBAR,RBAR,RHO,RHOBAR,RM

DOUBLE PRECISION TSALF(3,3),TSR(3,3),TSRBAR(3,3)

DOUBLE PRECISION ALCOSB,ALFA2,ASINB2,SIN3TB,TSRHO(3,3)

```

```

DOUBLE PRECISION ERALOW,RES,TMPA

INTEGER I,J,NITER,MAXITR

DOUBLE PRECISION C,MC,EGMA,LAMDAC,XI,G0,NU,D0,EM,
$      H1,H2,EN,H3,VRI,PATM,P1,P2,P3,HP,DP,
$      N1,N2,N3,WG,GS

COMMON /PRAMTR/C,MC,EGMA,LAMDAC,XI,G0,NU,D0,EM,
$      H1,H2,EN,H3,VRI,PATM,P1,P2,P3,HP,DP,
$      N1,N2,N3,WG,GS

EXTERNAL DOTT,INVARN

PARAMETER (MAXITR=10,ERALOW=1.D-6)

C*****
C Calculate Rho based on r and alpha
C*****

DO 10 I=1,3

DO 10 J=1,3

  TSRHO(I,J)=TSR(I,J)-TSALF(I,J)

10  CONTINUE

```

```

CALL DOTT(TSRHO,TSRHO,TMPA)

RHO=DSQRT(TMPA)

C*****
c Estimate Rhobar based on C=1

C*****

CALL DOTT(TSALF,TSALF,ALFA2)

CALL DOTT(TSALF,TSRHO,TMPA)

ALCOSB=TMPA/RHO

ASINB2=ALFA2-ALCOSB*ALCOSB

IF(ASINB2.LT.0.) THEN

  WRITE(6,765)ASINB2

765  FORMAT(1x,'asnib2 =',E15.5)

ENDIF

IF (RM*RM.LE.ASINB2) RM=DSQRT(ASINB2)+1.D-5

RHOBAR=DSQRT(RM*RM-ASINB2)-ALCOSB

C*****
c Iteration for true Rbar

```

```

C*****
NITER=1

20 TMPA=RHOBAR/RHO

DO 30 I=1,3

DO 30 J=1,3

TSRBAR(I,J)=TSALF(I,J)+TMPA*TSRHO(I,J)

30 CONTINUE

WRITE(6,1040)((TSRBAR(II,JJ),JJ=1,3),II=1,3)

1040 FORMAT(1X,'TSRBAR'/(3E15.5))

CALL INVARN(C,GTHETB,QBAR,RBAR,SIN3TB,TSRBAR)

RES=RM*GTHETB-RBAR

IF ((DABS(RES).GT.ERALOW*RM).AND.(NITER.LE.MAXITR)) THEN

RHOBAR=RHOBAR+RES

NITER=NITER+1

GOTO 20

ENDIF

RHOBAR=DMAX1(RHOBAR,RHO)

```

```

RETURN

END

C+++++++++++++++++++++++++++++++
SUBROUTINE UNORML(A,GTHETB,QBAR,RBAR,TSNBAR,TSRBAR)

INCLUDE 'ABA_PARAM.INC'

DOUBLE PRECISION A,GTHETB,QBAR,RBAR,TSNBAR(3,3)

DOUBLE PRECISION TSRBAR(3,3),TMPA,TMPB,TMPC

INTEGER I,J,K

DOUBLE PRECISION C,MC,EGMA,LAMDAC,XI,G0,NU,D0,EM,
$          H1,H2,EN,H3,VRI,PATM,P1,P2,P3,HP,DP,
$          N1,N2,N3,WG,GS

COMMON /PRAMTR/C,MC,EGMA,LAMDAC,XI,G0,NU,D0,EM,
$          H1,H2,EN,H3,VRI,PATM,P1,P2,P3,HP,DP,
$          N1,N2,N3,WG,GS

ASMV=1.E-17

WRITE(6,1030)RBAR

1030 FORMAT(1x,'RBAR =',E15.5)

```

```

IF(ABS(RBAR).LT.ASMVL) THEN

    TMPA=0.D0

    TMPB=0.D0

    ELSE

        TMPA=3.67423461417477D0*(1.D0-C)/C/RBAR/RBAR

        TMPB=1.D0/RBAR/GTHETB+TMPA*QBAR/RBAR/RBAR

    ENDIF

    DO 20 I=1,3

        DO 20 J=1,3

            TMPC=0.D0

            DO 10 K=1,3

                TMPC=TMPC+TSRBAR(K,I)*TSRBAR(J,K)

            10      CONTINUE

            TSNBAR(I,J)=TMPB*TSRBAR(I,J)-TMPA*TMPC

        20      CONTINUE

        TMPA=(TSNBAR(1,1)+TSNBAR(2,2)+TSNBAR(3,3))/3.D0

        TSNBAR(1,1)=TSNBAR(1,1)-TMPA

```

```

TSNBAR(2,2)=TSNBAR(2,2)-TMPA

TSNBAR(3,3)=TSNBAR(3,3)-TMPA

A=0.D0

DO 30 I=1,3

DO 30 J=1,3

A=A+TSNBAR(I,J)*TSNBAR(I,J)

30    CONTINUE

A=DSQRT(A)

DO 40 I=1,3

DO 40 J=1,3

TSNBAR(I,J)=TSNBAR(I,J)/A

40    CONTINUE

RETURN

END

C+++++++++++++++++++++++++++++++
SUBROUTINE ELAS(BULK,E,G,P,VR)

INCLUDE 'ABA_PARAM.INC'

```

```
DOUBLE PRECISION BULK,E(6,6),G,P,VR
```

```
DOUBLE PRECISION C,MC,EGMA,LAMDAC,XI,G0,NU,D0,EM,
```

```
$ H1,H2,EN,H3,VRI,PATM,P1,P2,P3,HP,DP,
```

```
$ N1,N2,N3,WG,GS
```

```
COMMON /PRAMTR/C,MC,EGMA,LAMDAC,XI,G0,NU,D0,EM,
```

```
$ H1,H2,EN,H3,VRI,PATM,P1,P2,P3,HP,DP,
```

```
$ N1,N2,N3,WG,GS
```

```
ASMVLL=1.E-17
```

```
IF((PATM*P).LT.0) THEN
```

```
765 FORMAT(1x,'PATM*(+P)',E15.5,2x,'PATM =',E15.5,2X,'P=',E15.5/
```

```
+ 1X, 'An attempt will be made to calculate a sqrt of a neg num')
```

```
WRITE(6,765)PATM*P,PATM,P
```

```
P=DABS(P)
```

```
G=G0*(2.973D0-VR)**2/(1.D0+VR)*DSQRT(PATM*(+P))
```

```
else
```

```
G=G0*(2.973D0-VR)**2/(1.D0+VR)*DSQRT(PATM*(+P))
```

```
ENDIF
```

```
BULK=G*(1.D0+NU)/(1.D0-2.D0*NU)/1.5D0

WRITE(6,900)G0,VR,PATM,P,G,NU

900 FORMAT(1X,'G0,VR,PATM,P,G,NU =',6E15.5)

E(1,1)=BULK+G/.75D0

E(2,2)=E(1,1)

E(3,3)=E(1,1)

E(4,4)=G

E(5,5)=G

E(6,6)=G

E(1,2)=BULK-G/1.5D0

E(1,3)=E(1,2)

E(2,3)=E(1,2)

E(2,1)=E(1,2)

E(3,1)=E(1,2)

E(3,2)=E(1,2)

RETURN

END
```

```

C+++++++++++++++++++++++++++++++
SUBROUTINE PLAS(D,EPPSUM,G,KP,KPBAR,P,RHO,RHOBAR,RL,RM,
+
+           VR,DSIGMA,GTHETB,RBAR)

INCLUDE 'ABA_PARAM.INC'

DOUBLE PRECISION D,EPPSUM,G,KP,KPBAR,P,RHO,RHOBAR,RL,RM,VR

DOUBLE PRECISION PMIN,PSI,TMPA,TMPB,TMPC,TMPD,TMPE,DGIGMA

DOUBLE PRECISION RBAR, GTHETB

DOUBLE PRECISION C,MC,EGMA,LAMDAC,XI,G0,NU,D0,EM,
$           H1,H2,EN,H3,VRI,PATM,P1,P2,P3,HP,DP

COMMON /PRAMTR/C,MC,EGMA,LAMDAC,XI,G0,NU,D0,EM,
$           H1,H2,EN,H3,VRI,PATM,P1,P2,P3,HP,DP

EXTERNAL DOTT,INVARN

KDBG=0

TMPA=RHO/RHOBAR

TMPB=MC

PSI=VR-(EGMA-LAMDAC*(+P/PATM)**XI)

WRITE(6,1000)PSI,TMPA,TMPB

```

```

1000 FORMAT(1X,'PSI,TMPA,TMPB =',3E15.5)

TMPC=RL/TMPB

PMIN=.002D0*PATM

TMPD=1.D0-DEXP((PMIN-P)/PMIN)

WRITE(6,1011)PMIN,PSI,TMPA,TMPB,TMPC,TMPD

1011 FORMAT(1X,'PMIN,PSI,TMPA,TMPB,TMPC,TMPD =',6E15.5)

D=D0*(DEXP(EM*PSI)/DSQRT(TMPA)-TMPC)

WRITE(6,1052)D

1052 FORMAT(1x,'D =',E15.5)

WRITE(6,1053)PSI

1053 FORMAT(1x,'PSI=',E15.5)

TMPB=TMPB/(RBAR/GTHETB)

TMPC=DEXP(EN*PSI)

TMPD=TMPA**10

TMPE=EPPSUM/P1

TMPE=H3*((1.D0-P3)/DSQRT((1.-TMPE)**2+TMPE/P2/P2)+P3)

TMPE=G*(H1-H2*VRI)*(TMPD+TMPE*(1.D0-TMPD))

```

```

KPBAR=TMPE*(TMPB/TMPC-1)

KP=TMPE*(TMPB/TMPA/TMPC-1)

WRITE(6,1061)KPBAR

1061 FORMAT(1x,'KPBAR =',E15.5)

WRITE(6,1062)KP

1062 FORMAT(1x,'KP =',E15.5)

RETURN

END

C+++++++++++++++++++++++++++++++
SUBROUTINE LDINDX(BULK,D,DEPSLN,G,KP,LINDEX,TSNBAR,TSR,TH,
$                 DPP,KPPP,NBPP)

INCLUDE 'ABA_PARAM.INC'

DOUBLE PRECISION BULK,D,DEPSLN(6),G,KP,LINDEX

DOUBLE PRECISION TSNBAR(3,3),TSR(3,3)

DOUBLE PRECISION TMPA,TMPB,TMPC,TH(3,3)

DOUBLE PRECISION DPP,KPPP,NBPP(3,3),B

INTEGER I,J

```

EXTERNAL DOTT

CALL DOTT(TSNBAR,TSR,TMPA)

CALL DOTT(TSNBAR,NBPP,TMPB)

TMPC=.816496580927726D0*BULK*DPP

B=(2.D0*G*TMPB-TMPC*TMPA)/(KPPP+TMPC)

TMPA=BULK*(TMPA+B)*1.5D0

TMPC=3.D0*G

TMPC=TMPB-0.816496580927726D0*TMPA*D+1.5D0*KP

DO 20 I=1,3

DO 20 J=1,3

TH(I,J)=TMPB*TSNBAR(I,J)

IF (I.EQ.J) THEN

TH(I,J)=TH(I,J)-TMPA

ENDIF

TH(I,J)=TH(I,J)/TMPC

20 CONTINUE

LINDEX=TH(1,1)*DEPSLN(1)+TH(2,2)*DEPSLN(2)+TH(3,3)*DEPSLN(3)

```

$      +TH(1,2)*DEPSLN(4)+TH(1,3)*DEPSLN(5)+TH(2,3)*DEPSLN(6)

RETURN

END

C+++++++++++++++++++++++++++++++
SUBROUTINE EPSTIFNB(BULK,CL,D1,E,G,LINDEX,AN,
+ TH,D2,KP2,AM)

INCLUDE 'ABA_PARAM.INC'

DOUBLE PRECISION BULK,AL(3,3,3,3),D1,E(6,6),G,LINDEX,AN(3,3)

DOUBLE PRECISION TH(3,3),TMPA,TMPB,TMPC(6),TMPCD(6),Z(3,3)

DOUBLE PRECISION D2,KP2,AM(3,3),FM(3,3),PI2,TMPE(6),ETT(6,6)

DOUBLE PRECISION ET(3,3,3,3),ETA(3,3,3,3),ZZ(3,3),CL(6,6)

DIMENSION NORD(3,3)

DATA ((NORD(IH,JH),JH=1,3),IH=1,3)/ 1,4,5,4,2,6,5,6,3 /

INTEGER I,J

NTENS = 6

ASMVLL=1.E-17

DO 5 IK=1,6

```

```

DO 5 JK=1,6

5  CL(IK,JK)=0.D0

ALAM=BULK-(2.D0/3.D0)*G

T1=BULK+(4.D0/3.D0)*G

T2=G

T3=BULK-(2.D0/3.D0)*G

DEN = KP2 + DSQRT( 2.D0 / 3.D0 ) * BULK * D2

FN3 = DSQRT( 2.D0 / 3.D0 ) * BULK * D1

WRITE(6,565)KP2,BULK,D2,DEN,FAC

565 FORMAT(/1X,'KP2,BULK,D2,DEN,FAC ='/5E15.5)

FAC1 = DSQRT ( 2.D0 / 27.D0 )

DO 80 I = 1, 6

DO 80 J = 1, 6

80    ETT(I,J)=0.D0

DO 20 II=1,3

DO 20 JJ=1,3

IF (JJ.GT.II) GOTO 19

```

IJ = NORD(II,JJ)

DIJ=0.D0

IF(II.EQ.JJ) DIJ=1.D0

DO 15 KK=1,3

DJK=0.D0

IF(JJ.EQ.KK) DJK=1.D0

DIK=0.D0

IF(II.EQ.KK) DIK=1.D0

DO 15 LL=1,3

KL = NORD(KK,LL)

DIL=0.D0

IF(II.EQ.LL) DIL=1.D0

DJL=0.D0

IF(JJ.EQ.LL) DJL=1.D0

DKL=0.D0

IF(KK.EQ.LL) DKL=1.D0

ETT(IJ,KL)= ALAM * DIJ * DKL + G * (DIK * DJL + DIL * DJK)

```
IF(ABS(ETT(IJ,KL)).GT.ASMVL) THEN  
  
    WRITE(6,700)IJ,JJ,KK,LL,IJ,KL,DIJ,DKL,DIK,DJL,DIL,DJK,ETT(IJ,KL)  
  
ENDIF  
  
700 FORMAT(1X,'**',6I5,6F8.0,E15.5)  
  
15 CONTINUE  
  
19 CONTINUE  
  
20 CONTINUE  
  
IF(LINDEX.LT.ASMVL) THEN  
  
    DO 60 IK=1,6  
  
        DO 60 JK=1,6  
  
            60 CL(IK,JK)=ETT(IK,JK)  
  
        goto 399  
  
    ENDIF  
  
    WRITE(6,1090)LINDEX  
  
1090 FORMAT(/1x,'*** PLASTIC. LINEX =',E15.5)  
  
    DO 10 I=1,3  
  
        DO 10 J=1,3
```

DIJ=0.D0

IF(I.EQ.J) DIJ = 1.D0

ZZ(I,J) = (BULK * DIJ - FN3 * TH(I,J))/DEN

10 CONTINUE

DO 50 I = 1 ,3

DO 50 J = 1, 3

IF (J.GT.I) GOTO 49

IJ = NORD(I,J)

DO 40 K = 1, 3

DO 40 L = 1, 3

KL=NORD(K,L)

DO 40 IP = 1, 3

DPK=0.D0

IF(IP.EQ.K) DPK=1.

DO 40 IQ = 1, 3

IPQ = NORD(IP,IQ)

DQL = 0.D0

```

IF(IQ.EQ.L) DQL = 1.

DPQ = 0.D0

IF(IP.EQ.IQ) DPQ = 1.

CON=1.D0

IF(IPQ.GT.3) CON = 0.5D0

TERM = CON * ETT(IJ,IPQ) * ( DPK*DQL -
+ ( AN(IP,IQ) + FAC1 * D1 * DPQ ) * TH(K,L) -
+ ( AM(IP,IQ) + FAC1 * D2 * DPQ ) * ZZ(K,L))

CL(IJ,KL) = CL(IJ,KL) + TERM

DM=DPK*DPQ

900 FORMAT(1X,4I5,4F9.0,E15.5)

40 CONTINUE

49 CONTINUE

50 CONTINUE

399 CONTINUE

450 CONTINUE

WRITE(6,1986)((CL(II,JJ),JJ=1,NTENS),II=1,NTENS)

```

```

1986 FORMAT(1X,'CL-1'/(6E15.5))

RETURN

END

C+++++++++++++++++++++++++++++++
SUBROUTINE UPDA(A,DEPSLN,DSIGMA,EPPSUM,EPSLON,KPBAR,
$      LINDEX,P,RL,RM,SIGMA,TSALF,TSR,VR,PM)

INCLUDE 'ABA_PARAM.INC'

DOUBLE PRECISION A,DEPSLN(6),DSIGMA(6),EPPSUM,EPSLON(6),KPBAR

DOUBLE PRECISION LINDEX,P,RL,RM,SIGMA(6),TSALF(3,3),TSR(3,3)

DOUBLE PRECISION VR,GTHETA,Q,R,SIN3TH,TSRHO(3,3),RHO,TMPA,PM

INTEGER I,J

INTEGER*4 ISEED

DOUBLE PRECISION C,MC,EGMA,LAMDAC,XI,G0,NU,D0,EM,

$      H1,H2,EN,H3,VRI,PATM,P1,P2,P3,HP,DP,

$      N1,N2,N3,WG,GS

COMMON /PRAMTR/C,MC,EGMA,LAMDAC,XI,G0,NU,D0,EM,

$      H1,H2,EN,H3,VRI,PATM,P1,P2,P3,HP,DP,

```

```
$          N1,N2,N3,WG,GS

EXTERNAL INVARN,DECOMP,DOTT

NTENS=6

WRITE(6,975)(SIGMA(JJ),JJ=1,NTENS)

975  FORMAT(1X,'SIGMA-11'/6E15.5)

DO 10 I=1,6

  SIGMA(I)=SIGMA(I)+DSIGMA(I)

10  CONTINUE

WRITE(6,976)(SIGMA(JJ),JJ=1,NTENS)

976  FORMAT(1X,'SIGMA-12'/6E15.5)

CALL DECOMP(P,SIGMA,TSR)

WRITE(6,977)(SIGMA(JJ),JJ=1,NTENS)

977  FORMAT(1X,'SIGMA-13'/6E15.5)

TMPA=.001D0*PATM

IF (P.LT.TMPA) THEN

  TMPA=TMPA-P

WRITE(6,750)TMPA,P
```

```
750    FORMAT(1X,'TMPA =',E15.5,2X,'P=',E15.5)
```

```
SIGMA(1)=SIGMA(1)+TMPA
```

```
SIGMA(2)=SIGMA(2)+TMPA
```

```
SIGMA(3)=SIGMA(3)+TMPA
```

```
CALL DECOMP(P,SIGMA,TSR)
```

```
ENDIF
```

```
WRITE(6,978)(SIGMA(JJ),JJ=1,NTENS)
```

```
978    FORMAT(1X,'SIGMA-14'/6E15.5)
```

```
CALL INVARN(C,GTHETA,Q,R,SIN3TH,TSR)
```

```
IF (R.LT.1.D-10) THEN
```

```
DO 20 I=1,6
```

```
ISEED=INT(VR*1.D3)
```

```
SIGMA(I)=SIGMA(I)+(RAN(ISEED)-.5)*P*1.D-8
```

```
20    CONTINUE
```

```
CALL DECOMP(P,SIGMA,TSR)
```

```
ENDIF
```

```
WRITE(6,979)(SIGMA(JJ),JJ=1,NTENS)
```

```

979 FORMAT(1X,'SIGMA-15'/6E15.5)

DO 30 I=1,3

DO 30 J=1,3

  TSRHO(I,J)=TSR(I,J)-TSALF(I,J)

30      CONTINUE

CALL DOTT(TSRHO,TSRHO,TMPA)

RHO=DSQRT(TMPA)

IF (RHO.LT.1.D-10) THEN

DO 40 I=1,6

  ISEED=INT(VR*1.D4)

  SIGMA(I)=SIGMA(I)+(RAN(ISEED)-.5)*P*1.D-8

40      CONTINUE

CALL DECOMP(P,SIGMA,TSR)

ENDIF

PM=DMAX1(PM,P)

CALL INVARN(C,GTHETA,Q,R,SIN3TH,TSR)

RL=R/GTHETA

```

```

RM=DMAX1(RM+A*LINDEX*KPBAR/1.5D0/P,RL,1.D-10)

VR=VR-(1.D0+VRI)*(DEPSLN(1)+DEPSLN(2)+DEPSLN(3))

DO 50 I=1,6

EPSLON(I)=EPSLON(I)+DEPSLN(I)

50    CONTINUE

EPPSUM=EPPSUM+LINDEX

RETURN

END

C+++++++++++++++++++++++++++++++
SUBROUTINE DECOMP(P,SIGMA,TSR)

INCLUDE 'ABA_PARAM.INC'

DOUBLE PRECISION P,SIGMA(6),TSR(3,3)

P=(SIGMA(1)+SIGMA(2)+SIGMA(3))/3.D0

TSR(1,1)=(SIGMA(1)-P)/P

TSR(2,2)=(SIGMA(2)-P)/P

TSR(3,3)=(SIGMA(3)-P)/P

TSR(1,2)=SIGMA(4)/P

```

```

TSR(1,3)=SIGMA(5)/P

TSR(2,3)=SIGMA(6)/P

TSR(2,1)=TSR(1,2)

TSR(3,1)=TSR(1,3)

TSR(3,2)=TSR(2,3)

RETURN

END

C+++++++++++++++++++++++++++++++
SUBROUTINE INVARN(C,GTHETA,Q,R,SIN3TH,TENSOR)

INCLUDE 'ABA_PARAM.INC'

DOUBLE PRECISION C,GTHETA,Q,R,SIN3TH,TENSOR(3,3)

DOUBLE PRECISION TMPA

INTEGER I,J,K

EXTERNAL DOTT

asmvl=1.E-17

CALL DOTT(TENSOR,TENSOR,TMPA)

IF (abs(TMPA).lt.asmvl) THEN

```

```

R=0.D0

Q=0.D0

SIN3TH=-1.D0

ELSE

R=DSQRT(TMPA)

Q=0.D0

DO 10 I=1,3

    DO 10 J=1,3

        DO 10 K=1,3

            Q=Q+TENSOR(I,J)*TENSOR(J,K)*TENSOR(K,I)

10      CONTINUE

SIN3TH=DMIN1(DMAX1(-4.5*Q/R/R/R,-1.D0),1.D0)

ENDIF

WRITE(6,1050)R

1050 FORMAT(1x,'R =',E15.5)

GTHETA=2.D0*C/((1.D0+C)+(1.D0-C)*SIN3TH)

RETURN

```

```

END

C+++++++++++++++++++++++++++++++
SUBROUTINE DOTT(A,B,DOT)

INCLUDE 'ABA_PARAM.INC'

DOUBLE PRECISION A(3,3),B(3,3),DOT

INTEGER I,J

DOT=0.D0

DO 10 I=1,3

    DO 10 J=1,3

        DOT=DOT+A(I,J)*B(I,J)

10 CONTINUE

RETURN

END

C+++++++++++++++++++++++++++++++
SUBROUTINE PROJP(DSIGMA,SIGMA0,PM,PALFA,PRHORA,DP)

INCLUDE 'ABA_PARAM.INC'

DOUBLE PRECISION DSIGMA(6),SIGMA0(6),PM,PALFA,PRHORA,

```

```

+ DP,P,PO

ASMVL=1.E-17

DP=(DSIGMA(1)+DSIGMA(2)+DSIGMA(3))/3.D0

WRITE(6,900)DP

900  FORMAT(1X,'DP =',E15.5)

IF (ABS(DP).LE.ASMVL) RETURN

P0=(SIGMA0(1)+SIGMA0(2)+SIGMA0(3))/3.D0

IF ((P0-PALFA)*DP.LT.ASMVL) PALFA=P0

P=P0+DP

IF (DP.LT.ASMVL) THEN

PRHORA=(PALFA-P)/PALFA

ELSE

PRHORA=(P-PALFA)/(PM-PALFA)

ENDIF

PRHORA=DMIN1(DMAX1(0.D0,PRHORA),1.D0)

RETURN

END

```

```

C+++++++++++++++++++++++++++++++
SUBROUTINE PLASP(DELТАP,P,PRHORA,TSR,DPP,KPPP,NBPP,G)

INCLUDE 'ABA_PARAM.INC'

DOUBLE PRECISION DELТАP,P,PRHORA,TSR(3,3),DPP,KPPP,NBPP(3,3)

DOUBLE PRECISION GTHETA,R,TMPA,TMPB,G

INTEGER I,J

DOUBLE PRECISION C,MC,EGMA,LAMDAC,XI,G0,NU,D0,EM,

$      H1,H2,EN,H3,VRI,PATM,P1,P2,P3,HP,DP

COMMON /PRAMTR/C,MC,EGMA,LAMDAC,XI,G0,NU,D0,EM,

$      H1,H2,EN,H3,VRI,PATM,P1,P2,P3,HP,DP

EXTERNAL INVARN

ASMVL=1.E-17

IF (ABS(DELТАP).LT.ASMVL) THEN

  KPPP=1.D10

  RETURN

ELSE

  CALL INVARN(C,GTHETA,TMPA,R,TMPB,TSR)

```

```

TMPA=MC*GTHETA/R

TMPB=DSIGN(1.D0,DELTAP)

KPPP=TMPB*HP*G*TMPA

$      /DMAZ1(PRHORA,1.D-10)

DPP=TMPB*DP*(TMPA-1.D0)

WRITE(6,1054)DPP

1054 FORMAT(1x,'DPP =',E15.5)

ENDIF

DO 10 I=1,3

DO 10 J=1,3

NBPP(I,J)=TSR(I,J)/R

10  CONTINUE

RETURN

END

C+++++++++++++++++++++++++++++++
SUBROUTINE PSUCTION(PSUC,VR)

INCLUDE 'ABA_PARAM.INC'

```

DOUBLE PRECISION PSUC,VR

DOUBLE PRECISION C,MC,EGMA,LAMDAC,XI,G0,NU,D0,EM,

\$ H1,H2,EN,H3,VRI,PATM,P1,P2,P3,HP,DP,

\$ N1,N2,N3,WG,GS

COMMON /PRAMTR/C,MC,EGMA,LAMDAC,XI,G0,NU,D0,EM,

\$ H1,H2,EN,H3,VRI,PATM,P1,P2,P3,HP,DP,

\$ N1,N2,N3,WG,GS

PSUC=PATM*N1*(1/((WG*2.6D0)**N2)-1/(VR**N2))**((N3/N2)

RETURN

END

APPENDIX D

MATRIC SUCTION TEST RESULTS OF CRREL SOILS

Soil Type: A-4							
Sample #	can (g)	can+wet (g)	can+dry (g)	moisture content (%)	degree of saturation (%)	matric suction (kpa)	Temperature (oC)
A4-1	10.33	15.79	15.72	1.2	10.0	4020	23.5
A4-2	10.25	17.45	17.35	1.4	10.9	6100	23.3
A4-3	10.34	18.83	18.65	2.1	16.8	1170	23.4
A4-4	10.52	17.14	16.98	2.4	19.2	870	23.8
A4-5	11.36	18.93	18.71	2.9	23.2	460	23.5
A4-6	10.41	17.27	17.02	3.7	29.3	220	23.7
A4-7	10.26	16.98	16.75	3.5	27.4	300	23.5
A4-8	10.56	17.96	17.6	5.1	39.6	120	23.4
A4-9	10.33	15.19	14.92	5.8	45.6	200	23.3
A4-10	10.33	15.48	15.16	6.6	51.4	180	23.5
A4-11	10.41	15.2	14.86	7.6	59.2	170	24.1
A4-12	10.72	14.97	14.63	8.6	67.4	270	24.2
A4-13	10.27	15.79	15.28	10.1	78.9	90	24.4
A4-14	4.42	9.5	9.01	10.6	82.8	100	24.4
A4-15	4.57	9.41	8.91	11.5	89.3	40	23.3
A4-16	6.07	11.58	10.95	12.9	100.1	-300	24.0
A4-17	4.48	9.18	8.59	14.3	111.3	-110	24.0
A4-18	5.1	11.75	10.88	15.0	116.7	-110	23.9
A4-19	4.45	10.88	9.96	16.6	129.5	-40	24.0
A4-20	5.02	11.43	10.48	17.3	135.0	-100	24.0
A4-21	4.87	11.06	10.09	18.5	144.1	-200	22.5
A4-22	5.15	11.82	10.76	18.8	146.6	-160	22.7
A4-23	4.7	11.06	10	20.0	155.1	-190	23.0
A4-24	6.44	13.78	13.64	1.9	15.0	1210	23.3
A4-25	6.66	13.95	13.8	2.1	16.3	1230	23.3
A4-26	4.77	11.87	11.68	2.7	21.3	960	23.4
A4-27	4.68	12.85	12.57	3.5	27.5	230	23.6
A4-28	4.54	12.61	11.37	18.1	140.8	-480	23.5
A4-29	6.24	13.25	12.12	19.2	149.1	-160	23.6
A4-30	10.33	14.23	13.52	22.2	172.6	-200	23.5
A4-31	4.77	13.08	13.06	0.2	1.8	46500	23.6

A4-32	4.77	13.14	13.06	0.9	7.4	5750	23.7
A4-33	10.33	18.33	18.22	1.3	10.8	3510	23.8
A4-34	10.25	17.49	17.41	1.1	8.6	8130	24.0
A4-35	10.34	17.45	17.39	0.8	6.6	14600	24.2
A4-36	10.53	17.16	17.11	0.7	5.8	16300	24.4
A4-37	11.37	17.16	17.12	0.6	5.3	32300	24.7
A4-38	10.4	15.08	15.07	0.2	1.6	46000	25.1

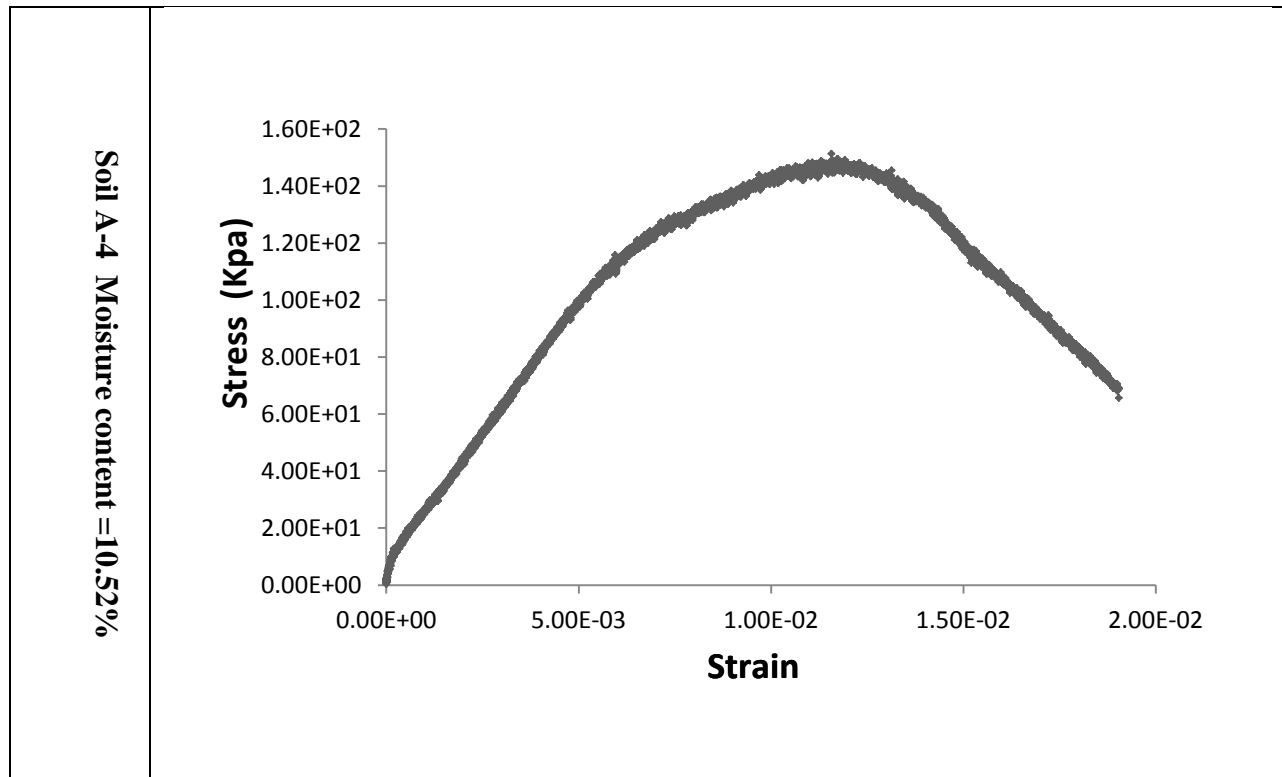
Soil Type: A-6							
Sample #	can (g)	can+wet (g)	can+dry (g)	moisture content (%)	degree of saturation (%)	matric suction (kpa)	Temperature (oC)
A6-0	10.25	12.69	12.67	0.8	4.5	>83600	23.5
A6-1	10.53	14.48	14.36	3.1	17.3	11900	23.6
A6-2	10.25	13.66	13.48	5.5	30.9	3720	23.7
A6-3	10.34	16.03	15.86	3.0	17.0	15200	23.7
A6-4	10.53	15.86	15.62	4.7	26.1	4610	23.6
A6-5	11.35	18.62	18.25	5.3	29.7	2620	24.2
A6-6	10.4	16.55	16.17	6.5	36.5	1850	24.3
A6-7	10.26	17.23	16.77	7.0	39.1	1710	24.0
A6-8	10.57	15.07	14.73	8.1	45.3	1330	24.0
A6-9	10.34	16.62	16.02	10.5	58.5	660	24.2
A6-10	10.34	15.55	15.04	10.8	60.1	620	24.1
A6-11	10.41	16.8	16.14	11.5	63.8	420	23.7
A6-12	10.72	17.9	17.09	12.7	70.5	360	23.7
A6-13	10.28	19.49	18.33	14.9	79.9	280	23.6
A6-14	4.42	8.48	7.96	14.6	81.4	160	23.8
A6-15	4.56	11.94	10.96	15.3	84.9	30	24.2
A6-16	6.07	12.0	11.17	16.2	90.2	90	24.2
A6-17	4.48	11.99	10.89	17.1	95.1	40	24.4
A6-18	5.11	11.17	10.22	18.5	103.1	100	24.3
A6-19	4.45	12.28	11.02	19.1	106.3	-110	24.1
A6-20	5.02	11.05	10.04	20.1	111.5	-50	24.1
A6-21	4.89	9.92	9.04	21.2	117.6	-330	24.0
A6-22	5.14	11.61	10.43	22.3	123.7	-10	24.1
A6-23	4.7	9.14	8.47	17.7	98.5	320	23.9
A6-24	6.45	14.22	13	18.6	103.3	-10	23.9
A6-25	6.66	12.16	11.26	19.5	108.5	-150	23.8
A6-26	4.78	12.23	11.97	3.6	20.0	9200	24.1
A6-27	4.69	10.09	9.73	7.1	39.6	1460	24.1
A6-28	4.54	9.48	9.27	4.4	24.6	5170	24.2

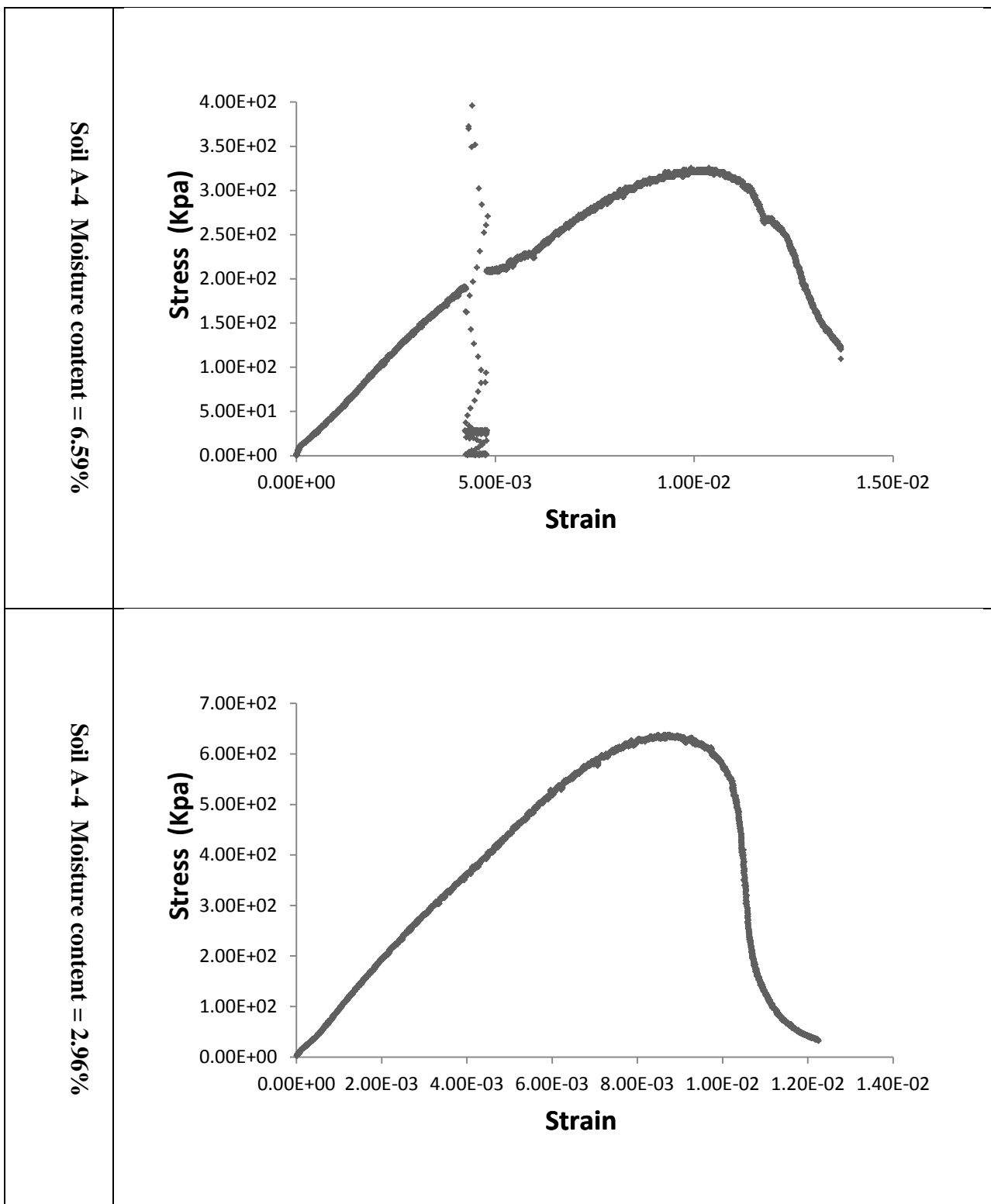
A6-29	6.24	12.14	12.03	1.8	10.5	37500	24.2
A6-30	6.53	13.21	13.06	2.2	12.7	27300	24.1
A6-31	4.96	12.27	12.13	1.9	10.8	45800	24.1
A6-32	6.07	12.56	12.49	1.0	6.0	59200	24.0

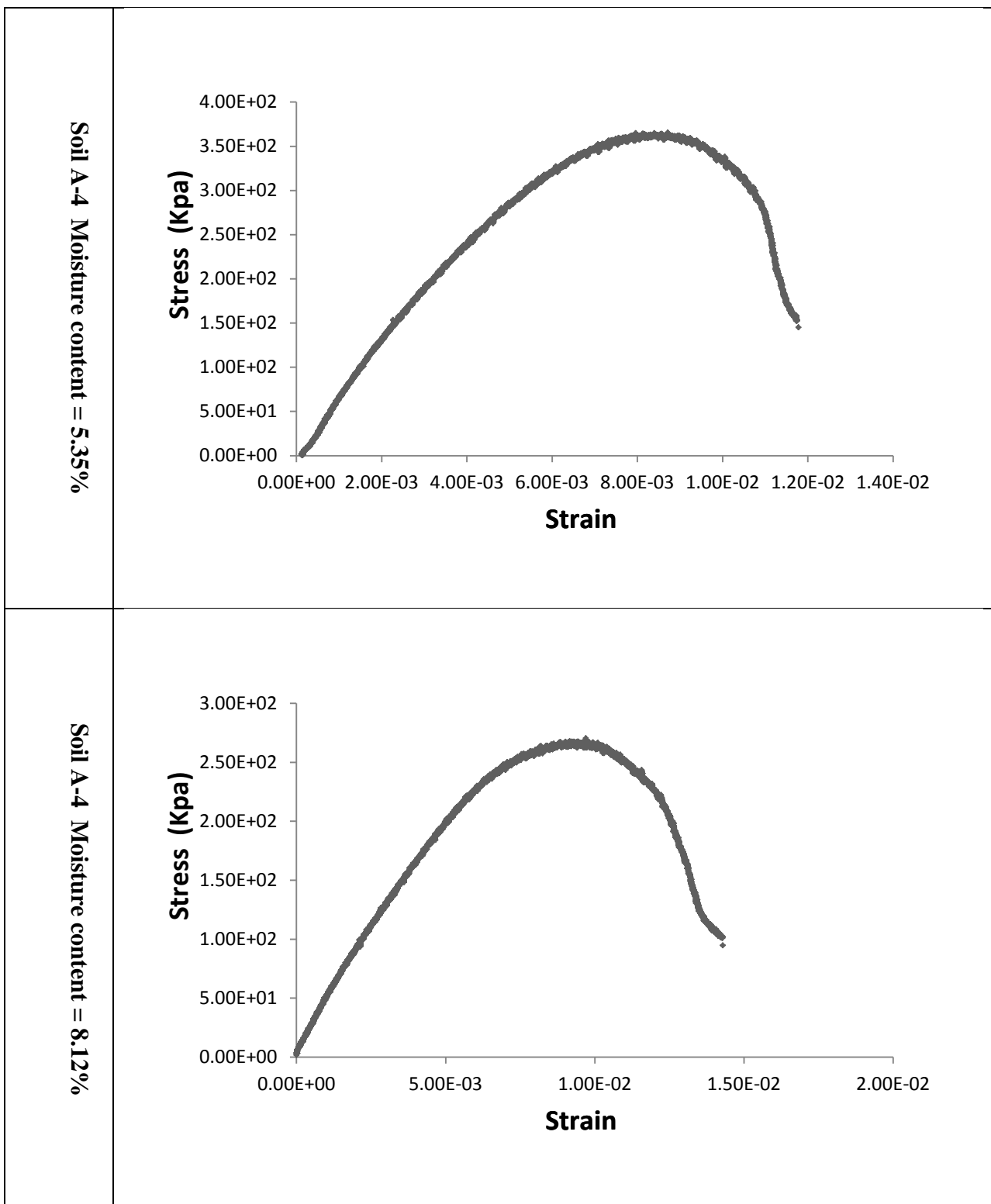
Soil Type: A-7-5							
Sample #	can (g)	can+wet (g)	can+dry (g)	moisture content (%)	degree of saturation (%)	matric suction (kpa)	Temperature (oC)
A75-1	10.33	19.76	19.64	1.2	7.4	83800	23.4
A75-2	10.25	18.5	18.39	1.3	7.8	67400	23.2
A75-3	10.35	17.63	17.49	1.9	11.3	42800	23.3
A75-4	10.52	16.91	16.74	2.7	15.8	18200	23.4
A75-5	11.37	19.82	19.63	2.3	13.3	30800	23.5
A75-6	10.41	17.51	17.25	3.8	22.0	10200	23.6
A75-7	10.25	17.06	16.75	4.7	27.6	5620	23.8
A75-8	10.57	17.77	17.48	4.1	24.3	7870	24.1
A75-9	10.33	17.07	16.71	5.6	32.6	4010	24.1
A75-10	10.34	18.09	17.68	5.5	32.3	4470	24.2
A75-11	10.42	16.23	15.85	6.9	40.5	2550	24.3
A75-12	10.72	17.35	16.85	8.1	47.2	1610	24.1
A75-13	10.27	17.5	16.19	22.1	128.2	-140	24.1
A75-14	4.42	9.87	9.45	8.3	48.3	1530	24.2
A75-15	4.56	10.28	9.78	9.5	55.4	1140	24.1
A75-16	6.08	10.44	10.01	10.9	63.3	990	24.2
A75-17	4.47	10.16	9.53	12.4	72.1	850	24.3
A75-18	5.11	11.01	10.35	12.5	72.9	700	24.2
A75-19	4.45	10.45	9.71	14.0	81.5	710	24.2
A75-20	5.01	10.84	10.09	14.7	85.5	420	24.3
A75-21	4.87	11.49	10.55	16.5	95.8	200	24.2
A75-22	5.15	10.42	9.66	16.8	97.6	240	24.2
A75-23	4.71	12.11	12.02	1.2	7.1	>83600	24.1
A75-24	6.44	12.75	12.66	1.4	8.3	>83600	23.4
A75-25	6.65	13.04	12.91	2.0	12.0	40600	23.5
A75-26	4.77	10.01	9.9	2.1	12.4	46600	23.7
A75-27	4.68	9.85	9.75	1.9	11.4	57900	23.8
A75-28	4.55	9.31	9.19	2.5	14.9	23600	23.9
A75-29	6.26	10.43	10.29	3.4	20.1	14900	24.0
A75-30	6.52	9.94	9.82	3.6	21.0	15200	24.2

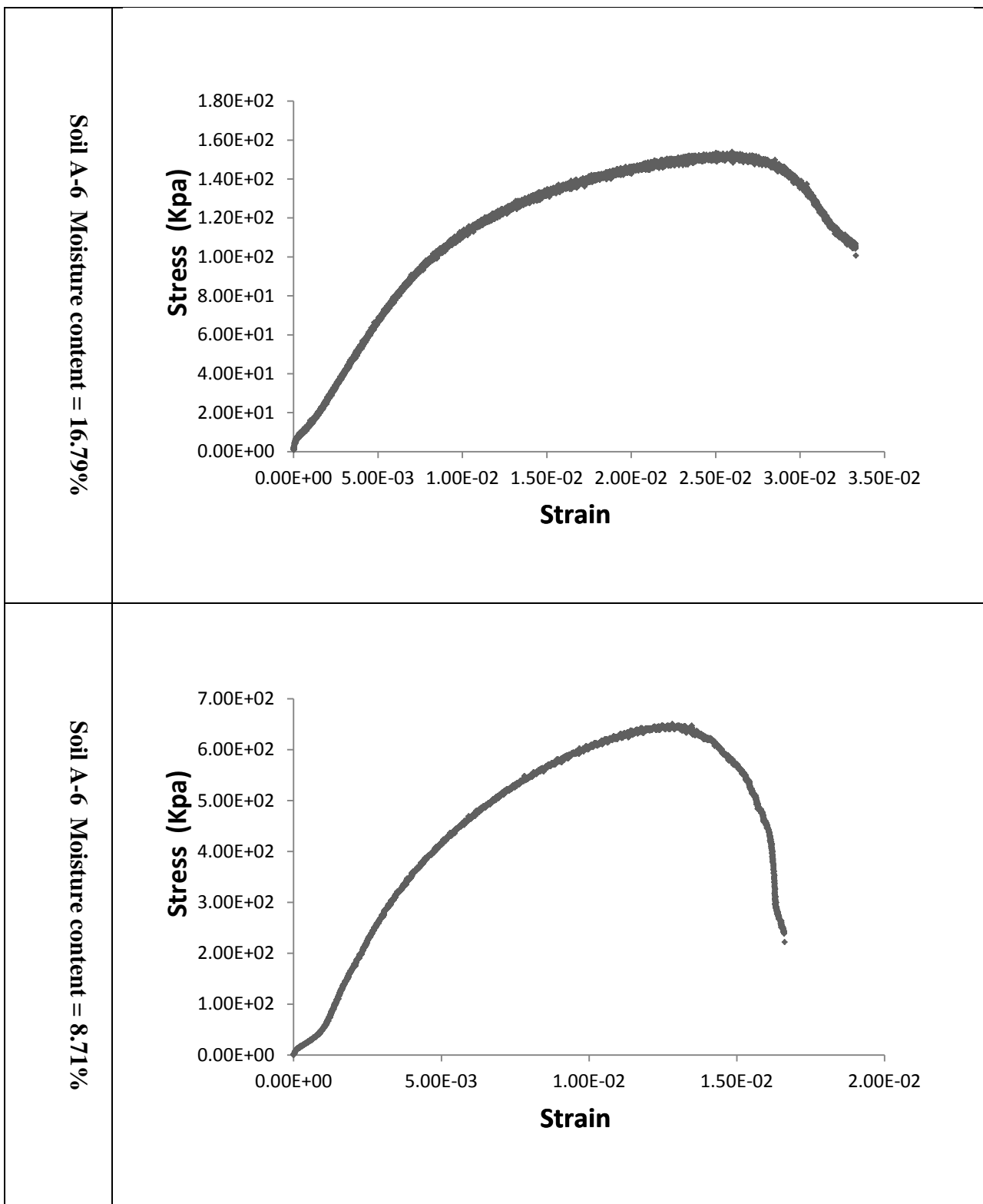
APPENDIX E

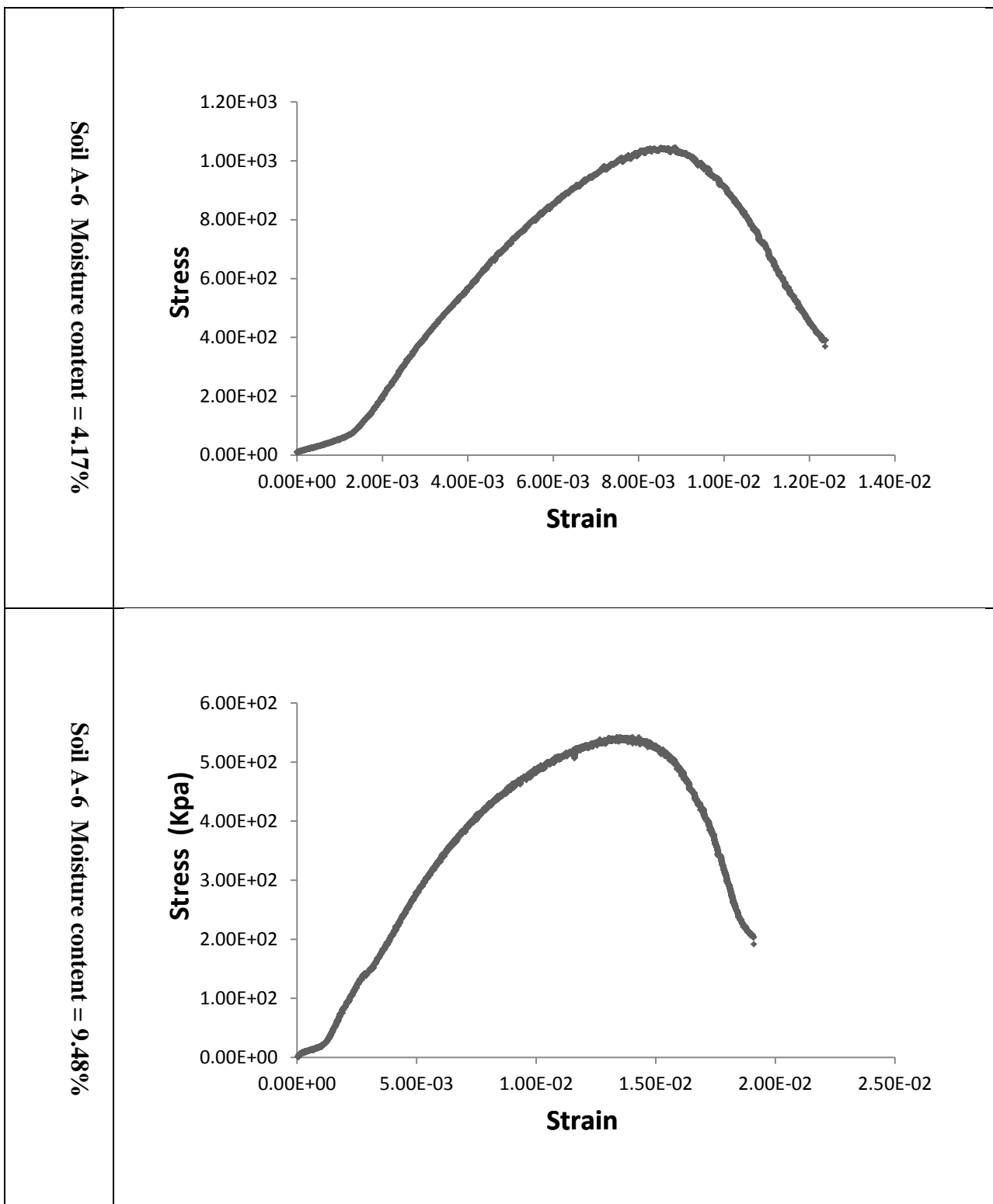
UNIAXIAL COMPRESSIVE STRENGTH TEST RESULTS OF CRREL SOILS

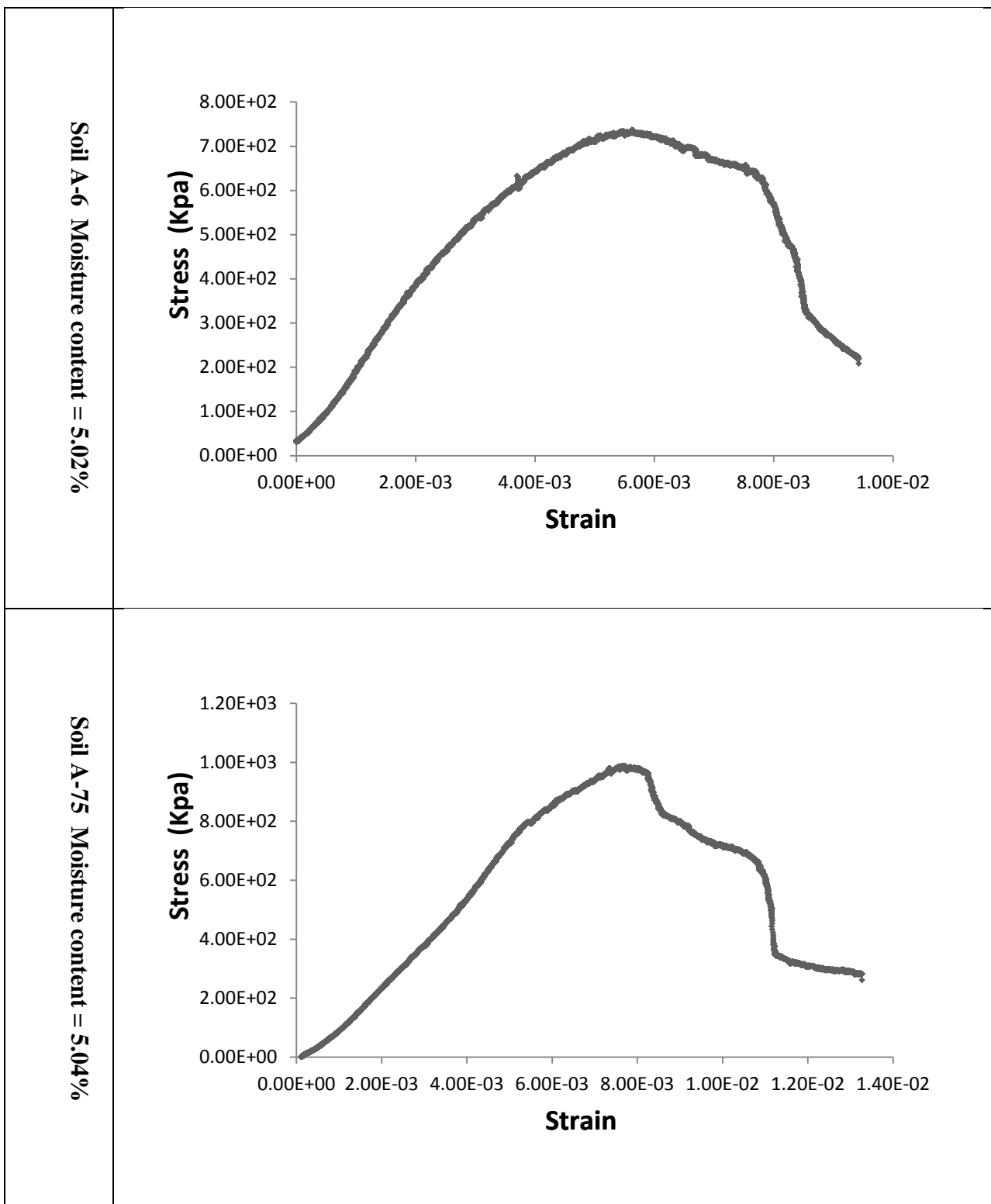


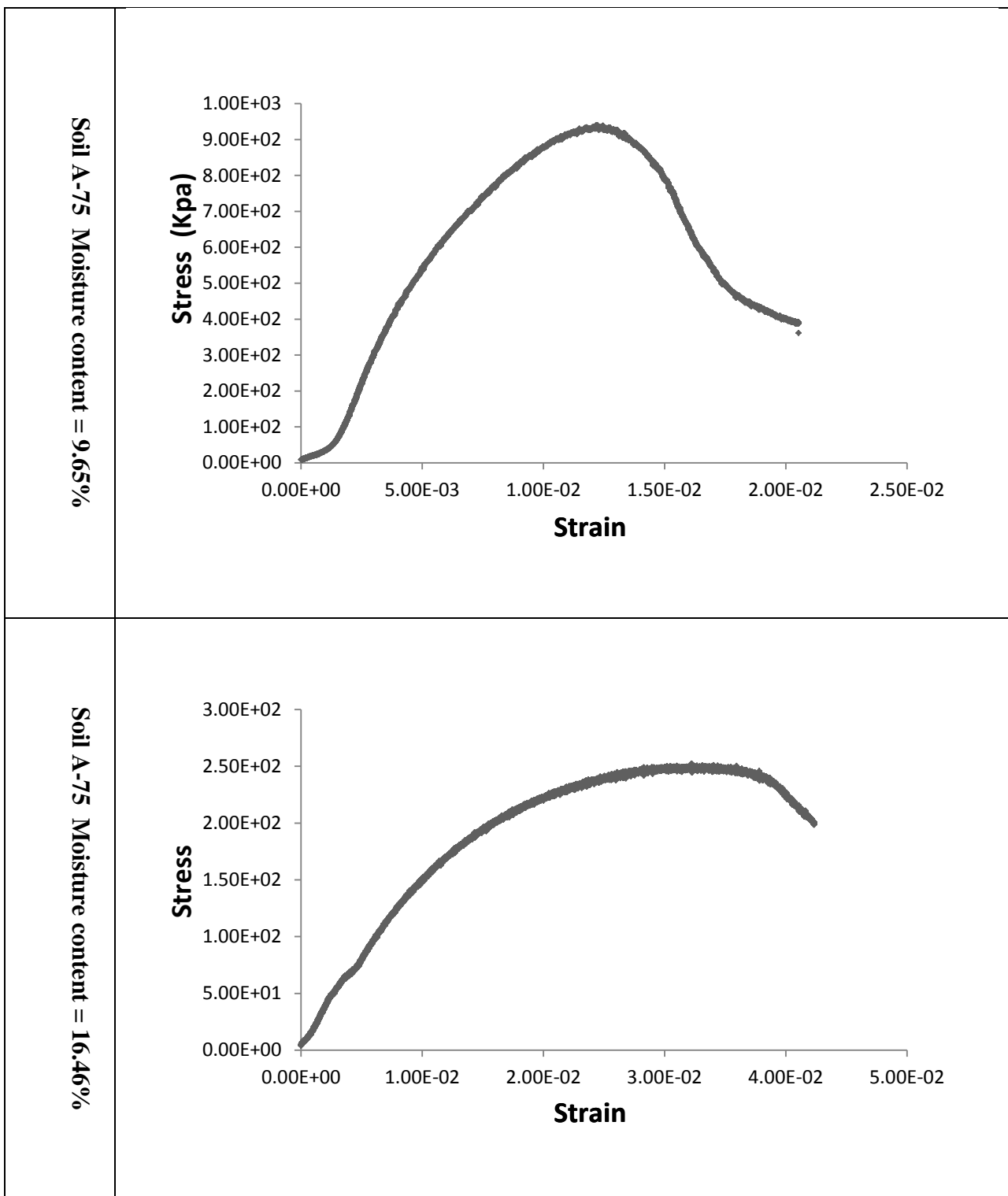


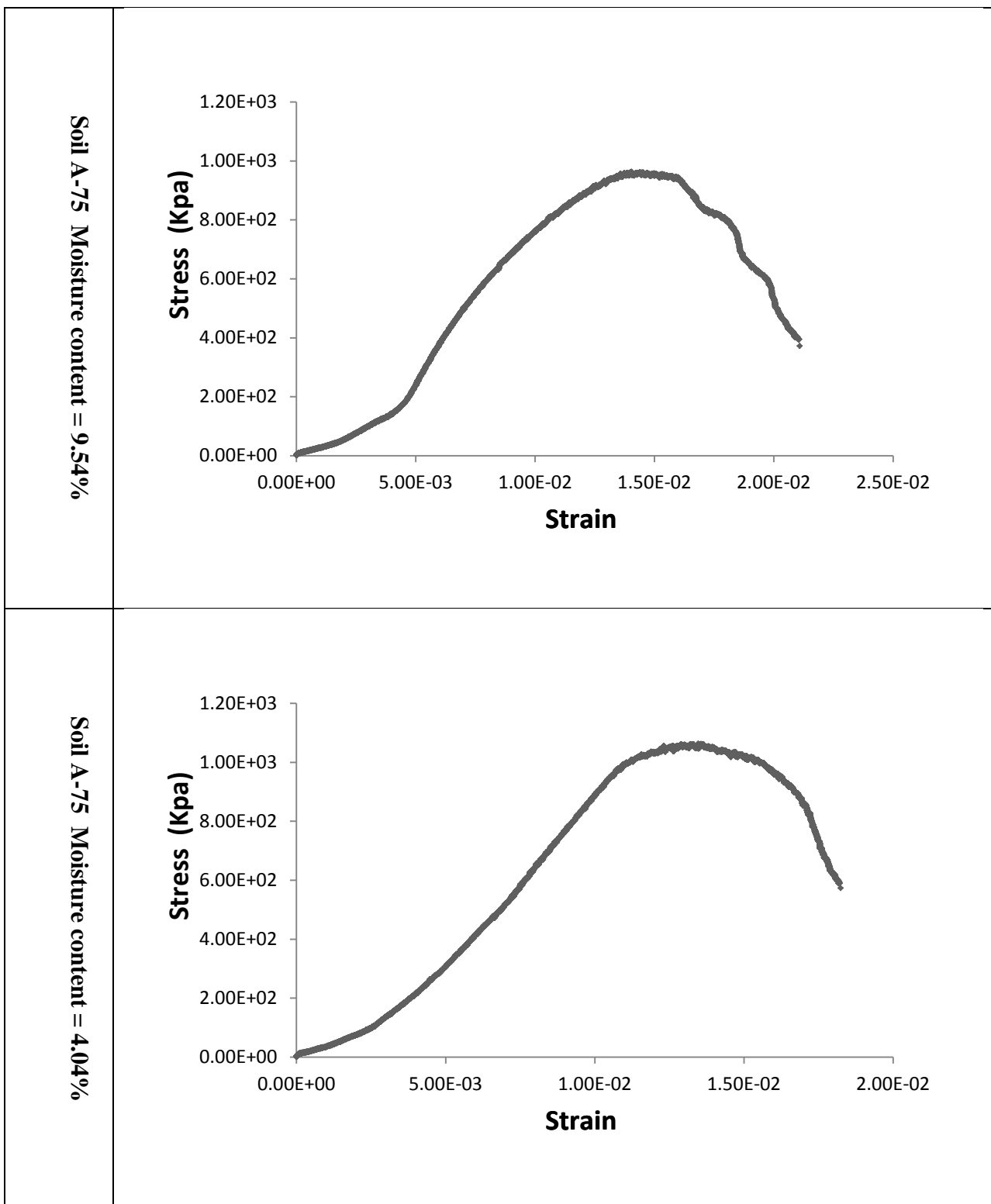












APPENDIX F

RESILIENT MODULUS TEST RESULTS ON BASE MATERIAL

Table F.1: Resilient Modulus Test Results – Sample 1

Sample 1 - MC=4.1%, DD=121.8 pcf = 88.7% of MDD				
Sequence	Deviator stress (kPa)	Contact stress (kPa)	Confine stress (kPa)	Axial Modulus (MPa)
1	4.833	2.078	22.297	172.53
2	6.922	4.038	21.577	97.51
3	9.678	6.242	21.476	79.30
4	5.956	3.454	34.496	147.49
5	13.032	6.993	34.497	100.51
6	23.431	10.388	34.5	102.03
7	16.819	6.852	68.899	159.09
8	40.648	13.719	68.892	151.25
9	66.991	20.605	68.89	154.95
10	17.493	6.843	103.396	202.92
11	30.163	10.229	103.395	184.34
12	70.993	20.58	103.39	186.90
13	31.772	10.253	134.951	213.70
14	46.016	13.704	134.991	211.52
15	100.206	27.47	134.999	213.84

Table F.2:: Resilient Modulus Test Results – Sample 2

SAMPLE 2: MC=3.8%, DD=120.5pcf = 87.8% of MDD				
Sequence	Deviator stress (kPa)	Contact stress (kPa)	Confine stress (kPa)	Axial Modulus (MPa)
1	4.624	2.082	22.647	333.44
2	5.219	4.201	21.843	120.84
3	13.364	6.342	21.736	159.86
4	5.58	3.486	34.498	175.15
5	16.086	7.02	34.499	185.75
6	25.145	10.479	34.498	151.39
7	17.763	6.983	68.899	282.65
8	39.645	14.058	68.896	197.75
9	66.616	20.806	68.891	184.75
10	17.523	6.869	103.396	365.39
11	29.381	10.397	103.393	253.06
12	71.598	20.733	103.386	222.61
13	29.742	10.712	135.196	271.99
14	44.19	13.894	135.226	271.47
15	100.497	27.694	135.234	243.84

Table F.3: Resilient Modulus Test Results – Sample 3

SAMPLE 3: MC=4.0%, DD=118.0pcf = 85.9% of MDD				
Sequence	Deviator stress (kPa)	Contact stress (kPa)	Confine stress (kPa)	Axial Modulus (MPa)
1	8.249	2.081	22.905	1,144.57
2	14.34	4.089	22.158	894.11
3	20.627	6.13	22.057	816.49
4	11.568	3.473	34.495	1,173.32
5	26.623	6.807	34.497	933.02
6	39.471	10.21	34.495	385.00
7	31.746	6.879	68.901	1,304.02
8	56.746	13.707	68.898	412.84
9	80.954	20.543	68.894	283.48
10	25.69	6.914	103.4	1,210.11
11	42.276	10.192	103.398	559.97
12	86.562	20.537	103.395	356.63
13	44.19	10.273	135.649	750.58
14	60.26	13.73	135.689	568.11
15	116.37	27.486	135.701	354.81

Table F.4: Resilient Modulus Test Results – Sample 4

SAMPLE 4: MC=4.1%, DD=127.4pcf = 92.7% of MDD				
Sequence	Deviator stress (kPa)	Contact stress (kPa)	Confine stress (kPa)	Axial Modulus (MPa)
1	2.881	2.03	22.967	71.57
2	7.072	4.05	22.276	105.07
3	10.932	6.397	22.205	84.38
4	4.189	3.419	34.497	90.08
5	13.85	7.069	34.497	99.89
6	23.976	10.405	34.496	100.89
7	17.169	6.849	68.899	152.84
8	42.069	13.688	68.895	152.18
9	67.484	20.558	68.89	155.19
10	18.301	6.789	103.397	191.90
11	31.891	10.207	103.396	182.37
12	73.676	20.57	103.392	190.97
13	34.554	10.253	136.037	218.40
14	49.129	13.746	136.059	219.88
15	105.206	27.515	136.054	226.89

Table F.5: Resilient Modulus Test Results – Sample 5

SAMPLE 5: MC=3.4%, DD=119.0pcf = 86.6% of MDD				
Sequence	Deviator stress (kPa)	Contact stress (kPa)	Confine stress (kPa)	Axial Modulus (MPa)
1	6.535	2.111	23.146	1,151.20
2	15.008	4.061	22.538	1,046.50
3	25.746	6.14	22.476	932.65
4	13.466	3.51	34.499	1,373.15
5	29.698	6.857	34.497	1,068.01
6	39.098	10.183	34.497	459.13
7	29.028	6.782	68.896	1,458.12
8	53.581	13.652	68.894	421.40
9	77.516	20.54	68.895	286.35
10	25.246	6.782	103.399	1,607.04
11	45.374	10.077	103.4	1,148.57
12	82.802	20.585	103.391	368.23
13	45.818	10.138	136.397	1,308.20
14	60.068	13.568	136.487	723.36
15	111.749	27.484	136.499	360.19

Table F.6: Resilient Modulus Test Results – Sample 6

SAMPLE 6: MC=4.3%, DD=126.7pcf = 92.3% of MDD				
Sequence	Deviator stress (kPa)	Contact stress (kPa)	Confine stress (kPa)	Axial Modulus (MPa)
1	1.63	2.102	22.915	385.66
2	12.858	4.02	22.283	643.97
3	21.356	6.183	22.236	459.52
4	8.219	3.452	34.498	918.66
5	23.456	6.864	34.5	387.27
6	31.662	10.341	34.498	227.03
7	25.275	6.827	68.899	623.39
8	47.209	13.706	68.896	255.01
9	72.554	20.588	68.893	215.20
10	21.435	6.827	103.399	578.61
11	35.155	10.167	103.398	336.38
12	77.728	20.515	103.393	265.85
13	37.514	10.186	135.893	414.70
14	52.634	13.696	135.955	359.56
15	106.902	27.46	135.952	280.94

Table F.7: Resilient Modulus Test Results – Sample 7

SAMPLE 7: MC=4.5%, DD=131.0pcf = 95.4% of MDD				
Sequence	Deviator stress (kPa)	Contact stress (kPa)	Confine stress (kPa)	Axial Modulus (MPa)
1	7.671	2.095	22.592	1,169.29
2	13.541	4.12	21.83	904.19
3	19.876	6.154	21.741	491.24
4	11.152	3.509	34.5	1,112.16
5	23.368	6.808	34.498	404.62
6	33.864	10.182	34.498	238.38
7	28.602	6.886	68.899	671.91
8	51.205	13.658	68.895	293.66
9	77.078	20.512	68.892	249.77
10	25.974	6.893	103.402	924.01
11	39.814	10.22	103.399	442.72
12	81.195	20.579	103.393	300.17
13	40.927	10.252	135.253	516.06
14	55.308	13.715	135.31	407.09
15	110.462	27.459	135.289	314.99

Table F.8: Resilient Modulus Test Results – Sample 8

SAMPLE 8: MC=4.4%, DD=132.8pcf = 96.7% of MDD				
Sequence	Deviator stress (kPa)	Contact stress (kPa)	Confine stress (kPa)	Axial Modulus (MPa)
1	7.642	2.083	22.166	1,142.23
2	13.952	4.107	21.200	1,006.66
3	22.128	6.138	21.050	895.02
4	11.086	3.474	34.503	1,170.83
5	28.873	6.818	34.499	1,000.93
6	44.794	10.226	34.498	661.19
7	31.279	6.887	68.898	1,164.08
8	60.526	13.674	68.898	603.05
9	83.939	20.567	68.896	357.87
10	26.857	6.882	103.150	1,236.57
11	47.736	10.216	103.211	1,181.84
12	88.438	20.580	103.210	451.28
13	47.445	10.238	134.328	1,222.01
14	66.605	13.743	134.353	1,151.86
15	115.764	27.486	134.364	406.70

Table F.9: Resilient Modulus Test Results – Sample 9

SAMPLE 9: MC=4.3%, DD=130.6pcf = 95.1% of MDD				
Sequence	Deviator stress (kPa)	Contact stress (kPa)	Confine stress (kPa)	Axial Modulus (MPa)
1	5.321	2.028	22.392	1,166.53
2	9.261	4.110	21.546	728.95
3	16.653	6.467	21.435	279.17
4	6.911	3.340	34.496	1,010.13
5	20.070	7.169	34.498	274.61
6	30.140	10.662	34.498	189.32
7	22.481	7.069	68.899	432.58
8	48.088	14.060	68.895	266.70
9	76.728	20.648	68.892	242.31
10	22.751	6.726	103.399	902.60
11	36.884	10.434	103.398	415.02
12	81.798	20.573	103.394	302.99
13	38.581	10.307	134.729	511.42
14	53.786	13.810	134.722	416.51
15	112.216	27.481	134.711	321.56

Table F.10: Resilient Modulus Test Results – Sample 10

SAMPLE 10: MC=4.5%, DD=127.4pcf = 92.8% of MDD				
Sequence	Deviator stress (kPa)	Contact stress (kPa)	Confine stress (kPa)	Axial Modulus (MPa)
1	4.390	2.098	22.435	1,079.66
2	15.836	4.102	21.554	1,098.42
3	19.789	6.074	21.430	1,347.83
4	13.824	3.522	34.498	1,416.64
5	20.697	7.050	34.500	1,332.98
6	40.752	10.382	34.496	557.83
7	24.040	7.052	68.896	1,680.93
8	55.801	13.986	68.897	525.22
9	84.005	20.838	68.897	352.36
10	23.395	7.283	103.399	1,868.16
11	45.084	10.533	103.398	1,400.13
12	88.236	20.718	103.393	448.60
13	44.285	10.480	134.680	1,566.42
14	62.344	13.793	134.680	1,115.52
15	119.653	27.490	134.664	432.34

Table F.11: Resilient Modulus Test Results – Sample 11

SAMPLE 11: MC=4.8%, DD=132.2 pcf = 96.2% of MDD				
Sequence	Deviator stress (kPa)	Contact stress (kPa)	Confine stress (kPa)	Axial Modulus (MPa)
1	3.133	2.098	22.989	720.75
2	9.671	4.185	22.418	462.50
3	15.272	6.505	22.335	177.07
4	6.609	3.494	34.498	657.83
5	19.408	7.125	34.495	224.78
6	29.463	10.507	34.496	175.64
7	23.597	6.968	68.898	461.81
8	47.773	13.789	68.897	246.04
9	75.763	20.628	68.894	225.36
10	22.432	6.814	103.4	890.29
11	36.729	10.287	103.398	407.93
12	81.15	20.616	103.393	283.61
13	39.095	10.243	136.372	540.64
14	54.589	13.734	136.437	419.40
15	111.698	27.55	136.401	303.03

Table F.12: Resilient Modulus Test Results – Sample 12

Sample 12 : MC=5.1%, DD=129.1pcf = 94% of MDD				
Sequence	Deviator stress (kPa)	Contact stress (kPa)	Confine stress (kPa)	Axial Modulus (MPa)
1	6.242	2.092	23.016	462.75
2	10.888	4.088	22.41	370.63
3	13.705	6.272	22.326	160.66
4	9.042	3.466	34.499	579.66
5	17.52	6.97	34.498	175.03
6	27.635	10.435	34.497	139.93
7	21.82	6.85	68.896	279.97
8	45.71	13.677	68.894	187.68
9	72.282	20.596	68.891	181.25
10	21.345	6.831	103.395	356.49
11	35.179	10.157	103.396	259.41
12	77.023	20.562	103.388	220.31
13	36.591	10.189	136.212	297.83
14	51.781	13.694	136.294	275.78
15	107.081	27.458	136.324	240.81

Table F.13: Resilient Modulus Test Results – Sample 13

SAMPLE 13: MC=5.0%, DD=132.0pcf = 96.1% of MDD				
Sequence	Deviator stress (kPa)	Contact stress (kPa)	Confine stress (kPa)	Axial Modulus (MPa)
1	2.365	2.099	22.006	492.93
2	11.517	4.106	20.934	388.26
3	17.254	6.113	20.782	208.37
4	10.289	3.482	34.503	623.37
5	22.241	6.874	34.497	253.92
6	33.647	10.191	34.494	206.04
7	25.923	6.932	68.898	405.07
8	52.277	13.730	68.895	272.90
9	80.544	20.617	68.894	254.61
10	25.312	6.903	102.509	583.98
11	39.957	10.267	102.567	384.53
12	84.580	20.665	102.538	305.34
13	41.042	10.267	133.950	440.44
14	56.730	13.759	133.959	389.87
15	115.39	27.580	133.959	331.76

Table F.14: Resilient Modulus Test Results – Sample 14

SAMPLE 14: MC=5.2%, DD=123.7pcf = 90.1% of MDD				
Sequence	Deviator stress (kPa)	Contact stress (kPa)	Confine stress (kPa)	Axial Modulus (MPa)
1	4.849	2.051	22.818	210.83
2	8.766	3.972	21.983	174.34
3	14.780	6.111	21.849	143.88
4	8.056	3.469	34.499	252.65
5	18.974	6.776	34.495	175.21
6	29.945	10.239	34.497	162.65
7	21.561	6.779	68.898	242.71
8	47.172	13.600	68.895	213.33
9	74.247	20.572	68.892	208.13
10	21.058	6.729	103.395	290.34
11	35.250	10.068	103.394	259.99
12	77.636	20.541	103.391	241.02
13	36.435	10.086	134.914	289.57
14	51.117	13.597	134.909	275.24
15	107.412	27.494	134.916	266.34

Table F.15: Resilient Modulus Test Results – Sample 15

SAMPLE 15: MC=5.5%, DD=125.8 pcf = 91.6% of MDD				
Sequence	Deviator stress (kPa)	Contact stress (kPa)	Confine stress (kPa)	Axial Modulus (MPa)
1	3.351	2.093	22.838	836.63
2	10.841	4.035	22.225	882.21
3	21.778	6.111	22.163	600.21
4	8.897	3.456	34.5	1,197.30
5	23.615	6.851	34.498	408.09
6	31.812	10.437	34.494	214.03
7	25.864	6.799	68.9	582.28
8	48.348	13.69	68.893	255.49
9	76.082	20.531	68.895	233.27
10	24.954	6.869	103.404	1,229.76
11	38.846	10.188	103.403	471.18
12	80.333	20.503	103.395	290.38
13	40.775	10.195	135.807	588.61
14	55.389	13.69	135.868	437.92
15	108.441	27.455	135.879	291.14

Table F.16: Resilient Modulus Test Results – Sample 16

SAMPLE 16: MC=5.5%, DD=132.1pcf = 96.2% of MDD				
Sequence	Deviator stress (kPa)	Contact stress (kPa)	Confine stress (kPa)	Axial Modulus (MPa)
1	6.695	2.109	23.052	956.31
2	16.962	4.097	22.464	1,118.88
3	20.757	6.197	22.419	1,202.82
4	13.886	3.497	34.499	1,231.94
5	28.95	6.894	34.498	766.69
6	37.373	10.522	34.497	548.98
7	21.631	6.84	68.896	1,489.56
8	51.137	13.874	68.896	403.11
9	77.621	20.571	68.893	283.44
10	20.249	6.792	103.401	1,611.08
11	42.013	10.248	103.399	1,341.70
12	81.729	20.504	103.391	338.72
13	41.598	10.179	136.398	1,416.31
14	57.044	13.69	136.507	676.37
15	109.967	27.422	136.425	324.73

Table F.17: Resilient Modulus Test Results – Sample 17

SAMPLE 17: MC=5.3%, DD=127.8 pcf = 93.1% of MDD				
Sequence	Deviator stress (kPa)	Contact stress (kPa)	Confine stress (kPa)	Axial Modulus (MPa)
1	5.733	2.082	22.801	593.17
2	7.077	4.249	22.139	177.98
3	13.563	6.438	22.081	122.24
4	6.715	3.452	34.501	562.89
5	17.868	7.139	34.499	179.03
6	27.361	10.48	34.494	157.27
7	21.895	6.983	68.901	370.48
8	44.704	13.786	68.893	241.37
9	69.812	20.642	68.891	221.46
10	20.612	6.846	103.403	643.49
11	34.065	10.264	103.403	355.85
12	73.788	20.595	103.393	268.40
13	34.936	10.25	135.78	400.87
14	49.265	13.72	135.787	351.07
15	102.405	27.521	135.792	291.52

Table F.18: Resilient Modulus Test Results – Sample 18

SAMPLE 18: MC=5.3%, DD=121.6pcf = 88.6% of MDD				
Sequence	Deviator stress (kPa)	Contact stress (kPa)	Confine stress (kPa)	Axial Modulus (MPa)
1	1.956	2.099	23.041	826.95
2	10.936	4.107	22.464	1,133.72
3	24.474	6.175	22.426	730.99
4	8.658	3.437	34.5	1,361.99
5	28.12	6.882	34.499	800.66
6	39.42	10.335	34.498	407.86
7	29.454	6.86	68.899	1,469.08
8	55.222	13.713	68.895	420.73
9	83.312	20.555	68.893	319.98
10	25.271	6.898	103.399	1,718.92
11	44.252	10.206	103.4	960.27
12	86.368	20.551	103.394	385.06
13	44.636	10.235	136.279	1,059.41
14	59.926	13.668	136.402	659.54
15	115.459	27.484	136.398	367.69

Table F.19: Resilient Modulus Test Results – Sample 19

SAMPLE 19: MC=5.7%, DD=132.6pcf = 96.6% of MDD				
Sequence	Deviator stress (kPa)	Contact stress (kPa)	Confine stress (kPa)	Axial Modulus (MPa)
1	6.576	2.103	23.168	578.92
2	14.439	4.076	22.615	397.39
3	17.206	6.156	22.547	197.08
4	12.209	3.504	34.498	553.37
5	20.567	6.829	34.497	215.12
6	29.684	10.271	34.498	162.68
7	24.353	6.883	68.896	362.89
8	48.087	13.715	68.893	218.89
9	74.876	20.59	68.895	199.94
10	23.735	6.887	103.396	487.97
11	37.099	10.228	103.397	302.50
12	80.074	20.594	103.387	244.88
13	38.872	10.239	136.694	355.89
14	54.453	13.771	136.686	322.93
15	111.601	27.533	136.676	277.29

Table F.20: Resilient Modulus Test Results – Sample 20

SAMPLE 20: MC=5.9%, DD=133.2pcf = 97.0% of MDD				
Sequence	Deviator stress (kPa)	Contact stress (kPa)	Confine stress (kPa)	Axial Modulus (MPa)
1	0.403	2.12	22.854	155.37
2	13.608	4.073	22.112	913.17
3	24.172	6.216	22.009	657.91
4	9.808	3.454	34.499	1,199.69
5	29.75	6.861	34.501	868.21
6	36.643	10.231	34.496	337.28
7	31.631	6.863	68.898	1,262.95
8	53.83	13.678	68.897	360.70
9	79.617	20.495	68.892	271.85
10	27.034	6.897	103.396	1,467.33
11	47.863	10.197	103.399	1,109.62
12	86.361	20.58	103.388	375.98
13	48.4	10.283	135.575	1,372.33
14	65.322	13.727	135.671	994.02
15	116.73	27.438	135.577	404.10

Table F.21: Resilient Modulus Test Results – Sample 21

SAMPLE 21: MC=5.9%, DD=126.0pcf = 91.8% of MDD				
Sequence	Deviator stress (kPa)	Contact stress (kPa)	Confine stress (kPa)	Axial Modulus (MPa)
1	4.045	2.055	23.087	143.78
2	7.682	4.036	22.547	118.13
3	12.089	6.242	22.519	108.91
4	7.246	3.448	34.498	168.81
5	14.734	7.118	34.498	131.06
6	24.701	10.613	34.497	128.96
7	15.246	7.232	68.9	172.41
8	41.113	14.104	68.893	167.99
9	69.579	20.983	68.89	178.86
10	14.482	7.073	103.395	221.00
11	29.323	10.484	103.394	206.77
12	73.423	20.95	103.389	207.90
13	30.318	10.456	136.272	226.83
14	46.126	14.017	136.355	229.57
15	103.771	27.779	136.359	229.54

Table F.22: Resilient Modulus Test Results – Sample 22

SAMPLE 22: MC=6.1%, DD=130.8pcf = 95.3% of MDD				
Sequence	Deviator stress (kPa)	Contact stress (kPa)	Confine stress (kPa)	Axial Modulus (MPa)
1	4.956	2.066	22.320	617.49
2	10.194	4.091	21.300	652.59
3	19.260	6.194	21.154	256.61
4	9.674	3.511	34.499	718.32
5	22.929	6.889	34.497	288.04
6	33.229	10.271	34.498	217.41
7	25.856	6.881	68.898	481.36
8	50.453	13.649	68.896	275.10
9	77.548	20.557	68.893	247.18
10	24.678	6.844	103.399	691.17
11	38.920	10.191	103.398	396.40
12	81.994	20.593	103.393	298.36
13	40.281	10.170	134.413	457.56
14	55.564	13.705	134.444	389.69
15	113.905	27.543	134.442	325.71

Table F.23: Resilient Modulus Test Results – Sample 23

SAMPLE 23: MC=6.2%, DD=123.4pcf = 89.9% of MDD				
Sequence	Deviator stress (kPa)	Contact stress (kPa)	Confine stress (kPa)	Axial Modulus (MPa)
1	4.114	2.097	22.349	737.22
2	14.956	4.103	21.400	796.83
3	18.121	6.301	21.262	1,134.15
4	13.13	3.500	34.494	915.64
5	21.601	7.241	34.497	1180.97
6	35.911	10.267	34.498	710.31
7	18.441	7.190	68.900	1,576.11
8	53.185	14.066	68.894	507.54
9	82.886	20.840	68.894	360.97
10	18.906	6.918	103.398	1,802.45
11	40.017	10.725	103.399	1,425.65
12	87.637	20.730	103.393	423.30
13	39.662	10.771	134.459	1,469.46
14	58.183	14.027	134.483	745.78
15	118.229	27.762	134.491	397.83

Table F.24: Resilient Modulus Test Results – Sample 24

SAMPLE 24: MC=6.5%, DD=128.0pcf = 93.2% of MDD				
Sequence	Deviator stress (kPa)	Contact stress (kPa)	Confine stress (kPa)	Axial Modulus (MPa)
1	1.313	2.115	23.276	372.23
2	10.178	4.019	22.754	502.38
3	17.767	6.189	22.703	280.70
4	8.148	3.419	34.498	857.98
5	21.155	6.878	34.498	275.91
6	32.466	10.244	34.497	211.45
7	23.519	6.873	68.897	395.11
8	48.97	13.696	68.894	256.41
9	76.447	20.571	68.892	234.33
10	22.242	6.854	103.397	542.07
11	37.164	10.175	103.393	358.93
12	80.715	20.606	103.386	280.80
13	38.155	10.195	136.506	401.41
14	53.399	13.694	136.613	352.56
15	110.656	27.526	136.547	297.96

Table F.25: Resilient Modulus Test Results – Sample 25

SAMPLE 25: MC=6.2%, DD=118.2pcf = 86.1% of MDD				
Sequence	Deviator stress (kPa)	Contact stress (kPa)	Confine stress (kPa)	Axial Modulus (MPa)
1	5.852	2.058	23.218	536.45
2	7.593	4.099	22.6	287.59
3	14.076	6.449	22.541	181.84
4	8.185	3.489	34.499	375.44
5	16.636	7.242	34.5	198.96
6	27.751	10.835	34.497	173.08
7	17.23	7.337	68.899	298.29
8	44.274	14.221	68.895	226.24
9	73.077	20.976	68.891	219.89
10	14.663	7.086	103.4	339.19
11	31.477	10.557	103.397	280.66
12	77.102	20.86	103.393	261.91
13	32.112	10.541	136.404	317.69
14	48.491	14.116	136.53	307.60
15	107.125	27.599	136.474	288.37

Table F.26: Resilient Modulus Test Results – Sample 26

SAMPLE 26: MC=6.6%, DD=136.7pcf = 99.6% of MDD				
Sequence	Deviator stress (kPa)	Contact stress(kPa)	Confine stress (kPa)	Axial Modulus (MPa)
1	6.169	2.078	23.13	680.50
2	15.361	4.079	22.519	1,016.87
3	23.155	6.201	22.464	563.17
4	9.158	3.441	34.5	979.34
5	25.655	6.855	34.5	531.12
6	35.362	10.374	34.501	284.93
7	26.79	6.818	68.896	792.93
8	51.137	13.667	68.896	310.98
9	77.129	20.564	68.893	254.00
10	25.633	6.847	103.398	1,338.19
11	39.438	10.223	103.397	490.36
12	81.536	20.56	103.393	310.41
13	40.792	10.204	136.448	570.30
14	56.022	13.655	136.503	459.09
15	110.755	27.476	136.508	321.18